Tidal Bridge Dynamics

Optimising the dynamic response due to wind, waves and current

G. Dorgelo

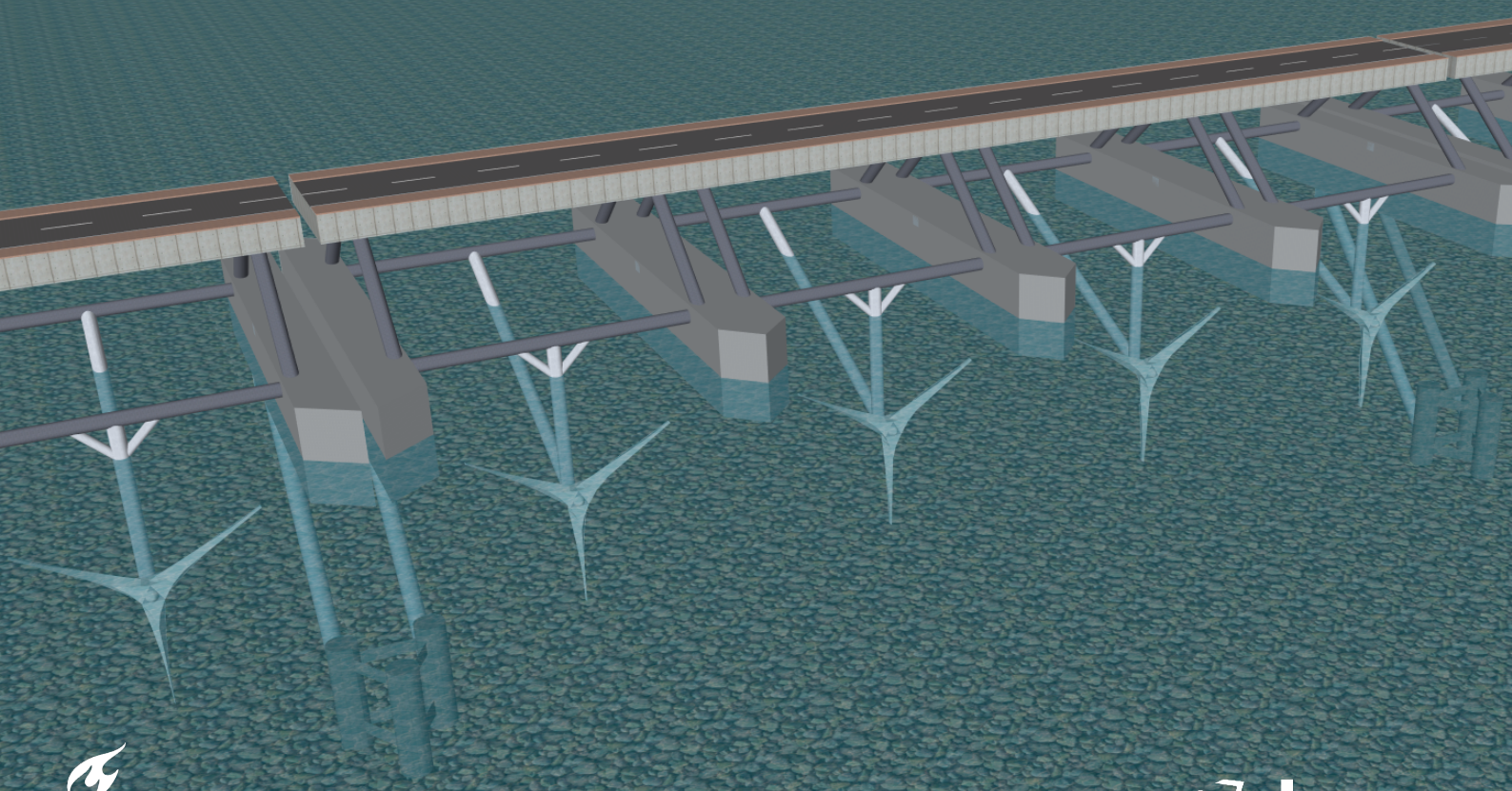

TU Delft

bam

Tidal Bridge Dynamics

Optimising the dynamic response due to wind, waves and current

by:
G. Dorgelo, 4363299

to obtain the degree of Master of Science
at the Delft University of Technology,
to be defended publicly on February 27, 2020 at 4:00 PM.

Project duration:	July 2019 – March, 2020	
Supervisors:	Prof. dr. ir. Uijttewaal, W.S.J. (Wim),	Delft University of Technology (Chairman)
	Ir. Molenaar, W.F. (Wilfred),	Delft University of Technology
	Ir. Vaniushkina, V. (Valentina),	Delft University of Technology
	Ir. Reedijk, B. (Bas),	BAM Infraconsult

TU Delft

bam

Preface

Before you lies the thesis named 'Tidal Bridge Dynamics; Optimising the dynamic response due to wind, waves and current', a report describing the computation of the dynamic behaviour of a new type of bridge: the Tidal Bridge. The report has been written to obtain a masters degree in Civil Engineering at Delft University of Technology, which combines the interest of two fields in Civil Engineering corresponding with the two tracks I followed at the university: 'Hydraulic Engineering' and 'Structural Engineering'. The floating structure examined in this thesis forms the perfect interface between the two subjects, keeping me engaged from July 2019 to February 2020.

The project was executed in collaboration with BAM Infraconsult; whom facilitated both a working environment and the appropriate necessities to create what is in this report. The expertise of the water-department helped me identify crucial investigation points, creating a well-defined overview of the elements needed to face the problem faced.

Without the help of my supervisors, this report would not be what it is today. I would like to thank all of them for their guidance in project direction and their knowledge concerning the different elements that contributed to the investigation. Furthermore, I would like to thank my parents in allowing me to use their backyard, to create and use a scale model of the Tidal Bridge. The space they provided was vital for my research. My brother was of great assistance too, helping me locate the appropriate materials for the experiments. Lastly, I would like to thank my friends with whom I have debated various challenges. Without their interest in the project and their ability to keep me motivated to find solutions, challenges would have formed larger obstructions.

I hope you enjoy reading this work.

Gerjan Dorgelo

Gouda, February 2020

Abstract

Currently, there is no infrastructure between the two Indonesian islands Flores and Adonara. The islands are separated by the Larantuka Strait, which has a width varying between 600 and 1000 meters. The local government would like a bridge between the two islands. However, as the water in the 18 meter deep strait is heavily subjected to tidal forces - creating a tidal amplitude of about 1.5 m and tidal flow velocities ranging up to 4.5 m/s - structural design is challenging. As traditional bridges were deemed too expensive, a new type of bridge was introduced: the 'Tidal Bridge'. The pendulum founded floating bridge, which is proposed to span the deepest 400 meters of the cross-section, is designed with tidal turbines attached to the bottom of the structure. The energy production mitigates the financial burden that the 225 million US dollar Palmerah Tidal Bridge will bring. At the time of writing, a pre-feasibility study has been performed by Antea, proposing initial structural dimensions. BAM took over the design process, which lead to questions regarding the dynamic stability of the design. The objective of this report is to answer the following two research questions:

1. How can the dynamic response due to two-dimensional forcing of a Tidal Bridge be determined?
2. What design choices can further optimise the dynamic behaviour of a Tidal Bridge?

A numeric tool has been created to predict the dynamics of the proposed design as function of an input of wind, waves, and current. Based on (experimental) literature, hydrodynamic coefficients determining the fluid-structure interaction were determined. The complex shape of the floaters did not allow appropriate validation of the accompanying added mass and radiation damping coefficients. Comparison with a model constructed in Ansys Aqwa showed values of similar magnitude, but precise magnitudes could not be determined. In order to find these important coefficients, a set of experiments has been performed to determine the added mass (moment of inertia) and radiation damping (moment of inertia) for heave and roll motion. The experiments showed that the added mass equations for heave were well defined, while the added mass moment of inertia equations for roll motion deviated up to 250 per cent. The acquired data was used to find better relations between the added mass (moment of inertia) and the floater dimensions. Please note, the empirical relations are based on limited data and with little mathematical background. Hence, the relations should be used with care. The radiation damping coefficients that were also extracted from the experiments showed no clear trend, but did confirm that the hand-calculations were of correct magnitude.

Using the constructed model, forcing characteristics of the Tidal Bridges are investigated. In these computations, the Palmerah Tidal Bridge dimensions are used as a case study. It was noted that the extreme non-linearity of different elements of the problem (changing pendulum angle, hydrodynamic pressure field, and particle velocity/acceleration field) do not allow for linear approximation. While a linear mass-spring system predicts that the natural period is about 6.7 seconds, the maximum dynamic amplitude is found for wave periods of 9 seconds. This coincides with the largest expected waves for the Palmerah Tidal Bridge location. Reducing the natural period of the design is recommended. Additionally, research was done into the contribution of the various types of forcing, where it was found that traffic weight has negligible effect on the dynamics. Wind forces add only a few percent to the pendulum forces, but do have a significant contribution to the displacements. Furthermore, research into the impact of an approaching wave field showed that accelerations during first impact may overshoot the maximum steady state acceleration by more than 200 per cent.

A parametric study on the dynamics of Tidal Bridges was performed, which did research into the the forcing combinations that lead to most amplification of the dynamics. It shows that different loading combinations are governing for accelerations in the three different degrees of freedom present in a two-dimensional system. In here, difference was found for the dynamic behaviour induced by waves from the two different wave directions, leading to two sets of three forcing combinations. This data was used to investigate the effect of three design parameters: the angle of the pendulum, the hinge location of the pendulum and the depth of the strait. Moreover, a sensitivity study is performed on a set of parameters defining the Tidal Bridge. It shows that the mass of the segment, the added mass, the floater length, the design turbine force, and the pendulum angle are most important if it comes to design optimisation. Based on the parametric study and the forcing characteristics, conclusions and recommendations are made for improvements of Tidal Bridge designs in general and more specifically: the Palmerah Tidal Bridge.

Contents

List of Figures

List of Tables

List of Symbols

Latin characters

a	=	Amplitude	[m]
	=	Observed value	[..]
	=	Boundary value	[..]
A	=	Area	[m^2]
A_c	=	Cross-sectional area of channel	[m^2]
A_s	=	Cross-sectional area of submerged structure	[m^2]
B	=	Width	[m]
c	=	Damping constant	[Ns/m]
C	=	Damping	[Ns/m]
C_a	=	Added mass coefficient	[-]
$C_{added,heave}$	=	Added mass coefficient for heave motion	[-]
$C_{added,roll}$	=	Added mass moment of inertia coefficient for roll motion	[-]
$C_{a,l,h}$	=	Added mass coefficient, large floater, horizontal	[-]
$C_{a,s,h}$	=	Added mass coefficient, small floater, horizontal	[-]
$C_{a,l,v}$	=	Added mass coefficient, large floater, vertical	[-]
$C_{a,s,v}$	=	Added mass coefficient, small floater, vertical	[-]
$C_{a,l,rot}$	=	Added mass coefficient, large floater, rotation about x	[-]
$C_{a,s,rot}$	=	Added mass coefficient, small floater, rotation about x	[-]
C_{damp}	=	Radiation damping coefficient	[-]
C_{DS}	=	Drag coefficient	[-]
C_{gap}	=	Reduction coefficient by influence of gap in between floaters	[-]
C_{inf}	=	Reduction coefficient for non-infinite width	[-]
$C_{Radiation}$	=	Radiation damping matrix	[-]
C_t	=	Turbine coefficient	[-]
C_{tip}	=	Reduction coefficient for pointed floaters	[-]
d	=	Draught	[m]
	=	Water depth	[m]
d_{fl}	=	Draught of floater	[m]
$d_{fl,l}$	=	Horizontal distance large floater to COG	[m]
$d_{fl,s}$	=	Horizontal distance small floater to COG	[m]
d_p	=	Distance between pendulums from single segment	[m]
D	=	Diameter	[m]
E	=	Young's modulus of steel	[N/m^2]
E_{spruce}	=	Young's modulus of spruce	[N/m^2]
f	=	Force	[N]
f_n	=	Natural frequencies	[rad/s]
F	=	Force	[N]
F	=	Fetch length	[m]
	=	Form Factor	[-]
F_{cr}	=	Critical buckling force	[N]
F_d	=	Drag force	[N]
$F_{d,fl}$	=	Drag force on floater	[N]
F_w	=	Inertia force	[N]
F_{hydro}	=	Hydrodynamic mass force	[N]
F_{krylov}	=	Krylov force	[N]
F_{load}	=	Longitudinal loading force	[N]
F_w	=	Wind force	[N]
g	=	Gravitational acceleration	[m/s^2]

h	=	Water depth	[m]
h_{COG}	=	Height of COG relative to bottom of floaters	[m]
h_{tide}	=	Tidal level	[m]
H	=	Height	[m]
	=	Wave height	[m]
H_{grid}	=	Height of grid cell	[m]
H_{max}	=	Maximum wave height	[m]
H_{plate}	=	Height of deck plate scale model	[m]
H_s	=	Significant wave height	[m]
i	=	Iteration step	[-]
I	=	Second moment of inertia	[m^4]
J	=	Moment of inertia	[kgm^2]
J_s	=	Moment of inertia of segment	[kgm^2]
J_t	=	Moment of inertia of traffic	[kgm^2]
$J_{f,s,z}$	=	Mass moment of inertia about z-axis for small floaters	[kgm^2]
k	=	Spring constant	[N/m]
	=	Wave number	[1/m]
$k_{c_{1,y}}$	=	Spring constant of connection 1, y-direction	[N/m]
$k_{c_{1,z}}$	=	Spring constant of connection 1, z-direction	[N/m]
$k_{c_{2,y}}$	=	Spring constant of connection 2, y-direction	[N/m]
$k_{c_{2,z}}$	=	Spring constant of connection 2, z-direction	[N/m]
k_{hydro}	=	Hydrostatic spring stiffness	[N/m]
$k_{hydro,l}$	=	Hydrostatic spring stiffness under large floater	[N/m]
$k_{hydro,s}$	=	Hydrostatic spring stiffness under small floater	[N/m]
k_p	=	Pendulum spring stiffness	[N/m]
k_{p_1}	=	Spring constant of pendulum 1	[N/m]
k_{p_2}	=	Spring constant of pendulum 2	[N/m]
k_r	=	Rotational spring stiffness	[N/rad]
k_{sp_1}	=	Spring constant of spudpole 1	[N/m]
k_{sp_2}	=	Spring constant of spudpole 2	[N/m]
K	=	Spring	[N/m]
K_c	=	Spring matrix due to segment connections	[-]
K_{hydro}	=	Spring matrix due to hydrostatic pressure	[-]
K_p	=	Spring matrix due to pendulums	[-]
K_{sp}	=	Spring matrix due to spudpoles	[-]
L	=	Length	[m]
	=	Wave length	[m]
L_{grid}	=	Length of grid cell	[m]
L_{fl}	=	Length of floater	[m]
$L_{fl,l}$	=	Length of large floaters	[m]
$L_{fl,s}$	=	Length of small floaters	[m]
L_s	=	Length of segment	[m]
L_p	=	Length of pendulum	[m]
L_{plate}	=	Length of deck plate scale model	[m]
m	=	Mass of object	[kg]
M	=	Mass of system	[kg]
	=	Bending moment	[N/m]
$M_{d,fl}$	=	Moment by drag force on floaters	[N]
M_{lorry}	=	Approximate mass of a lorry	[kg]
M_s	=	Mass of segment	[kg]
M_{own}	=	Own mass matrix	[kg]
M_{added}	=	Added mass	[kg]
$M_{added+MG}$	=	Added mass including marine growth	[kg]
$M_{added,heave}$	=	Added mass for heave motion	[kg]
$M_{added,roll}$	=	Added mass moment of inertia for roll motion	[kgm^2]

M_t	=	Mass of traffic	[kg]
M_{total}	=	Total mass	[kg]
N	=	Number of waves	[-]
N_{fl}	=	Number of floaters	[-]
$N_{fl,l}$	=	Number of large floaters	[-]
$N_{fl,s}$	=	Number of small floaters	[-]
N_{lanes}	=	Number of traffic lanes	[-]
$N_{segments}$	=	Number of segments	[-]
N_{Ursell}	=	Ursell number	[-]
p	=	Pressure	[N/m^2]
p_n	=	Natural period	[s]
q	=	Distributed load	[N/m]
q_w	=	Distributed load by wind	[N/m]
Q_{road}	=	Distributed load on top of road	[N/m^2]
$Q_{sidewalk}$	=	Distributed load on top of side walk	[N/m^2]
Rx	=	Rotation about x-axis	[rad]
Ry	=	Rotation about y-axis	[rad]
Rz	=	Rotation about z-axis	[rad]
t	=	Time	[s]
T	=	Draught	[m]
	=	Wave period	[s]
T_{smooth}	=	Force smoothening time	[s]
u	=	Flow velocity	[m/s]
$U_{10,max}$	=	Maximum wind speed	[m/s]
v	=	Structure velocity	[m/s]
V	=	Volume	[m^3]
	=	Shear force	[N]
V_l	=	Vessel limit velocity	[m/s]
V_s	=	Relative velocity submerged structure	[m/s]
V_R	=	Representative volume	[m^3]
w	=	Displacement	[m]
W	=	Width	[m]
W_{fl}	=	Width of floater	[m]
$W_{fl,l}$	=	Width of large floaters	[m]
$W_{fl,s}$	=	Width of small floaters	[m]
W_{road}	=	Width of road	[m]
W_{plate}	=	Width of deck plate scale model	[m]
$W_{sidewalk}$	=	Width of side walk	[m]
x	=	Displacement	[m]
	=	Longitudinal direction (surge)	[-]
	=	Variable	[..]
y	=	Transverse direction (sway)	[-]
y_p	=	y-coordinate of upper hinge relative to COG	[m]
$y_{p,bottom}$	=	y-coordinate of bottom hinge relative to COG for zero tide	[m]
$y_{p,bottom,tide}$	=	y-coordinate of bottom hinge relative to COG for deviating tide	[m]
z	=	Vertical direction (heave)	[-]
$z_{p,bottom}$	=	z-coordinate of bottom hinge relative to COG for zero tide	[m]
$z_{p,bottom,tide}$	=	z-coordinate of bottom hinge relative to COG for deviating tide	[m]
z_p	=	z-coordinate of upper hinge relative to COG	[m]
z_t	=	z-coordinate of centre of turbines relative to COG	[m]

Greek characters

α	=	Rotation angle	[rad]
α_0	=	Angle of pendulums at zero tide	[rad]
α_{p1}	=	Angle of pendulum 1	[rad]
α_{p2}	=	Angle of pendulum 2	[rad]
δ	=	Change	[-]
Δ	=	Difference	[-]
ϵ	=	Contribution factor	[-]
ζ	=	Damping ratio	[-]
η	=	Water level	[m]
θ	=	Rotation about transverse direction (pitch)	[-]
λ	=	Scale factor	[-]
μ	=	Mean value	[..]
ρ	=	Density	[kg/m^3]
ρ_m	=	Modelling density	[kg/m^3]
σ	=	Standard deviation	[..]
ϕ	=	Phase shift	[rad]
	=	Potential flow	[-]
	=	Rotation about longitudinal direction (roll)	[-]
	=	Rotation of member	[Nm]
ψ	=	Rotation about vertical direction (yaw)	[-]
ω	=	Angular frequency	[rad/s]
ω_0	=	Natural frequency	[rad/s]

Special operations and characters

ø	=	Diameter	[m]
$\mathcal{O}$	=	Big O notation	
$\dot{x}$	=	Derivative of x with respect to time	
$\ddot{x}$	=	Second derivative of x with respect to time	
$\hat{x}$	=	Amplitude x	
$\boldsymbol{x}$	=	Vector x	
$\boldsymbol{X}$	=	Matrix x	

Abbreviations

COG	=	Centre Of Gravity
DOF	=	Degrees Of Freedom
EOM	=	Equations Of Motion
FOV	=	Field Of View
FRP	=	Fibre-Reinforced Polymers
KC	=	Keulegan Carpenter
MSL	=	Mean Sea Level
RMSE	=	Root Mean Square Error
SLS	=	Serviceable Limit State
UC	=	Unity Check
ULS	=	Ultimate Limit State

1

Introduction

1.1. Background information

Indonesia is a country consisting out of 17,508 different islands. Two of the larger islands, Flores and Adonara, are currently separated by the Larantuka Strait, a waterway varying between 600 and 1000 meters wide. A connection between the two islands is desired, as they have a combined population of about two million and are developing at a fast pace. Originally, multiple types of bridge designs were considered. However, the large water depth combined with the large flow velocities made it hard to build traditional piers halfway the waterway. As a result, a bridge with a span of at least 400 meter without piers had to be designed. Common construction methods for spans this large only allow for two options: a cable stay bridge or a suspension bridge. Hence, a Japanese company proposed a suspension bridge spanning the full 800 meter cross section of the strait. However, the project was deemed too expensive as the costs were estimated on 400 million US dollars [1]. An alternative and innovative design was required.

A new concept was proposed by a collaboration between the startup Tidal Bridge B.V., Dutch Expansion Capital, and Antea and Strukton which are both part of Oranjewoud N.V. Strukton lost interest in the project due to changed policies in the company. This led to BAM International buying the shares in 2018 [2]. To combine the desire of the bridge with a sustainable idea, it was proposed to combine the future connection with a large tidal power facility. This idea resulted in a floating 'Tidal Bridge' that produces energy by connecting large turbines to the bottom side. By using floaters as intermediate supports, shorter spans can be created. The idea of using intermediate floating supports is not new, with evidence dating back to 2000 BC [3]. What is new, is the way the bridge will be connected to the foundation: the use of diagonal pendulums to connect segments to the bed of the strait. These are needed since end-supported foundations, which are the common way to connect a floating bridge to the ground, would need to withstand enormous forces due to the drag on the floaters and turbines. By making intermediate horizontal supports, forces can be distributed over various foundations. An initial cost estimate for this design (which is depicted in Figure 1.1) has been set to 225 million US dollars, improving the Japanese design by almost 50 percent [1].

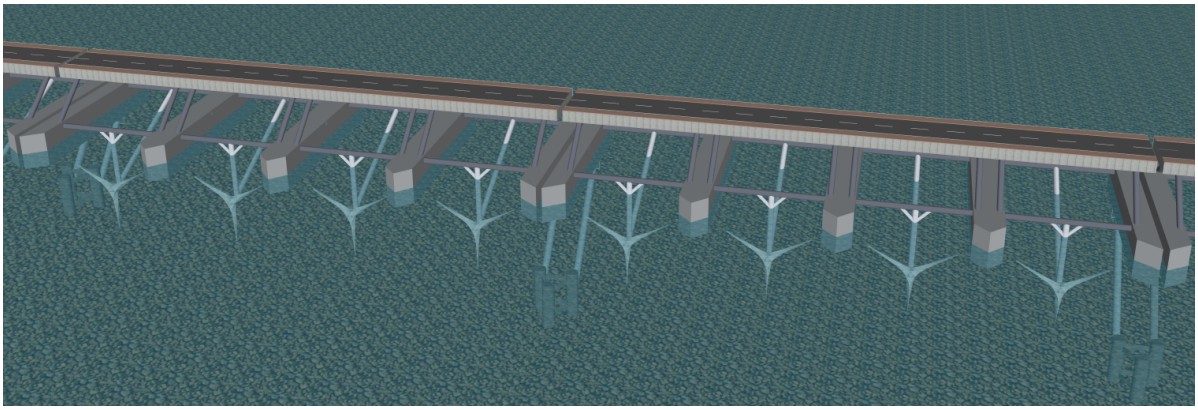

Figure 1.1: Pendulum founded floating bridge overview

1.2. Problem statement

The proposed Palmerah Tidal Bridge serves a combination of two functions: making a connection between the two neighbouring islands and generating electric power for the area. Currently, a construction proposal has been made in a pre-feasibility study. This study did not include a rigorous analysis of the dynamic behaviour of a pendulum founded floating bridge, meaning that there is little knowledge regarding this characteristic of these types of structures. Understanding of dynamic amplitudes and accelerations is vital before further designs can be made, as serviceability limits are not to be exceeded. Modelling software like Ansys can be used to find the interaction between fluid and structures for a single design, but are impractical to find design improvements. Because of this, it is desirable to create a parametrically defined model to find which factors influence the dynamic behaviour of the proposed structure most heavily. When the model is parametrically defined, it can be used to optimise the construction, but also be reused for similar projects, if the Tidal Bridge concept is deemed efficient.

This parametrically defined model should be able to correctly estimate the interaction with water waves and current. Four strategies can be used to obtain an accurate estimation. Firstly, literature can be used to determine/estimate the magnitude of certain forcing parameters. Secondly, a numerical model can be constructed to solve these required parameters. Another strategy is to make an interaction with already existing numerical software, which does require investigation on how to extrapolate the data acquired from the software to structures of other size. Lastly, small scale models can be used to define desired parameters. Multiple options can be combined to improve the model.

1.3. Research objective

The objective of this report is to quantify the dynamic response of a pendulum founded Tidal Bridge, as a consequence of a combined load by wind, waves, currents, and tidal range, by creating a simple dynamic model. This model should correctly quantify the dynamic limits by the induced loads, which can then be used to determine the dynamic behaviour of the proposed Palmerah Tidal Bridge. If the conceptual design of this construction is deemed efficient, the model can be reused in the analysis of the dynamic behaviour of future Tidal Bridges. These objectives are formulated into two main research questions and six sub-questions.

1. **How can the dynamic response of a Tidal Bridge induced by two-dimensional forcing be determined?**
   - In what way do the various structural elements influence the Tidal Bridge dynamics?
   - How can the magnitude of added mass and radiation damping be quantified?
   - What is the contribution of the individual loads on the dynamic response?
   - How can all combinations of loads be assessed efficiently to find the most extreme scenarios?

2. **What design choices can further optimise the dynamic response of a Tidal Bridge?**
   - Which parameters influence natural frequencies and dynamic amplitudes most?
   - What changes to the Tidal Bridge design affect the dynamic response most severely?

1.4. Scope and approach

The scope of this study is to assess the dynamic behaviour of Tidal Bridges using a pendulum foundation. The pre-feasibility design of the Palmerah Tidal Bridge will serve as a case study. By using this design, plausible dimensions and values can be implemented which gives insight in the contribution of the various structural and hydraulic elements. This report focuses solely on technical aspects, whether the solution is an economical or durable solution will not be considered. Excitation due to wind, waves, and current will be investigated, where wind will be considered as a constant horizontal force, while forces due to current and waves will be examined more closely by investigating the hydrodynamic behaviour. Loads caused by moving traffic will be ignored, static loads can be taken into account as additional eccentric masses. The effect of tide will also be taken into account, by changing the depth and equilibrium pendulum angle.

To find the desired dynamical behaviour, a numerical scheme representing the Tidal Bridge needs to be constructed. This scheme can be integrated over time, resulting in the dynamic behaviour of the system. Loads on the structure can be acquired by creating tools to approximate the different types of forcing. To take future design changes into account, the model needs to allow for variable input of dimensions and loads. Making

a tool describing the dynamics of Tidal Bridges given certain characteristics allows for fast optimisation of structural design. As part of this study, experiments on single segments are performed to improve the accuracy the model. The experiments, which are to be executed for various structure sizes, will be used to validate the added mass and radiation damping coefficients for heave and roll motion, which are initially approximated using simple shapes found in literature. These experiments introduce more insight in the fluid-structure interaction of the complex structural shape, creating better understanding into the dynamic behaviour.

Lastly, this study aims to find which parameters have most influence on the dynamic behaviour of the system, how the parameters influence the response in the degrees of freedom, and what design choices can be altered to improve the design. The combination of these elements will allow for further optimisation of the structure to make sure that serviceability limits are not exceeded.

1.5. Reading guide

This report is structured as schematised in the flowchart in Figure 1.2. First, the evaluated construction will be described in Chapter 2. In here, the shape and design choices for a Tidal Bridge will be discussed. The proposed Palmerah Tidal Bridge will form a guideline if it comes to the dimensions of elements. This data will be used in the setup of the dynamic model, which is elaborated in Chapter 3. Experiments to determine the added mass and radiation damping are elaborated in Chapter 4. Data obtained in these experiments is used in the dynamic model. Hence, there is a loop in the flowchart. Once the model is verified and validated, it can be used to find the dynamic behaviour of the proposed Palmerah Tidal Bridge. Chapter 5 describes this subject. Furthermore, a parametric study can be performed based on the constructed dynamic model. This is elaborated in Chapter 6. In here, a sensitivity analysis is performed and dimensionless characteristics of Tidal Bridges are described. In the appendices that follow after, several calculations, assumptions and methods are reported more thoroughly. When a certain appendix is needed for better understanding, it is referred to in the main document.

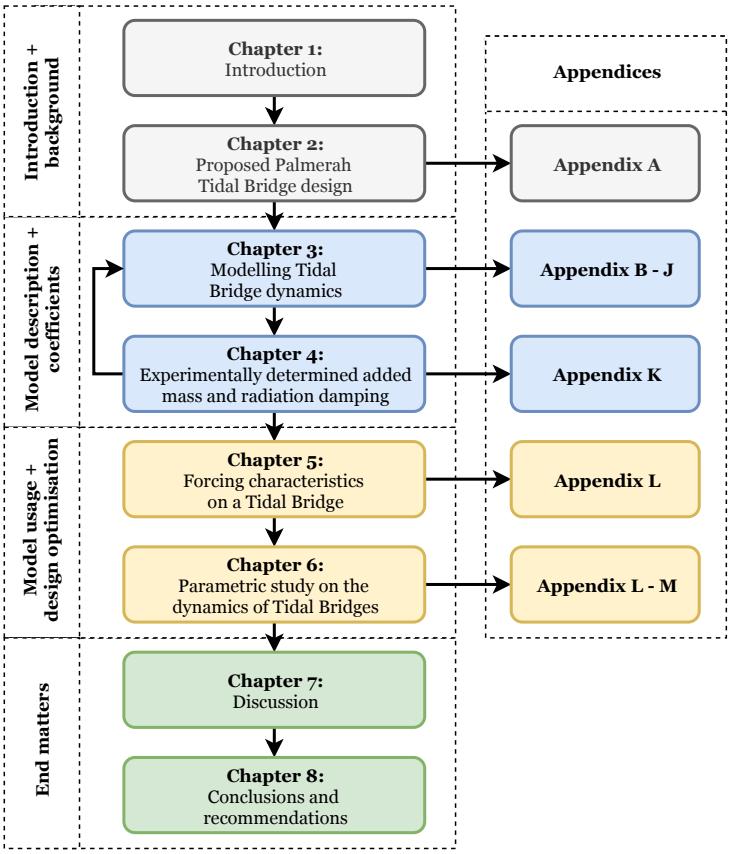

Figure 1.2: Flowchart describing the general structure of the report

2

Proposed Palmerah Tidal Bridge design

This chapter describes and shows the design for the Palmerah Tidal Bridge, as proposed by the pre-feasibility study performed by Antea [4]. The shapes and sizes proposed in this study will be used in the investigation in this report. The values are used as plausible dimensions, which can be used for the assessment of the dynamic behaviour in all following chapters.

2.1. Project location

A study has been performed to locate the connection between the two islands having the largest flow velocities and most limited cross-sectional span. Their result was the location as presented in Figure 2.1. As construction is not easy in the fast-flowing strait, pre-fabricated elements are highly recommended. The proposed idea takes this into account by making several segments, which can be transported to the location separately after constructing them elsewhere. It should be noted that the region does have difficult environmental conditions, such as the occurrence of tsunami, earthquakes, a significant tidal range, and possibly collisions with ships.

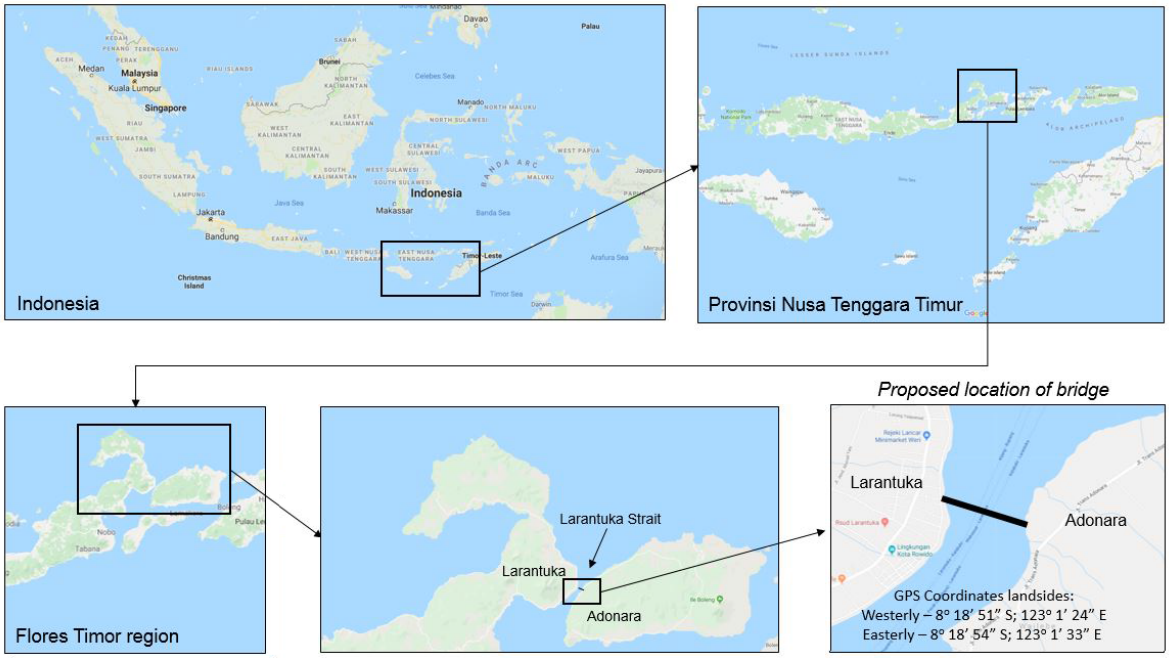

Figure 2.1: Location of the Palmerah Tidal Bridge [5]

The local government wants to fulfil multiple goals by the construction of the Palmerah Tidal Bridge, some of which are [4]:

- Accelerate development of infrastructure
- Generating power for about 100,000 inhabitants
- Economic development by construction and attraction of tourists
- Boost development of marine industry

2.2. Outline of the complete bridge

The pre-feasibility study of the Palmerah Tidal Bridge proposed a design that spans a total of 860 meters between the two islands. The design can be separated into five different sections, which can be characterised as follows below. A side view of the proposed system is presented in Figure 2.2.

- 250 meter traditional bridge (Flores side)
- 30 meter coupling element
- 400 meter Tidal Bridge
- 30 meter coupling element
- 150 meter traditional bridge (Adonara side)

The coupling elements allow for a continuous roadway at both tidal extremes, as the Tidal Bridge will move with it. The middle section, being the subject of this study, is divided into four so called 'segments'. These segments rest on three 'large floaters' and two 'small floaters' (see Figure 2.3). A detailed overview of the components of the proposed segment can be found in Section A.1, in which various characteristics of the components are specified. It is assumed that these segments are completely symmetrical in both horizontal directions. This report focuses solely on the middle 400 meters: the Tidal Bridge.

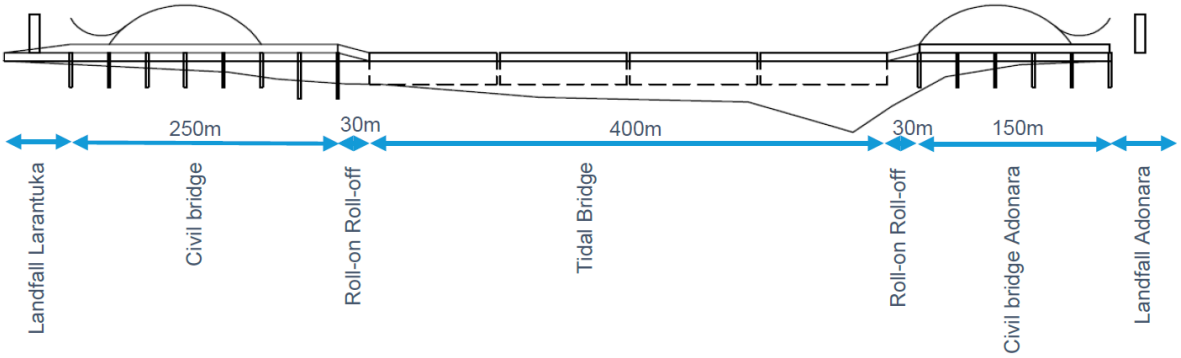

Figure 2.2: Side view of entire Palmerah Tidal Bridge [1]

2.3. Description of the unique mooring system

The outer floaters of each segment (if not connected to the coupling elements) are connected with a diagonal pendulum to the foundation. The length of these pendulums varies based on the local water depth. The function of this element is to withstand the horizontal forces due to current, waves and wind. The vertical forces are primarily taken by the floaters themselves. A schematic overview of the connection between the segments and the foundation is presented in Figure 2.3.

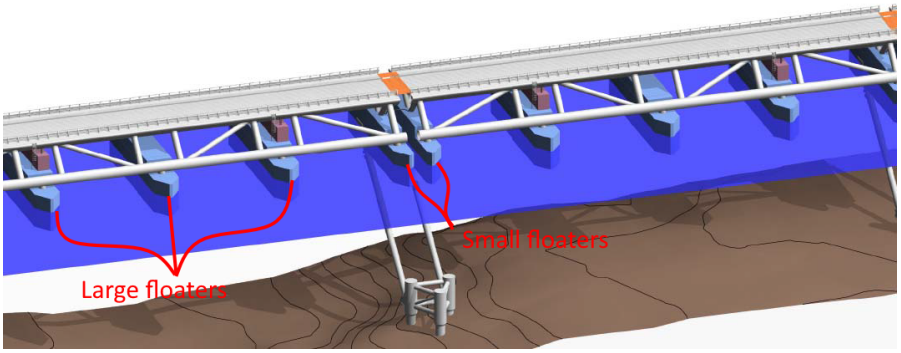

Figure 2.3: Three-dimensional view of the connection between segments and pendulums, displayed without turbines [4]

2.4. Traffic use of the Palmerah Tidal Bridge

The Palmerah Tidal Bridge is proposed to be a bridge for both pedestrians and vehicle traffic. According to Indonesian standards [6], two lanes of traffic require 7 m of width, plus 2 m of sidewalk on each side. Therefore, the traffic gauge has been proposed as is shown in Figure 2.4.

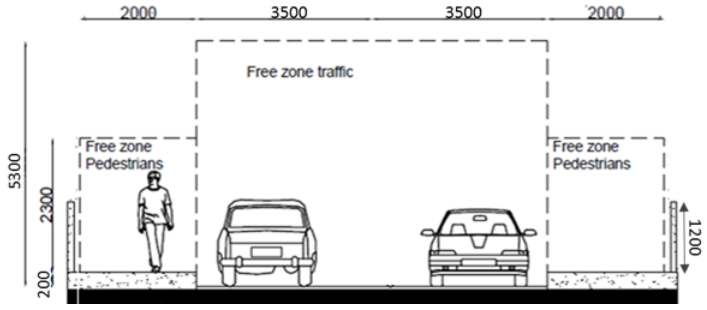

Figure 2.4: Structure gauge traffic heights [4]

The connection between the several segments (shown in orange in Figure 2.3) will function as a hinge or spring for vertical and horizontal (y) directions. For simplicity, it is assumed that this spring has no eccentricity. If dynamic accelerations are deemed too extreme, dampers can be attached to these locations as well. A connection plate for traffic needs to be designed, to create a relative smooth connection between the individual segments. The connection between the last/first segment and the traditional bridge has been proposed and named the RoRo (Roll off, Roll on). This element has been elaborated in Section A.3.

The turbines, which are to be attached on the bottom side of the bridge in between the floaters, have a maximum allowed horizontal force of 2080 kN per turbine (group). This force is centred 12 meter under the lower truss cord [4]. This research will assume that the proposed turbines which are to be discussed later, do fulfil these requirements. Interaction between flow and generation of electricity will not be studied in this report. When half of the turbines rotate clockwise and the other half rotate anti-clockwise, it may be assumed that the Dzhanibekov effect [7] and Gyroscopic precession can both be neglected.

2.5. Ansys Aqwa model of the Palmerah Tidal Bridge by Hoogsteder

Hoogsteder did research into the dynamic effects of a simplified structure in Ansys Aqwa [5]. Two main alterations to the structure were recommended by this study. The first was to mirror the connection of the pendulum, as that would result in having the pendulums in more tension / less compression during the most heavy waves. The other recommendation was to make the spud poles at both ends of the Tidal Bridge more stiff. This will increase the longitudinal tension in the system, just as the rope during the game 'skipping-rope' does. This last recommendation has not been taken into account, as other guidelines became available.

3

Modelling Tidal Bridge dynamics

This chapter elaborates on the setup of the dynamic model. Various elements are discussed which are needed to assess the dynamic behaviour as function of time of a Tidal Bridge. The complete dynamic model is split into five parts. These five parts can be schematised in a flowchart, shown in the different colours in Figure 3.1. As can be seen in the figure, there are two types of input parameters that need to be defined: structural parameters and environmental parameters. The former has already been discussed in Chapters 5 and 2, describing the proposed structure for the Palmerah Tidal Bridge. The environmental parameters will be discussed alongside with the different types of forcing.

In the first section below, the equations of motions (EOM) and other motion characteristics will be described, which form the core of the integration tool. After that, the elements describing the structural response will be evaluated. The structural parameters used for this tool are based on the proposed Palmerah Tidal Bridge design. The different elements of the forcing tool will be discussed after. At the end of this chapter, computational optimisation strategies and serviceable limit states (SLS) are discussed. The results of this chapter will be used in Chapter 6, where a parametric study on the behaviour of Tidal Bridges is performed.

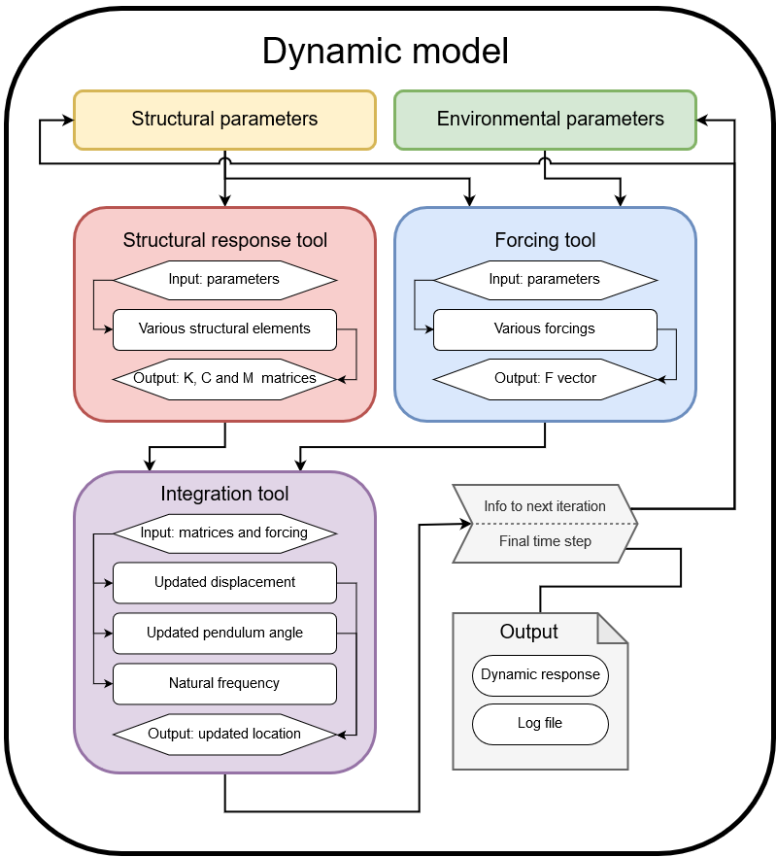

Figure 3.1: Flowchart of the complete dynamic model

3.1. Motion characteristics

Two dynamic formulations are common practice if it comes to building dynamic models: the first being the Lagrangian formalism, the second being based on Newton's second law; the displacement method. Although both forms are equally applicable and correct, the last method is used in this report. The core of the model formulates the EOM based on forces in all degrees of freedom. This formulation is an elaborated version of the classic form of Newton's second law. Using springs and dampers in multiple dimensions, that equation can be expanded to:

$$\boldsymbol{f}(t) = \boldsymbol{M}\ddot{\boldsymbol{x}} + \boldsymbol{C}\dot{\boldsymbol{x}} + \boldsymbol{K}\boldsymbol{x} \tag{3.1}$$

The left-hand side of this equation will be referenced as the forcing side of the equation, the right-hand side is the structural response. In the displacement method, the mass, damping and spring-stiffness matrices represent all degrees of freedom possible for the construction. The units of this matrix may differ per row, as freedom in displacement is influenced by a force in Newton, while a freedom in rotation is influenced by a rotating moment in newton-meter. For a standard, unforced 3DOF (three degrees of freedom) system, as schematised in Figure 3.2, the EOM are given by Equation (3.2).

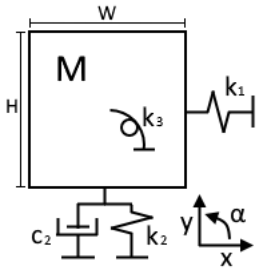

Figure 3.2: Example of simple two dimensional 3DOF system

$$\begin{matrix} \text{Horizontal [N]} \\ \text{Vertical [N]} \\ \text{Rotational [Nm]} \end{matrix} \begin{bmatrix} M & 0 & 0 \\ 0 & M & 0 \\ 0 & 0 & \frac{1}{12}M\left(H^2+W^2\right) \end{bmatrix} \begin{bmatrix} \ddot{x} \\ \ddot{y} \\ \ddot{\alpha} \end{bmatrix} + \begin{bmatrix} 0 & 0 & 0 \\ 0 & c_2 & 0 \\ 0 & 0 & 0 \end{bmatrix} \begin{bmatrix} \dot{x} \\ \dot{y} \\ \dot{\alpha} \end{bmatrix} + \begin{bmatrix} k_1 & 0 & 0 \\ 0 & k_2 & 0 \\ 0 & 0 & k_3 \end{bmatrix} \begin{bmatrix} x \\ y \\ \alpha \end{bmatrix} = \begin{bmatrix} 0 \\ 0 \\ 0 \end{bmatrix} \tag{3.2}$$

3.1.1. Coordinate system

The principal above can be extended into three dimensions for all considered segments, where a segments is assumed to be a rigid body. Figure 3.3 shows the six degrees of freedom and their representative names. It should be noted that conventionally, the positive x-axis in in the direction of flow, as is the case for ships. However, as the primary movement considered is that of the traffic on top of the bridge, tidal flow is now in y-direction. Acceptable magnitudes of movement will be discussed later, in Section 3.5.

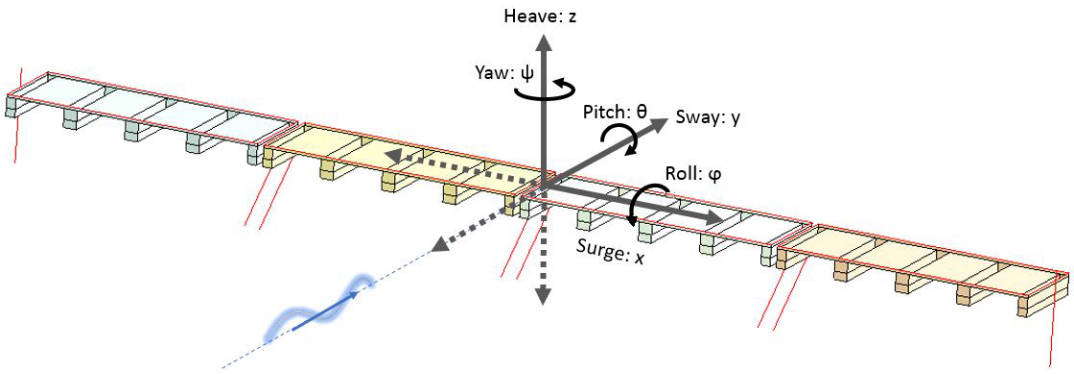

Figure 3.3: Classification of motion in the six degrees of freedom [5]

When looking at a single floater, where the analogy with ships is easily made, the coordinate system above is used. This results in a swaps between sway and surge direction, and in the rotational roll and pitch direction.

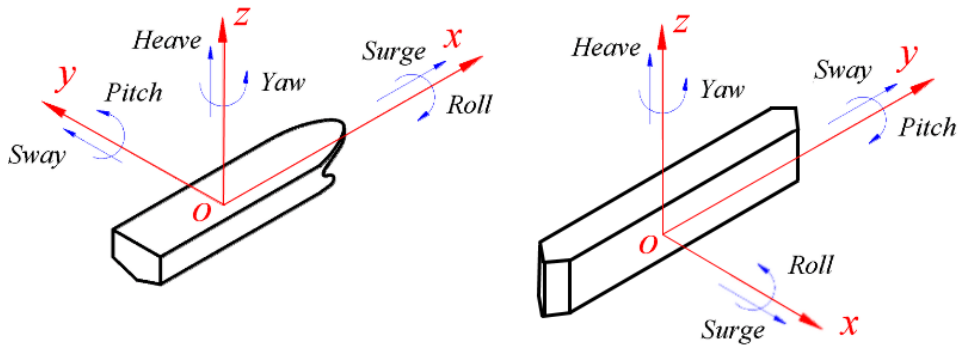

Figure 3.4: Difference between chosen classic ship coordinate system (left) and chosen coordinate system (right) [8]

When matrices are shown throughout this report, the degrees of freedom are always found in the same order: surge (x), sway (y), heave (z), roll (about x), pitch (about y), and yaw (about z), which is then to be repeated for all segments in consequential order from west to east. For all rotations, it is assumed that small angles are present. This assumptions simplifies a lot of the equations and allows for faster calculations. Surge is to be neglected, as the complete structure is locked in that direction. When the construction is in rest and aside from gravity and hydrostatic pressure no forcing is present, all displacements and rotations are of zero magnitude.

Dimensions used in the model are based on the presented design for the Palmerah Tidal Bridge. Special focus on to the size, shape and configuration of the floaters is important. In the drawings in Section B.3, model choices are specified. Stiffness and damping coefficients of all connecting elements have been elaborated and determined in Appendix C.

The Tidal Bridge, which is manifested in a six degree of freedom problem for every segment, can be characterised with a 6Nx6N matrix, N being the number of segments. In this section, various matrix elements will be discussed. To avoid the display of very large matrices, only small sections of the matrices are shown as repetitive behaviour is present in the matrices. After all, the size and shape of each segment is the same, meaning that the shown section for segment can be copied for all similar segments.

3.1.2. Resonance and natural frequencies

Resonance is the response of a model, when it is periodically forced close to its natural frequency. Occurrence of resonance in constructions is often unacceptable, as structures are not allowed to vibrate excessively. If possible, structures need to be designed in such a way that resonance cannot occur. Alternatively, dampers can be added to the system. The effect of resonance and linear dampers is illustrated in Figure 3.5.

When the damping ratio is far below 1, as is the case for oscillation structures in water, excitation close to a natural frequency will result in significant amplification of motion. Therefore, it is important to find the natural frequencies of the evaluated structure. For undamped free vibrations, the system can be described using Equation (3.3).

$$\boldsymbol{M}\ddot{\boldsymbol{x}} + \boldsymbol{K}\boldsymbol{x} = \boldsymbol{0} \tag{3.3}$$

Using an unknown amplitude vector $\hat{\boldsymbol{x}}$, the natural frequencies ($\boldsymbol{\omega_0}$) of a system can be found using the function given in Equation (3.4). As the sine of the function cannot be equal to zero at every moment in time, and the unknown amplitude vector being equal to zero would be a trivial solution, Equation (3.4) can be made more specific by narrowing it down to Equation (3.5), which can be solved easily. [10]

$$\left(-\omega_0^2\boldsymbol{M} + \boldsymbol{K}\right)\hat{\boldsymbol{x}}\sin\left(\omega_0 t + \phi\right) = \boldsymbol{0} \tag{3.4}$$

$$\det\left(-\omega_0^2\boldsymbol{M} + \boldsymbol{K}\right) = \boldsymbol{0} \tag{3.5}$$

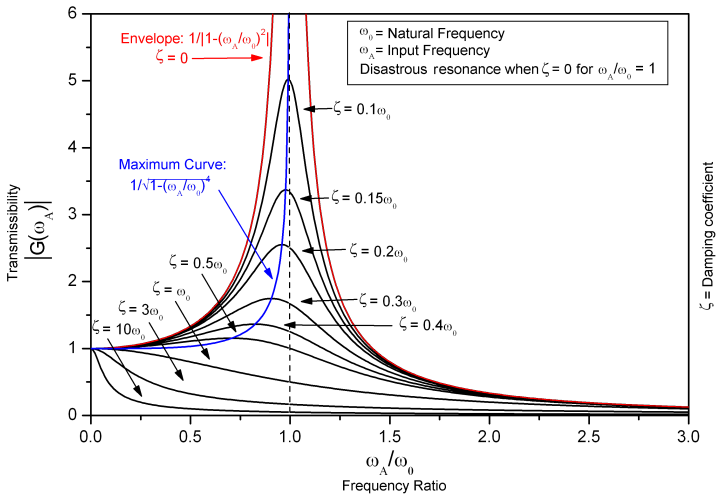

Figure 3.5: Resonance at natural frequency and the effect of dampers [9]

As damping ratios are to be expected far below one, maximum displacement will be found very close to the natural frequencies (see Figure 3.5). Excitation due to wind, waves and current with frequencies neighbouring this natural frequencies may form challenges. Complexities arise when taking into account the non-linearity of the problem: pendulum angles and wave field characteristics changing over time. No complete research into the natural frequencies of a Tidal Bridge and how to alter these frequencies has been performed yet.

3.1.3. Numerical integration

With complex forcing terms, analytical solutions are hard to find. Step-by-step integration methods do offer a solution. If computation steps are appropriately small, they can be used to represent the behaviour of the system [11]. Now, let the initial conditions in Equation (3.6) apply.

$$\begin{aligned} \boldsymbol{x}[0] &= \boldsymbol{x}(t=0) \\ \dot{\boldsymbol{x}}[0] &= \dot{\boldsymbol{x}}(t=0) \\ \ddot{\boldsymbol{x}}[0] &= \ddot{\boldsymbol{x}}(t=0) \end{aligned} \tag{3.6}$$

After each timestep Δt, Equation (3.7) applies. The last formula in this equation comes from Equation (3.1).

$$\begin{aligned} \boldsymbol{x}[i] &= \boldsymbol{x}[i-1] + \Delta\boldsymbol{x} \\ \dot{\boldsymbol{x}}[i] &= \dot{\boldsymbol{x}}[i-1] + \Delta\dot{\boldsymbol{x}} \\ \ddot{\boldsymbol{x}}[i] &= \boldsymbol{M}^{-1}\left(\boldsymbol{f} - \boldsymbol{C}\dot{\boldsymbol{x}}[i-1] - \boldsymbol{K}\boldsymbol{x}[i-1]\right) \end{aligned} \tag{3.7}$$

Change in location and speed can be approximated using Forward Euler and linear change of acceleration, as defined in Equation (3.8).

$$\begin{aligned} \Delta\boldsymbol{x} &= \dot{\boldsymbol{x}}[i-1]\Delta t + \frac{1}{2}\ddot{\boldsymbol{x}}[i-1]\cdot\Delta t^2 + \mathcal{O}(\Delta t^3) \\ \Delta\dot{\boldsymbol{x}} &= \ddot{\boldsymbol{x}}[i-1]\Delta t + \mathcal{O}(\Delta t^2) \end{aligned} \tag{3.8}$$

The first formula in Equation (3.8) can be further optimised as the Trapezoidal Method can be used for the integration of the velocity. This results in Equation (3.9).

$$\Delta\boldsymbol{x} = \frac{1}{2}\left(\dot{\boldsymbol{x}}[i-1] + \dot{\boldsymbol{x}}[i]\right)\Delta t + \frac{1}{2}\ddot{\boldsymbol{x}}[i-1]\Delta t^2 + \mathcal{O}(\Delta t^3) \tag{3.9}$$

After each iteration step, matrices **M** and **C** need to be updated. **M** and **C** will change as both added mass and radiation damping are not solely depending on the shape of the structure, but also on the vibration frequency. Buchholdt and Nejad state that in practice, it is sufficient to let the coefficients remain constant during a timestep Δt. Coefficients should be updated only at the end of each step. [11]

Stability

Numerical stability needs to be provided. However, both Forward Euler and the Trapezoidal Method do not have an absolute stability for positive timesteps [12]. See Figure 3.6 for the regions of absolute stability of the two methods.

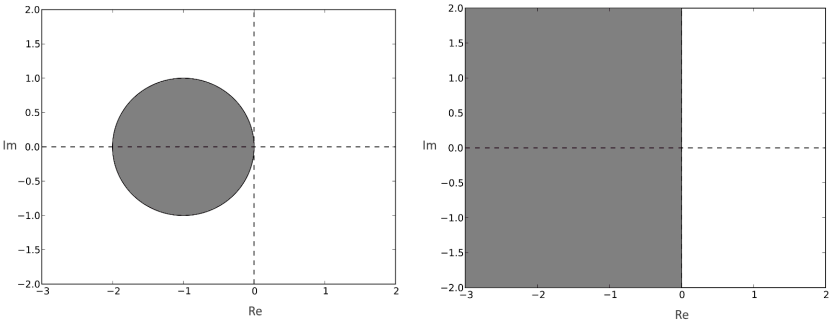

Figure 3.6: Region of absolute stability for Forward Euler (left) and Trapezoidal Method (right) [13, 14]

Although absolute stability cannot be provided, a solution can still be found. Simulation steps need to be of such size that the high natural frequencies can be modelled accurately. As a result, time steps need to be significantly smaller than the smallest fundamental period.

3.2. Structural response tool

The structural response tool defines the mass, damping and stiffness matrix of the combination of all structural elements. Complete assessment of the three matrices are needed as it defines the dynamic response for a given forcing. Multiple linear elements will be discussed in this section, non-linear effects such as damping due to drag are moved to the forcing side of the equation. The elements being described in this section are displayed in the flowchart below. All elements are elaborated in Appendix C, verification and validation of the model is shown in Appendix E.

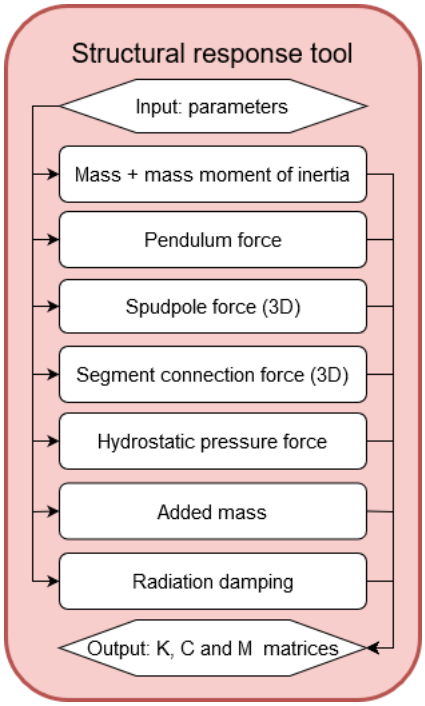

Figure 3.7: Flowchart of structural response tool

3.2.1. Mass, damper and spring matrix

The mass matrix is a superposition of four contributing elements: The mass of a segment, the hydrodynamic added mass (to be discussed later), the mass of marine growth, and the mass of traffic. Appendix C describes the formulation of the complete mass matrix, which is presented with a structure as shown in Equation (3.10). The mass of the pendulums and spudpoles have been neglected as their mass are negligible, even if added mass is included in that calculation (see Appendix B).

$$\boldsymbol{M}_{own} = \begin{bmatrix} \ddots & & & & & & \\ & M & 0 & 0 & 0 & 0 & 0 \\ & 0 & M & 0 & 0 & 0 & 0 \\ & 0 & 0 & M & 0 & 0 & 0 \\ & 0 & 0 & 0 & J_x & 0 & 0 \\ & 0 & 0 & 0 & 0 & J_y & 0 \\ & 0 & 0 & 0 & 0 & 0 & J_z \\ & & & & & & \ddots \end{bmatrix} \tag{3.10}$$

Appendix C also describes the spring and damping matrices for the dynamic model. As the two matrices have a very similar structure, they are often described simultaneously. The pendulums can be modelled as very stiff springs and weak dampers, which are diagonally attached to the segment. The difference between the forces caused by these two characteristics is found in the fact that spring force is a function of displacement, while the damper force is a function of rate of change of displacement. The similar structure allows for a simple integration of both components.

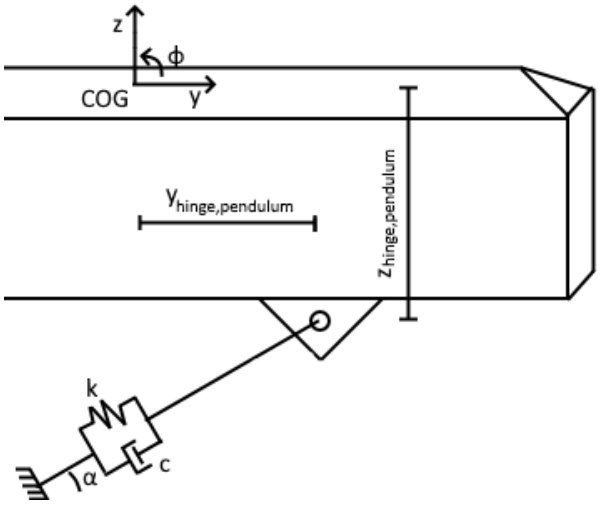

Figure 3.8: Spring and damper modelling the pendulum connection

A similar statement can be made for the influence of the spudpoles and the connection between the segments (if the three dimensional rotation enforced by the varying pendulum length and the spudpoles is taken into account as well). Both elements can be modelled as a combination of springs and weak dampers at the most outer end of a segment. What is unique, is the interaction with water. The spring matrix is additionally influenced by a hydrostatic pressure, which can be modelled as a spring. A damping term can also be found, when looking at radiation damping or drag. Radiation damping will be discussed in Subsection 3.2.3, drag will be discussed as a forcing element in Section 3.3.

3.2.2. Quantifying added mass

Movement of a body trough water is only possible if water is displaced as well. Two phenomena are observed because of this: added mass and radiation damping. Added mass represents the mass of the water that moves along with the body. Radiation damping is the effect describing the outwards going waves, generated by the body moving through the water. This section will focus on the magnitude of the added mass,

radiation damping is discussed in the next subsection. Det Norske Veritas (DNV) published a technical report on recommendations for modelling and analysis of marine operations [15]. In here, added mass recommendations are made for various fully submerged shapes. Two of the investigated shapes are presented in Figures 3.9 and 3.10.

Table A-2 Analytical added mass coefficient for three-dimensional bodies in infinite fluid (far from boundaries). Added mass is $A_{ij}=\rho C_A V_R$ [kg] where V_R [m^3] is reference volume

Body shape		*Direction of motion*	C_A		V_R
Square prisms	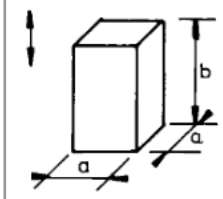	Vertical	*b/a* 1.0 2.0 3.0 4.0 5.0 6.0 7.0 10.0	 0.68 0.36 0.24 0.19 0.15 0.13 0.11 0.08	$a^2\ b$

Figure 3.9: Added mass for a square cuboid [15]

Table A-1 Analytical added mass coefficient for two-dimensional bodies, i.e. long cylinders in infinite fluid (far from boundaries). Added mass (per unit length) is $A_{ij} = \rho C_A A_R$ [kg/m] where A_R [m^2] is the reference area

Section through body		*Direction of motion*	C_A	A_R	*Added mass moment of inertia* [(kg/m)*m^2]		
					$\beta_1\rho\pi a^4$ or $\beta_2\rho\pi b^4$		
					a/b	β_1	β_2
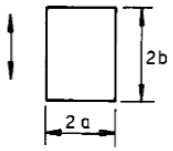	a / b = ∞ a / b = 10 a / b = 5 a / b = 2 a / b = 1 a / b = 0.5 a / b = 0.2 a / b = 0.1	Vertical	1.0 1.14 1.21 1.36 1.51 1.70 1.98 2.23	$\pi\ a^2$	0.1 0.2 0.5 1.0 2.0 5.0 ∞	- - - 0.234 0.15 0.15 0.125	0.147 0.15 0.15 0.234 - - -

Figure 3.10: Added mass for a moving or rotating rectangle [15]

As explained in the assumptions of the model in Section B.1.6, a frequency-constant added mass can be justified. Because of this, the rule-of-thumb equations are justified. However, as the floaters in this study are emerging out of the water, the formulations need to be altered slightly. When the height of the considered body is taken as double the draught, one can use the water level as a symmetry line. By applying this method, the average density of the fluid is equal to the summation of densities of salty water and air, divided by two. This modelled density is represented using ρ_m. Wendel [16] also quantified added mass independently of frequency, this time for floating structures of a specific size ratio. The relevant results of this study are shown in Figure 3.11. Their results confirm the alteration just proposed. Marine growth may have significant influence on the added mass, calculations in Appendix B.1.6 show that this is about 10 percent. To confirm the found values for heave and roll motion, experiments are performed in the next chapter.

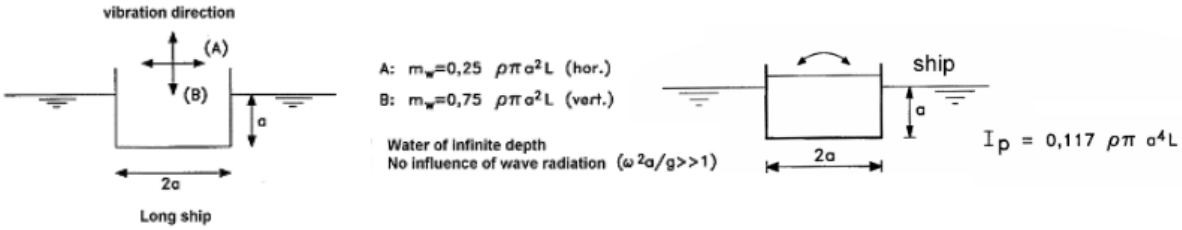

Figure 3.11: Added mass for a floating rectangle for heave, sway, and roll [16]

3.2.3. Quantifying radiation damping

As the floater moves through the water, outgoing waves will be created. Radiation damping, or added damping, is expected to be on of the two main sources of dynamic damping in the system, the other being drag. The model assumes that linear added damping describes the damping accurately. Experiments for vessels show that non-linear roll damping may have a significant presence as well [17]. However, the maximum roll motion allowed for the design is within the limit of small angles, for which the non-linear effects have negligible effects [18]. Additionally, roll motion of the ships displaces hardly any water compared to the viscous effects, while the Tidal Bridge design's roll motion does require significant water displacement. As a result, the linear effect will be significantly larger. As radiation damping is one of two main sources of damping, accurate estimation of the magnitude is of utmost importance. Especially if the natural frequencies of the system are close to their forcing frequencies.

Most literature describes the wave radiation per unit length, as an infinitely large 2D-structure is assumed. Lee [19] described the radiation of a floating rectangle as a consequence of heave, Zheng et al. [20] expanded this research by approximating the radiation by using Haskind's theorem [21] and diffracted potential for heave, sway and roll. In the graphs below, k is the angular wavenumber, h the depth, a the half width, d the draught, ω the angular velocity. The results of this study were in line with what Lee discovered earlier for heave and what a boundary element method described for the other two. The combined results are presented in Figure 3.12. Note that the damping coefficient is given per unit length.

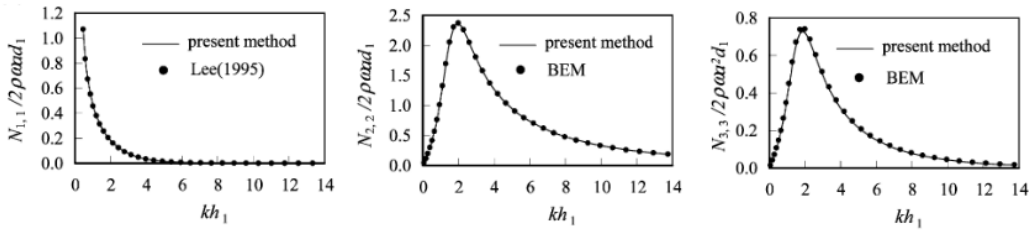

Figure 3.12: Dimensionless added damping coefficient for heave, sway and roll of a rectangular cross section ($h_1/d_1 = 3$, $W/d_1 = 1$) [20]

Vugts [22] performed experiments for heave, sway, and roll as well. They investigated the influence of different shapes of vessels. Results showed significant dependence on shape and shape-ratio (see Figure 3.13. A ratio of width / draught equal to 2 showed similar results as Zheng et al. [20] did. With Vugts covering more combinations and cases, their results will be used. The most relevant results from the study are presented below. It should be noted that the directions sway and roll direction do not match with the coordinate system defined in this report. Sway in the figure would mean surge for the Tidal Bridge, roll translates into pitch. As the width / draught ratio of the floaters is lower than 2, ad the graph only shows the results for the ratios 2, 4 and 8, an approximation needs to be made for lower values. The damping is (based on the figure) approximately linearly dependant on the B/T ratio. Therefore, it is assumed that the damping magnitude can be scaled to a lower B/T ratio using this linear relation. For Tidal Bridge sway, the B/T ratio is about 12. It has been assumed also this factor can be scaled linearly.

Because of the high wave frequency dependency, a constant value cannot be used to represent the radiation damping. As the used construction has pointed tips and interaction between the different floaters is not taken into account in the research done by Vugts, experiments are needed to make sure the data used is appropriate. If one was to try to estimate the magnitude of radiation based on the presented literature, using the same strategy as for added mass was done, the results presented in Appendix G are found. During a dynamic simulation in the model, one radiation damping value will be used, being the value corresponding with the wave frequency (corrected with the flow velocity). This can be modelled more accurately using impulse response functions (based on the work of Cummins [24]) and state space solutions. However, the very sine-like response allows for an accurate estimation for regular waves. In Appendix G, this is confirmed. To validate whether the found magnitudes represent reality well, experiments using a 1:100 scale model of the bridge are performed in the next Chapter.

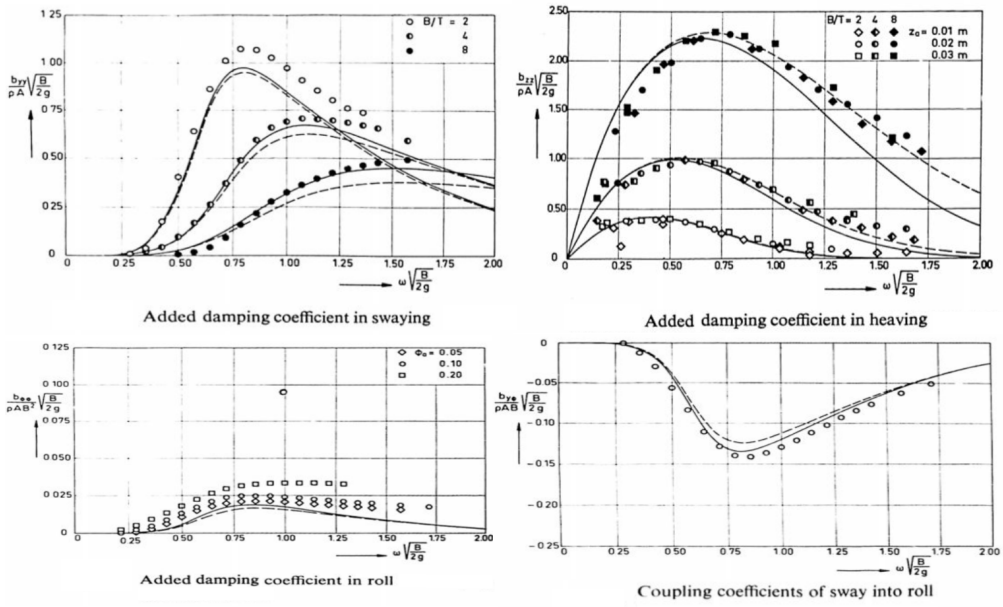

Figure 3.13: Dimensionless damping coefficients for sway, heave, roll, and sway/roll coupling of rectangular cross-sections for varying breadth / draught ratios [23]

3.3. Environmental conditions and forcing tool

This section describes the environmental conditions and different forcing. Four types will be discussed: tidal range, current, waves, and wind. Tidal range is not a type of forcing, but a change of conditions and equilibrium position. Therefore, the effect of the tidal range is to be taken into account as a change in resting position, water depth and pendulum angle. The current and waves do not act independently, but have significant interaction. Therefore, they cannot be evaluated separately. Each structural element subjected to water is induced by two types of loading: drag and inertia. As only the floaters are subjected to a significant inertia force (being the acceleration of water particles due to waves), only the floaters are evaluated for both drag and inertia. The other two submerged elements of the construction, the turbines and pendulums, are evaluated for drag solely. Besides water forces, wind forces on both the deck as the super structure are also implemented in the forcing tool. The complete overview has been schematised in a flowchart below.

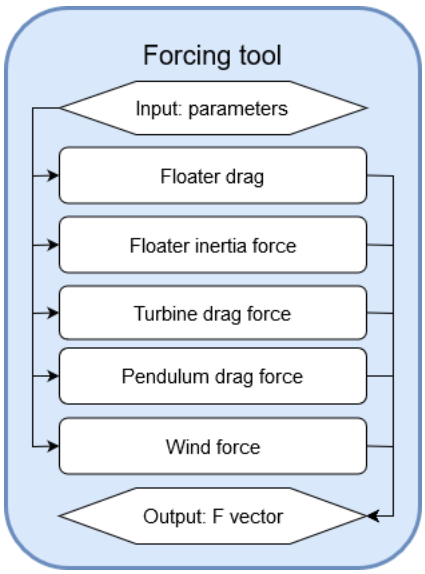

Figure 3.14: Flowchart of forcing tool

3.3.1. Tidal level and water depth

Bathymetry

The bathymetry of the location has been schematised in Figure 3.15. As can be noted, the water depth below the floaters varies between 15 and 31.5 meters, depending on location and tide. Squat may also have an influence on the local water depth. However, as shown in Appendix B, this is of neglectable magnitude.

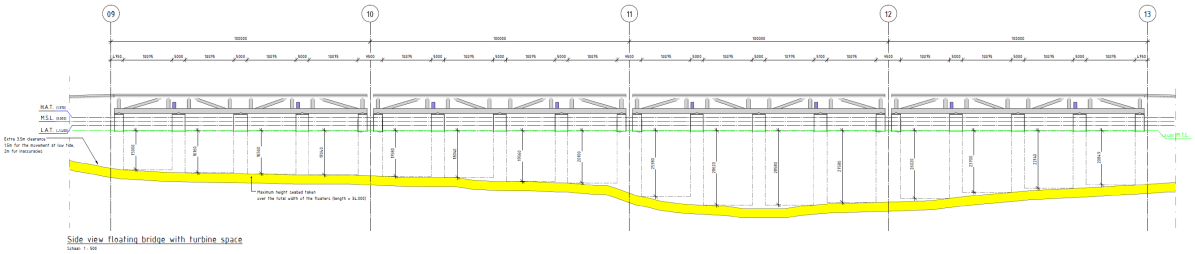

Figure 3.15: Bathymetry under Tidal Bridge relative to LAT [4]

Tidal constituents and range

The companies Aquatera and Bintang Subsea performed a study on the tidal behaviour of the area, in which they defined the relevant datum's and the amplitudes of the different constituents [25]. Their results are presented in Table 3.1 and Table 3.2.

Constituents	Amplitude	Phase
M_2	0.762 m	314.4°
S_2	0.340 m	22.2°
K_1	0.317 m	311.5°
O_1	0.183 m	277.4°

Table 3.1: Relevant tidal constituencies in the Larantuka Strait [25]

Related datum	Relative to MSL	Relative to LAT
Highest Astronomical Tide (HAT)	1.58 m	3.09 m
Mean High Water Spring (MHWS)	1.11 m	2.62 m
Mean High Water Neap (MHWN)	0.43 m	1.94 m
Mean Sea Level (MSL)	0.00 m	1.51 m
Mean Low Water Neap (MLWN)	−0.41 m	1.10 m
Mean Low Water Spring (MLWS)	−1.09 m	0.42 m
Lowest Astronomical Tide (LAT)	−1.51 m	0.00 m

Table 3.2: Related datum's in the Larantuka Strait [25]

In the data given in Table 3.1, it can be observed that the semi-diurnal tides slightly dominant. To express this dominance, the form factor can be defined as is shown in Equation (3.11). The tidal climate can be described as 'mixed, mainly semi-diurnal' [26].

$$\begin{aligned} F &= \frac{K_1 + O_1}{M_2 + S_2} \\ &= \frac{0.317 + 0.183}{0.762 + 0.340} = 0.45 \text{ m} \end{aligned} \tag{3.11}$$

Model implementation

As has been discussed in the assumptions of the model, all displacements are equal to zero when the system is at rest. When the tidal level is non-zero, a vertical displacement is trivial. This vertical translation is accompanied by a horizontal translation, as the structure rotates around the lower hinge of the pendulum. Instead

of needing to redefine all forces depending on the location compared to this new equilibrium position, it is also possible to fixate the axis based on the centre of gravity (COG) of the segments. As a result, a non-zero tidal level results in a translation of the bottom hinge of the pendulum. This translation is of course a function of the length of the pendulum. The equations for this are elaborated in Equation (3.12).

$$\begin{aligned} y_{p,bottom,tide} &= y_{p,bottom} - L_p \cdot \left(\cos(\alpha_0) - \cos\left(\arcsin\left(\frac{\left(\sin(\alpha_0) \cdot L_p\right) + h_{tide}}{L_p} \right) \right) \right) \\ z_{p,bottom,tide} &= z_{p,bottom} + h_{tide} \end{aligned} \tag{3.12}$$

After assessing the dynamics, it may be interesting to relocate the axis back to their Mean Sea Level position. This way, the total displacement as a consequence of nature can be assessed. Equation (3.13) shows how these values can be recalculated, assuming small angles for both connecting pendulums.

$$\begin{aligned} y_i(t) &= y_i(t) - h_{tide} \cdot \frac{\tan\left(\alpha_{p_1}\right) + \tan\left(\alpha_{p_2}\right)}{2} \\ z_i(t) &= z_i(t) + h_{tide} \\ Rz_i(t) &= Rz_i(t) + h_{tide} \cdot \frac{\tan\left(\alpha_{p_1}\right) - \tan\left(\alpha_{p_2}\right)}{L_s} \end{aligned} \tag{3.13}$$

3.3.2. Current forcing

As current velocities may rise to 4.5 m/s, drag will form a significant force on the floaters, turbines, and pendulums. The drag on the three elements will be discussed separately.

Floater drag

Drag forces due to flow are commonly described using Equation (3.14). In here, u is the flow velocity. For static structures where waves are not present, u is a constant. However, the floaters oscillate in the water, making the draught and flow velocity a function of time. Hence, v is added to represent the structure velocity. To make matters even more complex, waves contribute to this drag coefficient in two ways separate ways: firstly, they locally increase/decrease the draught making the facing area different, secondly, they influence the particle velocity field. These two effects may contribute to the total drag force significantly as waves are in the same order as the draught at still water and flow velocity is taken squared in the equation. Small changes of u will result in relative large changes in F_d.

$$F_d(t) = 1/2 \cdot \rho \cdot W \cdot d(t) \cdot C_{DS} \cdot (u - v)^2 \tag{3.14}$$

The drag around the floaters shall be split into two different types: drag due to horizontal flow and drag due to vertical flow. The former can be approximated using Figure 3.16. The values shown are valid for a Reynolds number of 170,000. The investigated design has a Reynolds number much larger, being in the order of 100,000,000. It has been assumed that this difference has little effect.

Table B-2
Drag coefficient on three-dimensional objects for steady flow C_{DS}.
Drag force is defined as $F_D = \frac{1}{2}\rho C_{DS} S u^2$.

S = projected area normal to flow direction [m^2].
R_e = uD/ν = Reynolds number where D = characteristic dimension.

Geometry	*Dimensions*	C_{DS}
Square rod parallel to flow	L/D	
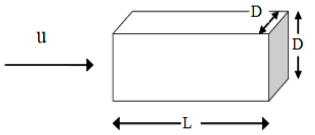	1.0 1.5 2.0 2.5 3.0 4.0 5.0	1.15 0.97 0.87 0.90 0.93 0.95 0.95
		$R_e = 1.7 \cdot 10^5$

Figure 3.16: Drag around a square prism [15]

Antea proposed to use the conservative C_{DS} value of 1.15, as marine growth may enlarge the drag coefficient over time. However, besides the fact that the current design proposes a L/D ratio of 34/5 which would represent a drag coefficient of about 0.95, the current design also proposes a pointed prism on both ends of the floater. Suribabu et al. did research on the drag coefficient of piers and concluded that triangular ends results in about 40 percent less drag [27]. The results of this study are shown in Figure 3.17. Because of these two effects, 1.15 may be too conservative. If pitch rotation is present at a time instance, drag forces vary between the floaters. This effect has been neglected.

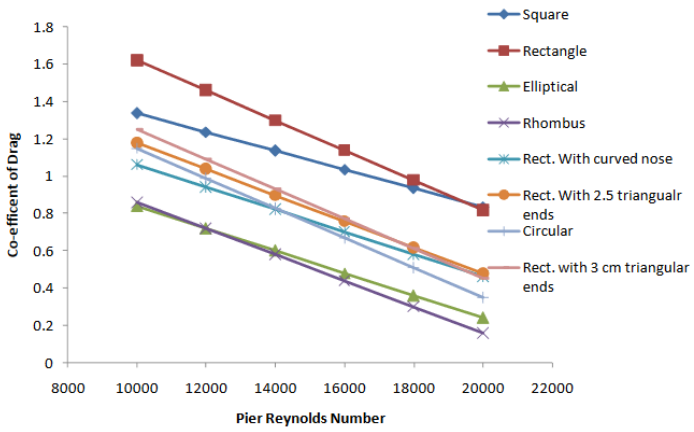

Figure 3.17: Drag of various shapes of piers with contraction ratio of 0.33 [27]

Vertical flow is hardly present and could almost be neglected, as it is assumed that the current is exactly horizontal. However, as the structure oscillates vertically, a relative flow will be present. The drag coefficient for this vertical direction is approximated using Figure 3.18. In here, the size ratio for the small and large floaters as proposed for the Palmerah Tidal Bridge are '34:3.5' and '34:5'. In reality, the floaters are slightly longer as they have pointed tips. Looking at the presented data, this results in a drag coefficient between 1.2 and 1.5. As the floaters emerge from the water, there will only be a drag effect on the bottom side of the floater. To take this into account, the drag forces must be halved. As marine growth will affect this value too, the drag coefficient has been set to 0.75. Roll rotation of the floater influences the vertical velocity of the floaters significantly at the tips. This has been taken into account by adding the vertical movement due to roll at a certain distance to the vertical velocity.

Table B-2

Drag coefficient on three-dimensional objects for steady flow C_{DS}.

Drag force is defined as $F_D = \frac{1}{2}\rho C_{DS} S u^2$.

S = projected area normal to flow direction [m^2].
R_e = uD/ν = Reynolds number where D = characteristic dimension.

Geometry	*Dimensions*	C_{DS}
Rectangular plate normal to flow direction	B/H	
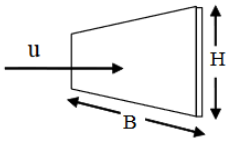	1 5 10 ∞	1.16 1.20 1.50 1.90
		$R_e > 10^3$

Figure 3.18: Drag around a flat plate [15]

Turbine drag

As discussed earlier, turbines will be connected to the bottom side of the Palmerah Tidal Bridge to generate electricity for the two islands. An illustration of the placement of these turbines is shown in Figure 3.19. It is also considered to construct a grid of 4x4 smaller turbines instead of a large turbine, as is now depicted in the figure.

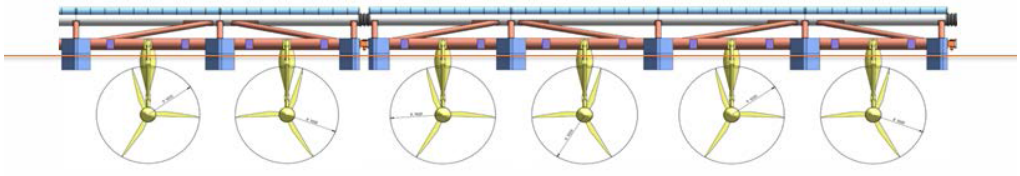

Figure 3.19: Location of turbines on Tidal Bridge [28]

Three types of turbines are currently investigated, which are shown in Figure 3.20. It has also been proposed to have a combination of different types, as flow velocities vary in the cross section.

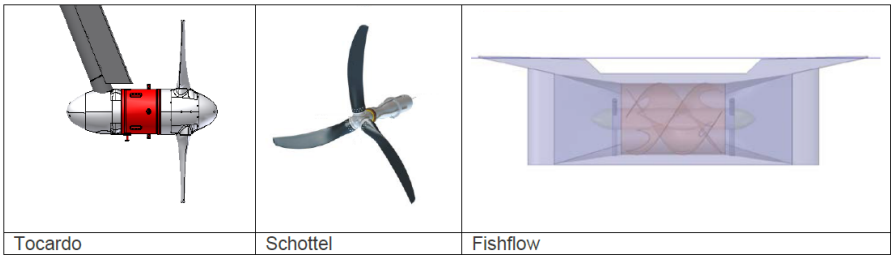

Figure 3.20: Types of turbines considered for Palmerah Tidal Bridge [1]

For the force on the turbines, a similar expression can be used. This expression is shown in Equation (3.15).

$$F_t = 1/2 \cdot \rho \cdot A \cdot C_t \cdot (u - v)^2 \tag{3.15}$$

As the force of the turbine is very dependent on the type of turbine, exact parametric determination of the force is very hard to predict. Therefore, it has been decided to take Antea's proposal, and set the force of a single turbine structure to 2080 kN [4]. This force is present at maximum flow velocity, forces during other flow velocities will be scaled appropriately. It should be noted that both the floater drag and the turbine drag have an eccentricity to the COG. For the floaters, this distance has been estimated to -5.1 meters. For the turbines, this is equal to -16.9. The extreme turbine force combined with the large eccentricity will form the main factor in determining the location of the upper hinge of the pendulum, as the optimal spot would result in zero roll motion.

Pendulum drag

The tidal flow around the pendulum will result in extra forces on the system. The drag of an ellipse-shaped structure (as the circular section is slanted) can be described according to Figure 3.21. The D/L ratio becomes a function of the angle of the pendulum. The drag coefficient is assumed to be linear in between the given values. As a result, Equation (3.16) applies for angles between 30° and 90°.

Table B-1 (Continued)
Drag coefficient on non-circular cross-sections for steady flow C_{DS}.
Drag force per unit length of slender element is $f = \frac{1}{2}\rho C_{DS} D u^2$.

D = characteristic width [m].
R_e = uD/ν = Reynolds number.

Adopted from Blevins, R.D. (1984) *Applied Fluid Dynamics Handbook*. Krieger Publishing Co.

Geometry	*Drag coefficient, C_{DS}*	
15. Ellipse	D/L	C_{DS} ($R_e \sim 10^5$)
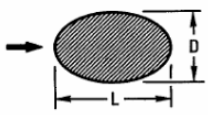	0.125 0.25 0.50 1.00 2.0	0.22 0.3 0.6 1.0 1.6

Figure 3.21: Drag around an ellipse [15]

$$C_{DS} = 0.8 \sin \alpha + 0.2 \tag{3.16}$$

With an angle of 40 degrees, the drag coefficient becomes approximately 0.71. For pendulums varying between 25.5 and 38 meters in length, and an assumed diameter of 1320 mm, the drag force becomes between 160 and 235 kN for a flow velocity of 4.5 m/s. As 50 percent of that is directly transferred to the foundation and only 50 percent is transferred to the floaters, an additional force between 80 and 118 kN per pendulums needs to be added to the segments at maximum flow velocity. It is assumed that this force is constant, as the drag coefficient hardly changes as a consequence of change in pendulum angle.

3.3.3. Wave forcing

Waves are expected to form the most troubling force, as the periodic motion may excite the structure close to its natural frequency. Therefore, estimation of the magnitude and period of this force will be of great importance. To avoid using computational fluid dynamics to solve three-dimensional Navier-Stokes equations, another method that is fast and relatively easy is preferred. To obtain this, Hemel [29] recommends (for their dynamic calculation of a submerged floating tunnels) to use a combination of velocity potential flow and a modified Morison equation. This combination of equations can be written for all degrees of freedom. However, only one is shown in Equation (3.17). The first and second term on the right hand side represent the modified Morison terms, the last part presents the velocity potential flow. Please note that current forcing also uses the drag term. As a results, wave drag force and current drag force should be combined in a non-linear way.

$$\begin{aligned} F_y &= F_{drag,y} + F_{hydro,y} + F_{Krylov,y} \\ &= \frac{1}{2}\rho C_{DS} A (u - v) |(u - v)| + \rho C_a V (\dot{u} - \dot{v}) + \rho V \dot{u} \end{aligned} \tag{3.17}$$

The hydrodynamic mass force can be written as an integral using Equation (3.18) and (3.19).

$$F_{y,hydro} = \rho C_{a,y} V \overline{\frac{\delta u_y - v_y}{\delta t}} \tag{3.18}$$

In which:

$$\overline{\frac{\delta u_y - v_y}{\delta t}} = \frac{1}{V} \int_{-d}^{\eta} \int_{-l/2}^{l/2} \int_{-b}^{b} \frac{\delta u_y - v_y}{\delta t} dx\, dy\, dz \tag{3.19}$$

As water pressures can be integrated over an volume to obtain a force, Equation (3.19) can be used to describe the Krylov-force on the structure. This force is the result of pressure gradients due to undisturbed waves [30]. Forces and rotational moments due to pressure gradients caused by waves can be based on this theory.

Wave properties

Tidal Bridge B.V. [31] published an estimation for the wave climate at the considered location. As measurement data is not available, hourly averaged wind measurements have been used. The data set containing just over 12 years of data, has been separated into directions bins of 20 degrees, resulting in directional histograms. This data is shown in Appendix D. It can be noted that wind velocities at the location are relatively low.

The extreme wind velocity for a probability of exceedance of once every 100 years can now be obtained when assuming that the data has the shape of a normal distribution. With Equation (3.20), the data per directional bin can be extrapolated into an 100-year estimate.

$$F(a) = \int_{-\infty}^{a} \frac{1}{\sigma\sqrt{2\pi}} e^{-\frac{1}{2}\left(\frac{x-\mu}{\sigma}\right)^2} dx \tag{3.20}$$

The obtained values for the extreme wind velocities per directional bin, can be converted into a significant wave height and a wave period using Bretschneider's formulas. These two formulas are presented in Equation (3.21) and Equation (3.22). In here it is assumed that the depth is constant over the strait.

$$H_s = \frac{U_{10,max}^2}{g} 0.283 \tanh\left(0.578\left(\frac{gd}{U_{10,max}^2}\right)^{0.75}\right)\tanh\left(\frac{0.0125\left(\frac{gF}{U_{10,max}^2}\right)^{0.42}}{\tanh\left(0.578\left(\frac{gd}{U_{10,max}^2}\right)^{0.75}\right)}\right) \tag{3.21}$$

$$T = \frac{2\pi U_{10,max}}{g} 1.20 \tanh\left(0.833\left(\frac{gd}{U_{10,max}^2}\right)^{0.375}\right)\tanh\left(\frac{0.077\left(\frac{gF}{U_{10,max}^2}\right)^{0.25}}{\tanh\left(0.833\left(\frac{gd}{U_{10,max}^2}\right)^{0.375}\right)}\right) \tag{3.22}$$

The wave length can now be calculated using the iterative formula given in Equation (3.23). Tidal Bridge B.V. makes a small error while using this equation, as the equation assumes linear wave theory is valid.

$$L = \frac{gT^2}{2\pi}\tanh\left(\frac{2\pi d}{L}\right) \tag{3.23}$$

The results of the computations of the three formula above for all directional bins can be found in Appendix D. In here, it becomes clear that the largest waves can be found more or less perpendicular to the brides longitudinal axis. To simplify calculations, it is assumed that this angle is exactly perpendicular. The largest waves expected from both sides of the structure have the characteristics as shown in Table 3.3.

Direction	310 – 330 °	210 – 230 °
Fetch	480,000 m	32,000 m
Average water depth	2,000 m	18 m
Wind velocity	13.0 m/s	8.5 m/s
Significant wave height	3.54 m	0.81 m
Significant wave period	7.59 s	3.44 s
Significant wave length	89.88 m	18.53 m

Table 3.3: Extreme wind and wave conditions in Larantuka Strait, exceedance once every 100 years [31]

When the obtained data presented in Table 3.3 is used to verify whether linear wave theory is valid, one comes to the conclusion that it is not. Figure 3.22 shows the ranges for validity and where the largest wave in the wave spectrum is expected to be found.

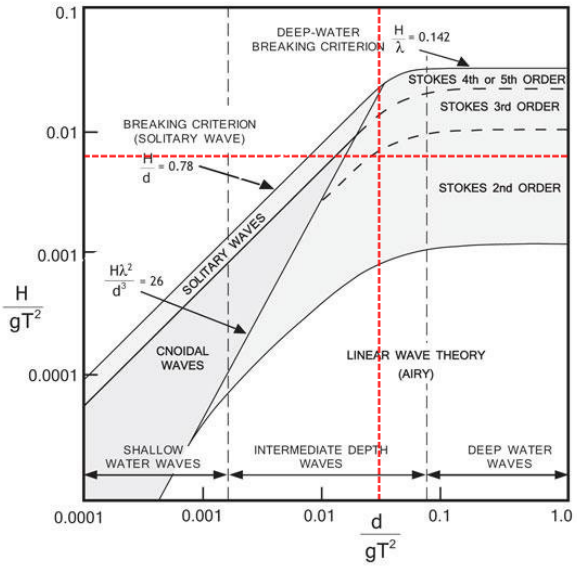

Figure 3.22: Ranges of validity for various wave theories, dotted red line for largest wave found [32]

The degree of non-linearity of waves can be expressed using the Ursell number, which is shown in Equation (3.24).

$$\begin{aligned} N_{Ursell} &= \frac{HL^2}{d^3} \\ &= \frac{3.54 \cdot 89.88^2}{18^3} \\ &= 4.9[\text{-}] \end{aligned} \tag{3.24}$$

For Nursell number values lower than 10, the theory of Stokes is applicable [33].

Wave theory

As waves form an important factor in the dynamic loading of a Tidal Bridge, the behaviour of linear waves and Stokes second order waves shall be analysed. Notation in this section is based on the work of Holthuijsen [33]. However, sine waves have been replaced with cosines, to simplify the equations for the second order stokes waves. Linear wave theory is the result of a series of idealisations of water. The fluid must be an ideal fluid, which assumes that the water is incompressible, constant in density, and without viscosity. Also, a continuous water body and small amplitudes are assumed. Two equations form the basis of the computation: the mass balance (Equation (3.25), presented in the form of the continuity equation) and the momentum balance (Equation (3.26), presented in the form of directional linearised equations).

$$\frac{\delta u_x}{\delta x} + \frac{\delta u_y}{\delta y} + \frac{\delta u_z}{\delta z} = 0 \tag{3.25}$$

$$\begin{aligned} \frac{\delta u_x}{\delta t} &= -\frac{1}{\rho}\frac{\delta p}{\delta x} \\ \frac{\delta u_y}{\delta t} &= -\frac{1}{\rho}\frac{\delta p}{\delta y} \\ \frac{\delta u_z}{\delta t} &= -\frac{1}{\rho}\frac{\delta p}{\delta z} - g \end{aligned} \tag{3.26}$$

Boundary conditions at the bottom and top of the water apply. Namely: vertical velocity at the bottom is equal to zero, and vertical velocity at the top is equal to the rate of change of water level. An analytical solution for the continuity equation combined with the boundary conditions is described by the Laplace equation, as shown in Equation (3.27).

$$\frac{\delta^2 \phi}{\delta x^2} + \frac{\delta^2 \phi}{\delta y^2} + \frac{\delta^2 \phi}{\delta z^2} = 0 \tag{3.27}$$

Where:

$$\begin{aligned} u_x &= \frac{\delta \phi}{\delta x} \\ u_y &= \frac{\delta \phi}{\delta y} \\ u_z &= \frac{\delta \phi}{\delta z} \end{aligned} \tag{3.28}$$

A similar transition can be made for the momentum balance equation in Equation (3.26), which results in Equation (3.29).

$$\frac{\delta \phi}{\delta t} + \frac{p}{\rho} + gz = 0 \tag{3.29}$$

For long-crested harmonic waves in positive x-direction, Equation (3.27) can be solved as follows in Equation (3.30).

$$\phi = \frac{\omega a}{k} \frac{\cosh(k(d+z))}{\sinh(kd)} \cos(\omega t - ky) \tag{3.30}$$

Where k, the wave number, is defined by the dispersion relation in Equation (3.31).

$$\omega^2 = gk \tanh(kd) \quad \text{or} \quad L = \frac{g}{2\pi} T^2 \tanh\left(2\pi \frac{d}{L}\right) \tag{3.31}$$

Now, the velocity in x-direction and z-direction can be defined by differentiating Equation (3.27) with Equation (3.28). This results in the particle velocities presented in Equation (3.32).

$$\begin{aligned} u_y &= \omega a \frac{\cosh(k(d+z))}{\sinh(kd)} \sin(\omega t - ky) \\ u_z &= \omega a \frac{\sinh(k(d+z))}{\sinh(kd)} \cos(\omega t - ky) \end{aligned} \tag{3.32}$$

The pressure as function of water depth can be constructed from the Bernoulli equation in Equation (3.29) and the velocity potential in Equation (3.30). The result, which is valid for z-coordinates below the still-water level, can be found in Equation (3.33). For coordinates above the still-water level, a constant pressure gradient can be assumed [33].

$$p = -\rho g z + \rho g a \frac{\cosh(k(d+z))}{\cosh(kd)} \sin(\omega t - ky) \tag{3.33}$$

The equations presented have very helpful implications for shallow and deep water, as the hyperbolic functions can be approximated linearly. However, the waves as described in Table 3.3 can only be described in the 'transitional water depth'-domain [34]. Therefore, these linear approximations cannot be used. As the waves in the Larantuka Strait cannot be described using linear wave theory solely, a correction needs to made. Stokes proposed adding extra harmonic waves to the basic sine waves [35]. This second order correction is presented in Equation (3.34). In the cosines, a correction has been added to allow for the effect caused by the flow velocity

$$\begin{aligned} \eta(y,t) &= \epsilon \eta_1(y,t) + \epsilon^2 \eta_2(y,t) \\ &= a \cos(\omega t + ukt - ky) + ka^2 \frac{\cosh(kd)}{4(\sinh(kd))^3} (2 + \cosh(2kd)) \cos\left(2(\omega t + ukt - ky)\right) \end{aligned} \tag{3.34}$$

The first term in Equation (3.34) is the wave defined by the linear wave theory, the second term is the effect of the second-order stokes wave. The particle velocities and wave pressure as function of depth can be written as shown in Equations (3.35) and (3.36). This presentation is a variation on the work of Demirbilek and Vincent [36] and Zhang [37], making notation and assumptions align with the work of Holthuijsen [33].

$$\begin{aligned} u_y &= \omega a \frac{\cosh(k(z+d))}{\sinh(kd)} \cos(\omega t + ukt - ky) + \frac{3}{4} \omega a^2 k \frac{\cosh(2k(z+d))}{(\cosh(kd))^3 \sinh(kd)} \cos\left(2(\omega t + ukt - ky)\right) \\ u_z &= -\omega a \frac{\sinh(k(z+d))}{\sinh(kd)} \sin(\omega t + ukt - ky) - \frac{3}{4} \omega a^2 k \frac{\sinh(2k(z+d))}{(\cosh(kd))^3 \sinh(kd)} \sin\left(2(\omega t + ukt - ky)\right) \end{aligned} \tag{3.35}$$

$$\begin{aligned} p = &-\rho g z + \rho g a \frac{\cosh(k(d+z))}{\cosh(kd)} \cos(\omega t + ukt - ky) \\ &+ \frac{3}{4} \rho g a^2 k \frac{\tanh(kd)}{(\sinh(kd))^3} \left(\frac{(\cosh(2k(d+z)))}{(\sinh(kd))^3} - \frac{1}{3} \right) \cos\left(2(\omega t + ukt - ky)\right) \\ &- \frac{1}{4} \rho g a^2 k \frac{\tanh(kd)}{(\sinh(kd))^2} (\cosh(2k(d+z)) - 1) \end{aligned} \tag{3.36}$$

Wave statistics

Significant wave height is defined in many different ways. When this report refers to significant wave height, as it did in Table 3.3, the average of the highest third of the waves is indicated. This can also be written in form of an equation as presented in Equation (3.37).

$$H_s = \frac{1}{N/3} \sum_{i=1}^{N/3} H_i \tag{3.37}$$

The significant wave period and significant wave length are defined in the same manner, but are not sorted based on their own value, but on the corresponding wave height. This definition of significant wave height has the mathematical ease that the maximum wave height in a storm can be defined as follows in Equation (3.38).

$$H_{max} \approx 2H_s \tag{3.38}$$

A random series of waves can be generated by using an Inverse Fourier Transform. However, no wave spectrum is known for the location. Therefore, regular waves will be used for this report. Using only the largest wave for both directions in the model, may result in an underestimation of the maximum displacement which can be expected in the structure. Wave less high, but with a wave period closer to the natural period, can result in extremer conditions. Therefore, a range of wave periods will have to be investigated.

3.3.4. Wind load

Based on the Indonesian Standard BMS bridge design manual [38], wind loads for ULS and SLS for the deck and superstructure are determined. The presented ULS values in Figure 3.23 are taken as initial estimates for added loading due to wind on the structure.

LIMIT STATE	UNIFORM LINE LOAD kN/m	
	COASTAL (within 5 km of Coast)	INLAND (greater than 5 km to Coast)
S.L.S	1.30	0.90
U.L.S	2.12	1.56

Width/Depth Ratio Solid Superstructure	Limit State Type	WIND PRESSURE kPa	
		COASTAL (within 5 km of Coast)	INLAND (greater than 5 km to Coast
Superstructure (all $^b/_d$)	U.L.S	1.06	0.78
b = Superstructure width between outer faces of parapets. d = Superstructure depth (including solid parapets).			

Figure 3.23: Wind load on structure for deck and superstructure [38]

Two uniform line loads have been implemented in the model: the ULS line load and the ULS pressure, both for the coastal area. In reality, the super structure is likely to be about 8 meters high. However, the open truss structure reduces the effective height at which the wind pressure is present on the structure. For the current Palmerah design, it has been estimated that the effective height of the super structure is about 3 meters high. As a result, the values presented in Table 3.4 have been implemented into the model.

Type of wind	Force [N/m]	Height with respect to COG [m]
Deck load	2120	7.16
Deck load	3000	3

Table 3.4: Implemented wind loads in model

3.4. Computation optimisation strategies

3.4.1. Calculation time for finding the steady state dynamics

As each computation starts with the structure having a displacement/rotation and velocity equal to zero, and large (current) forces are applied abruptly, large vibrations will be found initially. These large displacements and rotations will dampen out over time as the computation will tend to approach the steady state solution. An example of this phenomenon is given in Figure 3.24a. In reality, this cannot occur. Flow velocities are not represented by a heaviside step function, increasing from 0 m/s to 4.5 m/s in a manner of milliseconds. This process will take several hours. Therefore, these unrealistic computations must be mitigated. Note that rotations in the figure are displayed on the y-axis on the right-hand side.

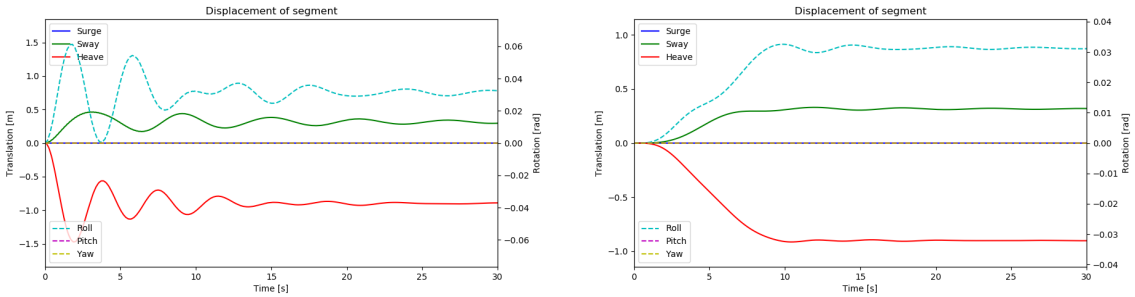

(a) Result of computation without smoothening

(b) Result of computation with 10 second smoothening

Figure 3.24: Computation optimisation by smoothening initial forces

To improve the computation time for finding the steady state response, the initial overshoot must be minimised. Therefore, an option has been added to the model to smoothen the first N seconds of the computation, creating a slow and steady increase of forces to avoid over-excitation. A function allowing for a smooth increase of the force is presented by the following conditions:

$$\begin{aligned} &\text{for } t = 0: \\ &\qquad y = 0 \\ &\qquad \dot{y} = 0 \\ &\text{for } t = N: \\ &\qquad y = 1 \\ &\qquad \dot{y} = 0 \end{aligned} \tag{3.39}$$

Although an infinite number of equations describe these four conditions, the following smoothening function has been implemented:

$$y = 0.5 - 0.5 \cdot \cos(\pi \cdot \frac{t}{T_{smooth}}) \tag{3.40}$$

If the smoothening function is applied to the same calculations as has been done for Figure 3.24a, Figure 3.24b will be obtained. It can be observed that initial spikes are mitigated and the computation will approach the steady state solution much faster. For calculations regarding the initial impact, this smoothing curve should not be used for the waves. This scenario can be approximated most optimally by smoothening the current and wind for a few dozen seconds first. When the equilibrium position is approximated, the wave impact can be simulated. How this impact is simulated can be found on the following page.

3.4.2. Mesh analysis on accurate estimation of wave inertia forces

To find the wave inertia forces on the floaters, the Morison equation is solved. To find the average relative acceleration of the water particles compared to the floater, a volumetric integral needs to be solved. This can be done by representing the floaters with a grid. For each cell of the grid, the water particle acceleration

in y- and z-direction is defined, it also contains information on the local width (x-direction) of the floater and whether water or air is present at that cell. The entire mesh can be presented as follows, where the four types of information are shown in the following order: "Local width, wave present, y-acceleration and z-acceleration". A complete grid can be used to find the average force.

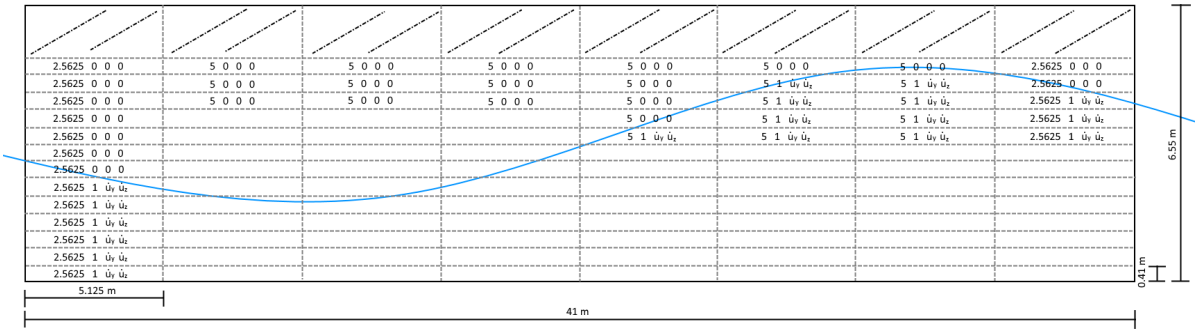

Figure 3.25: Mesh configuration for small floater, grids partially filled with values representing local data

A smaller gridsize allows for a more accurate result, but also requires significantly more computation time. Appendix J investigates which gridsize gives accurate results, but is still relatively fast. The results of this mesh study are as follows below, where the gridsize is taken as a function of wave parameters.

$$\frac{L}{L_{grid}} = 25 \tag{3.41}$$

$$\frac{H}{H_{grid}} = 15 + 10 \cdot H \tag{3.42}$$

3.4.3. Impact of approaching wave field

An option to find the impact of an approaching wave field has been added in the model. An instantaneous transition between "no wave" and "wave" is not possible, as it would inflict a jump or kink in the motion of the water. To make the connection between the two phases smooth and more realistic, it has been decided to let the two phases overlap temporarily. In this intermediate phase, the "no wave" phase dampens out using a cosine curve, while the "wave" phase increases from 0 to 100 per cent presence. The intermediate phase has a length of a quarter of the wave length, allowing for a fast but smooth transaction.

The transaction phase can be characterised using Figure 3.26, where the gradual increase and decrease of the two states are shown. The two lines represent all values that attached to a state. For example, the surface elevation can be defined using this graph: the surface elevation according to the 'no waves' state is 100 per cent present before the transition, while the surface elevation according to the 'waves' state is 100 per cent present after the transition. In the transition phase, a gradual and smooth interface is created. Note that the y-axis displays the presence as a percentage, meaning the combined presence of the two lines should always be 100. The definition of the lines are represented by a function similar to Equation (3.40).

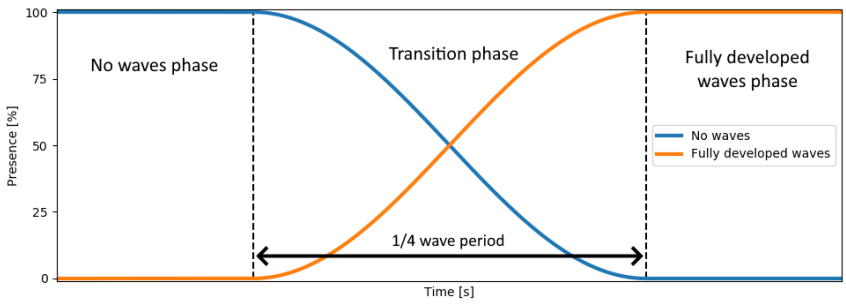

Figure 3.26: Method to describe transition between 'no waves' and 'waves'

3.4.4. Dimensionless heatmap analysis

In Section 6.1, heatmaps are created to perform a dimensionless analysis on several characteristics of a Tidal Bridge. As the mesh approximation of the waves takes a significant amount of computation time, and heatmaps require a significant amount of data points on both their x- and y-axis, long computation times are found. To reduce this computation time, two strategies are implemented. The first being that the model allows for multithread processing. For a standard quadcore processor with multithreading, the computation can be split over all 8 threads of the CPU. As a result, the computation time is reduced by about 80 per cent. For powerful CPUs used for intensive calculations, a reduction up to 95 per cent can be expected. The second method used is to use interpolation between the data points. Linear interpolation can be used, but would lose information regarding minimum and maximum values, when they are found in between data points. Cubic interpolation between the data points solves this problem: it enhances the quality of the plots, while estimating the maximums and minimums in between data points more accurately. As an example, two heatmaps are shown below. The first contains the raw data, the second being the enhanced plot for a 16x16 grid.

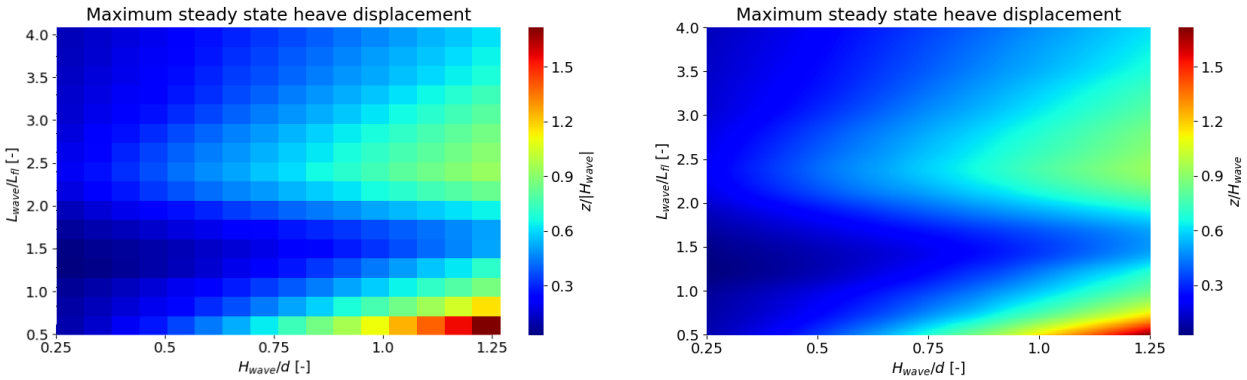

(a) Raw heatmap data

(b) Enhanced heatmap using cubic interpolation

Figure 3.27: Difference between raw data and the cubic interpolated enhanced heatmap

3.5. Serviceability limits

Although serviceability limits are defined differently depending on country or state, all regulations define the limits in such a way that 'safe' traffic passage can be guaranteed. Many researches have been done regarding acceptable motion. In these studies, distinction has been made between six types of motion, the six degrees of freedom in a three-dimensional space.

For the Palmerah Tidal Bridge, specific upper bounds for the six degrees of freedom are not defined yet. Translation and interpretation of local regulations was deemed impossible by the creators of the conceptual design. Therefore, upper and lower bounds of these limits are estimated using other regulations. For the Palmerah Tidal Bridge specifically, an allowable downtime of 5 per cent has been suggested [5], enabling allowance of exceedance of serviceability limits during extreme weather conditions.

As an upper bound of acceptable motion can be found when studying Figure 3.28, where ranges of acceleration are shown as function of the period. This specific graph is mainly used for sailing environments [39], hence an upper limit for a Tidal Bridge. As a general rule of thumb, an upper limit of about 0.08 g or 0.8 m/s can be assumed, as it keeps the oscillations into the 'bearable' or 'not perceptible' segment of the graph.

Lower limits can be found studying the proposed design of the Sognefjord bridge and the already existing design of the Bergsøysund bridge. Both Norwegian bridges use floating floaters for their bridge design. However, these floaters solely bear the vertical load of the bridge [40], while the Tidal Bridge studied in this report also bears horizontal loads induced by current and waves. The deflection and motion limits in the six degrees of freedom for both bridges are presented in Table 3.5. The limits defined for these bridges can be defined as lower limits, as these bridges are designed for traffic moving at respectively 80 [40] and 110 km/h [41], while the maximum speed on the Palmerah Tidal Bridge has been set to 50 km/h [4].

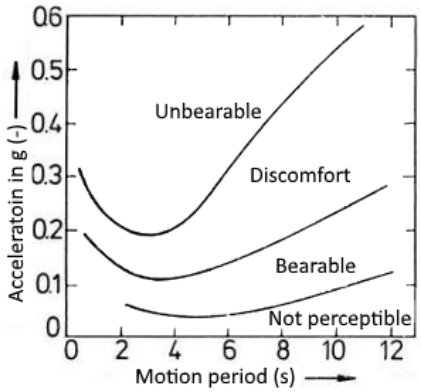

Figure 3.28: Motion categories for acceleration as function of specific period [39]

Wang and Wang introduced various recommendations for motion in their book Large Floating Structures; Technological Advances [42]. The results of their study at the University of Singapore showed very high horizontal en vertical motion tolerances. It was determined that accelerations of 0.3 g were acceptable. When comparing this data to Figure 3.28, the recommended values result in an 'Unbearable' or 'Discomfort' classification. It can be concluded that these tolerances are somewhat extreme.

With the defined upper and lower limits for acceleration, a narrow band is defined for acceptable motion for sway and heave. However, for rotational movement acceptable motions are not very well defined yet. As this is all information available, limits are defined by taking the maximum allowed value of the two Norwegian bridges. As the Tidal Bridge is constructed to be able to move in sway and heave direction, displacement limits are disregarded. Surge limits are not defined in the found literature, but with the proposed Tidal Bridge design these are expected to be minimal. The limits discussed are also shown in Table 3.5. These limits deviate from the values proposed by Hoogsteder [5], as other data became available.

	Sognefjord bridge		**Bergsøysund bridge**		**Tidal bridge**	
	Deflection	Motion	Deflection	Motion	Deflection	Motion
Surge	–	0.5 m/s^2	–	–	–	–
Sway	L/200 m	0.5 m/s^2	L/350 m	0.5 m/s^2	–	0.8 m/s^2
Heave	L/200 m	0.7 m/s^2	L/350 m	0.7 m/s^2	–	0.8 m/s^2
Roll	0.060 rad	0.070 rad/s^2	0.044 rad	0.107 rad/s^2	0.060 rad	0.107 rad/s^2
Pitch	0.044 rad	0.107 rad/s^2	0.03 rad	0.05 rad/s^2	0.044 rad	0.107 rad/s^2
Yaw	0.060 rad	0.050 rad/s^2	0.025 rad	0.07 rad/s^2	0.060 rad	0.07 rad/s^2

Table 3.5: Deflection and motion limits of the Sognefjord and Bergsøysund bridge [4, 40, 41]

4

Experimentally determined added mass and radiation damping

This chapter describes the experiments performed to confirm and validate the magnitude of the added mass and radiation damping, as determined in Section 3.2.2 and Section 3.2.3. Better understanding of the two parameters allows for a better understanding of the dynamic behaviour of the current design (Chapter 5). It also also improves the parametric study to be performed in Chapter 6, where accurate understanding of the dynamics as function of element size is vital.

4.1. Objective of experiment

The objectives of the experiments are to validate the found coefficients for added mass, and find appropriate coefficients for radiation damping. As the primary motion is found in sway, heave, and roll motion, a 2D analysis will be sufficient to find the most important factors. As sway motion cannot be an oscillating motion when the segment is not connected to a pendulum - which would make the experiment significantly easier to perform - and the mass/damping forces for sway motion are expected to be about 10 times smaller than they are for heave, sway will not be investigated as well. As a result of these simplifications and reductions, the added mass and radiation damping coefficients for heave and roll will be investigated. Curve-fitting of the displacement over time during a decay test will provide the information to this objective.

4.2. Experimental scaling

Scaling will be done using Froude scaling (Equation (4.1)), as inertia and gravity are the key factors in the experiments. This has as consequence that turbulence is not appropriately scaled. This will affect the damping terms.

$$Fr = \left[\frac{u}{\sqrt{g \cdot d}}\right]_p = \left[\frac{u}{\sqrt{g \cdot d}}\right]_m \tag{4.1}$$

Scaling factor λ will be used, based on the ratio between the size of the original structure and the size of the model. Dependence of density of water will also need to be accounted for, as there is a density difference between tap water and salty sea water. Scaling results in the information shown in Table 4.1.

4.3. Experimental methodology

4.3.1. Geometry of the scale model

During the decay experiments, multiple aspects of the segments are varied. These are: variation of length of the floaters, the width of the floaters, and weight of the total structure. The construction materials and variations of the elements are discussed below.

Test environment

The test object will be subjected to its own heave and roll motion, in a still bath of water. The bath should be sufficiently large compared to the model, so that influence by the reflective walls of the bath is prevented. The outdoor bath used for the experiments has a diameter of 2.5 meters and up to 0.58 meters in depth. The bath is surrounded by three walls ans a roof, to mitigate environmental influence by rain and wind as much as possible.

Physical parameter	Unit	Multiplication factor
Length	[m]	λ
Rotation	[rad]	1
Time	[s]	$\sqrt{\lambda}$
Mass	[kg]	$\lambda^3 \cdot \rho_P / \rho_M$
Mass moment of inertia	[kgm^2]	$\lambda^5 \cdot \rho_P / \rho_M$
Damping	[Ns/m]	$\lambda^{2.5} \cdot \rho_P / \rho_M$
Rotational damping	[Nsm]	$\lambda^{4.5} \cdot \rho_P / \rho_M$
Spring stiffness	[N/m]	$\lambda^2 \cdot \rho_P / \rho_M$
Rotational spring stiffness	[Nm]	$\lambda^4 \cdot \rho_P / \rho_M$
Force	[N]	$\lambda^3 \cdot \rho_P / \rho_M$
Moment	[Nm]	$\lambda^4 \cdot \rho_P / \rho_M$
Pressure	[N/m^2]	$\lambda \cdot \rho_P / \rho_M$
Velocity	[m/s]	$\sqrt{\lambda}$
Angular velocity	[rad/s]	$\sqrt{\lambda}^{-1}$
Acceleration	[m/s^2]	1
Angular acceleration	[rad/s^2]	λ^{-1}

Table 4.1: Scaling ratios for various physical parameters using Froude scaling [43]

The tests will be performed using a scale model of a single Palmerah Tidal Bridge segment, using a of scale 1:100 (and small deviations on this scale ratio). As a results, the dimensions of the scale model will be 1000 mm, 390 mm and 28 mm for length, width, and draught respectively. These dimensions will form the basic scenario for the tested bridge. Variations in structure dimensions will be made around this basic scenario. The water depth in the Strait at the Palmerah Tidal Bridge can be scaled as well, creating a water depth of 230 mm.

Construction materials

Floaters are constructed making use of polystyrene type EPS60. When submerged, this lightweight but solid material may absorb water over time. To prevent absorption, plastic is wrapped tightly around the material. No pendulums are connected to the floaters, as the pendulums only couple the vertical and horizontal motion. The density of the material has been measured, and was found to be 14 kg/m^3. The floaters used have a height of 75 mm.

The rigid connection between the floaters, which is a stiff truss structure in the Palmerah Tidal Bridge proposal, is modelled with a stiff spruce plank. The plank, with dimensions 1000x143x18, is to be rigidly connected to the floaters. The use of glue is to be avoided, to make the elements interchangeable without wasting resources. Long screws are used to create enough friction between the elements for which the connection can be assumed rigid. The plate is also assumed to be rigid, as is verified in Appendix K.3. Including the screws, the spruce planks weighs 1211 grams.

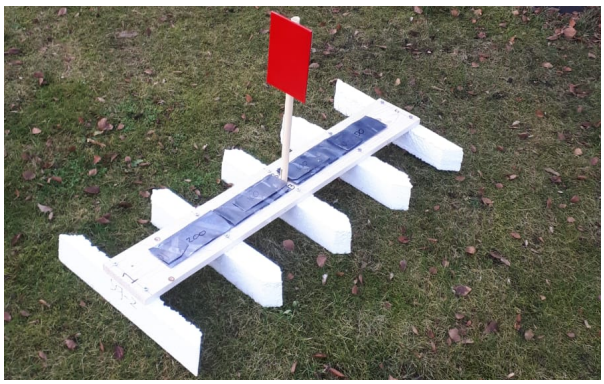

Figure 4.1: Photo of the 1:100 scale model

A vertical PVC tube is attached to the structure by drilling a 19 mm hole in the spruce plate, placing the tube in the hole and using glue to connect the two elements. The length of this tube is used to scale the rotational moment of inertia appropriately. It also functions as the support for a bright coloured piece of cardboard, which is used to track the motion of the bridge as function of time. Both the 480 mm long tube and the cardboard (dimensions 188x120 mm) were weighted, resulting in values of 51 and 52 grams respectively.

Extra weight, to obtain the wanted draught, is realised using small pieces of lead. The dense material, allows for an easy distributed load on top of the tested elements. The lead can also be used to correct the resting position of bridge, if it is non-symmetric in weight distribution. A list of all equipment is shown in Section K.2.

Small floater

The length of the small floaters will be varied between 280, 340, and 400 mm, the width will be varied between 28, 35, and 42 mm. This is in line with the original size of the Palmerah Tidal Bridge proposal, with the small floater having the size of 34x3.5m. The nine combinations are labelled as follows:

Label	Length [mm]	Width [mm]
S1	280	28
S2	280	35
S3	280	42
S4	340	28
S5	340	35
S6	340	42
S7	400	28
S8	400	35
S9	400	42

Table 4.2: Experiment variations of small floater with option labels

Large floater

Similar variations will be tested for the large floaters, where the original proposed width is equal to 5 meters. Again, deviations will be made in length and in width. The combinations and there labels are presented below:

Label	Length [mm]	Width [mm]
L1	280	40
L2	280	50
L3	280	60
L4	340	40
L5	340	50
L6	340	60
L7	400	40
L8	400	50
L9	400	60

Table 4.3: Experiment variations of large floater with option labels

Draught

The draught of the structure is varied three times, being 23, 28, and 33 mm. In order to obtain this, weights need to varied throughout the experiments, as the horizontal area changes depending on the floaters used. The options considered are:

Label	Draught [mm]
D1	23
D2	28
D3	33

Table 4.4: Experiment variations of draught with option labels

Differences in draught can be obtained by using weight. The use of small bags of sugar has been chosen, as the material is easy to distribute and has a low cost. Varying between the different setups, between 0 and 3000 grams of load needs to be applied.

4.3.2. Setup program

In the series of experiments, the 27 setups denoted in Appendix K.1 are performed. Every setup has been tested 10 times: 5 times for heave motion and 5 times for roll motion. The difference between these two motions is denoted with an 'H' for heave and 'R' for roll, behind the setup number. The 5 different tests per motion per setup are denoted using the Roman numerals I, II, III, IV, and V.

4.3.3. Instruments and measurements

A GoPro HERO5 has been used to track the motion of the model. The camera had been set to a frame-rate of 120 FPS, using a resolution of 1920x1080. GoPro is famous for their use of a wide-angle lens, commonly known as the fisheye effect. Distortion due to this effect is mitigated when the considered object is placed in the centre of the field of view (FOV) of the GoPro, and when optical zoom is used. Additionally, the Field Of View settings have been adjusted to the 'narrow'-setting, where the GoPro automatically corrects the lens distortion. As mentioned before, a vertical stick has been attached to model, placed exactly above the COG. At the tip of the stick a red coloured rectangle has been attached, see Figure 4.3a. The bright coloured rectangle has been chosen to form as much contrast to the background as possible. This way, software can be used to track the motion of the easily. The setup of the semi-enclosed testing facility is shown in Figure 4.2.

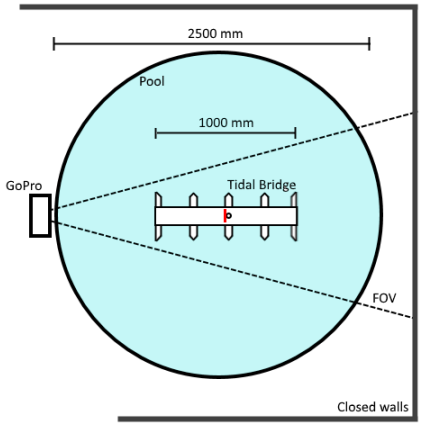

Figure 4.2: Top view sketch of semi-enclosed testing facility

As explained earlier, a vertical sticks made from PVC and being 480 mm long, is rigidly glued to decks, one to each. Ten long screws are drilled through the plate, forming the attachment to the EPS60 floaters. These floaters have pre-made holes, making the floaters interchangeable. Making the floaters interchangeable allows for a vast reduction in the number of plate decks needed. Pieces of lead being 50/100/200/400 grams per element are prepared. These pieces can be taped to the deck, forming extra weight to obtain the desired draught. Smaller elements are created to allow for more precise addition of weights.

Performing an experiment comes in 11 steps and 6 substeps:

1. Collect setup configuration materials
2. Register building elements used
3. Apply and distribute sufficient weight
4. Place model in water
5. Verify horizontal resting position
6. Start recording and verify object being clearly visible
7. Repeat heave test 5 times
   (a) Submerge segment by pressing on deck
   (b) Wait for still water
   (c) Sudden release of segment
8. Repeat roll test 5 times
   (a) Rotate segment by applying torque on pvc tube
   (b) Wait for still water
   (c) Sudden release of segment
9. Stop recording
10. Remove model from water
11. Remove weights and floaters from deck

4.4. Experimental results

4.4.1. Extracting the added mass and radiation damping

Video material of the experiments is used to track the motion over time. Python library cv2 is used to log the x- and y-coordinate of the centre pixel of the red-coloured cardboard. The library is also used to measure the angle over time. An illustration of the software is shown below, in Figure 4.3a. The photo shows the cyan dot, being the centre of the red rectangle and the yellow circumference of the rectangle.

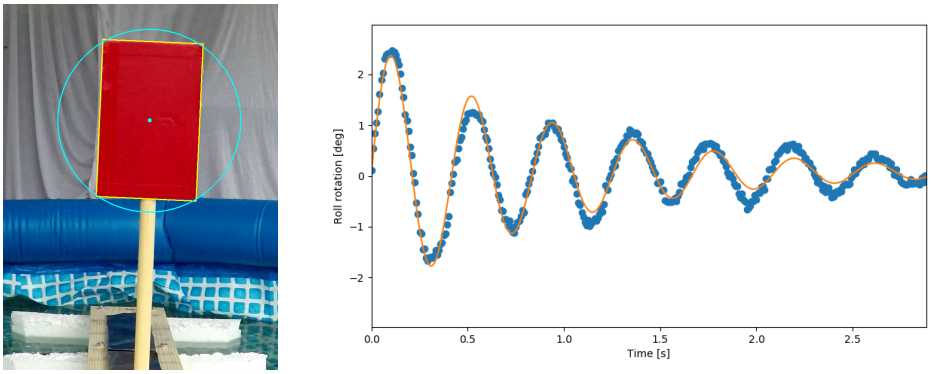

(a) Logging video data

(b) Tracked rotation angle over time and corresponding curve-fit

Figure 4.3: Processing of data; test 24-R-III

The obtained data is then used to curve-fit Equation (4.2), which represents the movement of a linear mass-damper-spring system. Using this equation assumes that the motion is uncoupled of motions in the other degrees of freedom and that surface tension is negligible. This last statement is appropriate, as calculating Webers number comes down to about 43, being much larger than 1. For rotations, the M term does not represent the mass, but the mass moment of inertia, C and K represent the rotational damping and rotational spring respectively. The most optimal curve-fit is obtained by minimising the Root Mean Square Error (RMSE) by adjusting the mass-term, damper-term, and initial velocity 'a'. The spring term is already known, as hydrostatic assumptions can be made. The magnitude of this spring term is elaborated in Section C.5.

$$y = a \cdot e^{-\zeta \cdot \omega_0 \cdot t} \cdot \sin\left(\sqrt{1-\zeta^2} \cdot \omega_0 \cdot t\right) \tag{4.2}$$

Where:

$$\omega_0 = \sqrt{\frac{K}{M}}$$
$$\zeta = \frac{C}{2 \cdot \sqrt{M \cdot K}} \tag{4.3}$$

An illustration of one of the RMSE fits is shown in Figure 4.3b. The curve has been fitted using the first 180 frames, meaning the first 1.5 seconds. After this, coupled motion becomes more and more visible. If the RMSE fit also accounts for these later data points, damping would be overestimated as motion gets transferred into other types of motion, or underestimated by the presence of reflecting waves.

As mentioned, the presented equations assumes linear springs and dampers. This implies that the non-linear drag and roll radiation damping terms are of negligible magnitude. As explained in Subsection 3.2.3, non-linear radiation damping due to roll can be neglected based on the shape and small rotation angles. While the drag term may not be neglected in the full-scale Tidal Bridge, the 1:100 scale model does allow for this reduction in terms. This can be shown using the following magnitude ratio between the drag damping and the radiation damping, where it is shown that drag damping is in the order of 1 per cent.

$$\begin{aligned} \frac{F_{drag}}{F_{radiation}} &= \frac{0.5 \cdot A \cdot C_{DS} \cdot \rho \cdot V^2}{C_{rad} \cdot V} \\ &\approx \frac{0.5 \cdot 0.00081 \cdot 0.75 \cdot 1000 \cdot 0.25^2}{7.5 \cdot 0.25} = \frac{0.018}{1.875} \approx 0.01 [-] \end{aligned} \tag{4.4}$$

Because radiation damping is the dominant source of damping, it is assumed that the C-term in Equation (4.2) is solely the radiation damping term. The found mass term equals the combination of added mass plus the own mass of the bridge (or the mass moment of inertia). The resulting added mass and radiation damping for the heave and roll motions are presented below, including the 90 percent interval error bars. The length of the floaters is indicated using colours, the hatch shows the width (Small floaters / Large floaters). This separation in size leaves groups of three test setups, where the difference can be found in the draught, respectively 23, 28, and 33 mm. See Appendix K.1 for a more detailed overview of the different setups.

- Green: Short floaters (280 mm)
- Orange: Medium floaters (340 mm)
- Red: Long floaters (400 mm)
- Diagonal: Slender floaters (28/40 mm)
- None: Medium floaters (35/50 mm)
- Dotted: Wide floaters (42/60 mm)

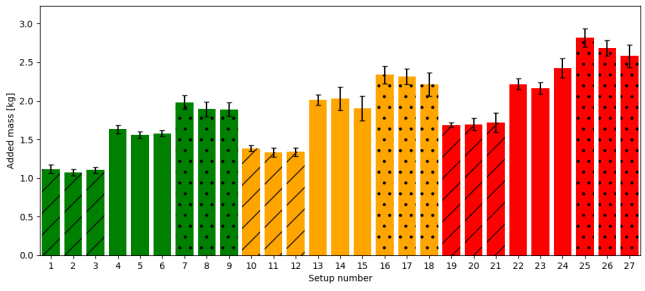

(a) Heave added mass

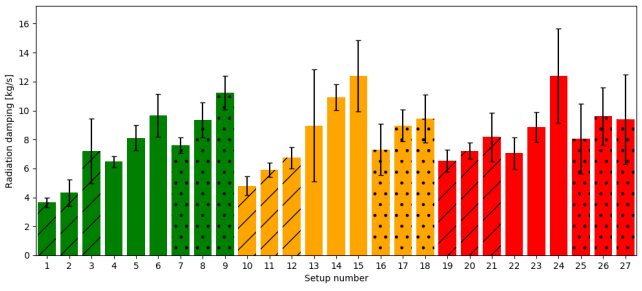

(b) Heave radiation damping

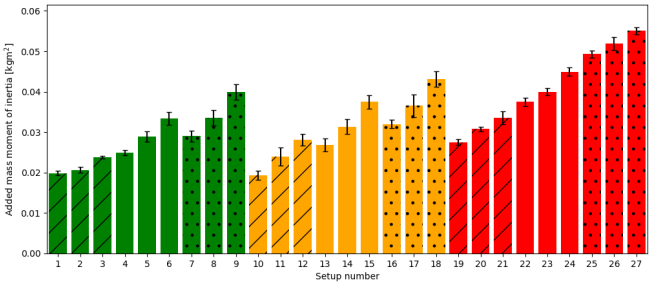

(c) Roll added mass moment of inertia

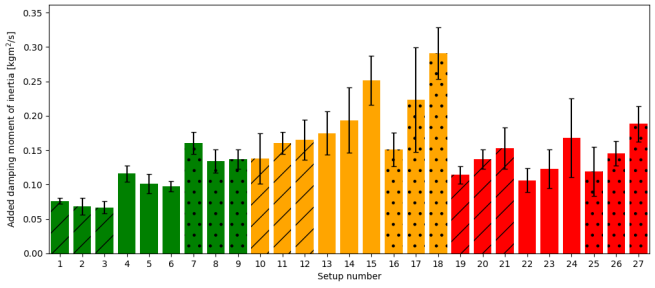

(d) Roll radiation damping moment of inertia

Figure 4.4: Experimentally determined added mass (moment of inertia) and radiation damping (moment of inertia)

4.4.2. Comparison with literature

The absolute values above will now be compared with the results according to the tool that was written based on the literature found in Section 3.2.2. The ratio between the results are presented below, where the dotted line represents perfect agreement. It can be noted that the added mass for heave is modelled quite accurately, a small distortion is found for wider floaters and increasing draught. Heave radiation damping is also modelled quite accurately, with a maximum average deviation of only 50 percent. The presented method to estimate the roll added moment of inertia does not appear to be very accurate. Increasing draught increases the added mass moment of inertia more than the tool predicts, while an increase of width and length creates an opposite correlation; smaller floaters lead to a significant underestimation of the added mass. The radiation damping moment of inertia for roll gives remarkable results; the absolute damping value as shown above decreases for the longer floaters. As a results, the ratio between the experimental results and the hand-calculations as presented below form a significant jump in between setup 18 (orange) and 19 (red).

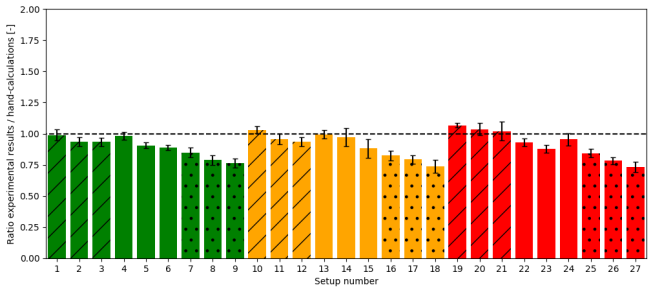

(a) Heave added mass

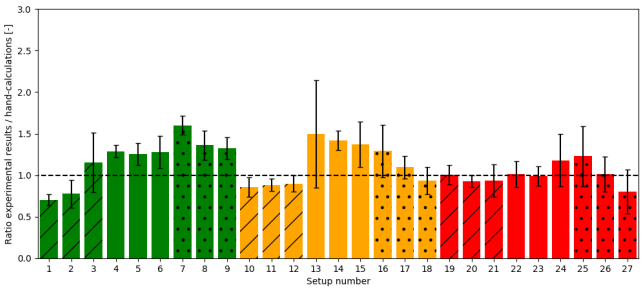

(b) Heave radiation damping

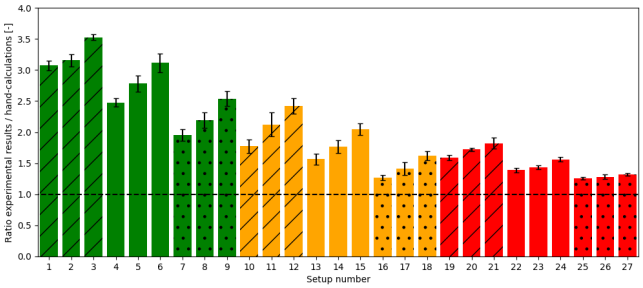

(c) Roll added mass moment of inertia

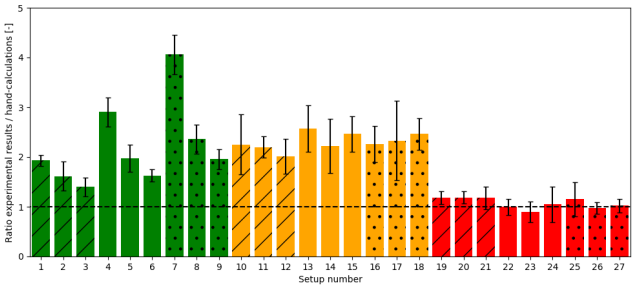

(d) Roll radiation damping moment of inertia

Figure 4.5: Ratio between experimental results and hand-calculations based on literature

4.4.3. Optimising the Tidal Bridge dynamics model

As the ratio between the experiments and the hand-calculations for the heave radiation damping is on average equal to about 1, it is assumed that the current state of the tool approximates the damping appropriately. As no clear trend is found in the data, no alterations will be proposed for this element. The prediction of added mass for heave is quite accurate as well. However, the clear trend allows for a better estimation. The added mass for heave for the used floater shape is better approximated using the following equation:

$$M_{added,heave} = \sum_{i=1}^{N_{fl}} C_{added,heave} \cdot \rho \cdot V_i \tag{4.5}$$

In the equation above, $C_{added,heave}$ is a parameter representing the shape of the structure. Based on the experimental results in Figure F.4, it can be concluded that the effect of draught is of negligible effect. This makes sense as heave motion makes the water interact with the horizontal shape of the floater profile. As V_i is a linear function of draught, while $M_{added,heave}$ is not dependent on draught, it can be concluded that $C_{added,heave}$ must be a function of draught^{-1}. As the horizontal shape (coloured green in Figure 4.6) of the floaters governs the added mass, a large shape-ratio dependence is to be expected. $f(W/L)$ represents this shape function. To make the complete $C_{added,heave}$ equation dimensionless, a length term has been added.

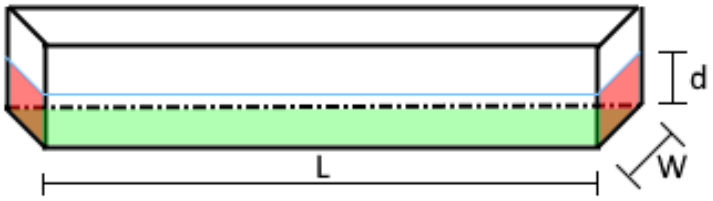

Figure 4.6: Interaction areas between floater and water

$$C_{added,heave} = f\left(\frac{W_{fl,i}}{L_{fl,i}}\right) \cdot \frac{L_{fl,i}}{d_{fl,i}} \tag{4.6}$$

Where:

$$\begin{aligned} f &= a + b \cdot \frac{W_{fl,i}}{L_{fl,i}} + c \cdot \left(\frac{W_{fl,i}}{L_{fl,i}}\right)^2 \\ &= 0.070 - 0.314 \cdot \frac{W_{fl,i}}{L_{fl,i}} + 1.926 \cdot \left(\frac{W_{fl,i}}{L_{fl,i}}\right)^2 \end{aligned} \tag{4.7}$$

The equation above shows a very good fit for the floaters with the presented shape. However, the limited number of experiments done and the lack of mathematical roots of the presented equation require the user to use this care.

The approximation for added mass moment of inertia in roll motion that was proposed earlier does seem to create a significant deviation to the experimentally found values. The need for a better approximation is needed, which comes in the following form:

$$\begin{aligned} M_{added,roll} = &\sum_{i=1}^{N_{fl}} C_{added,roll,b} \cdot \rho \cdot V_i \cdot L_{fl,i}^2 \\ &+ \sum_{i=1}^{N_{fl}} C_{added,roll,s} \cdot \rho \cdot V_i \cdot \left(h_{COG} - \frac{d_{fl,i}}{2}\right)^2 \end{aligned} \tag{4.8}$$

The equation is split into two parts: a contribution of the mass of the water which interacts with the bottom of the floaters (coloured green in Figure 4.6), and the contribution of water which interacts with the sides (coloured red in Figure 4.6). The relative height COG of the structure creates significant horizontal floater displacements for small roll rotations. Just as was done for heave motion, it is assumed that the amount of water interacting with the bottom side of the floater is not a function of the draught. Likewise, water interacting with sides of the floater are not influenced by an increase in length. As both parameters are (more or less) linearly present in V_i, compensations must be found in the coefficients. Again, shape functions are introduced representing the effect of the waterfront. To make the coefficients dimensionless, a length or width term had to be introduced as well.

$$\begin{aligned} C_{added,roll,b} &= f\left(\frac{W_{fl,i}}{L_{fl,i}}\right) \cdot \frac{L_{fl,i}}{d_{fl,i}} \\ C_{added,roll,s} &= g\left(\frac{d_{fl,i}}{W_{fl,i}}\right) \cdot \frac{W_{fl,i}}{L_{fl,i}} \end{aligned} \tag{4.9}$$

Where:

$$
\begin{aligned}
f &= a + b \cdot \frac{W_{fl,i}}{L_{fl,i}} + c \cdot \left(\frac{W_{fl,i}}{L_{fl,i}}\right)^2 \\
&= -0.00043 + 0.06347 \cdot \frac{W_{fl,i}}{L_{fl,i}} - 0.26994 \cdot \left(\frac{W_{fl,i}}{L_{fl,i}}\right)^2 \\
g &= a + b \cdot \frac{d_{fl,i}}{W_{fl,i}} + c \cdot \left(\frac{d_{fl,i}}{W_{fl,i}}\right)^2 \\
&= 6.672 - 3.413 \cdot \frac{d_{fl,i}}{W_{fl,i}} + 3.238 \cdot \left(\frac{d_{fl,i}}{W_{fl,i}}\right)^2
\end{aligned}
\tag{4.10}
$$

Again, the presented equation shows a very good fit for the performed experiments. However, use of the presented equations should be done cautiously. The radiation damping moment of inertia for roll does not appear to heave a clear trend. Because deviations are not of an order of magnitude and no better correlation can be found based on these experiments, no alterations have been made in the model. It could be hypothesised that no trend is observed due to an effect of the diffraction at the pointed tips, being of less magnitude for longer floaters.

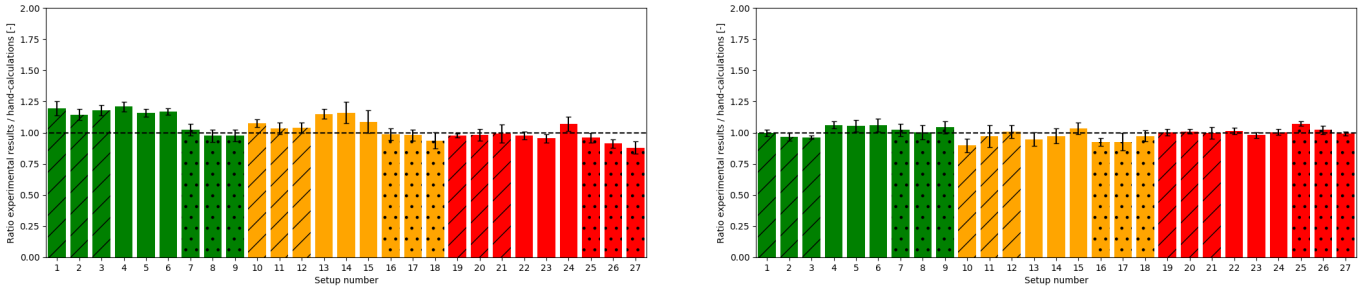

(a) Heave added mass

(b) Roll added mass moment of inertia

Figure 4.7: Ratio between experimental results and modified hand-calculations

As the presented modified coefficients are dimensionless, they can be directly implemented into the added mass and radiation damping tools. The added mass and radiation damping for degrees of freedoms not tested in the experiments have not been altered. Although errors may still be present in those calculations, their magnitude is of such magnitude lower that it will have little effect on the dynamic computations.

5

Forcing characteristics of a Tidal Bridge

Based on the dynamic model created in Chapter 3 and the experimentally determined coefficients in Chapter 4, this chapter describes the dynamic characteristics of the current Palmerah Tidal Bridge design and what the influence of the different types of forces are. After this, the influence of an initial impact is examined. The purpose of this chapter is to locate the most important factors determining the dynamics of a Tidal Bridge. This information will be used in the dimensionless parametric study, performed in Chapter 6.

5.1. Dynamic characteristics of the Palmerah Tidal Bridge

The current design of the Palmerah Tidal Bridge can, when in resting position during still water in a 2D-model, be described using a mass and three springs. The mass is given by the mass of a segment and the added mass, the three springs are as follows:

- Vertical spring: hydrostatic pressure
- Rotational spring: hydrostatic pressure
- Diagonal spring with eccentricity: pendulum foundation

This can now be schematised using the following system:

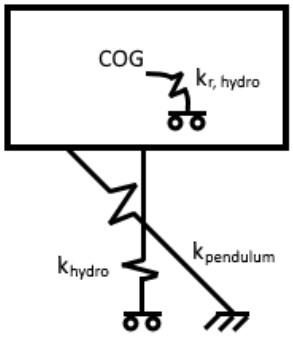

Figure 5.1: Simple 2D schematic of the Palmerah Tidal Bridge

This system can be represented by a mass and spring matrix, describing the behaviour in the three degrees of freedom: sway, heave, and roll.

$$\boldsymbol{M} = \begin{bmatrix} 24.98 & 0 & 7.85 \\ 0 & 47.08 & 0 \\ 7.85 & 0 & 3505.95 \end{bmatrix} \cdot 10^5 \qquad \boldsymbol{K} = \begin{bmatrix} 11.74 & 9.85 & 148.52 \\ 9.85 & 9.08 & 124.62 \\ 148.52 & 124.62 & 1967.16 \end{bmatrix} \cdot 10^7 \tag{5.1}$$

This matrices can be used to calculate the natural periods.

$$\boldsymbol{p_n} = \begin{bmatrix} 0.58 \\ 4.48 \\ 6.69 \end{bmatrix} \text{s} \tag{5.2}$$

The used method for calculating the natural periods contains two problems. Firstly, as the pendulums rotate a significant amount during the tests, and because both the horizontal and the vertical component of the

pendulum-spring are a function of the angle, it has the result that the pendulum spring is in fact a non-linear spring. Secondly, non-linear springs are also found for the vertical and rotational hydrostatic springs. Waves cause anything but hydrostatic pressures, the complex pressure field in both y- and z-direction makes both springs non-linear as well, being a function of draught, time and many wave parameters.

Finding the analytical solution for these non-linear springs is deemed impossible. However, the constructed python model can be used to find the amplitude as function of the forcing frequency. The natural frequency will be very close to the frequency for which the amplitude is maximum, as the damping is very low. Below, the amplitude of motion is given as function of the forcing period for 1 meter high waves (propagating in both directions). In this computation, the flow velocity has been set to 0 m/s and no wind is present. Remaining conditions are taken as present in Appendix L. Waves with a period lower than 3 seconds (~14 m) are not displayed, as the used Morison equations becomes increasingly invalid for shorter waves.

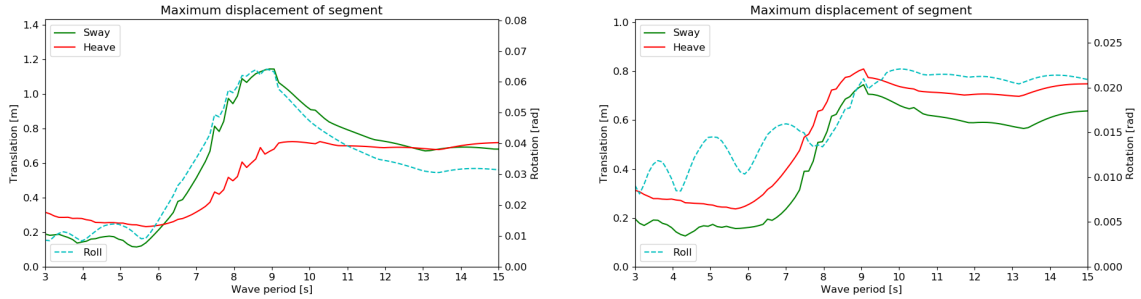

(a) Waves in positive direction

(b) Waves in negative direction

Figure 5.2: Maximum displacement as function of wave period

It can be noted that the magnitude of motion is for roll and sway significantly larger for waves propagating in positive direction. This indicates that the non-linear effect of the pendulum angle, wave pressure and particle velocity/acceleration is of greater magnitude for the current design. Section 6.1 will investigate whether that can be stated for all designs. It can also be noted that the maximum displacement is found for a period of about 8.8 seconds, while it was just stated that the current Palmerah Tidal Bridge design has a natural period of 6.7 seconds when linear springs are assumed. The non-linearity of the problem moves the natural frequency down. Furthermore, the maximum roll rotation seems to be amplified for multiples of 1.7 seconds. Lastly, it can be obtained from the graphs that magnitudes of translation do hardly change for wave periods below 6 seconds and above 12 seconds, corresponding to wave lengths of respectively 56 and 160 meters. This makes sense as large waves force the structure to move up and down with the waves, meaning that the response amplitude becomes solely a function of the wave height. For shorter waves, the structures interacts with the crest and through of the wave simultaneously. This results in a near-constant displacement, being nonzero as the structure interacts with the crests than the throughs.

5.2. Influence of individual forcing components

The forces influencing the dynamics of the Tidal Bridge can be separated into three categories: wind, current, and waves. These three different types of forcing have an impact on different elements of the bridge. As for example, wind forces are separated over the wind force on the deck and the wind force on the super structure. In this section, this is not evaluated separately but combined; resulting in the total influence of a given wind force. For each type of forcing, the (mean) steady state displacement for sway, heave, and roll are displaced. The (mean) steady state pendulum force has also been assessed. For the influence of waves, the characteristic is slightly changed: the maximum and minimum steady state displacements / pendulum forces are displaced. All types will be assessed for four scenarios; forcing in positive or negative direction combined with traffic being or not being present. The positive direction is defined as shown in Figure 3.3.

5.2.1. Influence of wind forcing solely

Dynamics due to wind solely are examined using the standardised computation settings as presented in Appendix L. The wind loads on the deck and super structure are of magnitude 2120 and 3000 N/m respectively.

The traffic load has been set to 128000 kg per segment. The following results are found:

Wind direction	Traffic	Sway [m]	Heave [m]	Roll [rad]	Pendulum force [kN]
Positive	No	0.175	−0.052	−0.010	333
Positive	Yes	0.175	−0.052	−0.010	333
Negative	No	−0.179	0.053	0.010	−336
Negative	Yes	−0.179	0.053	0.010	−336

Table 5.1: Influence of wind on the Palmerah Tidal Bridge

It should be noted that the addition of traffic has little to no effect on the steady state displacement, relative to the floating position without forcing. This resting position is 15 cm lower and 12 cm to the side, for the Tidal Bridge with traffic load on on top. This is a logical result as the wind force has been implemented with no dependence on the draught. What does make a difference is the response due to change in forcing: the case with traffic reacts slower due to a combined effect of extra mass of traffic and more added mass of the water in sway and roll. Change of direction influences not only the sign of the displacement and forces, but also influences the magnitude. This is due to the changing angle of the pendulum, creating a slightly different forcing balance.

5.2.2. Influence of current forcing solely

The influence of current is obtained using the same strategy, where the magnitude of the current velocity is 4.5 m/s; the maximum velocity found at the Palmerah Tidal Bridge. Remaining parameters are taken as is presented in the standardised settings in Appendix L.

Current direction	Traffic	Sway [m]	Heave [m]	Roll [rad]	Pendulum force [kN]
Positive	No	0.385	−0.919	0.034	6036
Positive	Yes	0.393	−0.922	0.033	6061
Negative	No	−0.583	1.000	−0.031	−6060
Negative	Yes	−0.594	1.005	−0.031	−6093

Table 5.2: Influence of current on the Palmerah Tidal Bridge

Although the traffic weight adds 6 per cent to the total mass of a segment, it has negligible effect on the steady state response. The large horizontal forces induced by the current translated to a diagonal force in the pendulums. This diagonal force also has a vertical component, exceeding the gravitational force significantly. Just as for the wind, it can be noted that the change in pendulum angle changes the distribution of displacements and forces. Although the forcing only changes with only one per cent, it can be noted that especially the sway movement deviates significantly. This large change indicates that the pendulum hinge is placed very far from its most optimal location for this loading scenario.

5.2.3. Influence of wave forcing solely

The influence of waves is more complex to analyse, as the oscillatory forcing does not result in a constant steady state response. Hence, three results are presented: one with the smallest (most negative) results and the largest (most positive) results. As the environmental conditions at the Palmerah Tidal Bridge deviate significantly if it comes to propagation direction, a constant wave height of 3 meter is assessed. Waves of this magnitude have a wave period of approximately 6.5 seconds and a length of approximately 60 meters. Again, the standardised settings presented in Appendix L are used for the remaining parameters.

Wave direction	Traffic	Sway [m]	Heave [m]	Roll [rad]	Pendulum force [kN]
Positive	No	−1.047 to 1.441	−0.996 to 0.429	−0.073 to 0.059	−2055 to 2056
Positive	Yes	−0.927 to 1.312	−0.925 to 0.389	−0.066 to 0.055	−1835 to 1868
Negative	No	−0.197 to 0.769	−0.795 to 0.200	−0.027 to 0.022	−1488 to 942
Negative	Yes	−0.208 to 0.752	−0.718 to 0.145	−0.027 to 0.023	−1398 to 888

Table 5.3: Influence of waves on the Palmerah Tidal Bridge

The motions in the three directions, which can all be very accurately described using a single sine, oscillates significantly more for positive waves with the current design. It also happens to be that the largest found waves in the Palmerah region are found in this direction. Again, the ranges for motion and forces can be mitigated when looking into the remaining settings. However, it can still be concluded that waves propagating in negative direction will most likely be of less importance. This is because the vertical and horizontal component of the waves accumulate into a pendulum rotation for positive directed waves, while partially cancelling each other for waves in negative direction. This is in line with the work of Hoogsteder [5] and the proposed design of Antea [1], where this result was also found. For this set of computations, traffic may influence the motion up to 10 per cent compared to the absence of traffic, making it not negligible. For larger waves, it may be assumed that traffic is not present, as the Tidal Bridge will be closed off during large storms.

5.3. Initial impact of an approaching wave field

The effect of an approaching wave field and its initial impact is studied in this section. In here, it is assumed that the segments are in their equilibrium position when enforced by current and wind, before the first wave approaches. The first wave may cause an overshoot in accelerations, which will then dampen out over time. This will lead to the steady state movement over time. To define the overshoot, the maximum acceleration in the complete time domain is compared to the maximum acceleration in the steady state solution. Variations investigated are:

1. Wave direction (positive and negative direction)
2. Wave height (1 to 3 m, 1 m increment)
3. Wave period (3 to 10 s, 0.5 s increment)
4. Flow velocity (-4.5 to 4.5 m/s, 2.25 m/s increment)

As wave length is linked to the wave period, this parameter has been scaled accordingly.

5.3.1. Positive directed waves

First, the influence will be investigated as function of wave period, for the various wave heights. Flow velocity is currently disregarded by setting this parameter to 0 m/s. This effect will be taken into account later. The figures below shows the relation for the overshoot in the three investigated degrees of freedom: sway, heave, and roll. The overshoot is displayed as a percentage.

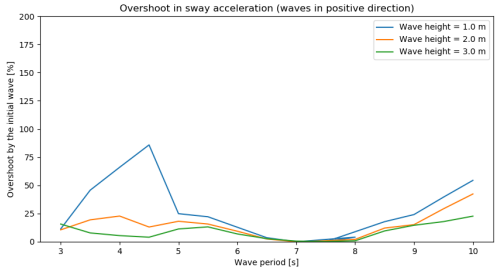

(a) Sway acceleration

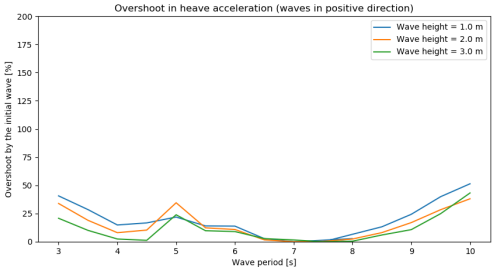

(b) Heave acceleration

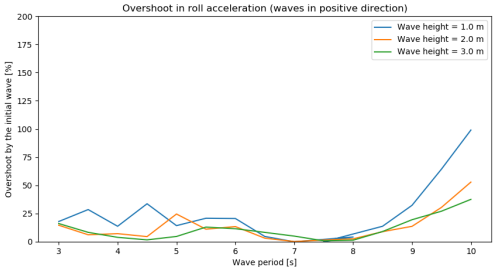

(c) Roll acceleration

Figure 5.3: Overshoot for waves in positive direction without tidal flow

Without the non-linear interaction between waves and current, it can already be concluded that overshoot can be of significant magnitude. The exact magnitude is a function of period and wave height, where larger waves inflict less overshoot. When currents are added, maximums shift accordingly. The flow velocity increases or decreases the impact rate, as velocity vectors of waves and current are added together. Still, the shape of the figures is more or less preserved. Flow velocities of 2.25 m/s in both direction are shown below:

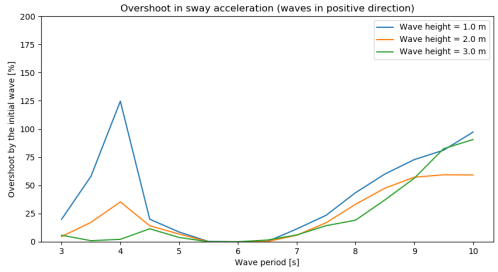

(a) Sway acceleration, negative current

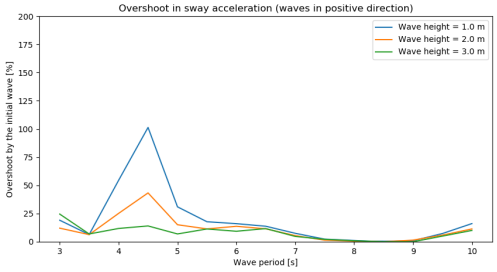

(b) Sway acceleration, positive current

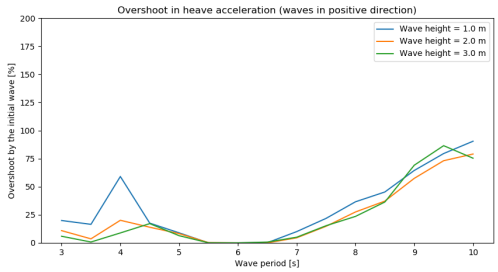

(c) Heave acceleration, negative current

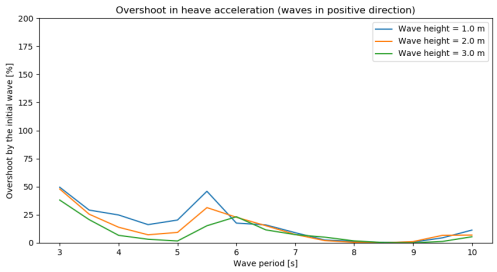

(d) Heave acceleration, positive current

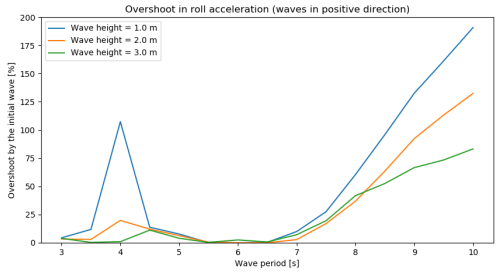

(e) Roll acceleration, negative current

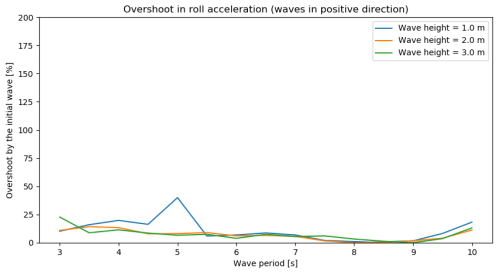

(f) Roll acceleration, positive current

Figure 5.4: Overshoot for waves in positive direction, with 2.25 m/s flow in both directions

5.3.2. Negative directed waves

Again, the flow velocity will first be set to 0 m/s, to investigate the effect of wave height and wave period solely. The results are shown on the following page. After this, the effects of tidal flow have been added to the problem, resulting in 6 more graphs. Again, it can be observed that wave height acts scalar-like, only slightly shifting the maxima. Wave period and flow velocity dominate the influence on the overshoot, where the latter shifts and magnifies the overshoot due to the non-linearity of the problem.

Waves with the same characteristics on top of flow velocities of 4.5 m/s show similar overshoot patterns as the flow velocities for 2.25 m/s do. The increase of tidal flow shifts the critical wave period further to the side, and makes the non-linearity of the problem even less predictable.

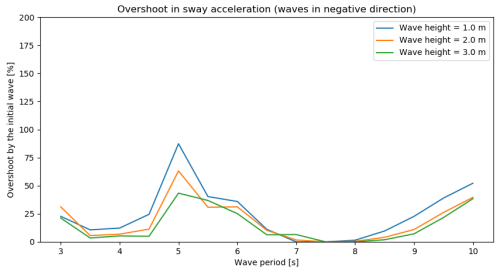

(a) Sway acceleration

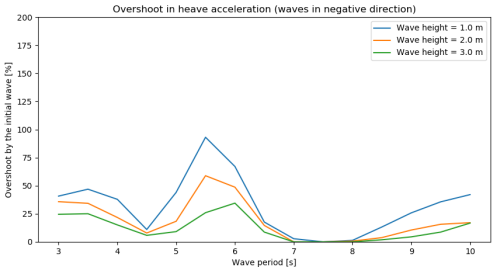

(b) Heave acceleration

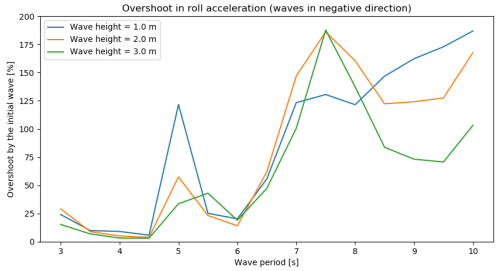

(c) Roll acceleration

Figure 5.5: Overshoot for waves in negative direction

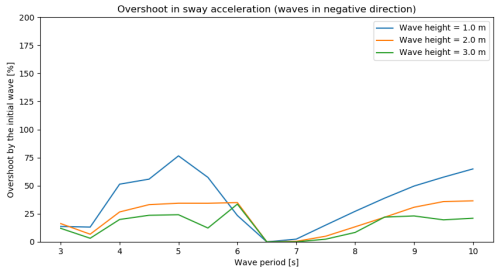

(a) Sway acceleration, negative current

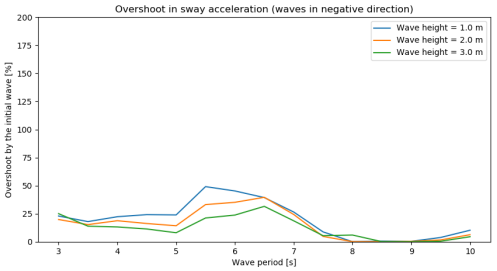

(b) Sway acceleration, positive current

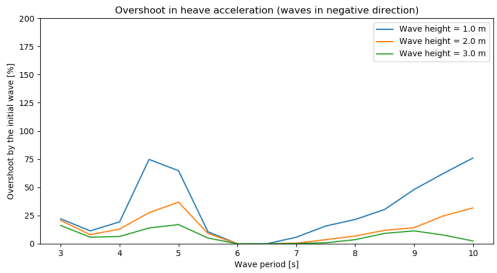

(c) Heave acceleration, negative current

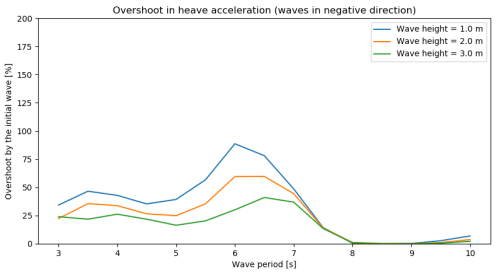

(d) Heave acceleration, positive current

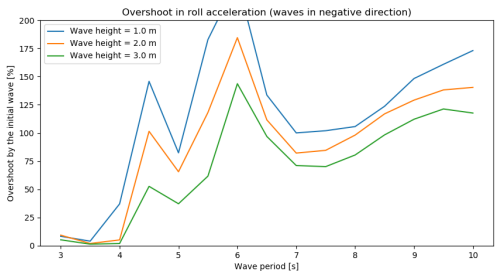

(e) Roll acceleration, negative current

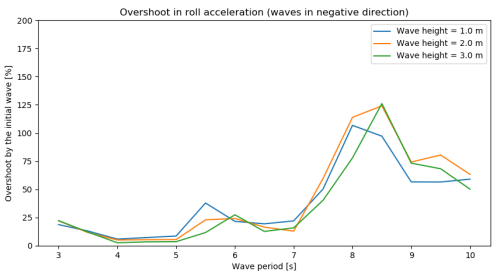

(f) Roll acceleration, positive current

Figure 5.6: Overshoot for waves in negative direction, with 2.25 m/s flow in both directions

6

Parametric study on the dynamics of Tidal Bridges

Based on the dynamic model created in Chapter 3 and the experimentally determined coefficients in Chapter 4, this chapter describes the expected dynamic behaviour of the current design for the Palmerah Tidal Bridge under various types of loading, and investigates the effect of design changes using a heat maps illustrating dimensionless Tidal Bridge characteristics. Using this, optimal design choices can be located. Once implemented, a sensitivity analysis is performed, to find the influence of all relevant parameters. To limit the cases to be considered, this chapter will mainly focus on the accelerations and whether they are acceptable.

6.1. Dimensionless Tidal Bridge characteristics

6.1.1. Wave height and wave length

In Subsection 5.2.3, it was found that waves travelling in negative direction (see Figure 3.3) induce less motion than waves propagating in positive direction. To proof this - and to see how the dynamics are related to the magnitude of wave height and wave length - sixteen figures are presented in Section M.1 and M.2. The eight figures in Section M.1 describe the motion for positive directed waves, the eight figures in in Section M.2 for waves propagating in negative direction. Both sets of eight figures show the maximum steady state displacement and acceleration for sway, heave, and roll, and the lowest and highest steady state pendulum forces as function of the dimensionless wave height (x-axis) and dimensionless wave length (y-axis). The dimensionless wave height is obtained by dividing the tested wave height by the static draught. Similarly, the dimensionless wave length is found by dividing the wave length by the (rectangular) length of a floater.

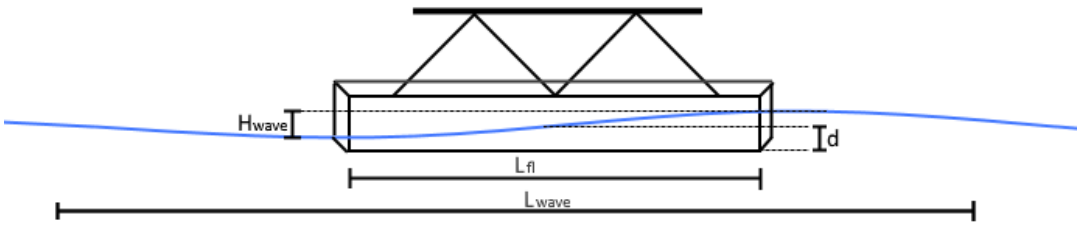

Figure 6.1: Illustration showing change of dimensionless wave height and wave length

The displacements, accelerations and forces are also presented in dimensionless values, where the wave height, gravitational acceleration, pendulum angle, and segment mass are used. For the computations in this subsection, wind and current forces are not taken into consideration. This is to examine the effect of waves solely. Traffic weight has also been neglected, as computations shown in Chapter 5 showed that this was of negligible size, while it can also be assumed that no traffic will be present during large storms. Remaining computation settings are set as shown in Appendix L.

When the difference between positive and negative directed waves are evaluated, it can be noted that the heatmaps for negative directed waves display values of less magnitude. An example of this comparison is shown in Figure 6.2, where the dynamics for sway acceleration are shown for the two wave directions. There is one exception for the previous statement: heave acceleration. The fact that waves propagating in negative direction cause less dynamics, can be explained when considering the time-averaged force on the floaters; the time-averaged force is found in the direction of wave propagation. As the pendulums produce a diagonal counter force, a vertical force will also be found. This vertical force reduces the draught for negative

directed waves, while increasing the draught for positive directed waves. As less draught creates less contact with waves (and current), dynamics are of less magnitude. The fact that heave motion does get magnified for waves in this direction, may indicate that the upper hinge of the pendulum is not located most optimally. This effect will be investigated when looking into the location of this upper hinge, which will discussed at the end of this chapter.

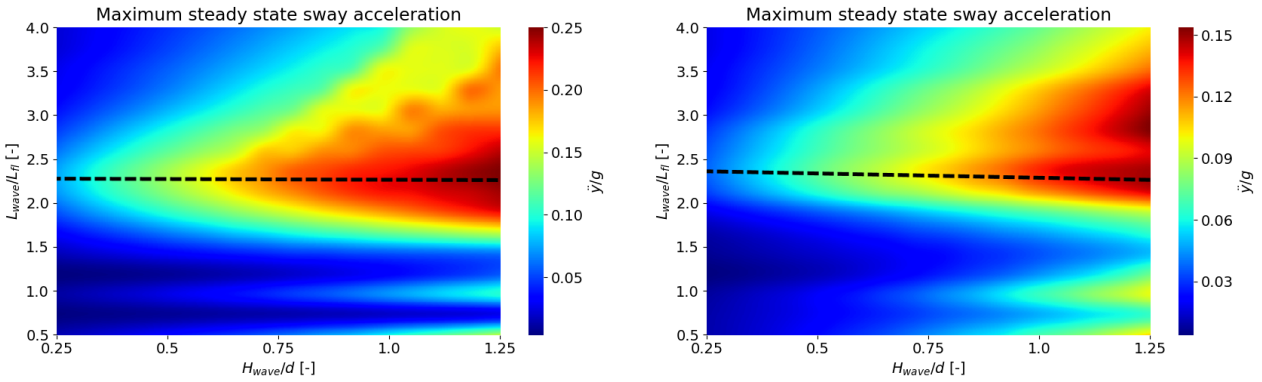

(a) Sway displacement

(b) Sway acceleration

Figure 6.2: Comparison between steady state motion characteristics for sway acceleration for waves in the two directions

For some of the presented heatmaps, strong non-linear dependencies are found for the extreme values. Maximum displacements / accelerations / forces are not always found at a specific wave length. Hence, it is impossible to consider the wave length a scalar. However, wave height does seem to have a scalar-like influence on the dynamics. To reduce the number of cases which have to be evaluated, acceleration characteristics are focused on, while other characteristics are disregarded. Maximum displacements found in the three degrees of freedom do not limit the usability of the bridge; they do define the necessary flexibility of the construction elements. Pendulum forces are assumed to be correlated to the accelerations in the three degrees of freedom. As the accelerations show the most vital information for investigation in the dynamics, critical lines have been defined and are added to the graphs. The lines are characterised by the following equations:

Case	Wave direction	Acceleration type	Equation	Note:
A1	Positive	Sway	$y = 2.28 - 0.02 \cdot x$	Almost a scalar
A2	Positive	Heave	$y = 2.12 + 0.52 \cdot x$	
A3	Positive	Roll	$y = 2.17 + 0.28 \cdot x$	
A4	Negative	Sway	$y = 2.39 - 0.09 \cdot x$	Almost a scalar
A5	Negative	Heave	$y = 2.19 + 0.37 \cdot x$	
A6	Negative	Roll	$y = 2.68 + 0.50 \cdot x$	

Table 6.1: Critical correlations between dimensionless wave length (y) and dimensionless wave height (x)

The relations can be inverted to find the most critical wave height, given a certain wave length. For wave heights exceeding the tested range (Dimensionless values outside 0.25-1.25 range, see Figure 6.2), the outer x-value is used.

6.1.2. Flow velocity, wave height, and wave length

In the previous section, it was determined that a wave height of 2 meters (propagating in negative direction) can be used for further computation. Waves slightly higher of slightly lower can be examined using a scalar, while changing the weave length influences the dynamic behaviour in a more complex way. This subsection will look into the dynamic behaviour as function of a changing flow velocity and wave length. In this computation, influence of wind and traffic has been disregarded. Again, dimensionless information is displayed: the flow velocity is scaled by the wave celerity, the wave length is scaled by the floater length. Eight heatmaps for the six cases "Case A1" to "Case A6" are displayed in Appendix M.3, using the same structure as was presented in the previous subsection.

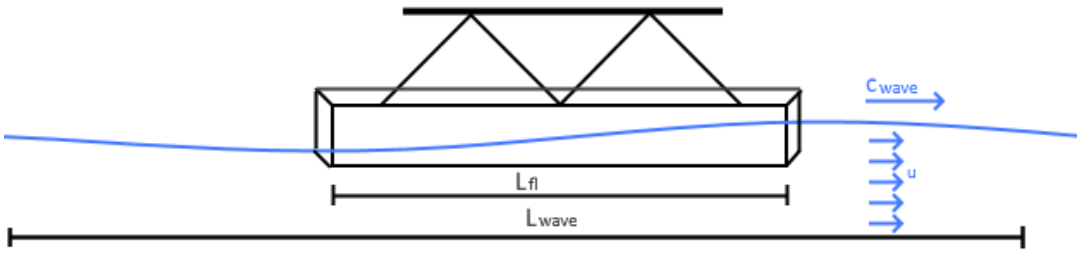

Figure 6.3: Illustration showing change of dimensionless flow velocity and wave length

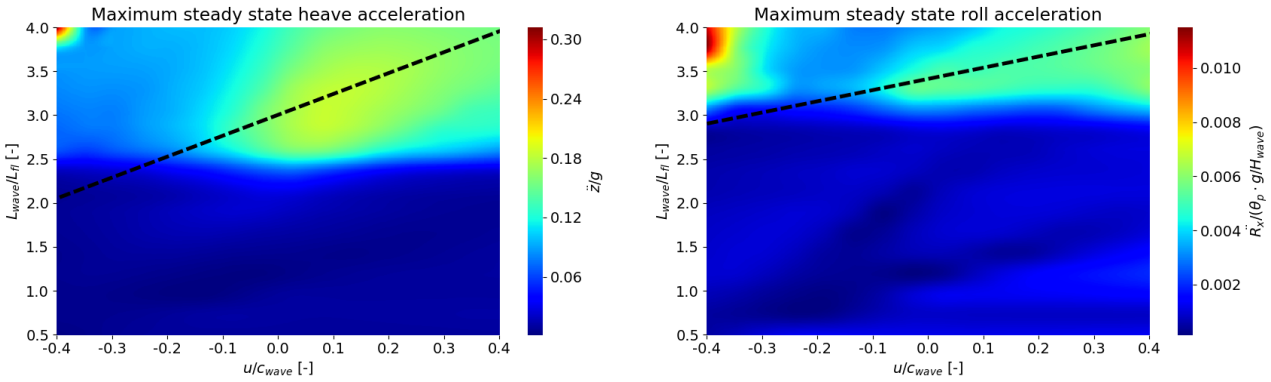

(a) Sway acceleration (Case A5)

(b) Roll acceleration (Case A6)

Figure 6.4: Steady state motion characteristics for addition of current; two relevant cases

In the figures above, it can be noted that an 'acceleration hot-spot' is found in the upper-left corner. This combinations of forces can be ignored, as the high dynamics are due to a numerical instability in the model. Flow velocities of that magnitude (~ 5.5 m/s) push the floaters temporarily out of the water, disabling all rotational stability introduced in the model. The rotation induced by this lack of stability makes one tip of the floater dip into water. The model, as it is defined now, assumes that both tips of the floaters are always submerged. This assumptions was made to simplify the drag around the floaters. As the forcing combination in the top-left corner does not satisfy those conditions, the model does not describe reality appropriately.

For 'Case A1', the critical wave height wave length relation was investigated for sway movement for positive directed waves. Adding a range of flow velocities and finding a new critical relation now including the dimensionless flow velocity introduces 'Case B1'. In this scenario, wave length can be varied, with both the wave height and the flow velocity as function of the wave length. This strategy is performed for all six cases as described in the previous subsection, resulting in 'Case B1' to 'Case B6'. The relations are described as follows:

Case	Wave direction	Acceleration type	Equation
B1	Positive	Sway	$y = 2.42 + 0.94 \cdot x$
B2	Positive	Heave	$y = 2.87 + 1.54 \cdot x$
B3	Positive	Roll	$y = 2.64 + 1.05 \cdot x$
B4	Negative	Sway	$y = 2.71 + 0.63 \cdot x$
B5	Negative	Heave	$y = 3.01 + 1.97 \cdot x$
B6	Negative	Roll	$y = 3.42 + 1.03 \cdot x$

Table 6.2: Critical correlations between dimensionless wave length (y) and dimensionless flow velocity (x)

6.1.3. Wind force, flow velocity, wave height, and wave length

Using the six B-cases introduced in the previous subsection, where critical flow velocities and critical wave heights are introduced as linear functions of the wave length, this subsection will add wind forces to the computation. The complete set of computations is shown in Appendix M.4. An example of two of the results are shown down below.

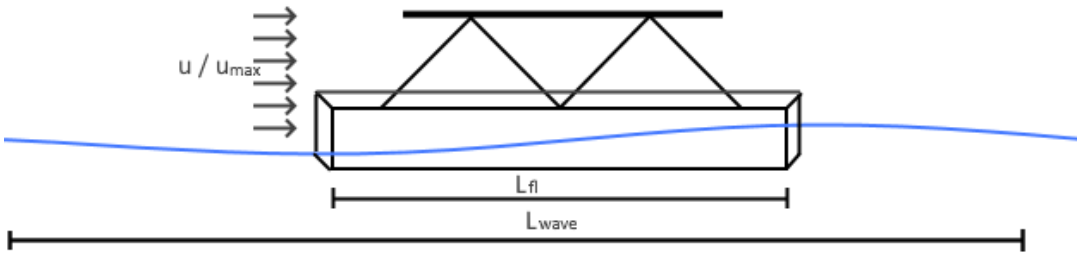

Figure 6.5: Illustration showing change of dimensionless wind force and wave length

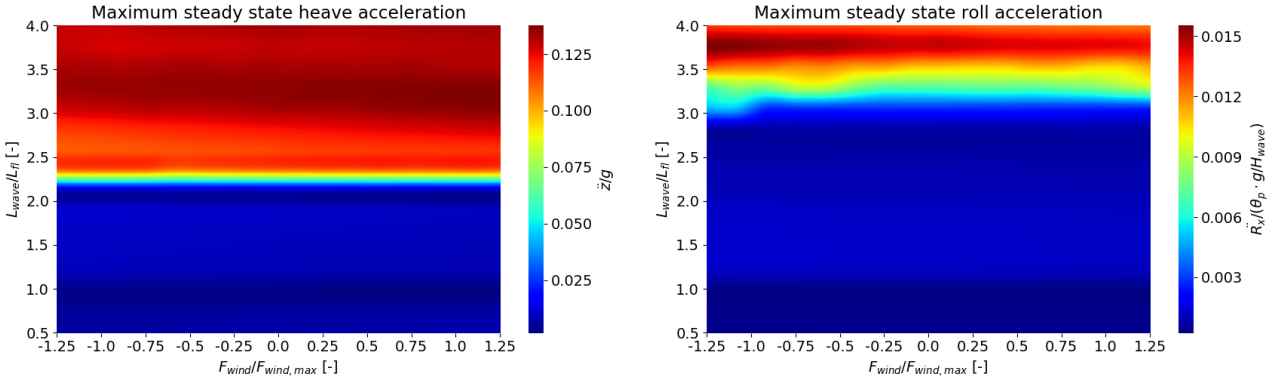

(a) Sway acceleration (Case B1)

(b) Roll acceleration (Case B6)

Figure 6.6: Steady state motion characteristics for addition of wind; two relevant cases

In these two figures, and in all figures in Appendix M.4, it can be seen that the wind force acts as a scalar, meaning that critical dynamics are not found for a different wave length, when the input parameter wind force is changed. Maximum sway accelerations are found for the largest positive directed winds, while heave and roll acceleration are largest for negative directed winds. Because of this, the maximum and minimum wind forces have been added to the loading cases 'Case B1' to 'Case B6', which form the final loading conditions 'Case C1' to 'Case C6'. It can also be noted that for some of the computations, the critical wave length is close to the top of the figure. Because of this, the computation boundaries are extended for all coming subsections.

6.1.4. Pendulum angle

Now that the most severe loading conditions are determined using 'Case C1' to 'Case C6', investigation can be done regarding the influence of design choices of the main structure. First, investigation into the angle of the pendulum is done. This pendulum angle is the angle that is found when no tidal level is present, and no environmental forces are found. Antea proposed [4] an angle of 40 degrees. Appendix M.5 investigates the effect of angles between 20 and 50 degrees. Pendulum angles larger than 50 degrees are not recommended, as the dynamics due to the environmental conditions may cause the pendulum angle to exceed 90 degrees, leading to structural failure. All figures showing roll or sway acceleration show that the magnitude decreases significantly for smaller pendulum angles. This can be explained when looking into the forcing balance: change of pendulum angle changes the vertical/horizontal force/stiffness component in the pendulum, resulting in a different contribution of the pendulum in the stiffness matrix. As the pendulums are by far the dominant counteracting force for horizontal loading, it is to be expected that redistribution of the horizontal and vertical component results in a change in dynamics.

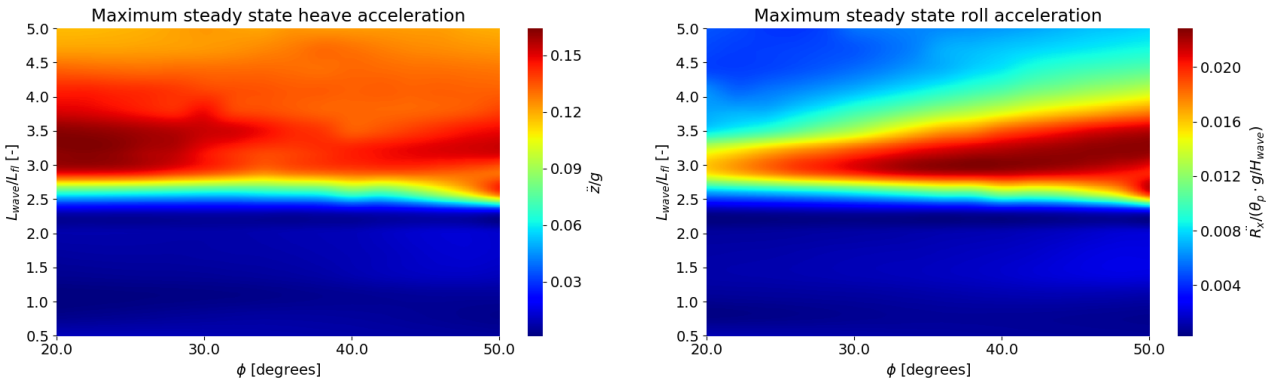

(a) Heave acceleration (Case C4)

(b) Roll acceleration (Case C4)

Figure 6.7: Steady state motion characteristics as function of pendulum angle; two relevant cases

6.1.5. Upper pendulum hinge location

The location of the upper pendulum hinge was initially determined using a forcing balance where wave forces were neglected. Using forcing of the tidal flow solely and requiring that the road is perfectly level finds that the pendulum hinge should be placed on a positive y-coordinate. Secondary effects by change in draught due to the vertical component of the counteracting pendulum force still result in some segment rotation, but is relatively minor. Now, the dynamic effects due to waves will be included into the investigation. Results of this computation are shown in Appendix M.6. An example is shown below, where the y-coordinate of the hinge is scaled against the z-coordinate of that same hinge (relative to the COG).

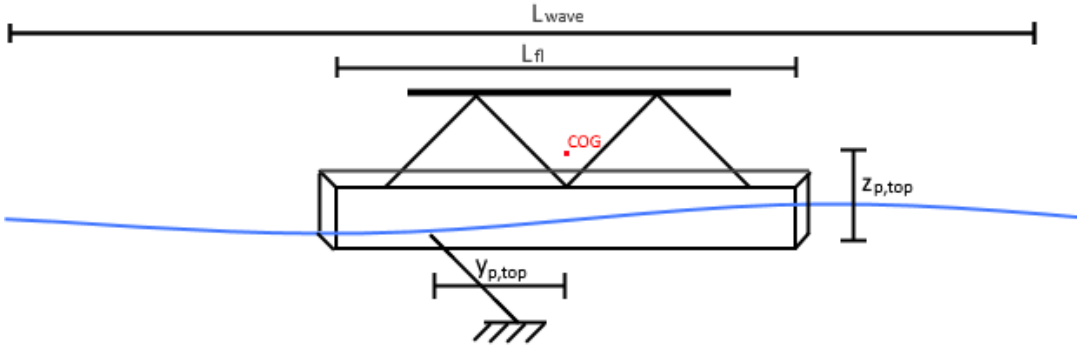

Figure 6.8: Illustration showing change of pendulum hinge and wave length

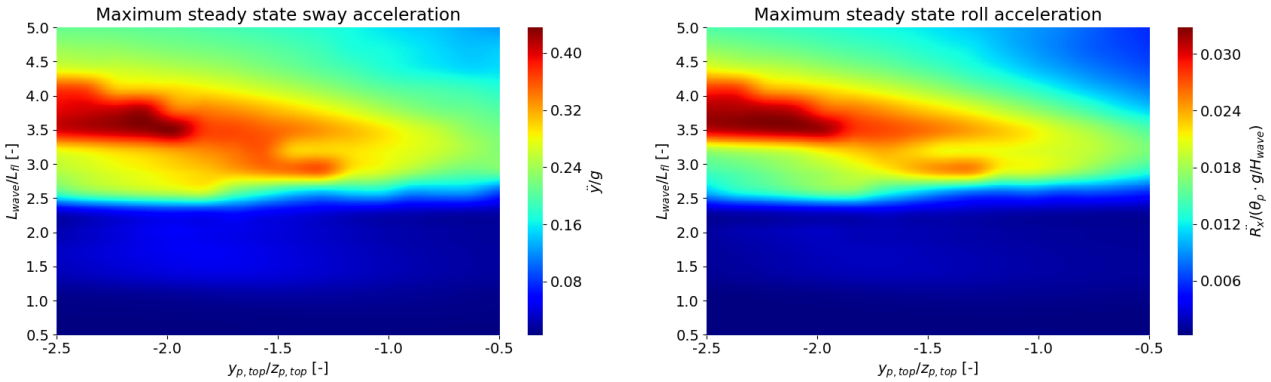

(a) Sway acceleration (Case C2)

(b) Roll acceleration (Case C2)

Figure 6.9: Steady state motion characteristics as function of hinge location; two relevant cases

As was just described, Antea determined the optimal spot solely based on a first order forcing balance while neglecting waves, resulting a dimensionless hinge location of about -0.9. Based on the computations, it can be concluded that roll and sway acceleration increases for lower dimensionless ratios, while heave acceleration tends to rise for higher ratios. However, the maximum found acceleration for heave is of little magnitude compared to that of sway, meaning that a ratio of -0.5 or even higher is recommended to minimize the dynamics induced by waves. The same conclusions are found for the displacement magnitudes: sway and roll increases for lower ratios, while heave displacement increases for higher ratios. Pendulum forces are almost independent on the hinge location. Although the dynamic response is more favourable for very high ratios, this does not mean that the hinge should be constructed on this location. Waves of this size only occur a few dozen times per 1000 years, meaning that the hinge location of the Palmerah Tidal Bridge will not be designed for that scenario. More common circumstances without (significant) waves and with maximum current would result in a constant and notable rotation angle.

6.1.6. Water depth

The effect of water depth is computed and the results are shown in Appendix M.7, where the depth of the strait is scaled against the draught of the structure. This also means that the length of the pendulum needs to move accordingly. It can be noted that ratios larger than 8 create no significant change in dynamics. Smaller ratios, meaning relatively shallow depths, become do show notable changes in roll and sway dynamics. It is hypothesized that the increase in non-linear behaviour of the changing pendulum angle as function of time causes this behaviour. In all computations in this report, pendulums with a length of 31 meters are used, as they form the average length of the pendulums found for the Palmerah Tidal Bridge design. Based on this computation, it can be concluded that the segments connected to pendulums of longer and shorter length are of equal magnitude.

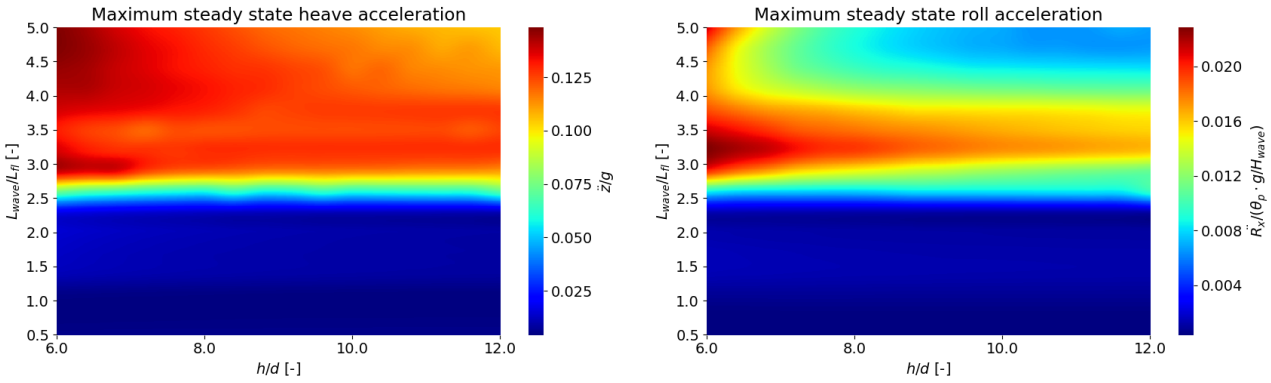

(a) Heave acceleration (Case C5)

(b) Roll acceleration (Case C5)

Figure 6.10: Steady state motion characteristics as function of water depth; two relevant cases

6.2. Sensitivity analysis on construction dimensions

The sensitivity analysis is performed by increasing the value of a single parameter by 10 percent. As the behaviour is dependent on the loading condition, three cases are evaluated:

- Negative directed current of 3 m/s
- No current
- Positive directed current of 3 m/s

All three cases are evaluated using regular waves of 2 meters high, 60 meters long with a period of 6 seconds (for still water), where the waves propagate in negative direction. Five dynamic characteristics are displayed: the accelerations in sway, heave and roll, and the minimum and maximum pendulum forces. It should be noted that forces with a positive percentage mean that the absolute magnitude rises. As both the minimum force and the maximum force are subzero for negative currents, a positive percentage has the consequence that compression forces increase. The same goes for the minimum force for the case without current; where the forces are found with negative magnitude. The remaining three forces are of positive magnitude, meaning that when positive percentages are displayed, larger tension forces are found.

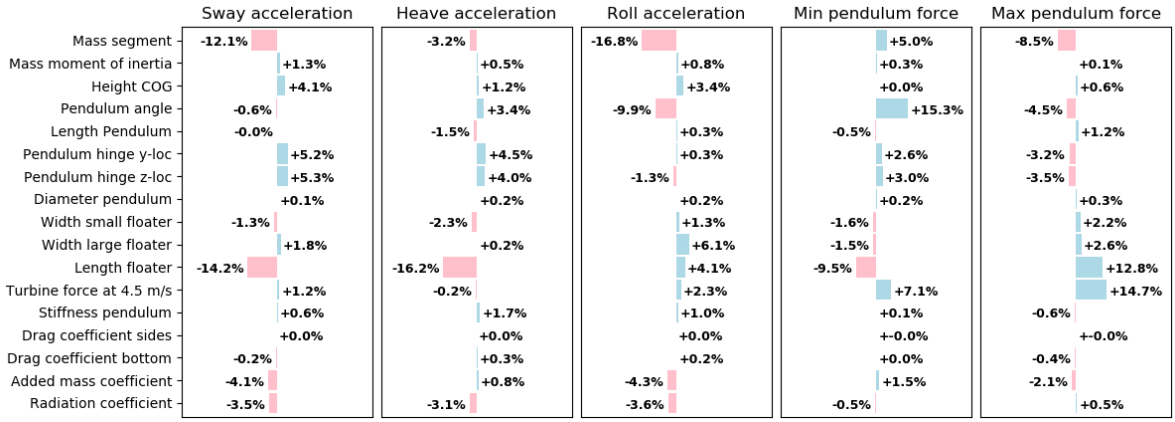

Figure 6.11: Sensitivity analysis by increasing a single parameter with 10 percent for negative currents

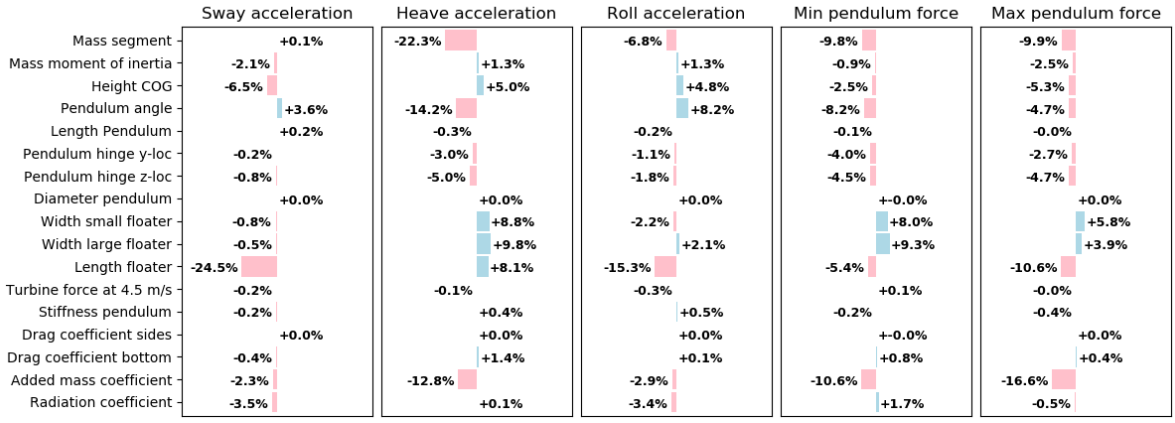

Figure 6.12: Sensitivity analysis by increasing a single parameter with 10 percent for no current

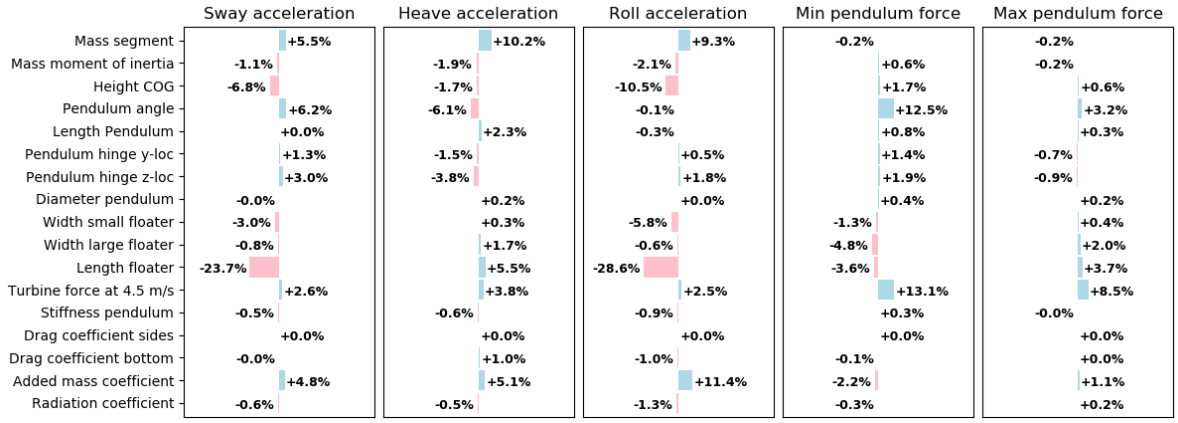

Figure 6.13: Sensitivity analysis by increasing a single parameter with 10 percent for positive currents

The complex non-linear interaction of waves and current does not allow for a simple answer on the question which parameter positively influences the dynamics, as it deviates per case. However, some conclusions can still be made. Obviously, the length of the floaters has significant effect on the behaviour of the structure. The increase of the submerged horizontal area generates an increase of forcing by waves, while also providing extra rotational stability. This is also due to the changing impact rate, which is dependent on both the 6 second interval period that the regular waves have, but also on the current on which they propagate. A negative current on top of the negative directed waves decrease the net impact period, while a positive directed current has the effect opposite effect. With the largest expected waves are characterised with a period of about 7.6 seconds for still water, the current moves the net impact period between 5.5 and 12.2 seconds. The current design proposal of the Palmerah Tidal Bridge has the largest natural period in the order of 6.6 seconds. With the expected range between 5.5 and 12.2 seconds and ignoring the non-linear effects (which would slightly increase the 6.6 seconds), it can be concluded that bringing the natural period down is the most effective way of reducing the dynamics. Overall, it can be stated that making the floaters longer, decreases the natural period of the system.

As increase of mass, or mass moment of inertia, changes the natural period of the system, it is not remarkable that the influence of these two parameters depends on the environmental testing conditions. Changing the mass (moment of inertia) either brings the natural frequency closer to the forcing frequency, or brings it farther from it. It depends on the loading condition whether more weight is preferable or not. Thirdly, the pendulum angle has a substitutional effect on the dynamics. Again, this parameter changes the natural frequencies as it is directly involved in the spring matrices.

As added mass is of significant contribution for the total mass of the system, and as it also plays a direct roll in the loading by waves, it is of no surprise that a relative large part of the dynamics can be influenced by alternating this parameter. This can be done by changing the shape of the floaters; for example by changing the rectangular shape to a semi-circle. Again, this would reduce bring the natural period down, which has a positive effect on the largest expected waves. This does have as side-effect that the radiation damping will decrease as well. Based on the figures above, it can be expected that decreasing the radiation damping coefficient has less effect on the dynamics than changing the added mass coefficient, meaning that the proposed change in shape has probably the desired effect. Based on literature, it was found that added mass (for heave) is in the order of the width of the floater squared. Wider floaters would significantly increase the total added mass. Based on the previous statement that added mass should be reduced, it is of no surprise that the figures above show an increase of dynamics where the floater width rises.

Finally, it can also be noted that the pendulum forces are significantly influenced by the turbine forces for the two cases with tidal flow. Before more investigation can be done in the mooring structure, the use of turbines in the Tidal Bridge should be understood better. Currently, little research has been done in which type of turbine should be used for Tidal Bridges, and what magnitude of forcing can be expected for the turbines under the Palmerah Tidal Bridge.

6.3. Palmerah Tidal Bridge design optimisation

The forcing characteristics discussed in Chapter 5, the dimensionless characteristics of the Tidal Bridge investigated in Section 6.1 and the sensitivity analysis performed in Section 6.2 are in this section, to propose design optimisation strategies for the Palmerah Tidal Bridge specifically.

Based on the calculations made regarding the natural period of the proposed Palmerah Tidal Bridge, it can be concluded that - in order to get the natural frequency out of the domain for which the largest waves are found (5.5-12.2 seconds, depending on the tidal flow), the structure must be altered. With the largest (non-linear) natural period being about 8.8 seconds, a choice should be made whether the natural period should be brought up or down. As design strategies for offshore structures are often guided by making the structure as (relatively) stiff as possible. Therefore, this will also be the guide for improving the Palmerah Tidal Bridge design. For Tidal Bridge designs subjected to short/small waves solely, the reverse may be desired, leading to opposite design recommendations.

An obvious way to bring the natural period down, is to decrease the weight of the system. The weight is a function of two systems: the mass of the segment and the added mass. An effective way to decrease the mass of the segments is to introduce other construction materials; the use of fibre-reinforced polymer (FRP) elements instead of steel elements may offer a solution. The density of FRP being five times as small while stress limits can reach similar magnitudes, offer a great way to reduce the overall weight of the structure. Additionally, the cyclic loading on the structure may result in fatigue behaviour of steel elements, while FRP elements hardly perish when subject to cyclic loading. However, the marine use in this scenario might require vast reduction in allowable stress, as the effect of a marine environment on the material is still debated [44, 45].

The current proposal of the Palmerah Tidal Bridge has significant weight in the deck of the structure as well. Investigation into the weight reduction of this area may offer additional natural period reduction. Added mass can be reduced by changing the vertical shape of the floaters to a more curved shape. The change from a rectangular shape to a semi-circle reduces the added mass coefficient about 30 percent [15]. This does not only reduce the natural period, but also reduces the impact by waves, making the dynamics more favourable. This choice does have influence on the radiation and drag damping, both will decrease with this change, making the dynamics less favourable. The absolute change of these effects combined is not investigated in report.

Longer floaters increase the rotational stability of the structure, which also brings the natural period down. This has as favourable side-effect that it decreases the draught, making wave and current impact from the sides less severe; resulting in less forcing on the structure. The width of the floaters has two main effects. The favourable effect is that it increases the vertical pressure (spring) forces on the bottom side of the floaters, making the system more stiff and bringing the natural period down. However, it also brings the unfavourable effect that it increases the added mass as function of width squared, where it was just concluded that it should be brought down. As the hydraulic stiffness is a function of the width linearly, while the added mass is a function of width squared, it is advised to make the floaters more slender. This may have a positive influence on the horizontal drag force on the floaters, as the floaters become less wide but have more draught. When the number of floaters per segment is increased, but the total horizontal area is not influenced (so the floaters become more slender), added mass will be reduced while not influencing the stability characteristics of the floaters.

In the computations in Section 6.1 it was observed that decrease of the pendulum angle has a positive influence on all dynamic characteristics. It does have as additional effect that the pendulums become longer, and that buckling of the member becomes an increasingly challenging problem. For the current design of the Palmerah Tidal Bridge, it is not advised to increase the pendulum angle above 50 degrees, as it results in stability problems due to the vertical component of the forces in the pendulum. For the current design, with the 40 degree angle, the largest compressive pendulum forces are found to be equal to 9500 kN, being slightly larger than Antea originally estimated (8600 kN). The force was found when combining the maximum experienced wind, with the maximum experienced waves and current in negative direction. A simple buckling calculation (performed below), shows that the Euler buckling force is about 4 times larger than this maximum found compression force, leaving significant room for safety factors and imperfections. This calculation uses the maximum pendulum length of 38 meters and the proposed circular cross-section with diameter 1320 mm and thickness 30 mm using S355. Hence, the proposed pendulum dimensions are of the correct order.

$$uc = \frac{F_{load}}{F_{cr}} = \frac{F_{load}}{\frac{\pi^2 \cdot E \cdot I}{L_p^2}} = \frac{9,500,000}{\left(\frac{\pi^2 \cdot 210,000 \cdot \left(\pi \cdot \frac{1,320^4 - (1,320-30)^4}{64}\right)}{38,000^2}\right)} = 0.26 \text{ [-]} \tag{6.1}$$

Furthermore, the heatmaps produced in Section 6.1 show that moving the location of upper pendulum further to sides has positive influence on the dynamics during wave impact. However, computations with tidal flow solely (which are more common in the Palmerah Tidal Bridge case) show this leads to a significant equilibrium roll rotation. As this is of such magnitude that it violates the serviceable limit states defined in Section 3.5, it is advices to determine the pendulum hinge location without regarding waves. Computations also show that secondary forcing effects cannot be ignored. The large horizontal drag forces which get counteracted by the diagonal pendulum result in vertical displacements in the order of one meter. This reduces or increases the drag effects, depending on the direction of flow. Using only wind and current, it is advised to move the pendulum hinge location from an offset of 6.5 meters to an offset of 10 meters in positive direction.

7

Discussion

This chapter will investigate the assumptions and simplifications made during the research presented in this report. Large assumptions and simplifications are discussed first, minor simplifications are discussed later.

- As a rule of thumb, diffraction effects can be ignored for waves that are multiple times longer than the structure. With the floaters being 34 meters long and waves ranging up to 100 meter, only a ratio of 3 is found for the longest waves. As the structure only limits the passage way of waves by about 22 percent, the amount of disturbance will be lowered. However, ignoring this diffraction effect will have influence on the forcing. Literature shows that the method used in this report will most-likely over-predict the forces, resulting in conservative acceleration values. In future design stages the diffraction should be included in the calculation, as the structure will influence the wave-field.

- Likewise, the modified Morison equations used in this report are increasingly non-accurate for smaller waves. The equations assume that the length of the waves are significantly larger than the structural diameter. With floaters of 3.5 and 5 meters wide, it can be safely stated that the equation should be used with care for waves shorter than 25 meters. Even for waves that do match the limitation above, the Morison equations have their own limitations. They assume that cases with intermediate Keulegan Carpenter numbers have can be approximated with asymptotic forms, which are only valid for small and large KC numbers.

- Thirdly, the model constructed for the investigation has not been validated in its entirety. All tools and subtools making up the model have been validated and verified using (experimental) literature for comparable cases. However, this does not guarantee that the integration of the tools and subtools has been done appropriately. A set of experiments which simulate the bridge in its connected position, influenced and forced by waves and current gives information regarding appropriate validation. As no physical research has been performed regarding Tidal Bridges, this limits the possibility to validate of the model.

- Furthermore, the structure may cause waves to break because of the limited passageway. Waves breaking against the structure can cause high loads for short durations. This has not only an influence on the structural integrity of the local elements, but also influences the dynamic profile. High and frequent loads by wave breaking may interact with higher natural frequencies.

- Oblique waves have not been taken into account in the current research. As waves approaching under angles hit the structure non-simultaneously, they may form amplification of higher frequencies. As the strait of the Palmerah Tidal Bridge is relatively straight, oblique waves will most likely be of little magnitude, as there is little room for wave build-up. Still, not regarding these waves forms a limitation of the current state of the model.

- The experiments that have been performed in this investigation were only performed for a small number of shapes. The 27 (3x3x3) configuration for length, width, and draught did show relations between added mass and the shape dimensions. However, the lack of mathematical justification and the limited number of ratios tested only allow for a formulation that has to be used with great care. Especially when considering that the floater construction materials are not completely smooth, had most likely small deviations from the intended dimensions, that the EPS floaters have a slight porosity, and that the

water pool was still subjected to small amounts of wind causing ripples in the wave field in the order of multiple millimetres. The last reason stated is most likely a big disrupter for the calculation in the radiation damping, as continuous forcing by these small ripples are of significant magnitude compared to the ripples formed by the movement of the floater.

- Additionally, the effect of the connections between neighbouring segments has been ignored in all computations. Assuming a relatively stiff spring connection between the segments, it can be approximated that the ends of the connecting segments move together. As the outer segments on both ends of the Tidal Bridge are connected to another form of mooring (spudpoles instead of pendulums), it can be stated that the outer segments will behave differently when looking at the dynamics. With the stiff connection, this will influence the motion of the second and second to last segment. This influence will dampen out for segments being farther away from the edges of the Tidal Bridge. As the proposal for the Palmerah Tidal Bridge only contains four segments, influence by the limited length of the bridge will be found.

- The current study only focusses on the movement in the two dimensional plane. Adding the third dimension allows for more types of movement that can be dynamically amplified. With one side of a segment having longer pendulums than the other side of the segment, three dimensional rotation is enforced. On one hand, it brings additional loading cases that must be investigated. On the other hand it also brings new forms of radiation damping into the system.

- Moreover, Ansys Aqwa was used to compare the magnitudes of the added mass and radiation damping coefficients calculated by the hand-calculations. The software package which is based on the Green's function is able to calculate the two coefficients for all loading frequencies. However, the software package makes errors for frequencies close to the natural frequency, its output becomes a infinite. Still, a well defined trend line can be observed by looking at the data Ansys Aqwa provides.

- Lastly, the complete model rests on the assumption that the bridge segments are fully rigid. Including dynamics and deformations within a segment allows for a whole new set of natural frequencies. The truss structure does make the segment very stiff, meaning that those frequencies will most likely be very high. This also allows for the stiff coupling between the floaters that has been assumed in this report.

8

Conclusions and recommendations

8.1. Conclusions

This report has split its research into two main question: the first determining how to model the dynamic response and to find the critical loading conditions, the second using that model to optimise the proposed Tidal Bridge structure. Likewise, the conclusions are split into two sections.

How can the dynamic response due to two-dimensional forcing of a Tidal Bridge be determined?
Interaction between structure and environmental conditions can be split into elements having the superposition property. Based on the Indonesian laws, wind forces could be separated into two categories: wind load on the super structure and wind load on the deck. Submerged structural elements require a more complex forcing calculation, based on the modified Morison equations. In the equations, distinction can be found in three types of forcing: the drag force (both current and waves), the hydrodynamic mass force (waves only) and Krylov force (waves only). Based on hand-calculations, it was concluded that only the drag forces are relevant for calculating the total Morison force on the deeply submerged turbines and pendulums. Both are submerged so far that waves hardly influence the velocity field. For the floaters, which are partially submerged and partially emerged, all three types of forcing are of significant magnitude and need to be evaluated.

The complex shape of the floaters did not allow for a simple computation of the added mass and radiation damping coefficients, especially for roll motion. Hand-calculations using simple shapes representing the floaters did show that both the added mass and radiation damping showed significant contribution in the mass and damper terms. Therefore, more intense research into these two parameters was deemed necessary. Calculations based on Green's function by using software package Ansys Aqwa also showed that both the added mass and the radiation damping magnitudes are non-negligible, but showed deviating results compared to the calculations based on literature. A set of experiments of a 1:100 scale model of the Palmerah Tidal Bridge (and 26 variations) showed that representing the floaters by a simple shape (a long rectangle), does result in a good approximation of the heave added mass. Representing roll motion by slicing the floaters into sections which 'approximately heave', only gives insight in the correct order added mass moment inertia. Deviations between the experimental results and the hand calculations were found to up to a factor of 3.5. The experimental results were used to find a function that describes the added mass (moment of inertia) for floaters of used shape better. This equation should be used with absolute care, as only a limited number of experiments were performed and little mathematical roots are used. The experiments also showed that the hand-calculations estimating the radiation damping based on the work of Vugts were in the correct order. A better correlation was not found due to the small number of experiments and the lack of a trend in the data.

Research into the contribution of the various forcing elements showed that wind forces are of little magnitude. Their contribution to the forcing is in extreme loading conditions only about three per cent of the total forcing. Because of the eccentricity, however, wind forces can cause a significant contribution in the roll rotation. Stationary traffic forces can be neglected, as the combined gravitational force of the segments and vertical forcing component of the diagonal pendulums exceeds the traffic weight by about factor 50. They do contribute a mere 15 centimetre in the static resting position. Using the proposed Palmerah Tidal Bridge design, hydrodynamic forces form by far the most significant forcing. Individually, the induce pendulum forces of about 2000 and 6000 kN for waves and current respectively. For the current forcing, this is mainly due to the forcing on the turbines. The interaction between current and waves can make the combined forcing about 15 per cent larger than linearly combining the two forces would.

The effect of an approaching wave field has been investigated, which concluded that the overshoot cannot be simply represented by a simple function. Overshoot of dynamics during the first impact of a 1 meter high wave may add over 200 per cent to the maximum found roll acceleration, and over 100 per cent for sway and heave. Higher waves decrease the overshoot percentage scalar-like, slight change in critical wave period is found when changing the approaching wave height. The non-linearity of the flow velocity on top of the wave field does not allow for a simple relation to find the overshoot. What can be observed, is that waves and current in the same direction make the critical wave period drop. This is logical, as the velocity vectors of the two elements are added together, making the impact period shorter than the wave period.

Furthermore, it can be concluded that the various dynamic behaviour characteristics form disagreeing extremes, meaning that extreme loading conditions for for example sway acceleration do not match with the extreme loading conditions for for example heave acceleration. This statement becomes even more complex when considering the fact that the Tidal Bridge is an asymmetric bridge in width direction, resulting in different behaviour for waves from either side. As eight dynamic characteristics were investigated (displacement and acceleration for sway, heave and roll, plus the minimum and maximum pendulum forces), this would lead to two sets of eight different loading criteria. To reduce the number of loading criteria, only the accelerations in the three degrees of freedom were considered further when looking into the design optimisation.

What design choices can further optimise the dynamic behaviour of a Tidal Bridge?
Based on the linear mass and spring matrices, the governing natural period has been calculated. A value of 6.7 seconds was found. However, maximum displacement is found for loading periods ranging around 9 seconds. The difference between these two values is the result of all non-linear wave effects; the wave pressure and particle velocity / acceleration fields that change as function of time and location result in a shift of critical loading period. Now that the tidal flow in the strait can reach up to 4.5 m/s in both directions and the largest waves are to be expected with a (still water) period of 7.6 seconds, arrival intervals between 5.5 and 12.2 seconds depending on the flow velocity can be expected. As a result, the critical loading period of 9 seconds is susceptible to the largest waves found for the Palmerah Tidal Bridge. To reduce and optimise the dynamic effects by these large waves, it is useful to alter the structure in such a way that the natural period is not in the 5.5-12.2 second range. It is advised to bring this natural period down by making the structure more relatively stiff. Waves with a shorter with length will now coincide with the natural period. However, these waves are generally of less height: resulting in less impact energy.

To investigate how the dynamics are influenced by the parameters in the model, a sensitivity analysis is performed. It concluded that the length of the floaters, the mass of the segments, the pendulum angle, the height of the COG and the added mass coefficient are of largest influence. It also showed that the effect of the parameters is very sensitive to the loading conditions, as addition of currents force the impact frequency to change accordingly. This has as effect that more (added) mass could bring the natural frequency *closer* to the forcing frequency, while the same environmental conditions with the tidal flow direction swapped would bring the natural frequency *further away* from the forcing frequency. Overall, it can be stated that it is necessary to change certain parameters for which the natural period is brought outside the 5.5-12.2 second range. One option is to alter the vertical shape of the floaters to a semi-circle. This reduces the impact of waves and will brings down the added mass. Another possibility is to increasing the length of the floaters as it increases the dynamic stability. Furthermore, it was observed that the turbines and the pendulum angles are most governing into determining the longitudinal pendulum forces.

From the computations using the constructed model, it was concluded that waves propagating in positive y-direction result in less motion than waves propagating in negative y-direction. For the Palmerah Tidal Bridge, where the waves from one side are about four times larger than the waves expected from the other side, a favourable layout can be defined: the side at which the mooring construction for the pendulums is found and the direction from which the dominant waves arrive must overlap. This statement does not require changes to the current Palmerah Tidal Bridge design proposal, as its current design is conform with that conclusion.

Besides the research into the effect of waves coming from different sides, investigation was done into the effects of deeper or shallower water. As expected, shallow water increases the non-linear effect of the changing pendulum angle. This results in a notable non-constant critical wave period for decreasing water depths. On top of that, it was observed that relatively large waves in shallow water may cause the pendulum angle to ex-

ceed 90 degrees, which is to be avoided at all times. Therefore, it is recommended to proceed carefully when implementing the Tidal Bridge design for shallow regions.

This last phenomenon of the pendulum angle exceeding 90 degrees also appeared for design cases where the pendulum angle is set to be more than 55 degrees. Strong currents combined with large waves with periods close to the natural period will cause violation of the limit states. Computations show that all dynamic characteristics are more favourable for pendulums with smaller angles. It does come with one major downside: it elongates the pendulums and their buckling length.

For the current Palmerah Tidal Bridge, the location of the upper hinge of the pendulum was solely based on a first order calculation only considering drag forces. This report concludes that the second order effects are of non-negligible magnitude. The horizontal drag forces on the floaters and the turbines are counteracted by the diagonal pendulums, which cause a vertical force resulting in a displacement in the order of 1 meter (direction depending on forcing direction). When waves are taken into account to find the most optimal hinge location and the criteria is solely based on minimising the acceleration, a complete different hinge location is found. Bringing the upper pendulum hinge further offset gives more stability, but creates an initial rotation of such magnitude that the bride is most likely not usable. As waves larger than one meter happen only a few times per year, it is advised to ignore the waves in finding the most optimal hinge location. This leads to a hinge location with an offset of 10 meters, while the current design has an offset of 6.5 meters. When looking into the maximum pendulum forces with the current design, it is found that compression forces up to 9500 kN can be expected. The proposed pendulum cross-section is in the correct order to withstand this force.

8.2. Recommendations

Based on the investigation performed in this report, a list of recommendations can be constructed. The recommendations are split into two categories: recommendations for model improvement and recommendations for future research.

Model improvement recommendations

- For future model improving, it is recommended to include the effects of wave diffraction on the floaters. As the floaters disrupt twenty per cent of the cross-section's surface level, diffraction of waves cannot be ignored in later design stages as the floaters will disturb the wave field. Addition of this effect may have a substantial effect on the loading, especially for smaller waves.

- Secondly, this report indicates that the choice of turbines and their corresponding characteristics are vital for the dynamic profile of the bridge. The turbine blades being far below the COG create a stabilizing effect due to the non-linear drag force. As the current state of the Palmerah Tidal Bridge proposal proposes various designs for the structure, significant changes to the dynamics may be observed if the choice of another turbine type is made.

- Furthermore, it is recommended to include waves from angles other than 90 degrees. This study only included waves that came perpendicular to the bridge. Including oblique waves into the design changes the way the waves interact with the floaters. Instead of the waves being smoothly separated by the pointed floaters, they may cause large impact forces on the sides of the floaters. This may create critical conditions for the force in pendulums. Additionally, oblique approaching waves do not reach all floaters simultaneously. This may trigger higher natural frequencies.

- This investigation into the Tidal Bridge dynamics only included regular waves, with a constant wave height and wave length. To make the model closer to reality, it is recommended to look at the effects of irregular waves as well. Addition of this wave field will need more information regarding the environmental conditions at the Palmerah Tidal Bridge, as there is no specific wave information available at the time writing. Moreover, the structure interacting with the fluid may cause waves to break. Including this effect into the computation is recommended for future research.

- Additionally, it is recommended to look into the first and last segment of a Tidal Bridge. The connection with the spudpole allows for unconstrained vertical motion, while limiting the horizontal motion almost completely. For large currents, this enforces a rotation of the outer segments, making the dynamics of these segments completely different than was described for the middle segments.

- To validate the complete model and to get better information regarding the hydrodynamic parameters (added mass and radiation damping), it is also recommended to build a scale model of a complete bridge segment. Connecting the bridge with the proposed pendulum mooring system and subjecting the scale model to a combination of waves and current gives better insight into the dynamics and can be used to calibrate the model on.

Future research recommendations

- More research is needed into the added mass characteristics of the presented structure. The limit number of experiments performed during this investigation gives insight into the correct magnitudes. However, more research will be needed to find appropriate expressions for the two investigated degrees of freedom. For the four remaining degrees of freedom no information is known, except for the approximations based upon literature. As the length of the pendulums on both sides of the segments are of varying size, pitch and yaw rotations will be enforced by the pendulums. This makes more research into the added mass characteristics vital. This report included a frequency constant added mass. Although this is proven to be quite accurate, a better model can be constructed when taking a frequency dependent function into account.

- Likewise, the exact magnitude of the radiation damping is currently unknown for all degrees of freedom. The pointed floater will create a pressure field, which will interact with the pressure field of nearby floaters. As the limited number of experiments performed in this investigation only confirmed that the magnitude was in the correct order, more investigation is needed. It is recommended to do a more controlled experiment into determining the coefficient. The sensitivity study in this report showed that small changes in the parameter could lead to notable changes in dynamics.

- Thirdly, it is recommended to look into the magnitude of approaching wave fields, as the computations showed that overshoot of acceleration are of significant magnitude. Especially when large swell or ship waves may approach suddenly, overshoot may cause high accelerations. Therefore, the impact of these waves may be governing in the design.

- Furthermore, it is recommended to alter the structure in such a way that the natural period will not overlap with the largest expected waves. This report recommends bringing the largest natural period down by changing the (vertically) rectangular floater profile to a more rounded shape. Additionally, elongating the floaters, minimising the mass by using lighter construction materials, lowering the pendulum angle and adjusting the pendulum-segment connection point result in more favourable dynamics. The changing magnitude of the fluid-structure interaction coefficients for different floater shapes and connections is something that future research must investigate. Changing the characteristic natural frequencies will affect the fatigue behaviour of the different elements of the bridge, which needs investigation as well.

- Additionally, it is recommended to look into the possibility of structural design changes. Instead of having a single pendulum at each end of a segment, one could have two pendulums of same angle behind each other (in y-direction, see Figure 3.3). This limits the roll motion, which was found critical for many loading combinations. This does have as downside that the number of pendulums will be doubled, resulting in extra foundation/mooring costs. Initial calculations using a modified version of the created tool show promising results regarding the overall dynamics of such a design change. However, no extensive research into this alteration has been performed.

- Lastly, active roll compensation can be added to the Tidal Bridge design, which can compensate the roll motion of the bridge deck. This has two major advantages: firstly, roll accelerations and roll rotations for vehicles on top of the bridge can be mitigated, being more pleasant for users of the bridge. Secondly, this improves the RoRo-connection which would otherwise need to allow for a torsional connection.

Bibliography

[1] R.J. Vos. Palmerah Tidal Bridge - management feasibility. Technical report, Tidal Bridge, 2017.

[2] Cobouw. Tidal Bridge gaat verder onder de vleugels van BAM, 2018. URL https://www.cobouw.nl/infra/nieuws/2018/05/tidal-bridge-gaat-verder-onder-de-vleugels-van-bam-101261357. Retrieved on 2019-08-02 (Dutch).

[3] E. Watanabe. Floating Bridges: Past and Present. *Structural Engineering International*, 2003.

[4] S. de Rijke. Design report Palmerah bridge. Technical report, Tidal Bridge, 2017.

[5] F.F.H.M. Hoogsteder. The Tidal Bridge; An analysis of the dynamic response of the Palmerah Tidal Bridge. Master's thesis, Delft University of Technology, 2019.

[6] Standard Nasional Indonesia. Bms7-c1. Technical report, Standard Nasional Indonesia, 1992.

[7] D. MacIsaac. The Dzhanibekov effect or tennis racket theorem. *The Physics Teacher*, 2015.

[8] R. de Winter. Designing Ships using Constrained Multi-Objective Efficient Global Optimization. Master's thesis, Leiden University, 2018.

[9] MasterHD. Resonance effect shown for various input frequencies and damping coefficients, 2008. URL https://commons.wikimedia.org/wiki/File:Resonance.PNG. Retrieved on 2019-08-07.

[10] J.M.J. Spijkers, A.W.C.M. Vrouwenvelder, and E.C. Klaver. *Lecture Notes Structural Dynamics CT 4140; Part 1 - Structural Vibrations.* Delft University of Technology, 2005.

[11] H.A. Buchholdt and S.E. Moossavi Nejad. *Structural Dynamics for Engineers.* ICE, 2012.

[12] C. Vuik, F.J. Vermolen, M.B. van Gijzen, and M.J. Vuik. *Numerical methods for ordinary differential equations.* VSSD, 2007.

[13] H. Podhaisky. Stability region for Euler method, 2010. URL https://commons.wikimedia.org/wiki/File:Stability_region_for_Euler_method.svg. Retrieved on 2019-08-22.

[14] H. Podhaisky. Stability region for Euler method, 2010. URL https://commons.wikimedia.org/wiki/File:Stability_region_for_trapezoidal_method.svg. Retrieved on 2019-08-22.

[15] DNV institute. Recommended Practice DNV-RP-H103. Technical report, DET NORSKE VERITAS, 2011.

[16] K. Wendel. Hydrodynamische Massen und hydrodynamische Massentragheitsmomente. *Jahrbuch der Schiffsbautechnischer Gesellschaft*, 1950. (German).

[17] J. Journée and W. Massie. Offshore hydromechanics. Technical report, Delft University of Technology, 2001.

[18] S. Chakrabarti. Empirical Calculation of Roll Damping for Ships and Barges. Technical report, Ocean Engineering, 2001.

[19] J.F. Lee. On the Heave Radiation of a Rectangular Structure. *Elsevier*, 1994.

[20] Y.H. Zheng, Y.G. You, and Y.M. Shen. On the radiation and diffraction of water waves by a rectangular buoy. *Elsevier*, 2003.

[21] M. Haskind. The Exciting Forces and Wetting of Ships in Waves. *Otdelenie Tekhnicheskikh Nauk*, 1957.

[22] J.H. Vugts. The Hydrodynamic Coefficients for Swaying, Heaving and Rolling Cyllinders in a Free Surface. *International Shipbuilding Progress*, 1968.

[23] Ir. J.H. Vugts. The Hydrodynamic Coefficients for Swaying, Heaving and Rolling Cylinders In A Free Surface. Technical report, TNO, 1970.

[24] W.E. Cummins. The Impulse Response Function And Ship Motions. Technical report, Hydromechanics Laboratory, 1962.

[25] Aquatera and Bintang Subsea. Larantuka Straits, NTT - Metocean Survey; Tidal Data Analysis Report. Technical report, Aquatera and Bintang Subsea, 2017.

[26] J. Bosboom and M.J.F. Stive. *Coastal Dynamics I - Lecture notes CIE4305*. VSSD, 2015.

[27] C.R. Suribabu, R.M. Sabarish, R. Narasimhan, and A.R. Chandhru. Backwater Rise and Drag Characteristics of Bridge Piers under Sub-critical Flow Conditions. *European Water*, 2011.

[28] R.J. Vos. Palmerah Tidal Bridge - technical feasibility. Technical report, Tidal Bridge, 2017.

[29] M.J. Hemel. Submerged floating tunnel; The dynamic response due to fluid structure interaction. Master's thesis, Delft University of Technology, 2019.

[30] O.M. Faltinsen. *Sea Loads on Ships and Offshore Structures*. Cambridge University Press, 1990.

[31] M. de Kloet. Estimation of extreme wave conditions Larantuka Strait. Technical report, Tidal Bridge, 2017.

[32] R. Zughayar. Eastern-Mediterranean Metocean Design Basis. Master's thesis, University of Stavanger, 2016.

[33] L.H. Holthuijsen. *Waves on oceanic and coastal waters*. Cambridge University Press, 2007.

[34] G.J. Schiereck and H.J. Verhagen. *Introduction to bed, bank, shore protection*. TU Delft, Department Hydraulic Engineering, 1993.

[35] G.G. Stokes. On the theory of oscillatory waves. *Transactions of the Cambridge Philosophical Society*, 1847.

[36] Z. Demirbilek and L. Vincent. *Water Wave Mechanics; Coastal Engineering Manual Outline*. Army Corps of Engineers, 2002.

[37] J. Zhang. Lecture on Stokes waves, 2014. URL `https://ceprofs.civil.tamu.edu/jzhang/ocen300/stokes.pdf`. Retrieved on 2019-08-21.

[38] Standard Nasional Indonesia. Bms6-m1. Technical report, Standard Nasional Indonesia, 1992.

[39] J. Gerritsma. *MT3408 - Hydromechanica 4: Scheepsbewegingen, sturen en manoeuvreren. Werktuigbouwkunde en Maritieme Techniek Sectie Scheepshydrodynamica*. Delft University of Technology, 2003. (Dutch).

[40] E. Hendriksen. Dynamic behaviour of the Sognefjord bridge; Analysis and review of the world's largest floating bridge design. Master's thesis, Delft University of Technology, 2018.

[41] C.E.M. Heuberger. Assessment of the dynamic response of a floating pontoon bridge with a fiber reinforced polymer superstructure. Master's thesis, Delft University of Technology, 2018.

[42] C.M. Wang, B.T. Wang, and editors. *Large Floating Structures ; Technological Advances*. Springer, 2015.

[43] Unknown. General Modelling and Scaling Laws. Technical report, UTNU, 2014.

[44] DNVGL. Composite components DNVGL-ST-C501. Technical report, DET NORSKE VERITAS, 2017.

[45] L. Ascione, E. Guttierez, S. Dimova, A. Pinto, and S. Denton. Prospect for new guidance in the design of FRP. Technical report, JRC, 2019.

[46] P.A. Kolkman and T.H.G. Jongeling. Dynamic behaviour of hydraulic structures. Technical report, Delft Hydraulics, 2007.

[47] W.F. Molenaar. Lecture slides - Jetties. Technical report, Delft University of Technology, 2011.

[48] D.F. Elger and B.C. Williams. *Engineering Fluid Mechanics*. John Wiley and Sons Inc., 2013.

[49] DNV. Environmental Conditions and Environmental Loads. Technical report, DET NORSKE VERITAS, 2007.

[50] Offshore Engineering Group. Lecture slides - Offshore Hydrodynamics. Technical report, Delft University of Technology, 2005.

[51] HM.H. Patel and J.A. Witz. Compliant Offshore Structures. *Elsevier*, 2013.

[52] NEN. NEN-EN 1993-1-1+C2+A1 (nl). Technical report, Koninklijk Nederlands Normalisatie, 2016. (Dutch).

[53] F. Orban. Damping of materials and members in structures. *Journal of Physics: Conference Series*, 2011.

[54] H. Mevada and D. Patel. Experimental determination of structural damping of different materials. *Elsevier*, 2015.

[55] NEN. NEN-EN 1991-1-1+C1 (nl). Technical report, Koninklijk Nederlands Normalisatie, 2011. (Dutch).

[56] E.J. Kaspersr. Traffic induced vibrations in floating thoroughfares. Master's thesis, Delft University of Technology, 2010.

[57] F.F.H.M. Hoogsteder. Ansys Aqwa simulations, 2019.

[58] J.N. Pan, D.T. Wang, X.G. Wang, and F. Nie. WAVE-CURRENT FORCE ON BRIDGE FOUNDATION. Technical report, APAC, 2013.

[59] sharetechnote. DE - Modeling, 2017. URL `http://www.sharetechnote.com/html/DE_Modeling_Example_SpringMass.html`. Retrieved on 2019-10-03.

[60] R. Murray and J. Colby. Added-Mass Effects on Verdant Power's GEN5B Hoirzontal-Axis Tidal Turbine. Technical report, National Renewable Energy Laboratory Golden and Verdan Power Inc., 2018.

[61] H.G. Moll, F. Vorpahl, and H.G. Busmann. Dynamics of Support Structures for Offshore Wind Turbines in Fully-coupled Simulations - Influence of Water Added Mass on Jacket Mode Shapes, Natural Frequencies and Loads. Technical report, Fraunhofer Institute for Wind Energy and Energy System Technology, 2015.

[62] Composites World. Tidal turbine blade toughened for turbulent salt sea, 2019. URL `https://www.compositesworld.com/articles/tidal-turbine-blade-toughened-for-turbulent-salt-sea`. Retrieved on 2019-10-22.

[63] Ansys Inc. Aqwa Theory Manual. Technical report, Ansys Inc., 2015.

[64] NEN. NEN-EN 14081-1:2016 en. Technical report, NEN, 2016.

A

Components and sizes of elements in Palmerah Tidal Bridge

This appendix is an elaboration on Chapter 2, in which the conceptual design proposed by Antea was explained. This appendix will go further into detail on the characteristics of all the elements of the Palmerah Tidal Bridge.

A.1. Overview of Tidal Bridge segments

As mentioned earlier, the Tidal Bridge is divided into four segments. Each 100 meter long segments rests on three large floaters and two small floaters. Each small floater (except for the floaters connected to the RoRo connection, discussed later), which can be found at each end of a segment is connected to a pendulum, connecting it to the foundation at the riverbed. A segment of the bridge has been shown in Figure A.1. In between the floaters, large turbines will be placed to generate energy.

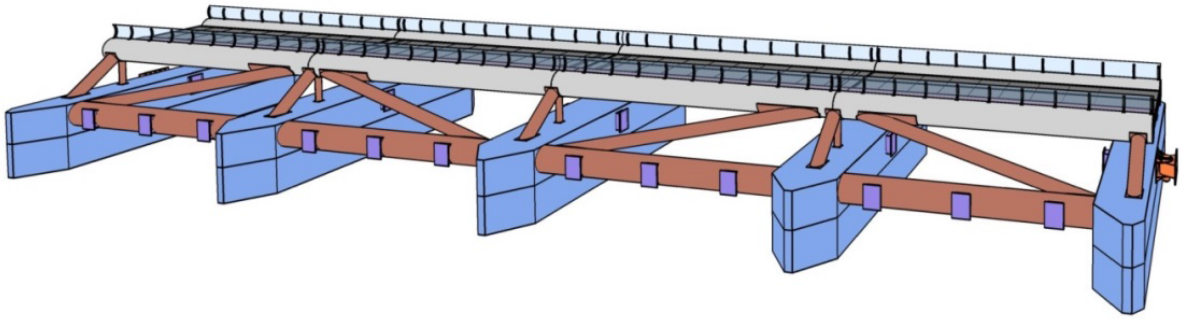

Figure A.1: Three-dimensional view of single segment [4]

A distinction can be made between the various components in a segment. in Table A.1 all these components of a single section are shown, together with their centre of gravity, mass and mass moment of inertia. Most of this data has been extracted from Antea's rapport [4]. However, changes have been made to the mass moment of inertia of the floaters and turbines. Antea proposed to estimate the mass moment of inertia around the z-axis of a single small floater by using the upper formula in Equation A.1. Using that equation, the effect of the parallel axis theorem has been neglected. Taking that factor into account as well, drastic changes are found, as can be seen in the lower formula in Equation A.1. For the mass moment of inertia of the other directions of all floaters and turbines similar decisions were made. These are all corrected. The location of the gravitational centres of elements are defined compared to the gravitational centre of the middle floater, as this makes a good reference point.

$$
\begin{aligned}
J_{f,s,z} &= \frac{1}{12} M_{fs} \left(W_{fs}^2 + L_{fs}^2 \right) \\
&= \frac{1}{12} \cdot 48{,}000 \cdot \left(3.5^2 + 34^2 \right) \\
&= 4.673 \cdot 10^6 \text{ kg m}^2 \\
J_{f,s,z} &= \frac{1}{12} M_{fs} \left(W_{fs}^2 + L_{fs}^2 \right) + M_{fs} \left(\Delta x^2 + \Delta y^2 \right) \\
&= \frac{1}{12} \cdot 48{,}000 \cdot \left(3.5^2 + 34^2 \right) + 48{,}000 \cdot \left(47.75^2 \right) \\
&= 114.116 \cdot 10^6 \text{ kg m}^2
\end{aligned}
\tag{A.1}
$$

Component	**Size [x,y,z]**	**Gravitational centre [x,y,z]**	**Mass**	**Mass moment of inertia [x,y,z]**
Road	[100 , 11 , 2] m	[0 , 0 , 10.525] m	400,000 kg	[24.57 , 353.9 , 337.4] 10^6 kg m^2
Truss	[100 , 22 , 5.5] m	[0 , 0 , 7.2775] m	900,000 kg	[52.38 , 766.1 , 786.3] 10^6 kg m^2
Small floater 1	[3.5 , 34 , 6.55] m	[−47.75 , 0 , 0] m	48,000 kg	[4.796 , 109.7 , 114.1] 10^6 kg m^2
Small floater 2	[3.5 , 34 , 6.55] m	[47.75 , 0 , 0] m	48,000 kg	[4.796 , 109.7 , 114.1] 10^6 kg m^2
Large floater 1	[5 , 34 , 6.55] m	[−23.875 , 0 , 0] m	68,000 kg	[6.794 , 39.15 , 45.45] 10^6 kg m^2
Large floater 2	[5 , 34 , 6.55] m	[0 , 0 , 0] m	68,000 kg	[6.794 , 0.385 , 6.692] 10^6 kg m^2
Large floater 3	[5 , 34 , 6.55] m	[23.875 , 0 , 0] m	68,000 kg	[6.794 , 39.15 , 45.45] 10^6 kg m^2
Turbine 1	[15 , 3 , 25] m	[−37.5 , 0 , −7.5] m	150,000 kg	[8.438 , 219.4 , 210.9] 10^6 kg m^2
Turbine 2	[15 , 3 , 25] m	[−12.5 , 0 , −7.5] m	150,000 kg	[8.438 , 31.88 , 23.44] 10^6 kg m^2
Turbine 3	[15 , 3 , 25] m	[12.5 , 0 , −7.5] m	150,000 kg	[8.438 , 31.88 , 23.44] 10^6 kg m^2
Turbine 4	[15 , 3 , 25] m	[37.5 , 0 , −7.5] m	150,000 kg	[8.438 , 219.4 , 210.9] 10^6 kg m^2
Equipment	[2.3 , 12 , 3] m	[0 , 0 , 4.4] m	120,000 kg	[1.660 , 0.273 , 1.493] 10^6 kg m^2
Total		[0 , 0 , 3.36] m	2,296,000 kg	[142.3 , 1921.0 , 1919.7] 10^6 kg m^2

Table A.1: Components and structural properties of section of Palmerah Tidal Bridge [4]

A.2. Overview of the pendulum foundation

The pendulums are to be connected to six of the eight small floaters. The two remaining small floaters are connected to the RoRo, which is discussed later. The initial design stated that the pendulums are connected with a 40 degree angle to the foundation, with a variable length depending on the local water depth. The length of these pendulums are: 25.5, 31, and 38.5 meter. An initial estimate based solely on buckling determined that the pendulum should be fabricated using a CHS1320-36 [4]. A three dimensional view of the pendulum foundation has been depicted in Figure A.2a. In Figure A.2b, a more detailed view of the connection at both ends of the pendulum can be found.

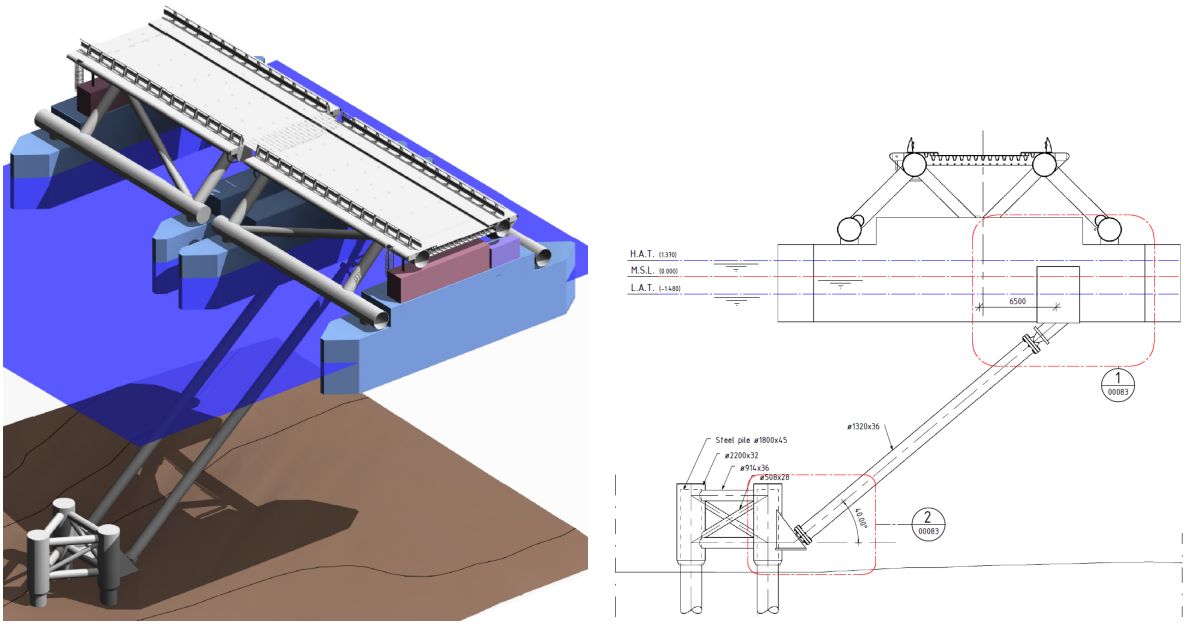

(a) Three-dimensional view of the pendulum foundation

(b) Side view of connection pendulum

Figure A.2: Schematisation of the pendulum mooring system [4]

A.3. Overview of the RoRo connection

The RoRo, which connects the traditional bridge with the Tidal Bridge, should create a relative smooth connection between the two elements. While the traditional bridge has a static height, the Tidal Bridge rises and sinks 3.09 meters due to the tide. A rotational connection on both sides of the RoRo allows for this vertical displacement. In Figures A.3 and A.4, overview drawings are shown on the situation and the connection.

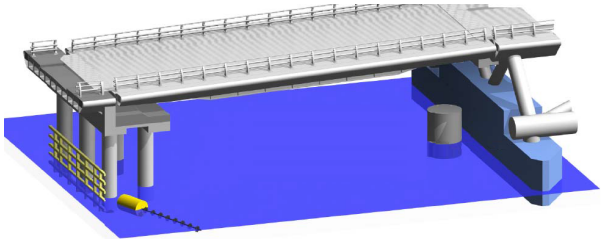

Figure A.3: Three-dimensional view of the RoRo [4]

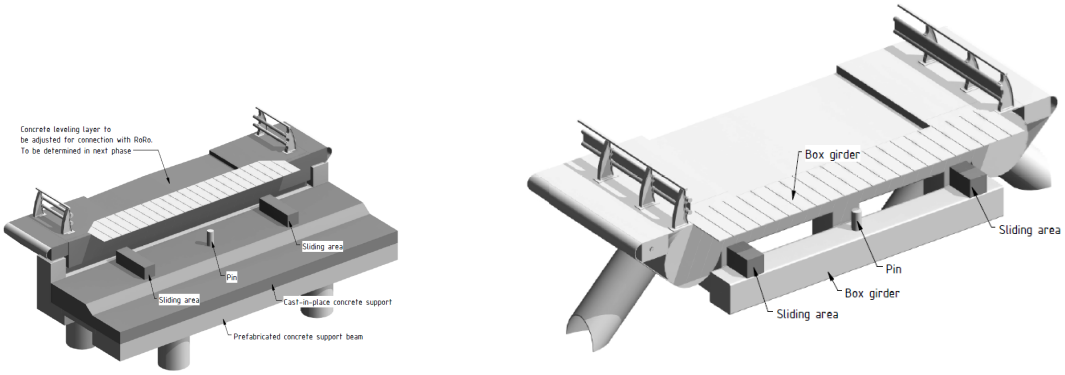

(a) Traditional bridge side

(b) Floating bridge side

Figure A.4: Three-dimensional view of RoRo connection points [4]

A.4. Spudpole end-connection

The outer pontoons of the outer segments, are connected to a spudpole instead of a pendulum. The spudpole limits the movement in x- and y-direction. As forces in x-direction are relatively small, and the proposed connection is relatively stiff in that direction, movements in x-direction will be very limited. For the y-direction, a spring-like behaviour will form as the construction may bend as a cantilever beam. The connection is presented in Figure A.5.

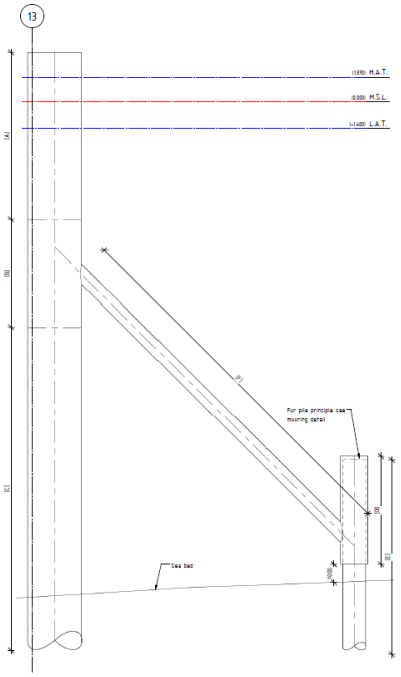

Figure A.5: Side-view of proposed spupole connection [4]

B

Assumptions and definitions of the Tidal Bridge dynamics model

This appendix elaborates on the justification of several assumptions made throughout the construction of the model of Tidal Bridge dynamics. The elements discussed in this appendix are discussed shortly in Chapter 3.

B.1. Tidal Bridge structural properties

B.1.1. Segment properties

The current design of the Palmerah bridge consists out of 4 segments. Although the foundation differs, as it depends on the local strait depth, the segments themselves are assumed to be fully identical. This includes dimensions, weight and current load by traffic. To simplify the segments even more, they are assumed to be symmetrical in x- and y-direction. This also includes the distribution of weight by traffic. For all connections, linear springs and dampers are assumed.

The segments are assumed to be rigid bodies. This is to simplify the model and optimise the computation time. Use of rigid bodies is valid when the distance between any two points is approximately constant, regardless of the forces present, deformations must be very limited. This simplification can be justified as the segment, which rests on multiple floaters, has a stiff truss structure. Although significant transnational deformation happens at relative low forces, longitudinal deformation requires very large forces. Now, as a truss structure has its elements loaded in longitudinal direction primarily. Since the segments are taken rigid, deformation does not play a role in the dissipation of energy. The long pendulums are not assumed to be fully rigid, as elements ranging from 25 to 38 meters loaded by very large forces may display significantly. These elements are represented by longitudinal springs and dampers. This way, the foundation effects can also be considered in these springs and dampers.

The spudpoles on each end of the Tidal Bridge, limit the movement in x-direction. Current design of these spudpoles are shown in Appendix A. Forces in surge movement are therefore be fully ignored. This can be justified as the significant force are all directed in y- and z-direction (discussed later), forces in x-direction are expected to be relatively small.

B.1.2. Equilibrium position

The equilibrium position of a Tidal Bridge without forcing, is defined to represent exactly zero movement. All movements presented in the dynamic model are relative to this initial position. If a nonzero tidal level is present, the coordinate system moves along with the segments, to their new initial equilibrium position.

When coordinates are presented, they are relative to the COG of a segment. This way, the hinge connection between pendulum and segment is always on the same coordinate. Forces can also be defined at a relative position, creating an easy definition for the rotational torque forces.

B.1.3. Small rotations

Most rotational movement is expected to occur in the roll direction. Rotation in pitch and yaw will be quite minimal, but are needed to allow for the boundary conditions at the spudpoles. Rotations of yaw due to the tidal range can be estimated using the equation below, which calculates the horizontal displacement of a pendulum connection and divides it by the length of a segment. The rotation of 0.75 ° can be assumed to be

small. Pitch rotation is enforced by the vertical difference of movement of the pendulums. In the equilibrium position, this will be equal to zero. Deviations will be found when heave movement of the segments is not in phase or not similar in amplitude. However, as forcing on the segments will be similar, segments are identical and are all connected, this difference will be small and the rotations can be assumed to be small as well.

$$\begin{aligned}\psi &\approx \frac{h_{tide} \cdot \tan(\alpha)}{L_s} \\ &\approx \frac{1.5 \cdot \tan(40)}{100} \\ &\approx 0.72\,^{\circ}\end{aligned} \tag{B.1}$$

B.1.4. Pendulum mass

The rotational moment of inertia about the end of a rod is defined as shown in Equation (B.2).

$$\begin{aligned}J &= \frac{1}{3} \cdot M_s \cdot L_p^2 \\ &= \frac{1}{3} \cdot \left(7800 \cdot \frac{\pi \cdot 1.320^2}{4} - (7800 - 1025) \cdot \frac{\pi \cdot (1.320 - 2 \cdot 0.036)^2}{4}\right) \cdot \begin{pmatrix} 25.5^3 \\ 31.0^3 \\ 38.5^3 \end{pmatrix} = \begin{pmatrix} 13.2 \\ 23.7 \\ 45.4 \end{pmatrix} \cdot 10^6 \text{ kg m}^2\end{aligned} \tag{B.2}$$

Even if added mass is included, this mass moment of inertia is completely overshadowed by the 1.1 million kg half-segment that is attached to a single pendulum. The mass moment of inertia of the segment about the bottom hinge of the pendulum has been approximated in Equation (B.3). Because of this, it has been decided to neglect the mass moment of inertia of the pendulum itself.

$$\begin{aligned}J &= M_s \cdot L_p^2 \\ &= 1,148,000 \cdot \begin{pmatrix} 25.5^2 \\ 31.0^2 \\ 38.5^2 \end{pmatrix} = \begin{pmatrix} 746.5 \\ 1103.2 \\ 1701.6 \end{pmatrix} \cdot 10^6 \text{ kg m}^2\end{aligned} \tag{B.3}$$

B.1.5. Submerged floaters

It is assumed that a part of the floaters is always submerged and forcing will never be of such magnitude that the structure becomes fully emerged. Vortex induced vibrations may also play a role on the structure. However, based on expert judgement, these vibrations will not have a significant effect on the dynamic behaviour of the structure [4].

Roll rotation will be induce drag patterns that deviate from standard shapes, as the prism is now inclined. This phenomenon has been ignored, to simplify the drag equations. Pitch movement results in a gradient in draught across the various floaters. This extra or reduced draught will influence the drag and wave forces, and will create a nonzero rotational moment. Because of the small rotations, asymmetric forces will be relatively small as well. Therefore, this effect has been neglected as well.

Small rotations in yaw will result in a drag and wave forces that are not exactly perpendicular to the floaters. As rotations in yaw are very small, the cosine of a small angle is approximately one and surge forces are neglected, effect of yaw on these forces is ignored.

B.1.6. Floater added mass

Effect of free water surface

The use of a constant value for added mass is justified according to Delft Hydraulics (now Deltaris) [46]. They state: "In the absence of a free water surface, the added water mass is completely independent of the frequency." However, Delft Hydraulics continues with "when calculating the added water mass (where surface water is present) ... the influence of the waves generated by vibrations may be ignored."

Effect of marine growth

Marine growth creates extra mass in a direct and indirect way. The mass itself contributes to the total mass of a segment, but marine growth also affects the added mass. When assuming that marine growth is limited to 100 mm in thickness, and given the fact that added mass is a function of width squared, the following equation holds for the two types of floaters:

$$\begin{aligned} \frac{M_{added+MG}}{M_{added}} &= \frac{5.2^2}{5^2} = 1.08 \text{ [-]} \\ &= \frac{3.7^2}{3.5^2} = 1.12 \text{ [-]} \end{aligned} \tag{B.4}$$

To simplify these ratios, it is assumed that added mass adds 10 percent in the added mass [47]. The weight of the marine growth itself is included in the total weight of segments. Additional drag due to the marine growth is included by assuming that the pointed tips of the floaters compensate the addition of marine growth excluded.

B.1.7. Connections between segments

It is assumed that the connection between the segments is relatively stiff, and that it is located on the x-axis. This last assumption simplifies a significant amount of the equations, as no eccentricity is presented now. As the exact stiffness and damping ratios are unknown, it assumed that no damping is present, and stiffness is similar to that of the pendulums.

B.1.8. Turbine dynamics

Describing the dynamics of rotating objects may form many challenges. The Dzhanibekov effect, also known as the tennis racket theorem, describes the tendency of objects with three principal moments of inertia to periodically flip in the second (by size) principal direction. As this movement is limited by the stiff connection to the truss structure, and water limits the free movement of the turbines, this effect has been neglected. It is assumed that gyroscopic precession can be ignored, as turbines on opposite ends could be designed to spin in reversed direction. This evens out the possible effect that gyroscopic precession could have.

B.2. Water properties

B.2.1. Squat

As the presence of the partly submerged floaters reduce the effective cross section of the strait, an effect named squat will be observed. As Bernoulli's principle describes, water level drops when flow velocity increases [48]. The magnitude of this effect can be calculated using the method of Schijf, which is depicted in Figure B.1.

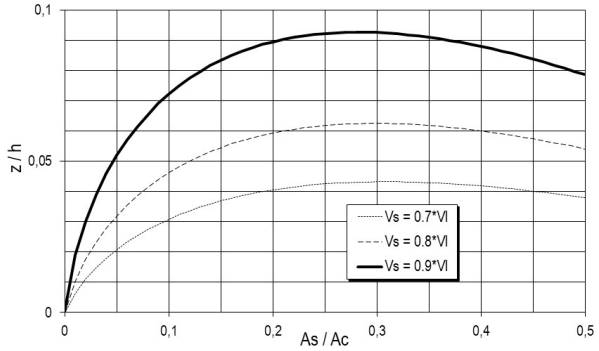

Figure B.1: Graphical representation of the method of Schijf [34]

The (approximate) values below hold for the case study the Palmerah Tidal Bridge. As both ratios are very low and the effect will be in the order of a few centimetres, squat may be neglected.

$$\begin{aligned}\frac{V_s}{V_l} &= \frac{u}{\sqrt{g \cdot d}} \\ &\approx \frac{4.5}{\sqrt{9.8 \cdot 18}} \\ &\approx 0.34 \text{ [-]} \\ \frac{A_s}{A_c} &\approx \frac{N_{segments}\left(N_{fl,l}\left(hW_{fl,l}\right) + N_{fl,s}\left(hW_{fl,s}\right)\right)}{dW} \\ &\approx \frac{4 \cdot (3 \cdot (3 \cdot 5) + 2 \cdot (3 \cdot 3.5))}{18 \cdot 860} \\ &\approx 0.017 \text{ [-]}\end{aligned} \tag{B.5}$$

B.2.2. Morison equation validity

DNV states that "For slender structural members having cross-sectional dimensions sufficiently small to allow the gradients of fluid particle velocities and accelerations in the direction normal to the member to be neglected, wave loads may be calculated using Morison's load formula being a sum of an inertia force proportional to acceleration and a drag force being proportional to the square of velocity." [49] The structure considered has - in wave direction - a length of almost 40 meters and a facing area of 5 meters wide and 3 meters high. With waves ranging up to 90 meters, the statement above is valid.

The recommendations of DNV continue with: "When the length of the member is much larger than the transverse dimension, the end-effects can be neglected and the total force can betaken as the sum of forces on each cross-section along the length." [49] This implies that the drag contribution of the waves can be neglected. To confirm this, the Keulegan Carpenter number is used. The KC number describes the interaction between water and structure. It is defined as follows:

$$\begin{aligned}KC &= \frac{V \cdot T}{L} \\ &= \frac{2 \cdot 7.5}{39} \\ &= 0.38 \text{ [-]}\end{aligned} \tag{B.6}$$

However, the conclusion that drag forces due to waves can be ignored is incorrect, as this KC rule of thumb may only be applied when there is no current. If no current were present, it could be assumed that drag forces due to waves can be ignored. This would imply that the inertia forces due to the very long floaters have significantly more influence than the relatively small facing area. Very small and very large KC numbers make the drag and inertia terms of the Morison equation simpler, as drag can be ignored for KC < 3 and inertia can be ignored for KC > 45 [50]. As a result, interaction between flow velocities due to the tidal movement and the circulating velocities due to the waves could potentially be ignored, simplifying the model. This simplification would be justified due to the following ratios at peak force and average force:

$$\begin{aligned}\frac{F_D}{F_I} &= \frac{\frac{1}{2} \cdot \rho \cdot C_{DS} \cdot A \cdot u^2}{\rho \cdot C_a \cdot V \cdot \dot{u}} \\ &\approx \frac{\frac{1}{2} \cdot 1.15 \cdot (3 \cdot 22) \cdot 2^2}{1.15 \cdot (36 \cdot 3 \cdot 22) \cdot \frac{2 \cdot 2 \cdot \pi}{7.5}} \\ &\approx 0.33 \text{ [-]} \\ &\approx \frac{\frac{1}{2} \cdot 1.15 \cdot (3 \cdot 22) \cdot 1.3^2}{1.15 \cdot (36 \cdot 3 \cdot 22) \cdot \frac{1.3 \cdot 2 \cdot \pi}{7.5}} \\ &\approx 0.022 \text{ [-]}\end{aligned} \tag{B.7}$$

Although an error of a bit more than 2 percent is induced by this decision, it does simplify the equation tremendously. However, current is present. Drag will increase from 4.5^2 to 5.8^2, making a difference of 68 percent. It is clear that this may not be ignored.

Furthermore, it has been assumed that wave diffraction has no significant contribution to the Morison equation. This effect can be neglected when the wave length is significantly larger than the length of the structure. This is not entirely valid [51]. However, to simplify the model it is still neglected.

B.2.3. Wave and current simplification

To simplify the interaction between water and structure, it is assumed that waves and current approach the structure exactly perpendicular. The proposed location of the Palmerah Tidal Bridge has been chosen in such a way that this is quite accurate [4]. The largest waves and highest flow velocities are found perpendicular to the structure. Significant waves and large flow velocities are also found at angles just larger or just smaller than 90 degrees. However, these are ignored.

The waves are described using the second order Stokes equation. It is assumed that the most important waves can be correctly described using this theory. It is also assumed that the varying depth over the length of the bridge does not influence the shape of the incoming waves. A constant depth provides a sufficient approximation of the waves.

B.3. Definition of dimensions

As the floaters are rectangular with a pointed end, the definition for the length of a floater can be made in two ways: the first being the distance between the outer tips, the second being the length of the inner rectangle. The second definition has been chosen, as has been depicted in Figure B.2. It should also be noted that the large floaters and the small floaters differ in shape. The reason for this, is the fact that the small floaters are found at the outer end of all segments, meaning that another small floater is directly besides them. The configuration of all floaters is shown in Figure B.3, in which one full segment plus the neighbouring small floaters are shown.

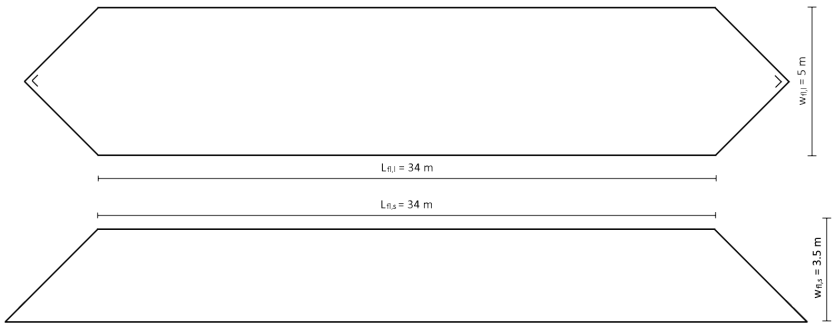

Figure B.2: Size and shape of the floaters

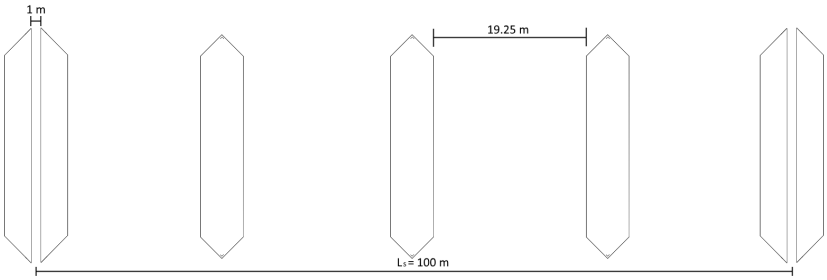

Figure B.3: Configuration and size of the floaters in a segment

C

Computation of matrices in structural response tool

This appendix elaborates on the various elements in the structural response tool, as explained in section 3.2. This information is needed as it will describe the movement of a structure given a certain forcing. Two difficult topics are left out in this evaluation: added mass and radiation damping. These two elements are handled in Appendix F.

C.1. Mass and moment of inertia

Each segment has its own mass and moment of inertia, which is one of the two elements that make the mass matrix of the computation. The other element making the mass matrix is the phenomenon called 'added mass', which is to be discussed in Section 3.2.2. Equation (C.1) presents a part of the full 6Nx6N mass matrix.

$$\boldsymbol{M}_{own} = \begin{bmatrix} \ddots & & & & & & \\ & M_s & 0 & 0 & 0 & 0 & 0 \\ & 0 & M_s & 0 & 0 & 0 & 0 \\ & 0 & 0 & M_s & 0 & 0 & 0 \\ & 0 & 0 & 0 & J_{s,x} & 0 & 0 \\ & 0 & 0 & 0 & 0 & J_{s,y} & 0 \\ & 0 & 0 & 0 & 0 & 0 & J_{s,z} \\ & & & & & & \ddots \end{bmatrix} \tag{C.1}$$

In addition to the own mass of the structure, pedestrians and traffic will form an extra mass on the bridge. Using Eurocode recommendations, one can calculate that this extra mass can rise to 850,000 kg per segment. Compared to the 2,320,000 kg bridge segment, this is a significant extra mass. To simplify the analysis, it is assumed that this extra load is a point mass, directly above the COG of a segment. The z-coordinate of this mass is assumed to be exactly two meter above the centre of the deck. As a result of this assumption, the mass moment of inertia about the y ans z axis is not influenced. Although this does not represent reality fully, it can be assumed that movement in this direction is relatively low and adding the mass will not influence the model significantly. Adding the mass of traffic, requires Equation (C.1) to be supplemented with Equation (C.3).

$$\begin{aligned} M_t &= \frac{L_s \cdot W_{road} \cdot Q_{road} + L_s \cdot W_{sidewalk} \cdot Q_{sidewalk}}{g} \\ &= \frac{100 \cdot 7 \cdot 9000 + 100 \cdot 4 \cdot 5000}{9.8} \\ &= 850,000 \text{ kg} \end{aligned} \tag{C.2}$$

$$\boldsymbol{M}_{own} = \begin{bmatrix} \ddots & & & & & & \\ & M_t & 0 & 0 & 0 & 0 & 0 \\ & 0 & M_t & 0 & 0 & 0 & 0 \\ & 0 & 0 & M_t & 0 & 0 & 0 \\ & 0 & 0 & 0 & J_{t,x} & 0 & 0 \\ & 0 & 0 & 0 & 0 & 0 & 0 \\ & 0 & 0 & 0 & 0 & 0 & 0 \\ & & & & & & \ddots \end{bmatrix} \tag{C.3}$$

Where:

$$J_t = M_t \cdot z_t^2 \tag{C.4}$$

If, instead of Eurocode recommendations, fully loaded lorries are modelled and weight of pedestrians is ignored, the following calculations can be presented:

$$\begin{aligned} M_t &= M_{lorry} \cdot N_{lanes} \cdot \frac{L_s}{L_{lorry}} \\ &= 8000 \cdot 2 \cdot \frac{100}{12.5} \\ &= 128{,}000 \text{ kg} \end{aligned} \tag{C.5}$$

Where the Eurocode prescribes an additional mass of 36 percent of the segments, this calculations shows that a mere 5.5 percent can be found. It is expected that this value represents the traffic load on a segment more, as the Eurocode value represents a statistical highly unlikely force to find the maximum force on members. Contrarily, the calculation using the weight of lorries focuses on estimating the weight correctly, not the maximum force.

C.2. Influence of pendulums

The pendulum connection to the segments influence the movement of the segments significantly. Instead of a traditional heave movement of floating objects, a rotational movement around the pendulum foundation is now made. As the pendulum functions as both a spring and a (weak) damper, spring and damper matrices need to be constructed. As the formulation is very similar, it will only be shown once for the spring-like behaviour of the element. Alterations to obtain the damper-like behaviour will be discussed after. It should be noted that the influence of the location of the upper hinge of the pendulum relative to the COG of the segment (y_p for horizontal and z_p for vertical distance) is very important for the dynamic behaviour, as the eccentricity may generate large moments. For the first and last segment, no pendulum is found on the landside of the segment. Respectively, k_{p_1} and k_{p_2} must be neglected, as these are non-existent. For this reason, and the fact that not all pendulums have the same stiffness value, is each element of the matrix described as a function of both pendulums separately. The generalised spring matrix for a single segment for the influence of the pendulums can be found in Equation (C.6). As the matrix is dependent on the angle of the pendulum, and this angle changes as a function of time, the matrix needs to be updated constantly.

$$\boldsymbol{K}_p = \begin{bmatrix} \ddots & & & & & & \\ & 0 & 0 & 0 & 0 & 0 & 0 \\ & 0 & a & b & c & d & e \\ & 0 & b & f & g & h & i \\ & 0 & c & g & j & k & l \\ & 0 & d & h & k & m & n \\ & 0 & e & i & l & n & o \\ & & & & & & \ddots \end{bmatrix} \tag{C.6}$$

Where:

$$
\begin{aligned}
a &= k_{p_1} \cdot \cos(\alpha_1) \cdot \cos(\alpha_1) + k_{p_2} \cdot \cos(\alpha_2) \cdot \cos(\alpha_2) \\
b &= k_{p_1} \cdot \sin(\alpha_1) \cdot \cos(\alpha_1) + k_{p_2} \cdot \sin(\alpha_2) \cdot \cos(\alpha_2) \\
c &= y_p \cdot k_{p_1} \cdot \sin(\alpha_1) \cdot \cos(\alpha_1) - z_p \cdot k_{p_1} \cdot \cos(\alpha_1) \cdot \cos(\alpha_1) \\
&\quad + y_p \cdot k_{p_2} \cdot \sin(\alpha_2) \cdot \cos(\alpha_2) - z_p \cdot k_{p_2} \cdot \cos(\alpha_2) \cdot \cos(\alpha_2) \\
d &= 1/2 \cdot d_p \cdot k_{p_1} \cdot \sin(\alpha_1) \cdot \cos(\alpha_1) - 1/2 \cdot d_p \cdot k_{p_2} \cdot \sin(\alpha_2) \cdot \cos(\alpha_2) \\
e &= -1/2 \cdot d_p \cdot k_{p_1} \cdot \cos(\alpha_1) \cdot \cos(\alpha_1) + 1/2 \cdot d_p \cdot k_{p_2} \cdot \cos(\alpha_2) \cdot \cos(\alpha_2) \\
f &= k_{p_1} \cdot \sin(\alpha_1) \cdot \sin(\alpha_1) + k_{p_2} \cdot \sin(\alpha_2) \cdot \sin(\alpha_2) + k_{p_2} \cdot \sin(\alpha_2) \cdot \sin(\alpha_2) \\
g &= y_p \cdot k_{p_1} \cdot \sin(\alpha_1) \cdot \sin(\alpha_1) - z_p \cdot k_{p_1} \cdot \cos(\alpha_1) \cdot \sin(\alpha_1) \\
&\quad + y_p \cdot k_{p_2} \cdot \sin(\alpha_2) \cdot \sin(\alpha_2) - z_p \cdot k_{p_2} \cdot \cos(\alpha_2) \cdot \sin(\alpha_2) \\
h &= 1/2 \cdot d_p \cdot k_{p_1} \cdot \sin(\alpha_1) \cdot \sin(\alpha_1) - 1/2 \cdot d_p \cdot k_{p_2} \cdot \sin(\alpha_2) \cdot \sin(\alpha_2) \\
i &= -1/2 \cdot d_p \cdot k_{p_1} \cdot \cos(\alpha_1) \cdot \sin(\alpha_1) + 1/2 \cdot d_p \cdot k_{p_2} \cdot \cos(\alpha_2) \cdot \sin(\alpha_2) \\
j &= z_p \cdot k_{p_1} \cdot \cos(\alpha_1) \cdot \cos(\alpha_1) \cdot z_p - z_p \cdot k_{p_1} \cdot \cos(\alpha_1) \cdot \sin(\alpha_1) \cdot y_p + y_p \cdot k_{p_1} \cdot \sin(\alpha_1) \cdot \sin(\alpha_1) \cdot y_p \\
&\quad - y_p \cdot k_{p_1} \cdot \sin(\alpha_1) \cdot \cos(\alpha_1) \cdot z_p + z_p \cdot k_{p_2} \cdot \cos(\alpha_2) \cdot \cos(\alpha_2) \cdot z_p \\
&\quad - z_p \cdot k_{p_2} \cdot \cos(\alpha_2) \cdot k_{p_2} \cdot \sin(\alpha_2) \cdot \sin(\alpha_2) \cdot y_p - y_p \cdot k_{p_2} \cdot \sin(\alpha_2) \cdot \cos(\alpha_2) \cdot z_p \\
k &= 1/2 \cdot d_p \cdot k_{p_1} \cdot \sin(\alpha_1) \cdot \sin(\alpha_1) \cdot y_p - 1/2 \cdot d_p \cdot k_{p_1} \cdot \sin(\alpha_1) \cdot \cos(\alpha_1) \cdot z_p \\
&\quad - 1/2 \cdot d_p \cdot k_{p_2} \cdot \sin(\alpha_2) \cdot \sin(\alpha_2) \cdot y_p + 1/2 \cdot d_p \cdot k_{p_2} \cdot \sin(\alpha_2) \cdot \cos(\alpha_2) \cdot z_p \\
l &= -1/2 \cdot d_p \cdot k_{p_1} \cdot \cos(\alpha_1) \cdot \sin(\alpha_1) \cdot y_p + 1/2 \cdot d_p \cdot k_{p_1} \cdot \cos(\alpha_1) \cdot \cos(\alpha_1) \cdot z_p \\
&\quad + 1/2 \cdot d_p \cdot k_{p_2} \cdot \cos(\alpha_2) \cdot \sin(\alpha_2) \cdot y_p - 1/2 \cdot d_p \cdot k_{p_2} \cdot \cos(\alpha_2) \cdot \cos(\alpha_2) \cdot z_p \\
m &= 1/2 \cdot d_p \cdot k_{p_1} \cdot \sin(\alpha_1) \cdot \sin(\alpha_1) \cdot 1/2 \cdot d_p + 1/2 \cdot d_p \cdot k_{p_2} \cdot \sin(\alpha_2) \cdot \sin(\alpha_2) \cdot 1/2 \cdot d_p \\
n &= -1/2 \cdot d_p \cdot k_{p_1} \cdot \cos(\alpha_1) \cdot \sin(\alpha_1) \cdot 1/2 \cdot d_p - 1/2 \cdot d_p \cdot k_{p_2} \cdot \cos(\alpha_2) \cdot \sin(\alpha_2) \cdot 1/2 \cdot d_p \\
o &= 1/2 \cdot d_p \cdot k_{p_1} \cdot \cos(\alpha_1) \cdot \cos(\alpha_1) \cdot 1/2 \cdot d_p + 1/2 \cdot d_p \cdot k_{p_2} \cdot \cos(\alpha_2) \cdot \cos(\alpha_2) \cdot 1/2 \cdot d_p
\end{aligned}
\tag{C.7}
$$

$\boldsymbol{C}_p$ can be evaluated using the same set of equations. However, spring stiffnesses k_{p_1} and k_{p_2} need to be replaced by their counterparts c_{p_1} and c_{p_2}, which represent the damping. The spring stiffness of a longitudinal forced element can be modelled as is shown in Equation (C.8).

$$
k_p = \frac{EA}{L} \tag{C.8}
$$

As the current design proposes a CHS1320-36 profile [4], the stiffness of a single member can be model as follows in Equation (C.9). A set of different lengths has been shown in this equation since the pendulums vary in length based on the location of the bridge. For a 2D-analysis of a segment, the found values need to multiplied with a factor of 2, as two pendulums are connected to a segment. The modulus of elasticity has been set to 210 GPa, as is recommended by the Eurocode [52].

$$
k_p = \frac{210 \cdot 10^9 \cdot \left(\frac{\pi \cdot 1.320^2}{4} - \frac{\pi \cdot (1.320 - 2 \cdot 0.036)^2}{4} \right)}{\begin{pmatrix} 25.5 \\ 31.0 \\ 38.5 \end{pmatrix}} = \begin{pmatrix} 1.196 \\ 0.984 \\ 0.792 \end{pmatrix} \cdot 10^9 \text{ N/m} \tag{C.9}
$$

As the foundation is not fully rigid as well and connections may be flexible, an additional fictive spring will be found. To take this into account, a series of springs need to be modelled. Exact behaviour of the combination of the pendulum and foundation is unknown, but will be approximated by reducing the stiffness by a factor 10.

Damping in the pendulum is low, as structural steel hardly damps. Orban [53] and Mevada et al. [54] experimentally found damping ratios of respectively <0.01 and 0.0069. Theoretically, the value should equal 0.0077 [53]. For the pendulums, this results in Equation (C.10). In here, a specific density of 7800 kg/m^3 is used for steel [55] and 1025 kg/m^3 for salt water [4].

$$c_p = \zeta 2\sqrt{km}$$
$$= 0.007 \cdot 2 \cdot \sqrt{\begin{pmatrix}1.196\\0.984\\0.792\end{pmatrix} \cdot 10^9 \cdot \left(7800 \cdot \frac{\pi \cdot 1.320^2}{4} - (7800-1025) \cdot \frac{\pi \cdot (1.320 - 2 \cdot 0.036)^2}{4}\right) \cdot \begin{pmatrix}25.5\\31.0\\38.5\end{pmatrix}} = \begin{pmatrix}119400\\119400\\119400\end{pmatrix} \text{ Ns/m} \tag{C.10}$$

Again, the foundation will have influence on the damping. Further research is needed to address this accurately. For simplicity, it is assumed that the foundation does have no effect on the combined damping value. However, even if added to the calculation the damping in the pendulums of little magnitude.

C.3. Influence of spudpoles

The outer segments are not connected to a pendulum, but to a spudpole. As discussed earlier, the spudpole limits the movement in x- and y-direction. As all movement in x-direction is neglected in this study, only the spring and damping stiffness in y-direction needs to be considered. Spudpole characteristics are presented in Table C.1

Side	**Profile**	**Length**
Larantuka side	ø3000x50	18 m
Adonara side	ø3000x50	25.5 m

Table C.1: Spudpole characteristics [4]

Again, the matrix for the spring-like behaviour and the damper-like behaviour are very similar and will only be presented once for the spring matrix. Alterations to obtain the damper matrix will be discussed after. Equation (C.6) presents the influence of the spudpoles on the spring matrix. Please note that the formulations only describe the first and last segment.

$$\boldsymbol{K}_{sp} = \begin{bmatrix} 0 & 0 & 0 & 0 & 0 & 0 & & & & & & \\ 0 & a & 0 & 0 & 0 & b & & & & & & \\ 0 & 0 & 0 & 0 & 0 & 0 & & & & & & \\ 0 & 0 & 0 & 0 & 0 & 0 & & & & & & \\ 0 & 0 & 0 & 0 & 0 & 0 & & & & & & \\ 0 & b & 0 & 0 & 0 & c & & & & & & \\ & & & & & & \ddots & & & & & \\ & & & & & & & 0 & 0 & 0 & 0 & 0 & 0 \\ & & & & & & & 0 & d & 0 & 0 & 0 & e \\ & & & & & & & 0 & 0 & 0 & 0 & 0 & 0 \\ & & & & & & & 0 & 0 & 0 & 0 & 0 & 0 \\ & & & & & & & 0 & 0 & 0 & 0 & 0 & 0 \\ & & & & & & & 0 & e & 0 & 0 & 0 & f \end{bmatrix} \tag{C.11}$$

Where:

$$\begin{aligned} a &= k_{sp_1} \\ b &= -1/2 \cdot L_s \cdot k_{sp_1} \\ c &= 1/2 \cdot L_s \cdot k_{sp_1} \cdot 1/2 \cdot L_s \\ d &= k_{sp_2} \\ e &= 1/2 \cdot L_s \cdot k_{sp_2} \\ f &= 1/2 \cdot L_s \cdot k_{sp_2} \cdot 1/2 \cdot L_s \end{aligned} \tag{C.12}$$

Again, this structure can be used to obtain the damping matrix as a consequence of the influence of the spudpoles as well. $\boldsymbol{C}_{sp}$ is obtained when k_{sp_1} and k_{sp_2} are replaced by c_{sp_1} and c_{sp_2}. The magnitude of the springs for both spudpoles are determined as follows in Equation (C.13). The dampers have been set equal to

that of the pendulums, which is 119,400 Ns/m. The exact value has little influence on the results. However, it is important that a nonzero value is attributed to prevent never ending motion.

$$\begin{aligned} k_{sp} &= \frac{3EI}{L^3} \\ &= \frac{3 \cdot 210 \cdot 10^9 \cdot \left(\frac{\pi}{64} \cdot \left(3^4 - 2.9^4\right)\right)}{\begin{pmatrix} 18 \\ 25.5 \end{pmatrix}^3} \\ &= \begin{pmatrix} 54,000,000 \\ 19,000,000 \end{pmatrix} \text{ N/m} \end{aligned} \tag{C.13}$$

C.4. Influence of segment connections

Equation (C.14) represents the influence of neighbouring segments on a segment as a result of spring-like behaviour. In the equation, a set of three 6x6 matrices are shown. The middle 6x6 matrix is the segment being considered, the interaction with neighbouring segments is shown in the 6x6 matrices next to the centre 6x6 matrix. Also for this computation, the damping matrix $\boldsymbol{K}_c$ can be easily extracted, by replacing $k_{c_1,y}$, $k_{c_1,y}$, $k_{c_2,y}$, and $k_{c_2,z}$ with respectively $c_{c_1,y}$, $k_{c_1,y}$, $c_{c_2,y}$, and $c_{c_2,z}$.

$$\boldsymbol{K}_c = \begin{bmatrix} \ddots & & & & & & & & & & & & & & & & & & \\ & 0 & 0 & 0 & 0 & 0 & 0 & 0 & 0 & 0 & 0 & 0 & 0 & 0 & 0 & 0 & 0 & 0 & 0 & \\ & 0 & a & 0 & 0 & 0 & b & 0 & g & 0 & 0 & 0 & h & 0 & m & 0 & 0 & 0 & n & \\ & 0 & 0 & c & 0 & d & 0 & 0 & 0 & i & 0 & j & 0 & 0 & 0 & o & 0 & p & 0 & \\ & 0 & 0 & 0 & 0 & 0 & 0 & 0 & 0 & 0 & 0 & 0 & 0 & 0 & 0 & 0 & 0 & 0 & 0 & \\ & 0 & 0 & d & 0 & e & 0 & 0 & 0 & j & 0 & k & 0 & 0 & 0 & p & 0 & q & 0 & \\ & 0 & b & 0 & 0 & 0 & f & 0 & h & 0 & 0 & 0 & l & 0 & n & 0 & 0 & 0 & r & \\ & & & & & & & & & & & & & & & & & & \ddots \end{bmatrix} \tag{C.14}$$

Where:

$$\begin{aligned} a &= -k_{c_1,y} \\ b &= -1/2 \cdot L_s \cdot k_{c_1,y} \\ c &= -k_{c_1,z} \\ d &= 1/2 \cdot L_s \cdot k_{c_1,z} \\ e &= 1/2 \cdot L_s \cdot k_{c_1,y} \cdot 1/2 \cdot L_s \\ f &= 1/2 \cdot L_s \cdot k_{c_1,z} \cdot 1/2 \cdot L_s \\ g &= k_{c_1,y} + k_{c_2,y} \\ h &= -k_{c_1,y} \cdot 1/2 \cdot L_s + k_{c_2,y} \cdot 1/2 \cdot L_s \\ i &= k_{c_1,z} + k_{c_2,z} \\ j &= k_{c_1,z} \cdot 1/2 \cdot L_s - k_{c_2,z} \cdot 1/2 \cdot L_s \\ k &= 1/2 \cdot L_s \cdot k_{c_1,y} \cdot 1/2 \cdot L_s + 1/2 \cdot L_s \cdot k_{c_2,y} \cdot 1/2 \cdot L_s \\ l &= 1/2 \cdot L_s \cdot k_{c_1,z} \cdot 1/2 \cdot L_s + 1/2 \cdot L_s \cdot k_{c_2,z} \cdot 1/2 \cdot L_s \\ m &= -k_{c_2,y} \\ n &= 1/2 \cdot L_s \cdot k_{c_2,y} \\ o &= -k_{c_2,z} \\ p &= -1/2 \cdot L_s \cdot k_{c_2,z} \\ q &= 1/2 \cdot L_s \cdot k_{c_2,y} \cdot 1/2 \cdot L_s \\ r &= 1/2 \cdot L_s \cdot k_{c_2,z} \cdot 1/2 \cdot L_s \end{aligned} \tag{C.15}$$

The magnitude of the springs have been set to 10^8 N/m. The damping values have been set equal to 50,000 Ns/m. This value will most likely deviate from the true value, but as this damping is only a very minor ele-

ment of the total damping, it will not influence the end results. The spring force will influence the response. However, as no specification is made for the connection, this estimate has been chosen.

C.5. Influence of hydrostatic pressure

Oscillations in water due to the spring-like behaviour of a floater in water can also happen in still water, as the first term of Equation (3.36) acts as a spring. When a floating body has a vertical displacement with respect to their equilibrium draft, the net vertical force on that body is equal to the weight of the displayed mass. This principle, which is a small change on Archimedes' principle, can be used to determine the spring stiffness of a floating body on water. This spring stiffness can be defined for both vertical translation and rotation. A schematic overview of the forces in these two situations can be found in Figure C.1. In here, motion for heave and pitch/roll is shown.

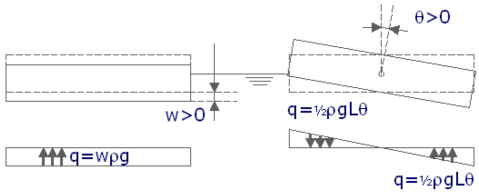

Figure C.1: Theory of buoyancy for heave and pitch/roll [56]

The distributed forces shown in Figure C.1 can be converted into a vertical force by integrating the distributed force over the complete length. A rotational moment can be found when the integrating the distributed force multiplied with the distance to the centre of gravity. When this force or rational moment is then considered per unit displacement or rotation, spring forces can be determined. These spring forces can be found in Equations (C.16) and (C.17). Please note, the equation for the rotational spring is only valid for rectangular cross sections.

$$k_z = \int_A \frac{dp}{dz}\, dA = \rho \cdot g \cdot A \tag{C.16}$$

$$k_r = \int_A \frac{dp}{d\phi} r\, dA = \frac{1}{12} \cdot \rho \cdot g \cdot L \cdot W^3 \tag{C.17}$$

For cases including the presence of waves, the solution of these integrals become more complicated and can be approximated numerically. Without waves, the spring matrix due to the hydrostatic pressure is shown in Equation (C.18).

$$\boldsymbol{K}_{hydro} = \begin{bmatrix} \ddots & & & & & & \\ & 0 & 0 & 0 & 0 & 0 & 0 \\ & 0 & 0 & 0 & 0 & 0 & 0 \\ & 0 & 0 & a & 0 & 0 & 0 \\ & 0 & 0 & 0 & b & 0 & 0 \\ & 0 & 0 & 0 & 0 & c & 0 \\ & 0 & 0 & 0 & 0 & 0 & 0 \\ & & & & & & \ddots \end{bmatrix} \tag{C.18}$$

Where:

$$\begin{aligned} a &= \rho \cdot g \left(N_{fl,s} \cdot \left(W_{fl,s} \cdot L_{fl,s} + W_{fl,s} \cdot W_{fl,s} \right) + N_{fl,l} \cdot \left(W_{fl,l} \cdot L_{fl,l} + W_{fl,l} \cdot 0.5 \cdot W_{fl,l} \right) \right) \\ b &= \frac{1}{12} \cdot \rho \cdot g \cdot \left(N_{fl,s} \cdot W_{fl,s} \cdot \left(L_{fl,s} + 0.5 \cdot W_{fl,s} \right)^3 + N_{fl,l} \cdot W_{fl,l} \cdot \left(L_{fl,l} + 2 \cdot 0.25 \cdot W_{fl,l} \right)^3 \right) \\ c &= N_{fl,s} \cdot \rho \cdot g \cdot \left(W_{fl,s} \cdot L_{fl,s} + W_{fl,s} \cdot W_{fl,s} \right) \cdot (1/2 \cdot d_{fl,s})^2 \\ &\quad + \sum_{i=1}^{N_{fl,l}} \left(\rho \cdot g \cdot \left(W_{fl,l} \cdot L_{fl,l} + W_{fl,l} \cdot 0.5 \cdot W_{fl,l} \right) \cdot d_{fl,l,i}^2 \right) \end{aligned} \tag{C.19}$$

D

Significant wave height and occurrence

This appendix is an elaboration on Subsection 3.3.3, in which the significant wave height, wave period and wave length as function of direction was shown. In this appendix, the raw data will be shown. The measured wind velocities have been divided into directional bins. This separated data has been transformed into histograms, which are presented in Figure D.1. In the data-set which is slightly longer than 12 years no measurements higher than 13 m/s were found, indicating a moderate wind-climate.

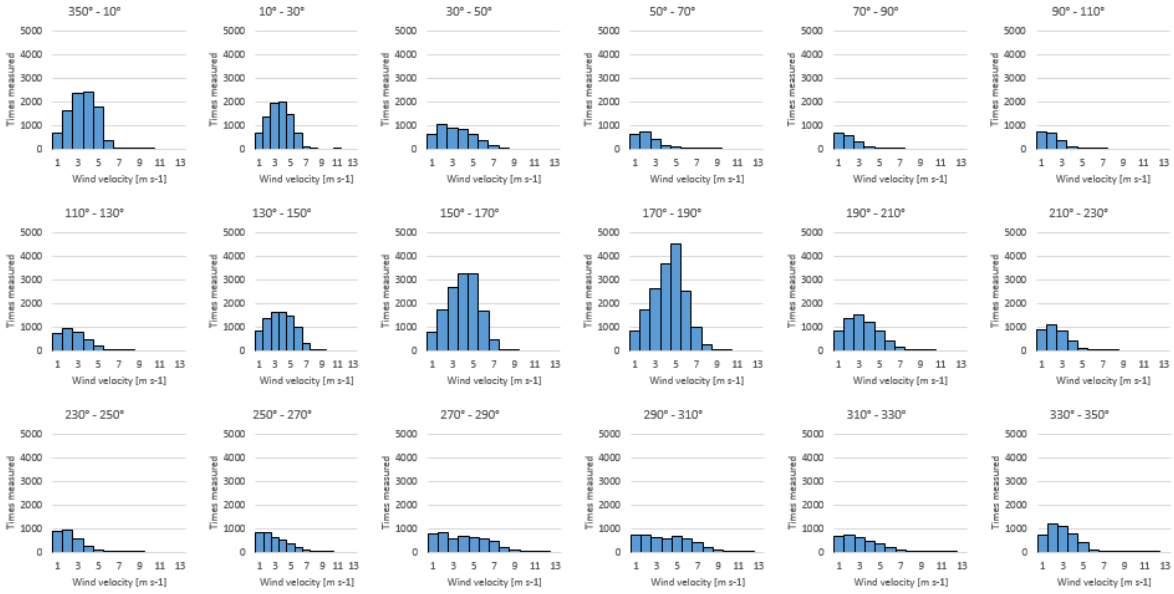

Figure D.1: Histogram of wind velocities per directional bin [31]

Using Equations 3.21, 3.22, and 3.23, Table D.1 can be computed.

Direction	Fetch	Average water depth	Wind velocity	Wave height	Wave period	Wave length
350 – 010 °	316,000 m	2,000 m	9.7 m/s	2.05 m	5.79 s	52.37 m
010 – 030 °	750,000 m	2,000 m	10.6 m/s	2.81 m	6.87 s	73.66 m
030 – 050 °	660,000 m	2,000 m	11.9 m/s	3.32 m	7.40 s	85.61 m
050 – 070 °	1,161,000 m	2,000 m	10.2 m/s	2.78 m	6.94 s	75.24 m
070 – 090 °	315,000 m	2,000 m	7.2 m/s	1.28 m	4.62 s	33.30 m
090 – 110 °	1,000 m	18 m	6.8 m/s	0.16 m	1.48 s	3.43 m
110 – 130 °	1,000 m	18 m	9.2 m/s	0.22 m	1.73 s	4.67 m
130 – 150 °	1,000 m	18 m	11.8 m/s	0.30 m	1.96 s	6.00 m
150 – 170 °	1,000 m	18 m	11.1 m/s	0.28 m	1.90 s	5.65 m
170 – 190 °	1,000 m	18 m	11.9 m/s	0.30 m	1.97 s	6.06 m
190 – 210 °	1,000 m	18 m	11.4 m/s	0.29 m	1.93 s	5.80 m
210 – 230 °	32,000 m	18 m	8.5 m/s	0.81 m	3.44 s	18.53 m
230 – 250 °	3,000 m	18 m	8.4 m/s	0.32 m	2.12 s	7.03 m
250 – 270 °	1,000 m	18 m	12.4 m/s	0.32 m	2.01 s	6.31 m
270 – 290 °	1,000 m	18 m	15.5 m/s	0.41 m	2.25 s	7.89 m
290 – 310 °	1,000 m	18 m	15.8 m/s	0.42 m	2.27 s	8.04 m
310 – 330 °	480,000 m	2,000 m	13.0 m/s	3.54 m	7.59 s	89.88 m
330 – 350 °	350,000 m	2,000 m	10.5 m/s	2.37 m	6.22 s	60.45 m

Table D.1: Extreme wind and wave conditions for every direction in Larantuka Strait, exceedance once every 100 years [31]

E

Verification and validation of the dynamic model

As described in Chapter 3, the complete dynamic model consists out of three tools: the structural response tool, the forcing tool, and the integration tool. This chapter will verify and validate the output values of the three tools and their elements.

E.1. Structural response tool

The structural response tool determines the mass-, damper-, and spring-matrix for the dynamic calculation. Each connecting element to a segment will induce spring-like and damper-like forces on the segments. The matrix tool has been split into five different 'subtools': the mass subtools, the pendulum subtools, the spud-pole subtools, the segment connection subtools and the hydrostatic pressure subtools. The first subtools mentioned is a direct input of the user, as they implement the mass and mass moment of inertia themselves. Traffic mass is added to these values. The remaining four subtools of the structural response tool are verified and validated below. Two other subtools, the added mass subtools and the radiation damping subtools, are not discussed in this appendix, as they will be described in Appendix F and Appendix G.

E.1.1. Pendulum subtool verification

When the pendulum subtools is invoked, using the settings presented in Table E.1, the subtool returns the matrix given in Equation (E.1) for the middle segment. Only a case for the spring-like behaviour will be presented, as the calculations for the damper-like behaviour are identical, as explained before.

Setting	**Value**
Segments	3 -
Length_segment	100 m
free_space_between_segments	1 m
characteristics_small_floater	[2, 3.5, 34] -, m, m
Angle_Pendulum	$\pi/180 \cdot [40, 40, 40, 40]$ rad
Pendulum_hinge_top_location	[6.5, −7.2] m
kc_pendulum	$[10^9, 10^9, 10^9, 10^9]$ N/m
Three_Dimensional_Calculation	$True$

Table E.1: Pendulum spring matrix verification settings

$$\boldsymbol{K}_p = \begin{bmatrix} \ddots & & & & & & \\ & 0 & 0 & 0 & 0 & 0 & 0 \\ & 0 & a & b & c & 0 & 0 \\ & 0 & b & d & e & 0 & 0 \\ & 0 & c & e & f & 0 & 0 \\ & 0 & 0 & 0 & 0 & g & h \\ & 0 & 0 & 0 & 0 & h & i \\ & & & & & & \ddots \end{bmatrix} \tag{E.1}$$

Where:

$$\begin{aligned} a &= 1.17364818 \cdot 10^{9} \\ b &= 9.84807753 \cdot 10^{8} \\ c &= 1.48515173 \cdot 10^{10} \\ d &= 8.26351822 \cdot 10^{8} \\ e &= 1.24619027 \cdot 10^{10} \\ f &= 1.87933292 \cdot 10^{11} \\ g &= 1.74856046 \cdot 10^{12} \\ h &= -2.08385321 \cdot 10^{12} \\ i &= 2.48343954 \cdot 10^{12} \end{aligned} \tag{E.2}$$

As all pendulums have the same angle and have the same stiffness, interaction between sway/heave/roll and pitch/yaw is not expected to be found. For forcing in the y- and z-direction only, which are the only forces present in this model, the matrix can be even further simplified to the 2D-case: sway, heave and roll. Although the values g, h, and i are still present, structure forcing and therefore displacement as well, will always be of magnitude zero. It can also be noted that the following relations hold:

$$\begin{aligned} \frac{a}{2 \cdot (\cos 40)^2} &= \text{kc\_pendulum} \\ \frac{d}{2 \cdot (\sin 40)^2} &= \text{kc\_pendulum} \\ \frac{b}{\sin(40)} &= \frac{a}{\cos(40)} \\ \frac{d}{\sin(40)} &= \frac{b}{\cos(40)} \\ \frac{g}{\sin(40)} &= -\frac{h}{\cos(40)} \\ \frac{h}{\sin(40)} &= -\frac{i}{\cos(40)} \end{aligned} \tag{E.3}$$

Now, two extreme cases will be examined: Angle_pendulum = 0° and Angle_pendulum = 90°. For the former case, values b, d, e, g, and h drop to zero. This is expected as the values interact with heave and pitch, which are vertical movements for the pendulums. With an angle of 0 degrees, vertical movement is an exact rotational movement of the pendulum, meaning the spring-like behaviour is not present. It should also be noted that value a becomes $2 \cdot 10^9$, being exactly 2 times the stiffness of a single pendulum. This is expected as a single segment is connected to two pendulums.

For a 90 degrees angle, the exact opposite occurs: values a, b, c, h, and i drop to zero. This can be explained using the same strategy, but heave and pitch movement should be interchanged with sway and yaw movement, which are both horizontal movements for the pendulum connections. Again, this would mean an exact rotation. Also here holds that value d becomes $2 \cdot 10^9$.

For the Palmerah Tidal Bridge, pendulums will vary in length. Therefore, stiffness and potentially the angle will vary as well. This will cause interaction between sway/heave/roll and pitch/yaw, making the spring matrix more complex.

E.1.2. Spudpole subtool verification

The spudpole subtool can be invoked using the settings presented in Table E.2. As only the top left and bottom right corners of the output matrix are relevant, as these represent the outer segments which interact with the spudpoles, these are shown solely in Equation (E.4). Again, only a case for the spring-like behaviour will be presented, as the calculations for the damper-like behaviour are identical.

Setting	**Value**
Segments	3 -
Length_segment	100 m
kc_pendulum	$[10^7,\ 2\cdot10^7]$ N/m
Three_Dimensional_Calculation	$True$

Table E.2: Spudpole spring matrix verification settings

$$\boldsymbol{K}_{sp} = \begin{bmatrix} 0 & 0 & 0 & 0 & 0 & 0 & & & & & & \\ 0 & a & 0 & 0 & 0 & b & & & & & & \\ 0 & 0 & 0 & 0 & 0 & 0 & & & & & & \\ 0 & 0 & 0 & 0 & 0 & 0 & & & & & & \\ 0 & 0 & 0 & 0 & 0 & 0 & & & & & & \\ 0 & b & 0 & 0 & 0 & c & & & & & & \\ & & & & & & \ddots & & & & & \\ & & & & & & & 0 & 0 & 0 & 0 & 0 & 0 \\ & & & & & & & 0 & d & 0 & 0 & 0 & e \\ & & & & & & & 0 & 0 & 0 & 0 & 0 & 0 \\ & & & & & & & 0 & 0 & 0 & 0 & 0 & 0 \\ & & & & & & & 0 & 0 & 0 & 0 & 0 & 0 \\ & & & & & & & 0 & e & 0 & 0 & 0 & f \end{bmatrix} \tag{E.4}$$

Where:

$$\begin{aligned} a &= 1.0\cdot10^7 \\ b &= -5.0\cdot10^8 \\ c &= 2.5\cdot10^{10} \\ d &= 2.0\cdot10^7 \\ e &= 1.0\cdot10^9 \\ f &= 5\cdot10^{10} \end{aligned} \tag{E.5}$$

The values above show that the model works as expected, as the following equations hold:

$$\begin{aligned} a &= \text{kc\_spudpole}[1] \\ b &= -\text{kc\_spudpole}[1]\cdot\frac{\text{Length\_segment}}{2} \\ d &= \text{kc\_spudpole}[1]\cdot\left(\frac{\text{Length\_segment}}{2}\right)^2 \\ d &= \text{kc\_spudpole}[2] \\ e &= \text{kc\_spudpole}[2]\cdot\frac{\text{Length\_segment}}{2} \\ f &= \text{kc\_spudpole}[2]\cdot\left(\frac{\text{Length\_segment}}{2}\right)^2 \end{aligned} \tag{E.6}$$

Changing the former of latter value of the input, results in linear scaling of the output, as is expected.

E.1.3. Segment connection subtool verification

The segment connection subtool can be invoked using the settings presented in Table E.3. Note that the array given for the connection stiffness represents the stiffness in y- and z-direction. The output of the tool is shown in Equation (E.7), where the wide matrix represents a set of three 6x6 matrices. The former being the connection to the previous segment, the second being the investigated segment, and the latter being the

Setting	**Value**
Segments	3 -
Length_segment	100 m
kc_connection_segments	$[10^6, 3 \cdot 10^6]$ N/m
Three_Dimensional_Calculation	$True$

Table E.3: Segment connection spring matrix verification settings

following segment. For this computation as well, the effects of a spring connection in between the segments is shown solely. The calculation for a damper in between the segments is identical.

$$\boldsymbol{K}_c = \begin{bmatrix} & & & & & & \vdots & & & & & & \vdots & & & & & & \\ 0 & 0 & 0 & 0 & 0 & 0 & 0 & 0 & 0 & 0 & 0 & 0 & 0 & 0 & 0 & 0 & 0 & 0 \\ 0 & a & 0 & 0 & 0 & b & 0 & g & 0 & 0 & 0 & h & 0 & m & 0 & 0 & 0 & n \\ 0 & 0 & c & 0 & d & 0 & 0 & 0 & i & 0 & j & 0 & 0 & 0 & o & 0 & p & 0 \\ 0 & 0 & 0 & 0 & 0 & 0 & 0 & 0 & 0 & 0 & 0 & 0 & 0 & 0 & 0 & 0 & 0 & 0 \\ 0 & 0 & d & 0 & e & 0 & 0 & 0 & j & 0 & k & 0 & 0 & 0 & p & 0 & q & 0 \\ 0 & b & 0 & 0 & 0 & f & 0 & h & 0 & 0 & 0 & l & 0 & n & 0 & 0 & 0 & r \\ & & & & & & \vdots & & & & & & \vdots & & & & & & \end{bmatrix} \tag{E.7}$$

Where:

$$\begin{aligned} a &= -1.0 \cdot 10^6 \\ b &= -5.0 \cdot 10^7 \\ c &= -3.0 \cdot 10^6 \\ d &= 1.5 \cdot 10^8 \\ e &= 2.5 \cdot 10^9 \\ f &= 7.5 \cdot 10^9 \\ g &= 2.0 \cdot 10^6 \\ h &= 0 \\ i &= 6.0 \cdot 10^6 \\ j &= 0 \\ k &= 5.0 \cdot 10^9 \\ l &= 1.5 \cdot 10^{10} \\ m &= -1.0 \cdot 10^6 \\ n &= -1.5 \cdot 10^8 \\ o &= -3.0 \cdot 10^6 \\ p &= 5.0 \cdot 10^7 \\ q &= 2.5 \cdot 10^9 \\ r &= 7.5 \cdot 10^9 \end{aligned} \tag{E.8}$$

It makes sense that the two values h and j are zero, as pitch and yaw rotation excite the springs to the two neighbouring segments in opposite direction, cancelling each other out.

E.1.4. Hydrostatic pressure subtool verification

The hydrostatic pressure acts like a spring, which can be easily verified using hand calculations. When the subtool is invoked with the settings presented in Table E.4, output as given in Equation (E.9). This subtool is only used when no waves are presented, as waves make the hydrostatic assumption invalid. As the calculation for the natural frequencies assumes no waves as well, this subenine can be used for that purpose.

Setting	**Value**
Segments	3 -
Length_segment	100 m
free_space_between_segments	100 m
characteristics_small_floater	[2, 3.5, 34] -, m, m
characteristics_large_floater	[3, 5, 34] -, m, m
rho	1025 kg/m^3
g	9.8 m/s^2
Three_Dimensional_Calculation	$True$

Table E.4: Hydrostatic spring matrix verification settings

$$\boldsymbol{K}_{hydro} = \begin{bmatrix} \ddots & & & & & & \\ & 0 & 0 & 0 & 0 & 0 & 0 \\ & 0 & 0 & 0 & 0 & 0 & 0 \\ & 0 & 0 & a & 0 & 0 & 0 \\ & 0 & 0 & 0 & b & 0 & 0 \\ & 0 & 0 & 0 & 0 & c & 0 \\ & 0 & 0 & 0 & 0 & 0 & 0 \\ & & & & & & \ddots \end{bmatrix} \tag{E.9}$$

Where:

$$\begin{aligned} a &= 8.13645000 \cdot 10^6 \\ b &= 8.78303004 \cdot 10^8 \\ c &= 8.10201684 \cdot 10^9 \end{aligned} \tag{E.10}$$

Value a can be verified by calculating the horizontal area of the floaters and multiplying with that with $\rho \cdot g$. b can be approximated using rectangular shapes with roll motion. Value c can be approximated by calculating the heave component of the outer four floaters multiplied with the distance to the COG squared. The pointed tips and precise distances will make the true values deviate slightly.

$$\begin{aligned} a &\approx \left(N_{fl,s} \cdot L_{fl,s} \cdot W_{fl,s} + N_{fl,l} \cdot L_{fl,l} \cdot W_{fl,l}\right) \cdot \rho \cdot g \\ &\approx (2 \cdot 34 \cdot 3.5 + 3 \cdot 34 \cdot 5) \cdot 1025 \cdot 9.8 = 7.5 \cdot 10^6 \\ b &\approx \frac{1}{12} \cdot \left(N_{fl,s} \cdot L_{fl,s}^3 \cdot W_{fl,s} + N_{fl,l} \cdot L_{fl,l}^3 \cdot W_{fl,l}\right) \cdot \rho \cdot g \\ &\approx \frac{1}{12} \cdot \left(2 \cdot 34^3 \cdot 3.5 + 3 \cdot 34^3 \cdot 5\right) \cdot 1025 \cdot 9.8 = 7.210^8 \\ c &\approx \left(N_{fl,s} \cdot L_{fl,s} \cdot W_{fl,s} \cdot \left(\frac{L_s}{2}\right)^2 + 2 \cdot L_{fl,l} \cdot W_{fl,l} \cdot \left(\frac{L_s}{4}\right)^2\right) \cdot \rho \cdot g \\ &\approx \left(2 \cdot 34 \cdot 3.5 \cdot \left(\frac{100}{2}\right)^2 + 2 \cdot 34 \cdot 5 \cdot \left(\frac{100}{4}\right)^2\right) \cdot 1025 \cdot 9.8 = 8.1 \cdot 10^9 \end{aligned} \tag{E.11}$$

E.1.5. Added mass subtool validation

Based on the experiments of the Vugts [23], the added mass subtool is verified. Below, four graphs are presented which show the validity of the program. On the left, the experimental data found by Vugts is presented, on the right the prediction by the subtool. The first row presents the sway motion, the second the sway motion. Rotational motions could not be validated as the three dimensional structure cannot be appropriately schematised using the work of Vugts.

For sway motion, a B/T ratio (width / draught) equal to eight represents the Palmerah Tidal Bridge most closely. Therefore, these data points will be compared. For the heave motion, the B/T = 2 comes closer to reality. It can be noted that the frequency constant added mass estimation by the subtool represents the frequency dependent added mass value of Vugts very well for heave. For sway, it only comes close on the right-hand side of the graph. For the Palmerah Tidal Bridge design, which has a width of 34 meters, high x-axis values will be found, meaning that the subtool creates a suitable approximation.

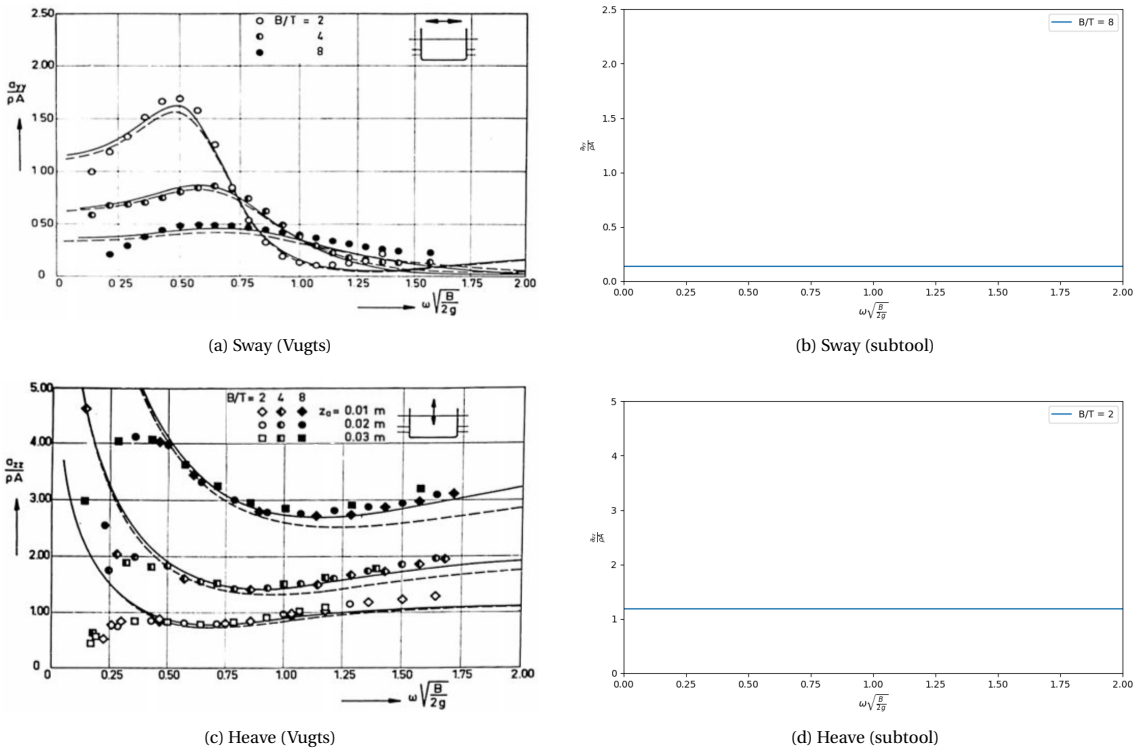

(a) Sway (Vugts)

(b) Sway (subtool)

(c) Heave (Vugts)

(d) Heave (subtool)

Figure E.1: Comparison between experimental data by Vugts and the subtool for added mass in sway and heave [23]

E.1.6. Radiation damping subtool validation

For the validation of the radiation damping subtool, the same strategy is used as was done for the added mass. Below, four graphs are presented comparing the experimental results of Vugts with the results of the subtool. It should be noted that the core of the subtool is based on Vugts' work, meaning that similarities in the results mean that the model works as it is expected to. Again, the sway motion is best represented using the ratio B/T = 8, for heave this ratio is set to B/T = 2.

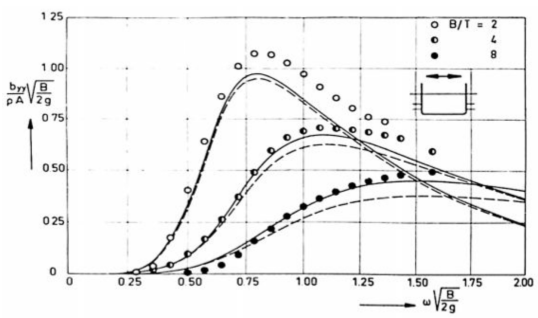

(a) Sway (Vugts)

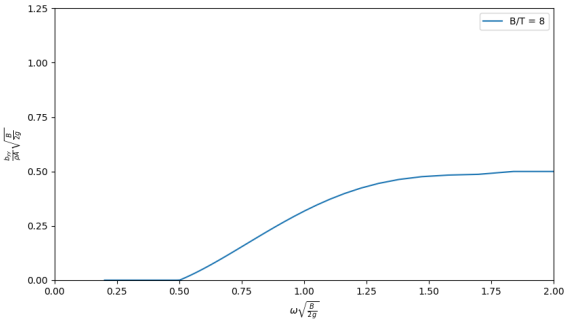

(b) Sway (subtool)

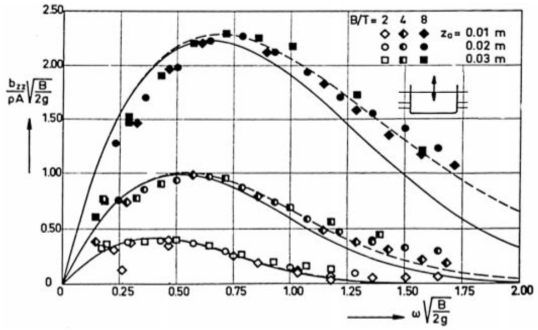

(c) Heave (Vugts)

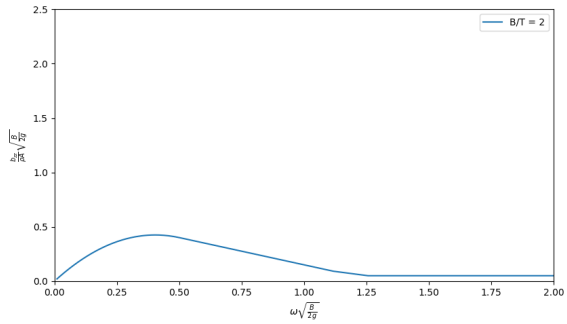

(d) Heave (subtool)

Figure E.2: Comparison between experimental data by Vugts and the subtool for radiation damping in sway and heave [23]

E.2. Forcing tool

The forcing tool is separated into various subtools, all representing a single type of force. The subtools are: the pendulum drag subtool, the turbine subtool, the wind subtool, the floater drag subtool, and the wave subtool. The four subtools are elaborated below.

E.2.1. Pendulum drag subtool verification

The subtool discussed in this subsection estimates the drag on the pendulums. It is assumed that 50 percent of this drag force is transferred to the segments. To simplify the model and to neglect complex motion, it is also assumed that the pendulums are static. The subtool is invoked using the settings shown in Table E.5.

Setting	**Value**
iteration_step	0 -
Segments	3 -
steps	1 -
Length_segment	100 m
free_space_between_segments	1 m
characteristics_small_floater	[2, 3.5, 34] -, m, m
Length_Pendulum	[20, 20, 30, 30] m
Angle_Pendulum	$[35, 35, 40, 40]/180 \cdot \pi$ rad
Pendulum_hinge_top_location	[6.5, −7.2] m
flow_velocity	4.5 m/s
Three_Dimensional_Calculation	$True$

Table E.5: Pendulum drag verification settings

Results show as follows for the middle segment:

$$\boldsymbol{F}_t = \begin{bmatrix} 0 \\ 146,109 \\ 0 \\ 1,051,982 \\ 0 \\ 2,032,654 \end{bmatrix} \text{ N(m)} \tag{E.12}$$

These values can be confirmed using the following hand calculation:

$$\begin{aligned} F_y &= \frac{1}{2} \cdot \left(\frac{1}{2} \cdot \rho \cdot (0.8 \cdot \sin(\alpha_1) + 0.2) \cdot (D_1 \cdot L_1 \cdot \sin(\alpha_1)) \cdot u \cdot |u| \right) \\ &\quad + \frac{1}{2} \cdot \left(\frac{1}{2} \cdot \rho \cdot (0.8 \cdot \sin(\alpha_2) + 0.2) \cdot (D_2 \cdot L_2 \cdot \sin(\alpha_2)) \cdot u \cdot |u| \right) \\ &= \frac{1}{2} \cdot \left(\frac{1}{2} \cdot 1025 \cdot \left(0.8 \cdot \sin(\frac{35 \cdot \pi}{180}) + 0.2 \right) \cdot \left(1,320 \cdot 20 \cdot \sin(\frac{35 \cdot \pi}{180}) \right) \cdot 4.5 \cdot |4.5| \right) \\ &\quad + \frac{1}{2} \cdot \left(\frac{1}{2} \cdot 1025 \cdot \left(0.8 \cdot \sin(\frac{40 \cdot \pi}{180}) + 0.2 \right) \cdot \left(1.320 \cdot 30 \cdot \sin(\frac{40 \cdot \pi}{180}) \right) \cdot 4.5 \cdot |4.5| \right) \\ &= 51,770 + 94,338 = 146,109 \end{aligned} \tag{E.13}$$

$$\begin{aligned} M_x &= -F_h \cdot z \\ &= -146,109 \cdot -7.2 = 1,051,982 \end{aligned}$$

$$\begin{aligned} M_z &= -F_{h_1} \cdot d_p + F_{h_2} \cdot d_p \\ &= -51,770 \cdot 47.75 + 94,338 \cdot 47.75 \\ &= 2,032,654 \end{aligned}$$

This combination of settings, and all others tested, are correct according to the hand calculations.

E.2.2. Turbine subtool verification

The turbine subtool is a relative simple subtool, as it does not calculate the forcing based on the design of a turbine. The turbine specifications of the current design for the Palmerah Tidal Bridge specify the maximum allowable force for a steady bridge. This force is re-scaled for different flow velocities and includes the horizontal movement of the bridge itself. As the the turbines are placed at a very low z-coordinate, roll movement of the entire bridge is effectively sway motion for the turbines. Therefore, roll movement is included as well. Input of the settings into this subtool is shown in Table E.6.

Setting	**Value**
iteration_step	0 -
xdot_list	[0, 0, 0, 0, 0, 0] m/s or rad/s
Segments	1 -
steps	1 -
z_location_turbines	-15 m
Max_Turbine	[$4 \cdot 2,080,000$, 4.5] N, m/s
flow_velocity	4.5 m/s
Three_Dimensional_Calculation	$True$

Table E.6: Turbine force verification settings

$$\boldsymbol{F}_t = \begin{bmatrix} 0 \\ 8.320 \cdot 10^6 \\ 0 \\ 1.248 \cdot 10^8 \\ 0 \\ 0 \end{bmatrix} \text{ N(m)} \tag{E.14}$$

For this maximum flow velocity of 4.5 meters per second, the horizontal force was already given to be equal to 2080 kN per turbine. As four turbines are present per segment, a force of 8320 kN per segments should come as no surprise. The bending moment equals the force multiplied with the arm, being 15 meter in this test. The torque of 124,800 kNm.

When the turbine force is scaled to other flow velocities, a quadratic relation should appear. Figure E.3 shows this relation. Again, a horizontal motion induced by sway or roll equal to the flow velocity should bring the horizontal force to zero. Tests show that the model does this correctly.

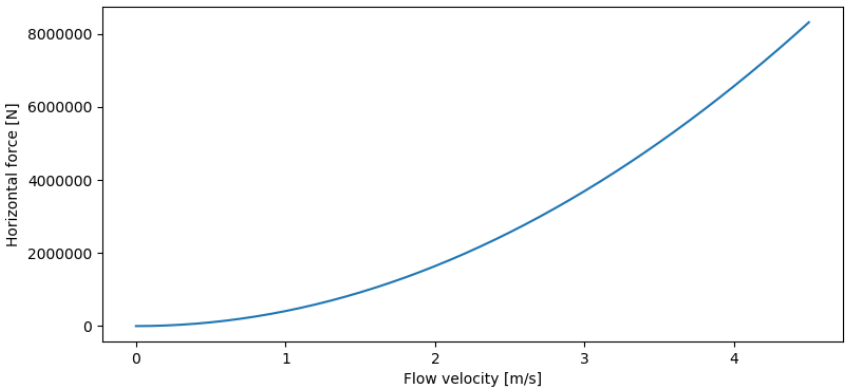

Figure E.3: Horizontal turbine force as function of flow velocity

E.2.3. Wind subtool verification

Wind forces are considered to be constant forces, making the wind subtool simple. Still, it has been separated into two parts: the force on the deck, and the force on the super structure. This is since the Indonesian law proposes two different distributed forces on these elements. For wind on the super structure, this load has been set to 3000 N/m, for the deck it has been set to 2120 N/m. A verification test has been performed on the combination of these two loads using the input as presented in Table E.7. The results are presented in Equation (E.15).

Setting	**Value**
Segments	1 -
steps	1 -
Length_segment	100 m
z_location_deck	8.5 m
z_location_Super_Structure	3 m
Wind_Distribution_deck	2120 N/m
Wind_Distribution_Super_Structure	3000 N/m
Three_Dimensional_Calculation	$True$

Table E.7: Wind force verification settings

$$\boldsymbol{F}_w = \begin{bmatrix} 0 \\ 512000 \\ 0 \\ -2702000 \\ 0 \\ 0 \end{bmatrix} \text{N(m)} \tag{E.15}$$

A simple hand calculation shows that the horizontal force is correct, as a length of 100 meters multiplied 5120 N/m (3000 + 2120) results in the shown horizontal force. The torque can be calculated and verified as follows below:

$$\begin{aligned} q_w &= -F_{deck} \cdot z_{deck} - F_{ss} \cdot z_{ss} \\ &= -2120 \cdot 100 \cdot 3 - 3000 \cdot 100 \cdot 8.5 \\ &= -2702000\ Nm \end{aligned} \tag{E.16}$$

E.2.4. Floater drag subtool verification and validation

The drag force on the floaters is mainly a function of the draught. As the draught changes over time, this force cannot be taken as a constant. The torque created by this drag force is dependent on the draught squared, as the force is linearly dependent on the draught and the arm of the torque decreases with increasing draught. Extra complications are found as the drag force is a function of relative velocity. As the structure moves horizontally, this should be taken into account as well. Table E.8 shows the settings used to invoke the subtool. After that, Equation (E.17) shows the output.

Setting	**Value**
iteration_step	0 -
x_list	[0,0,0,0,0,0] m or rad
xdot_list	[0,0,0,0,0,0] m/s or rad/s
Segments	1 -
steps	1 -
characteristics_small_floater	[2, 3.5, 34] -, m, m
characteristics_large_floater	[3, 5, 34] -, m, m
M_segment	2320000 kg
C_drag_pointed_rectangle	0.8 -
z_location_bottom_floater	−8 m
Tidal_level	0 m
flow_velocity	1025 m/s
rho	1025 kg/m^3
Wave_hlp	[0, 90, 7.5] m, m, s
depth	18 m
Wave_Force	$True$
Three_Dimensional_Calculation	$True$

Table E.8: Floater drag verification settings

$$\boldsymbol{F}_{d,f} = \begin{bmatrix} 0 \\ 510,400 \\ 0 \\ 3,370,085 \\ 0 \\ 0 \end{bmatrix} \text{ N(m)} \tag{E.17}$$

With the presented settings, the draught can be expected to be about 2.8 meter. Hand calculations will show the following force and moment, which give answers of the same size.

$$\begin{aligned} F_{d,fl} &= \frac{1}{2} \cdot A \cdot C_d \cdot \rho \cdot u^2 \\ &= \frac{1}{2} \cdot (2.8 \cdot (3 \cdot 5 + 2 \cdot 3.5)) \cdot 0.8 \cdot 1025 \cdot 4.5^2 \\ &= 511,434\ N \\ M_{d,fl} &= F_{d,fl} \cdot z \\ &= 511,434 \cdot \left(8 - \frac{2.8}{2}\right) \\ &= 3,375,464\ Nm \end{aligned} \tag{E.18}$$

Extreme cases can be used to verify the model: the drag force should be zero when the vertical displacement is equal to the draught, and when the horizontal velocity of the segment is equal to the flow velocity. If the floater is fully emerged, a drag coefficient of zero is expected to be found. All appear to be correct.

When waves are added to the calculation, the flow velocity is evaluated halfway the tips. It is assumed that the front tip and back tip contribute to the drag coefficient equally. Although this is hard to validate, drag values for triangles and a rotated square show this characteristic. The evaluated long rectangles with tips will also experience drag on the long side, this is neglected as well. See Figure E.4 for an illustration of this. In an example calculation, the wave height has been set to 1 meter, the flow velocity was still set to 4.5 m/s. The following output was found:

$$\boldsymbol{F}_{d,fl} = \begin{bmatrix} 0 \\ 563,532 \\ 0 \\ 3,688,389 \\ 0 \\ 0 \end{bmatrix} \text{N(m)} \tag{E.19}$$

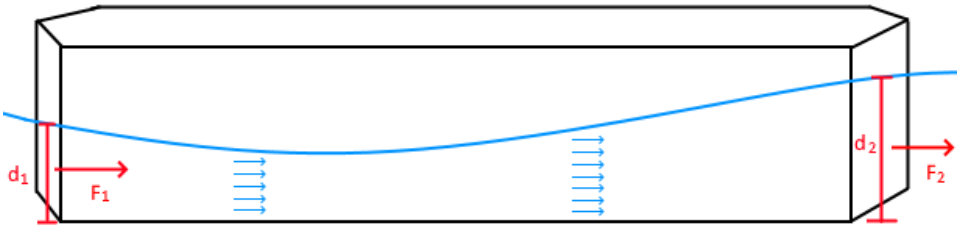

Figure E.4: Drag evaluated halfway the points of the floaters

First, it should be noted that small waves can contribute significantly to the forces. In this example, the forces rises with about 10 per cent. The waves contribute in two ways: they increase/decrease the local draught, and increase/decrease the particle velocity. The combination of these two effects may result in significant change sin force, especially for larger waves.

Now, the presented force can be calculated using the equations below. For simplicity, the integral is evaluated to z=0.1 m, as the local water level during t=0 with the presented wave settings is very close to that specific value. The presented equations is simplified, as it only calculated for the large floaters using Airy waves. This will initiate a small mistake.

$$\begin{aligned} F &= \frac{1}{4} \cdot C_{DS} \cdot d \cdot \left(N_{fl,s} \cdot W_{fl,s} + N_{fl,l} \cdot W_{fl,l}\right) \cdot \rho \cdot \left(\frac{\int_{-d}^{0.1} u_y(18.25)\ z}{d+0.1} \right)^2 \\ &\quad + \frac{1}{4} \cdot C_{DS} \cdot d \cdot \left(N_{fl,s} \cdot W_{fl,s} + N_{fl,l} \cdot W_{fl,l}\right) \cdot \rho \cdot \left(\frac{\int_{-d}^{0.1} u_y(-18.25)\ z}{d+0.1} \right)^2 \\ &= 2 \cdot 277,590 \\ &= 555,181 \text{ N} \end{aligned} \tag{E.20}$$

Where:

$$u_y(y) = \omega \cdot a \cdot \frac{\cosh\left(k \cdot (d+z)\right)}{\sinh(k \cdot d)} \cdot \cos(\omega \cdot t - k \cdot y) \tag{E.21}$$

As similar results are found for this case, but also for all other cases tested, the model is verified. Drag forces on the floaters have been validated simultaneously with the inertia force on the floater, which is to be discussed below:

E.2.5. Floater inertia subtool verification and validation

The wave subtool is the most complex, and most likely the most important subtool of the forcing. Although forces may not be the highest, the oscillating motion can excite the structure close to its natural frequency. The subtool in this verification is invoked using the presented value in Table E.9. The value for iteration step has been looped, to obtain the graphs presented below the table. Every graph contains four lines, for the four different grid-sizes that are tested. The computation has been executed for three different wave periods, varying from relative short waves to relative long waves. As the M_added matrix to large to present in the table in a practical way, and it also depends on the frequency, it has been left out from the settings below. For the computation of this matrix, the Ansys results from Hoogsteder [57] have been used.

Setting	**Value**
iteration_step	i -
Total_time	3 / 6 / 9 s
x_list	[0, 0, 0, 0, 0, 0] m
xddot_list	[0, 0, 0, 0, 0, 0] m
segments	1 -
steps	41 -
characteristics_small_floater	[2, 3.5, 34] -, m, m
characteristics_large_floater	[3, 5, 34] -, m, m
M_segment	2,320,000 kg
z_location_bottom_floater	−7 m
Tidal_level	0 m
Wave_hlp	[1, $10 \cdot Total\_time$, $Total\_time$] m, m, s
depth	18 m
rho	1025 kg/m^3
g	9.8 m/s^2
M_added	[6x6] kg
gridsize	0.125x0.125 / 0.25x0.25 / 0.5x0.5 / 1x1 m
Three_Dimensional_Calculation	$True$

Table E.9: Wave force verification settings

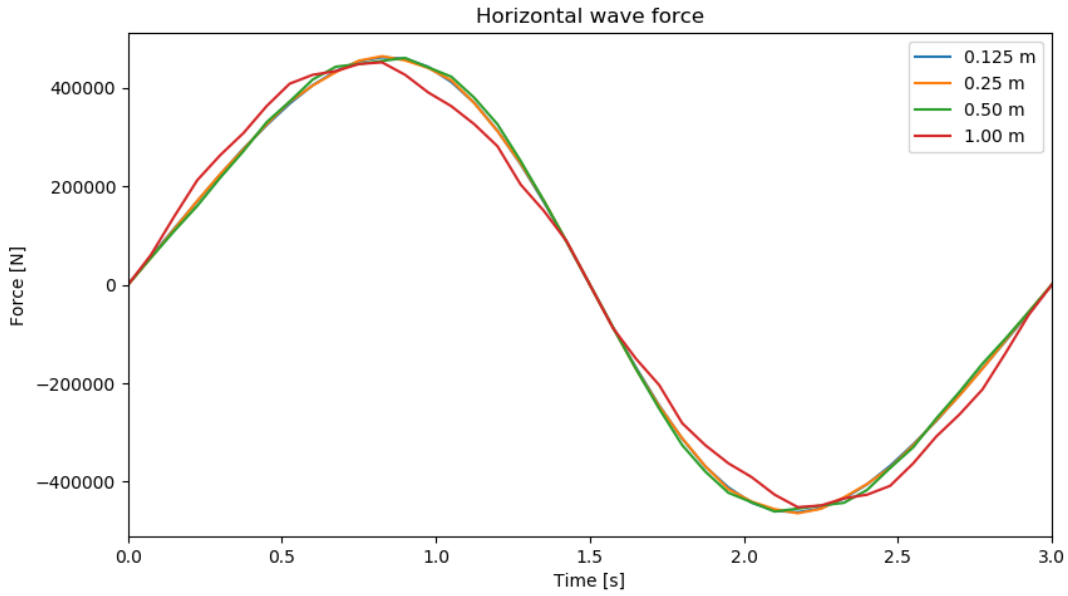

Figure E.5: Horizontal force with wave period of 3 seconds for various square grids

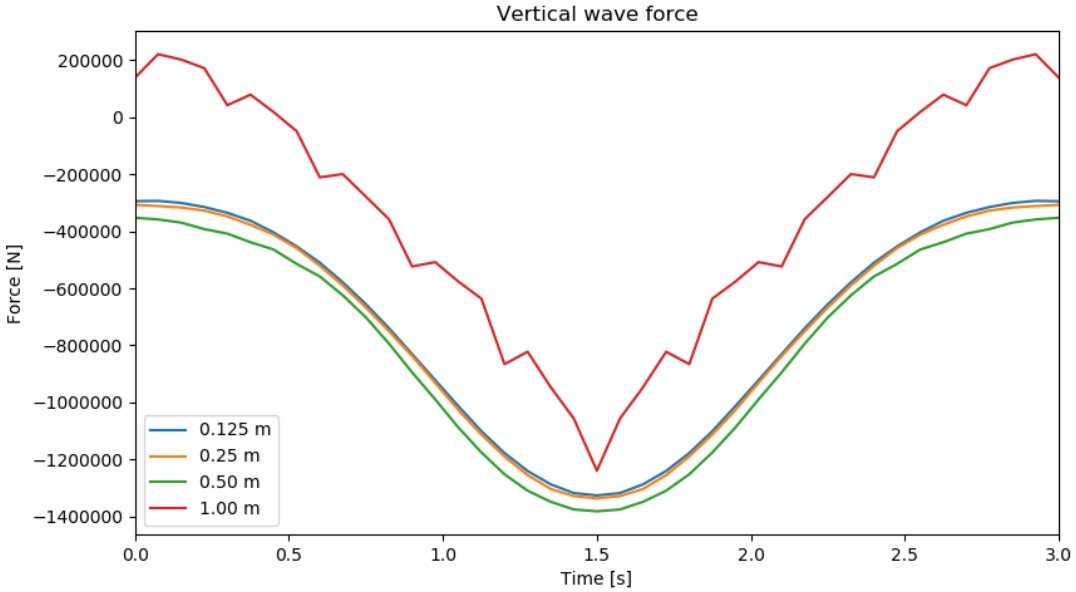

Figure E.6: Vertical force with wave period of 3 seconds for various square grids

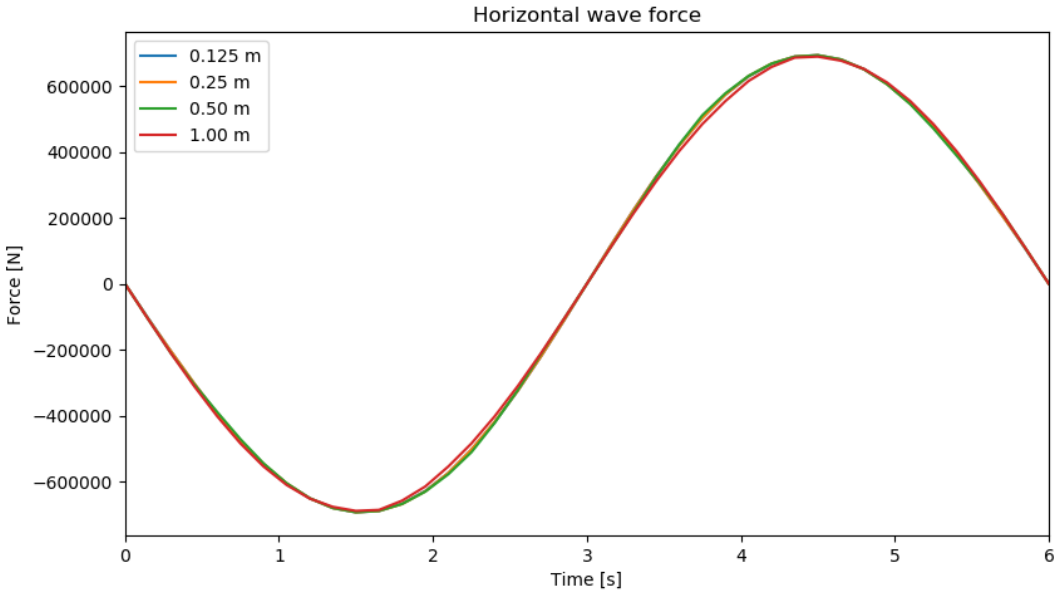

Figure E.7: Horizontal force with wave period of 6 seconds for various square grids

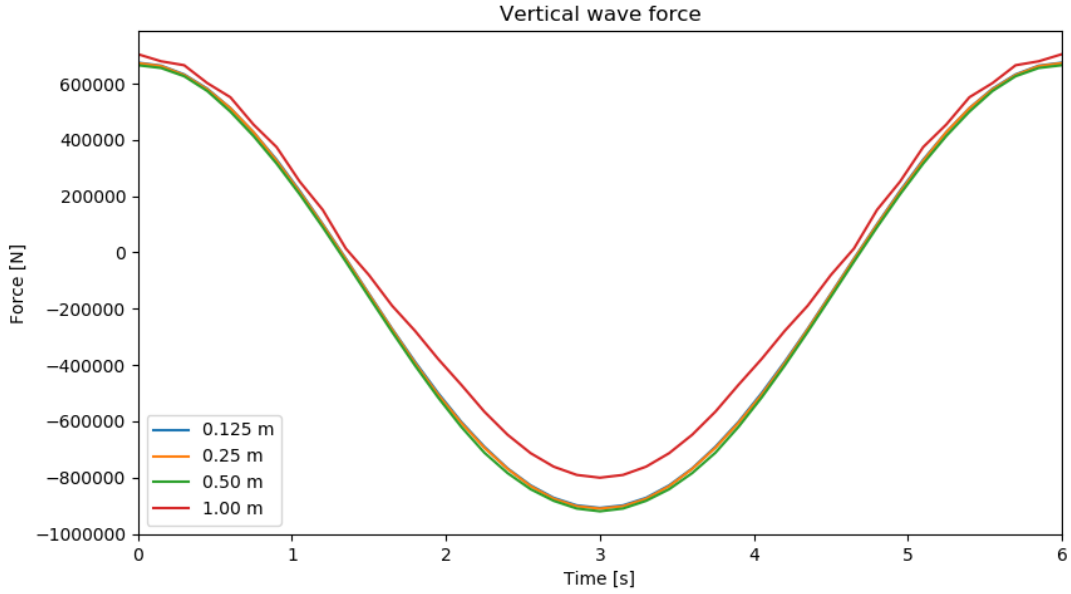

Figure E.8: Vertical force with wave period of 6 seconds for various square grids

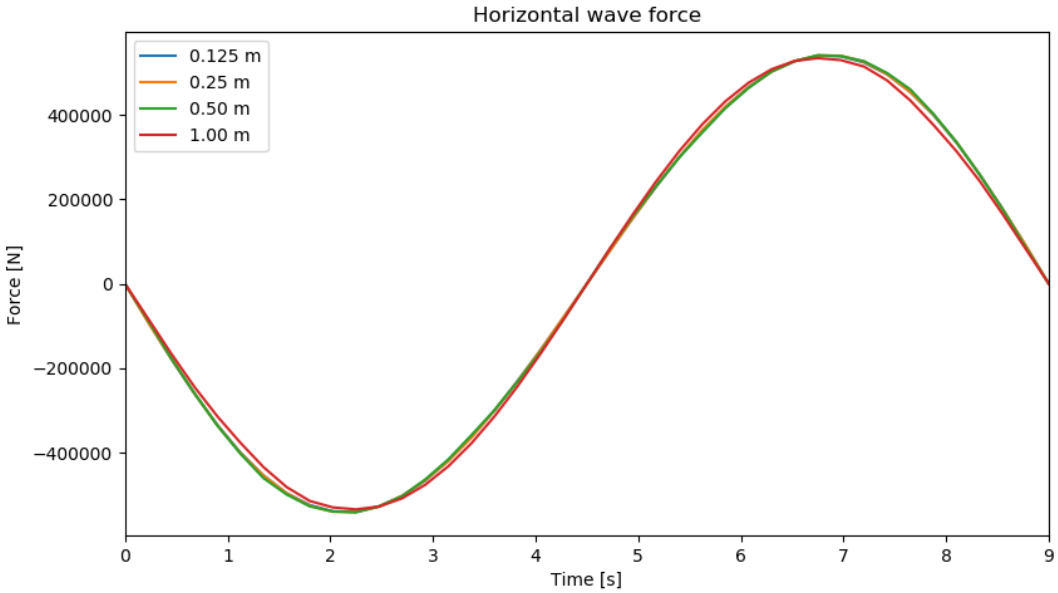

Figure E.9: Horizontal force with wave period of 9 seconds for various square grids

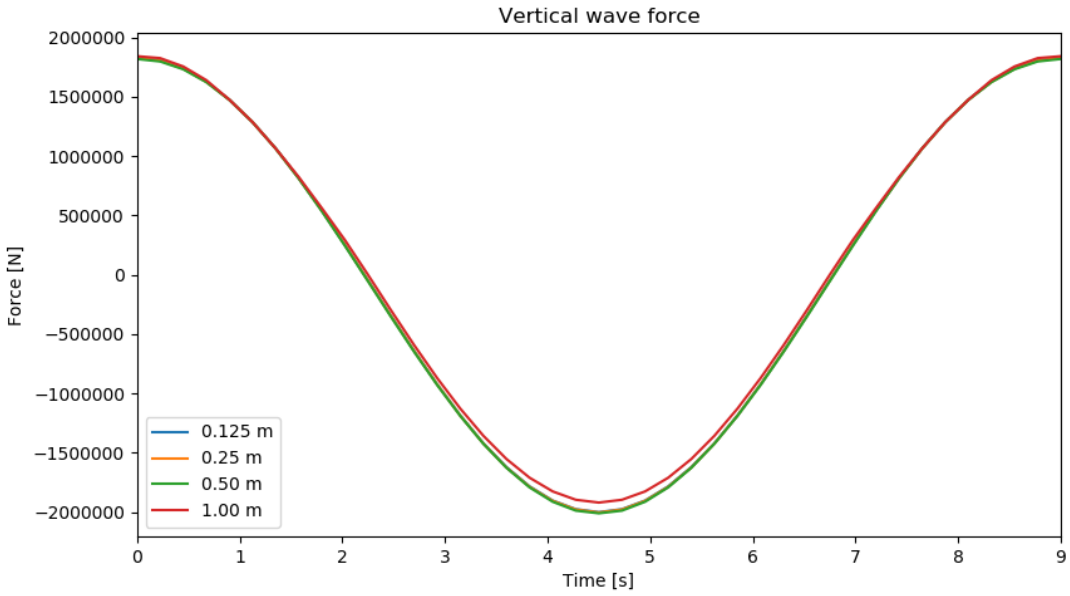

Figure E.10: Vertical force with wave period of 9 seconds for various square grids

It can be noted that for especially the short waves, large gridsizes create significant errors. Because of this, it is recommended to use a gridsize of 0.25 m or smaller. More research into the needed gridsize is shown in Appendix J.

Hand calculations for simple cases confirm the results of the subtool. In the hand calculations, small errors will be found as the pointed tips of the floaters are ignored, movement of the floater is ignored, and only the Airy waves are taken into account, meaning that the second order correction is neglected. As especially the former simplification results in significant differences, the pointed tips had been temporarily disabled in the subtool. For various moments in time, horizontal forces and vertical forces are determined, by integrating the particle acceleration over the wetted volume of the floaters. This can be represented with the following two equations:

$$\begin{aligned} F_y(t) &= \int_{-L/2}^{L/2}\int_{-d}^{a\cdot\cos(\omega\cdot t-k\cdot y)}\int_{-b}^{b} \frac{\delta u_y}{\delta t}\cdot C_{a,y}\cdot\rho\, dx\, dy\, dz \\ F_z(t) &= \int_{-L/2}^{L/2}\int_{-d}^{a\cdot\cos(\omega\cdot t-k\cdot y)}\int_{-b}^{b} \frac{\delta u_z}{\delta t}\cdot C_{a,z}\cdot\rho\, dx\, dy\, dz \\ &\quad + \int_{-L/2}^{L/2}\int_{-b}^{b} \rho\cdot g\cdot a\frac{\cosh(k\cdot(d-d_r))}{\cosh(k\cdot d)}\cos(\omega\cdot t-k\cdot y)\, dx\, dy \end{aligned} \tag{E.22}$$

Torque due to the wave forces can simply be found by integrating the found results over the distance to the COG. The results for the three wave lengths and corresponding wave periods at various time intervals are shown in Table E.10 and Table E.11. The values in the tables are similar to what was calculated in the hand calculations. This is not only the case for the present settings, but also when the wave height is varied, the depth is altered, or other parameters are changed.

Wave		**Time interval**				
Length	**Period**	**0 s**	**T/8 s**	**T/4 s**	**T/2 s**	**T s**
30 m	3 s	0 N	276,468 N	454,320 N	0 N	0 N
60 m	6 s	0 N	−476,496 N	−693,776 N	0 N	0 N
90 m	9 s	0 N	−400,234 N	−540,387 N	0 N	0 N

Table E.10: Verification of horizontal forces by waves

Wave		Time interval				
Length	**Period**	**0 s**	**T/8 s**	**T/4 s**	**T/2 s**	**T s**
30 m	3 s	−278,641 N	−358,605 N	−650,938 N	−1,326,770 N	−278,642 N
60 m	6 s	671,910 N	425,683 N	−146,251 N	−904,430 N	754,111 N
90 m	9 s	1,825,932 N	1,285,302 N	−47,040 N	−1,997,870 N	1,825,932 N

Table E.11: Verification of vertical forces by waves

As should be expected, horizontal wave force is zero when the crest or trough of a wave is exactly below the COG of the segment. Maximum forces are found about a quarter of a wave period earlier or later. for vertical forces, similar effects are found. Here, the maximum forces are found when the crest or trough is directly below the COG. Forces equal to zero are found about a quarter of a wave period earlier or later. For both the hand calculation and the numerical approximation, it can be observed that the vertical force and the horizontal force are out of phase by a quarter. These results are expected as this is defined by the wave theory used.

Horizontal displacement of the segments will result in a time-shift of the wave force, as the waves no need to travel further / less far. To verify the working of this element in the subtool, a constant horizontal displacement in y-direction has been entered. It was noted that the force as function of time was shifted, as was expected. sThis subtool, and the previously discussed subtool, are validated using the work of Pan et al. [58], whom did research into the wave current force on bridge foundations. Research has been done regarding the wave forcing on square and rectangular (1:2) bridge piers. Below, the results are compared between their experimental work (dashed line) and the wave force according to the subtools (red line). It should be noted that for kd values larger than 3.5, the method used in the subtools is not entirely valid. This is because the diameter-wavelength ratio becomes larger than 0.2, making the Morison equation faulty. For lower kd values, the lines show similar values.

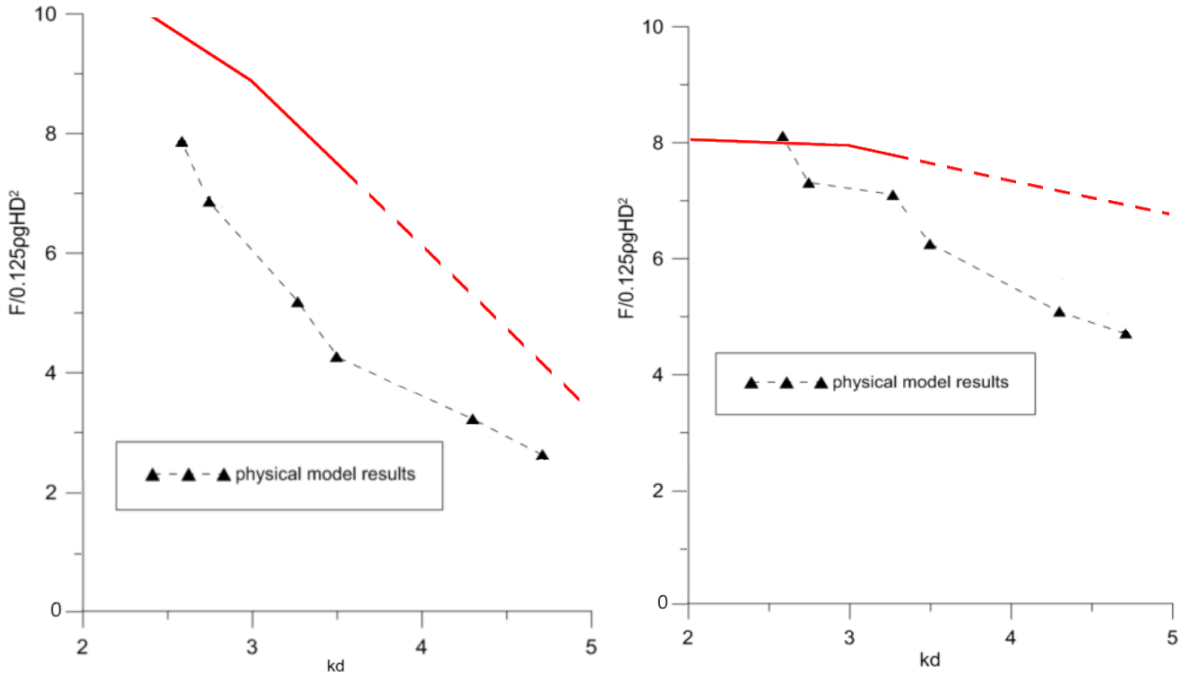

(a) Rectangular (2:1) bridge pier

(b) Square bridge pier

Figure E.11: Comparison between wave forces on bridge piers according to Pen et al. (dashed black line) and the subtools (red line)

.

E.3. Dynamic tool

The dynamic tool is also separated into subtools: one being able to calculate the acceleration and to predict the velocity and location at the next timestep, the other being able to calculate the natural frequencies of the system. The former subtool is embedded in the model at every time step, the latter is only invoked once to

find relevant information the structure.

E.3.1. Movement subtool verification

This subtool is solely based on the famous second law of Newton: F=m*a. By knowing the force and the mass, the acceleration can be found. It then integrates this acceleration to find the velocity. A second integral finds the location. To verify whether the subtool is functional, a classic literature example is used: a two dimensional mass-damper-spring system. For visual guidance, see Figure E.12.

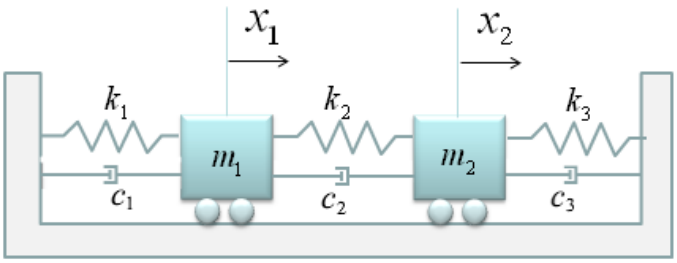

Figure E.12: Example for verification of dynamic scheme [59]

The structure can be modelled using the equation below:

$$\begin{bmatrix} m_1 & 0 \\ 0 & m_2 \end{bmatrix} \begin{bmatrix} \ddot{x_1} \\ \ddot{x_2} \end{bmatrix} + \begin{bmatrix} c_1 + c_2 & -c_2 \\ -c_2 & c_2 + c_3 \end{bmatrix} \begin{bmatrix} \dot{x_1} \\ \dot{x_2} \end{bmatrix} + \begin{bmatrix} k_1 + k_2 & -k_2 \\ -k_2 & k_2 + k_3 \end{bmatrix} \begin{bmatrix} x_1 \\ x_2 \end{bmatrix} = \begin{bmatrix} F_1 \\ F_2 \end{bmatrix} \tag{E.23}$$

The masses have been set to respectively 1 and 2 kilograms, the damping coefficients have been set to respeciviely 0.5, 1, and 1.5 Ns/m, spring stiffnesses to respectively 1, 2, and 3 N/m. The forcing has been set to respectively 0.5 and 1 N. Using these values, the matrix above can be reduced to:

$$\begin{bmatrix} 1 & 0 \\ 0 & 2 \end{bmatrix} \begin{bmatrix} \ddot{x_1} \\ \ddot{x_2} \end{bmatrix} + \begin{bmatrix} 0.5 & -1 \\ -1 & 1.5 \end{bmatrix} \begin{bmatrix} \dot{x_1} \\ \dot{x_2} \end{bmatrix} + \begin{bmatrix} 3 & -2 \\ -2 & 5 \end{bmatrix} \begin{bmatrix} x_1 \\ x_2 \end{bmatrix} = \begin{bmatrix} 0.5 \\ -1 \end{bmatrix} \tag{E.24}$$

The following initial conditions apply:

$$\begin{aligned} x_1 &= 0 \\ x_2 &= 0 \\ \dot{x_1} &= 0 \\ \dot{x_2} &= 0 \end{aligned} \tag{E.25}$$

Solving the equations analytically using maple, and finding the solution according to the subtool results in the following two graphs:

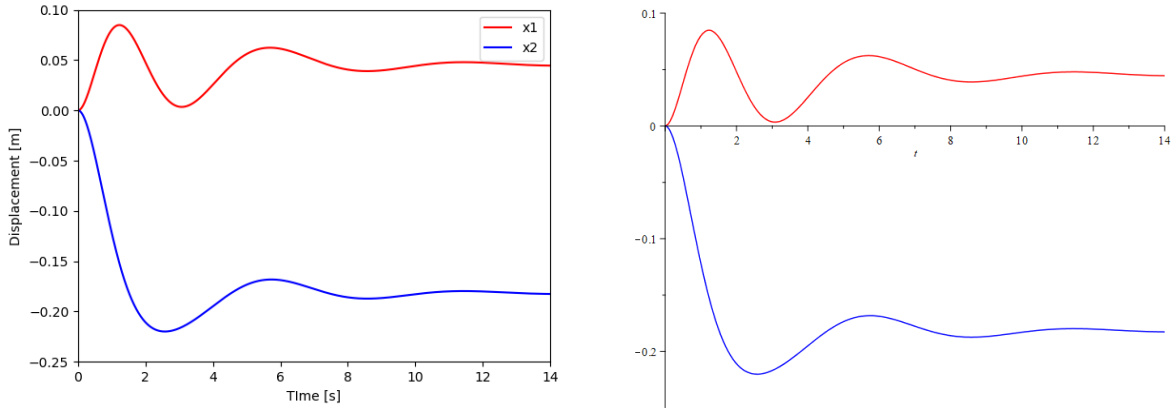

(a) Subtool results

(b) Maple result

Figure E.13: Result comparison between the numerical subtool and the analytical equation according to Maple

For these settings, and for all other tested settings, the analytical solution confirms that the subtool is working appropriately.

One numerical instability in the subtool is known. When during the forcing of wave, the floater comes close to the water surface level, the used timestep is too large. As a result, oscillations are starting to build up in longitudinal pendulum direction. This numeric instability can be prevented by examining the jerk, being the derivative of the acceleration. This method is able to spot and filter the instability before it influences the results notably.

E.3.2. Pendulum angle subtool verification

This subtool updates the current angle of all pendulums, as function of the tidal level and the current displacement of the segment. This is simply done by using the predefined location of the bottom hinge of the pendulums, calculating the new position of the upper hinge and using the basic geometry to find the angle.

E.3.3. Natural frequencies subtool verification

The natural frequency subtool, programmed using only 8 lines of code, can be verified using the same set of equations. Both the analytical solution and what was found using the subtool, result in the natural frequencies as shown below. The subtool works as expected.

$$\boldsymbol{f_n} = \begin{bmatrix} 2.046 \\ 1.146 \end{bmatrix} \text{ rad/s} \tag{E.26}$$

F

Added mass determination

In this appendix, the added mass of the structure will be evaluated. In here, the data presented in Subsection 3.2.2 will be used to find the magnitude of the added mass based on literature. After this, the obtained values will be compared with a simulation in Ansys Aqwa, which is able to find the added mass and radiation damping based on the Greene's function.

F.1. Hand calculations

A section of the complete added mass matrix due to the floaters has been shown in equation (F.1).

$$\boldsymbol{M}_{added} = \begin{bmatrix} \ddots & & & & & & \\ & 0 & 0 & 0 & 0 & 0 & 0 \\ & 0 & a & 0 & b & 0 & 0 \\ & 0 & 0 & c & 0 & 0 & 0 \\ & 0 & b & 0 & d & 0 & 0 \\ & 0 & 0 & 0 & 0 & e & 0 \\ & 0 & 0 & 0 & 0 & 0 & f \\ & & & & & & \ddots \end{bmatrix} \tag{F.1}$$

Where:

$$\begin{aligned} a &= C_{tip} \cdot \left(N_{fl,s} \cdot C_{a,s,h} \cdot 2 \cdot d \cdot W_{fl,s} \cdot L_{fl,s} \cdot \rho_m + N_{fl,l} \cdot C_{a,l,h} \cdot 2 \cdot d \cdot W_{fl,l} \cdot L_{fl,l} \cdot \rho_m\right) \\ b &= \left(C_{tip} \cdot \left(N_{fl,s} \cdot C_{a,s,h} \cdot 2 \cdot d \cdot W_{fl,s} \cdot L_{fl,s} \cdot \rho_m + N_{fl,l} \cdot C_{a,l,h} \cdot 2 \cdot d \cdot W_{fl,l} \cdot L_{fl,l} \cdot \rho_m\right)\right) \cdot (-z_t - 0.5 \cdot d) \\ c &= N_{fl,s} \cdot L_{fl,s} \cdot C_{a,s,v} \cdot \pi \cdot (W_{fl,s}/2)^2 \cdot \rho_m + N_{fl,l} \cdot L_{fl,l} \cdot C_{a,l,v} \cdot \pi \cdot (W_{fl,l}/2)^2 \cdot \rho_m \\ d &= C_{inf} \cdot \pi \cdot \rho_m \cdot \left(\int_{-L_{fl,s}/2}^{L_{fl,s}/2} N_{fl,s} \cdot C_{a,s,v} \cdot (W_{fl,s}/2)^2 \cdot y \, dy + \int_{-L_{fl,l}/2}^{L_{fl,l}/2} N_{fl,l} \cdot C_{a,l,v} \cdot (W_{fl,l}/2)^2 \cdot y \, dy\right) \\ e &= N_{fl,s} \cdot C_{a,s,v} \cdot L_{fl,s} \cdot \pi \cdot (W_{fl,s}/2)^2 \cdot \rho_m \cdot d_{fl,s}^2 + \sum_{i=1}^{N_{fl,l}} \left(C_{a,l,v} \cdot L_{fl,l} \cdot \pi \cdot (W_{fl,l}/2)^2 \cdot \rho_m \cdot d_{fl,s,i}^2\right) \\ f &= C_{tip} \cdot \left(N_{fl,s} \cdot C_{a,s,h} \cdot 2 \cdot d \cdot W_{fl,s} \cdot L_{fl,s} \cdot \rho_m \cdot d_{fl,s}^2 + \sum_{i=1}^{N_{fl,l}} \left(C_{a,l,h} \cdot 2 \cdot d \cdot W_{fl,l} \cdot L_{fl,l} \cdot \rho_m \cdot d_{fl,s,i}^2\right)\right) \end{aligned} \tag{F.2}$$

In the formulations in Equation (F.2), two corrections are made. C_{tip} represents the reduction in added mass during horizontal movement of floaters (either sway or yaw) of the pointed floaters compared to their cuboid counterpart. Using a pointing angle of 45 degrees, it can be estimated that this coefficient will be approximately 0.8. This estimation is based on the difference in drag coefficient of a non-angled square and that of a 45-degree angled square [15]. For numerical comparison with the work of Hoogsteder, this factor will be taken equal to 1, as she did not include the pointed tips in her analysis.

As only limited data is available, approximations have been made for the rotational movements. For pitch and yaw, it has been assumed that the added mass can be adequately approximated by calculating the added mass in respectively heave and sway for a single floater, than multiplying with the distance to the COG squared (Steiners theorem).

For roll, an alternative approach has been used: the floaters have been split into multiple slices. When looking at the sketch in Figure F.1, where flow patterns under a floater are schematised, it can be observed that the flow is very similar to that of heave. As a result, the added mass equation for heave can be justified. To account for the increasing fictive 'heave velocity' due to roll as a function of distance to the COG, Steiner"s theorem is applied again. For a schematising of this method, see Figure F.2. As the heave assumption is not entirely valid for the outer slices, as the flow pattern will not be mainly in width direction, a correction has been added, named C_{inf}. As the outer slices will have most influence on the added mass for roll motion, this correction factor has been set to 0.7.

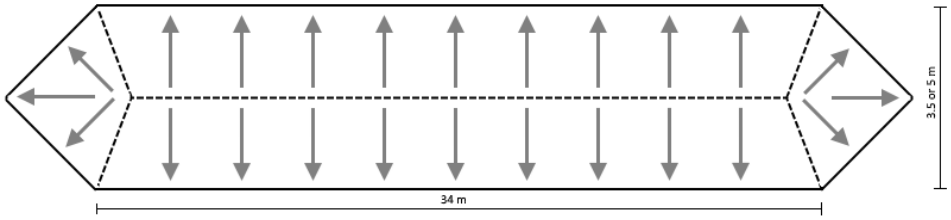

Figure F.1: Approximate direction of flow under a slender floater

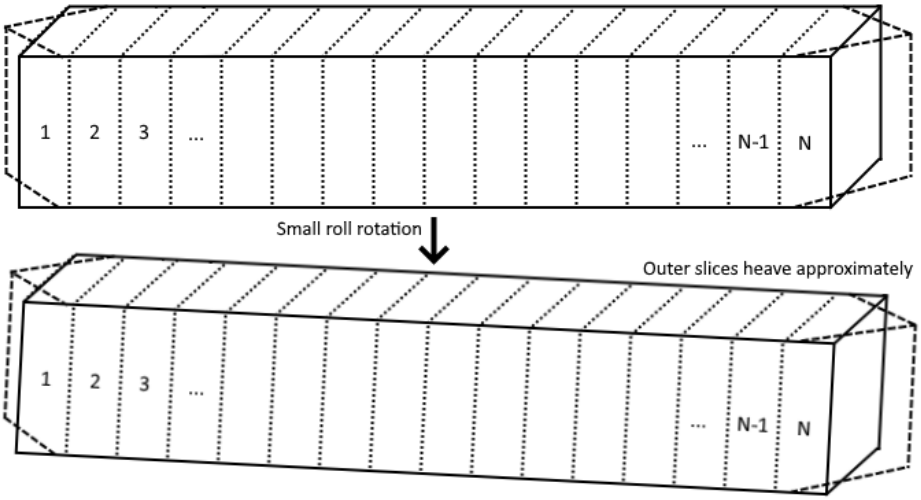

Figure F.2: Roll addded mass approximation with multiple heave slices

All equations above assume that no interaction between the degrees of freedom is present. This is a false assumption, as roll movement will push heavy water to one side and light air to the other. As a consequence, interaction between roll and sway will be severely present in the added-mass matrix. Similar results will be found for interaction between heave and roll, but this interaction will be of less magnitude.

F.2. Comparison with Ansys Aqwa

Based on these equations, values for added mass for the five considered degrees of freedom are found. These estimations are compared with the results of the work of Hoogsteder [57]. In this comparison, no pointed tips on the floaters have been taken into account, as she did not include them as well. The results are presented in Figures F.3 - F.7. As can be noted, significant deviation can be found at specific frequencies. However, the hand calculations average the Ansys Aqwa results quite accurately. As the most important natural frequencies and wave frequencies are in the order of 0.1-0.3 Hz, numerical values in this range should match narrowly. For deeper understanding in the computations of Ansys Aqwa, Appendix I forms as guide. Form the

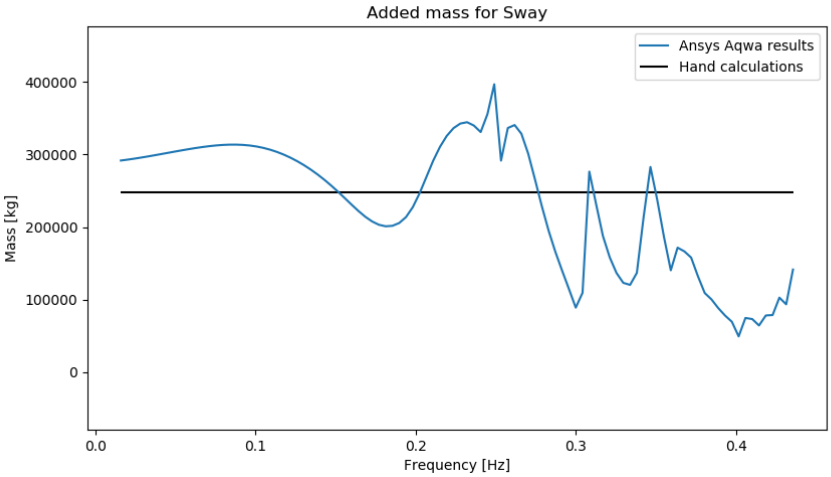

Figure F.3: Added mass comparison between hand calculations and Ansys Aqwa for sway

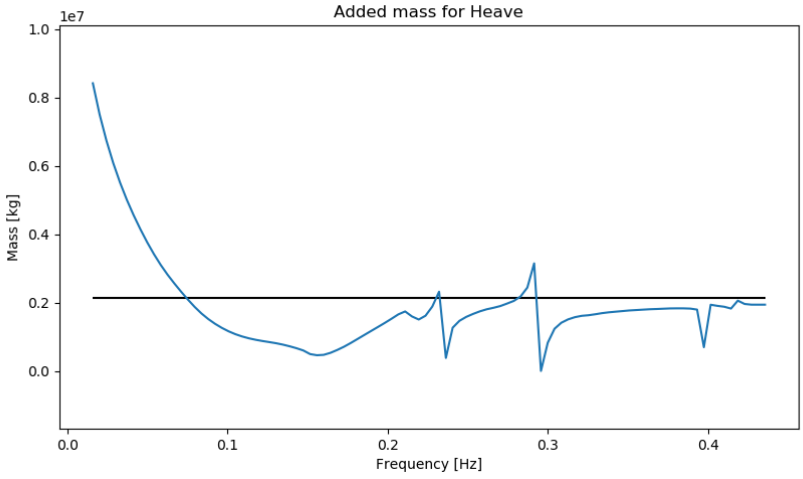

Figure F.4: Added mass comparison between hand calculations and Ansys Aqwa for heave

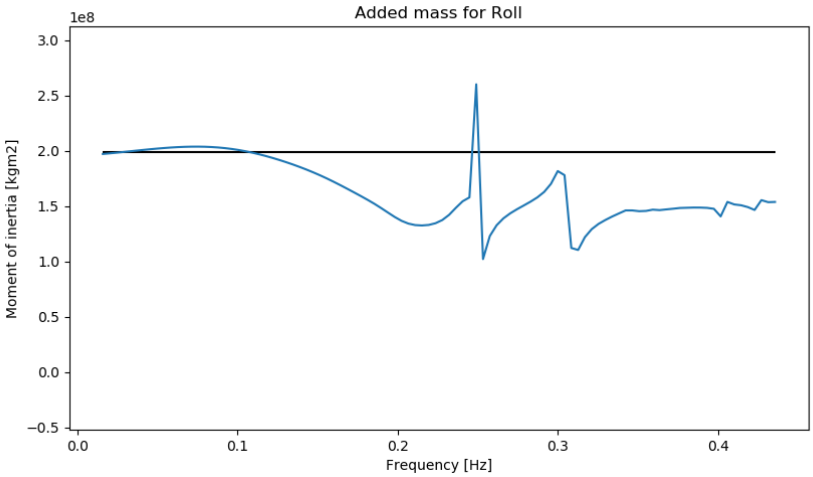

Figure F.5: Added mass comparison between hand calculations and Ansys Aqwa for roll

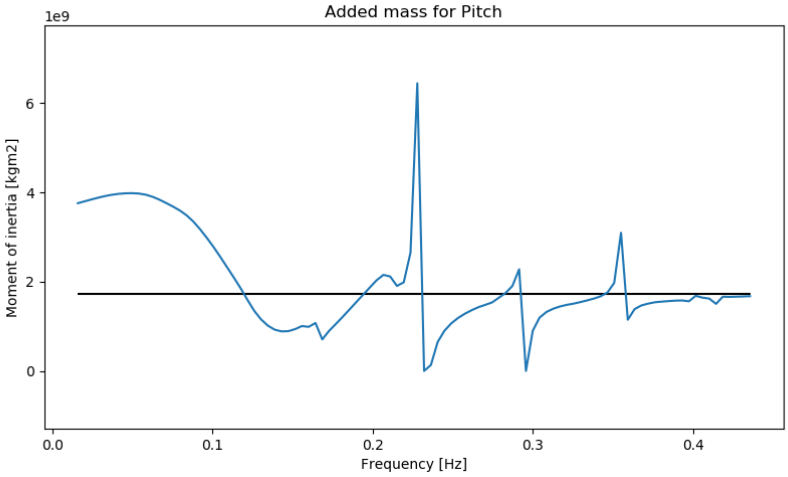

Figure F.6: Added mass comparison between hand calculations and Ansys Aqwa for pitch

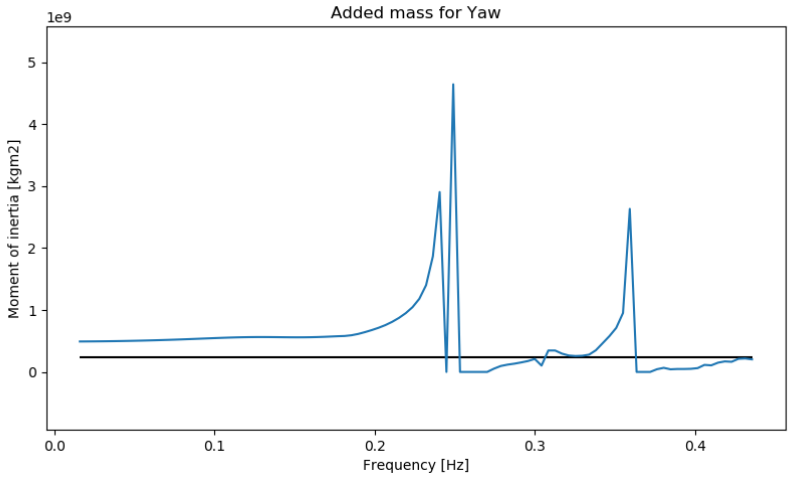

Figure F.7: Added mass comparison between hand calculations and Ansys Aqwa for yaw

F.3. Turbine influence

Many turbines experience hardly any added mass, as most of them are wind turbines. Contrarily, water turbines experience significant added mass. Murray and Colby [60] did research on the added mass effects of the Verdant Power's GEN5B horizontal-axis tidal turbine at still water. Their research recommends the use of an added mass coefficient equal to 1. Moll et all [61] confirmed this recommendation in their research on the influence of added mass on jacket mode shapes, natural frequencies and loads.

When a design is taken similar to the Andritz Hydro Hammerfest HS1000 Tidal Turbine, it is found that every turbine has a volume of about 5 m^3. The mentioned turbine has been taken as example, as it is designed for roughly the same conditions as the turbines under the Palmerah Tidal Bridge will experience. Including the connecting elements, the complete volume can be estimated to be about 7 m^3 per turbine, or 28 m^3. Using the added mass coefficient of 1, an additional weight of 28,700 kg can be added to both the y- and z-direction of the added mass matrix. For the roll movement, it is assumed that the average arm is found exactly at the midpoint of the turbine. This results in the following addition to the added mass matrix:

$$\begin{aligned} J_{added} &= M_{added} \cdot z_t^2 \\ &= 28700 \cdot 16.89^2 \\ &= 8.19 \cdot 10^6 \text{ m}^2 \end{aligned} \tag{F.3}$$

Addition of the added mass contribution of the turbine for sway, heave, and roll, increases the total added mass value with respectively 12, 1 and 4 per cent.

G

Radiation damping determination

As was done for the added mass, a hand calculations using experiments found in literature and a simulation using Ansys Aqwa will be performed for radiation damping as well. The data presented in Subsection 3.2.3 will be used in this Appendix.

G.1. Hand calculations

Using the same strategy for the determination of the magnitude of radiation damping, as has been done for the determination of the magnitude of added mass, requires information of damping coefficients based on the shape. As limited research is available, infinite long rectangles will be used, as investigated by Vegts. Using Figure 3.13, the matrix below can be constructed.

It should be noted that the coordinate system used in Figure 3.13 does not match the coordinate system used in this report. See Figure 3.4 for the difference between the two coordinate systems.

Movement in surge direction is neglected in this calculation, as movement is obstructed in that direction. Heave and sway motion could be directly extracted from the experiments from Vegts, the remaining rotations could not. Just as with the calculations for added mass, roll has been approximated by considering slices of the floaters and simulate them as heave motion (see Figure G.1. Also the calculation strategy for pitch and yaw are performed as was done for the added mass. In here, the heave and sway radiation damping of single floaters was evaluated and then transformed to the COG using Steiner's theorem.

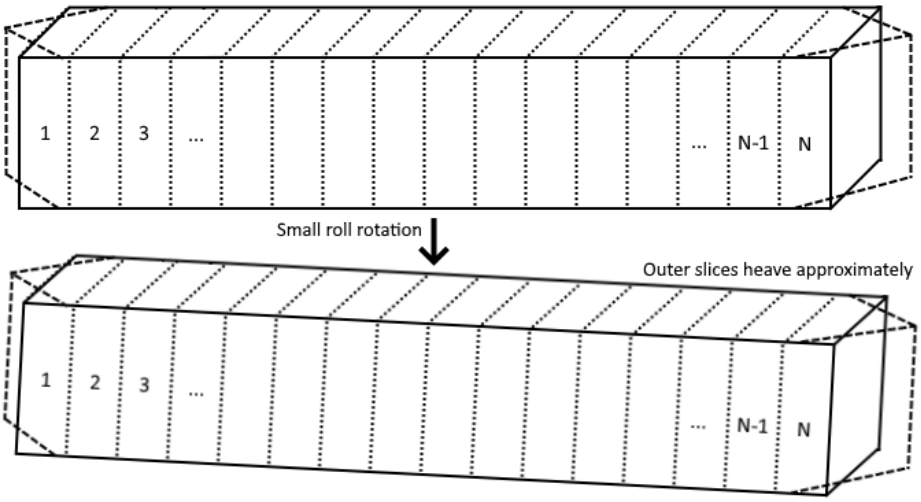

Figure G.1: Roll radiation damping approximation with multiple heave slices

$$\boldsymbol{C}_{radiation} = \begin{bmatrix} \ddots & & & & & & \\ & 0 & 0 & 0 & 0 & 0 & \\ & 0 & a & 0 & b & 0 & \\ & 0 & 0 & c & 0 & 0 & \\ & 0 & b & 0 & d & 0 & \\ & 0 & 0 & 0 & 0 & e & \\ & 0 & 0 & 0 & 0 & 0 & f \\ & & & & & & \ddots \end{bmatrix} \tag{G.1}$$

Where:

$$\begin{aligned} a &= C_{tip} \cdot C_{damp,y} \cdot \frac{\rho \cdot d \cdot \overline{L_{fl}}}{\sqrt{\frac{\overline{L_{fl}}}{2 \cdot g}}} \cdot \sum W_{fl} \cdot C_{gap} \\ b &= \left(C_{tip} \cdot C_{damp,y} \cdot \frac{\rho \cdot d \cdot \overline{L_{fl}}}{\sqrt{\frac{\overline{L_{fl}}}{2 \cdot g}}} \cdot \sum W_{fl} \cdot C_{gap} \right) \cdot (-z_t - 0.5 \cdot d) \\ c &= \sum_{i=1}^{N_{fl}} C_{damp,z} \cdot \frac{\rho \cdot d \cdot W_{fl}}{\sqrt{\frac{W_{fl}}{2 \cdot g}}} \cdot L_{fl} \\ d &= \int_{-L_{fl}/2}^{L_{fl}/2} \sum_{i=1}^{N_{fl}} C_{damp,z} \cdot \frac{\rho \cdot d \cdot W_{fl}}{\sqrt{\frac{W_{fl}}{2 \cdot g}}} \cdot y \, dy \\ e &= \sum_{i=1}^{N_{fl}} C_{damp,z} \cdot \frac{\rho \cdot d \cdot W_{fl}}{\sqrt{\frac{W_{fl}}{2 \cdot g}}} \cdot L_{fl} \cdot x_{fl}^2 \\ f &= \sum_{i=1}^{N_{fl}} C_{tip} \cdot C_{damp,y} \cdot \frac{\rho \cdot d \cdot \overline{L_{fl}}}{\sqrt{\frac{\overline{L_{fl}}}{2 \cdot g}}} \cdot \sum W_{fl} \cdot C_{gap} \cdot x_{fl}^2 \end{aligned} \tag{G.2}$$

In the equations above, the C_{damp} coefficients are taken from the graphs presented in Figure 3.13. Coefficient C_{tip} has been set to 1.0, to allow comparison with the work from Hoogsteder [57]. The influence of the turbines has been neglected completely, as very little is known on the effect of this structure on radiation damping. Coefficient C_{gap} has been introduced to allow for reduction in wave radiation due to there being a gap in between the floaters. This gap allows for current around the floaters, instead of the water being pushed away.

G.2. Comparison with Ansys Aqwa

For the three evaluated motions in the hand calculation, a comparison can be made with results from Ansys Aqwa. The file constructed by Hoogsteder [57] has been used for this manner. The results for radiation damping for sway, heave, roll, and pitch are presented below. Spikes can be found in the calculations by Ansys Aqwa, due to singularities in the calculation for frequencies close to the natural frequency. Especially the calculation for roll shows significant differences between the two methods. However, this has little effect on the dynamic motion of the bridge as turbine drag is the main cause of roll damping.

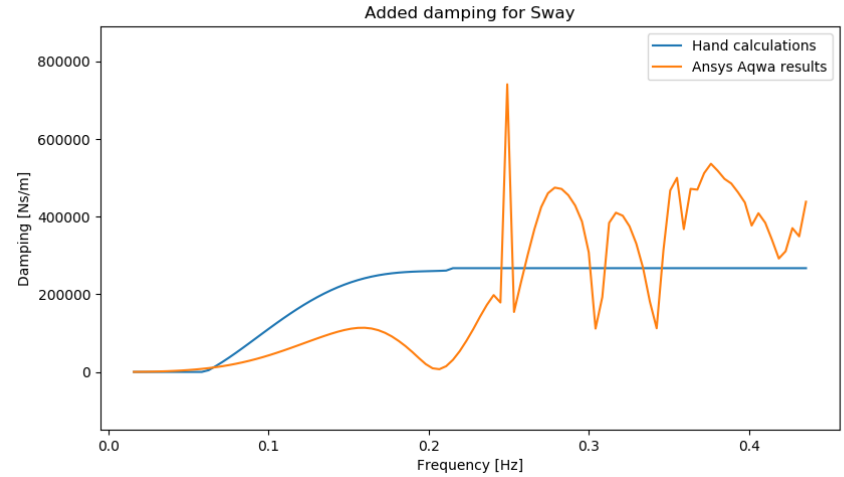

Figure G.2: Radiation damping comparison between hand calculations and Ansys Aqwa for sway

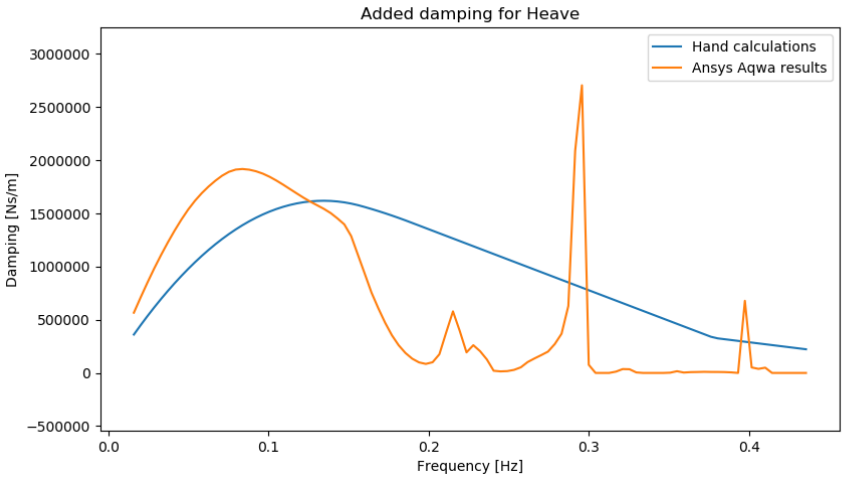

Figure G.3: Radiation damping comparison between hand calculations and Ansys Aqwa for heave

For large waves, it may occur that the bottom side of the structure emerges from the water partially. The model does not take into account that radiation damping is not present at that time-interval. This would lead to an overestimation of the damping. However, this effect is countered by a large splash that would occur when the bottom side of the floaters returns to a fully submerged state. This effect would lead to significant damping. As the model does not take this into account as well, it would lead to an underestimation of the damping at the specific instant. It is assumed that the combined effect of these two assumptions if it comes to damping has little effect on the dynamics of the structure.

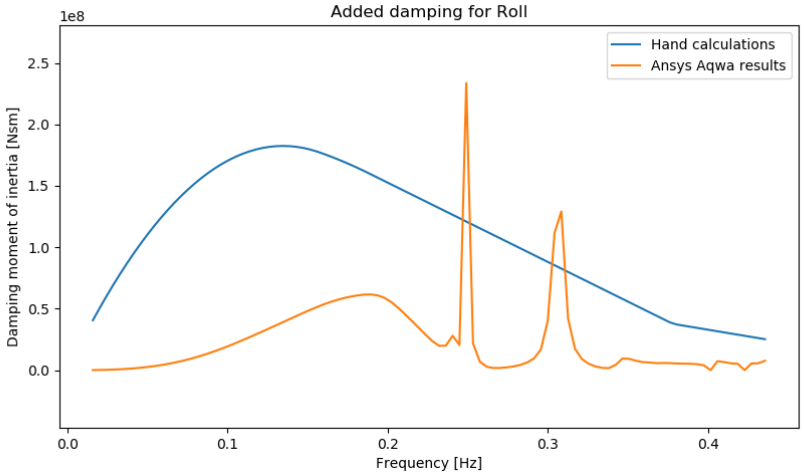

Figure G.4: Radiation damping comparison between hand calculations and Ansys Aqwa for roll

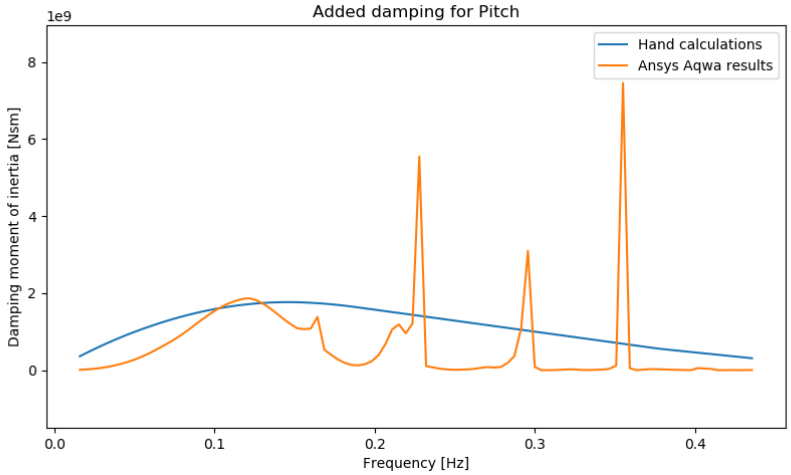

Figure G.5: Radiation damping comparison between hand calculations and Ansys Aqwa for pitch

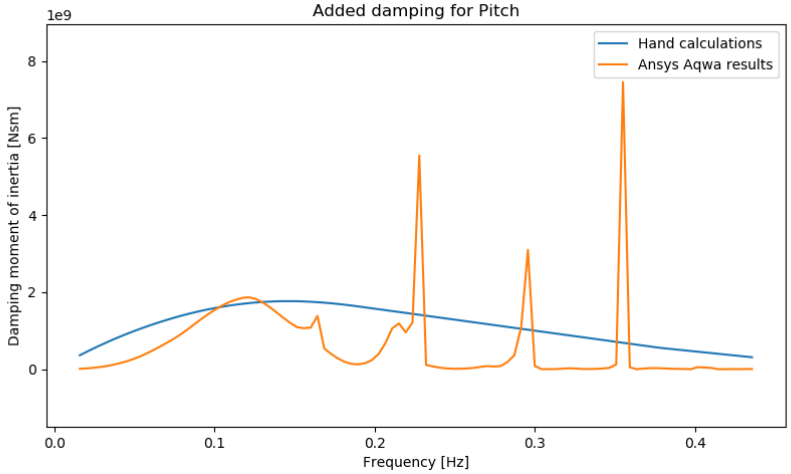

Figure G.6: Radiation damping comparison between hand calculations and Ansys Aqwa for yaw

For every simulation, the wave period and flow velocity needs to be specified. This can be used to calculate the impact frequency, which is used to allocate a radiation damping value. This value can be taken constant over time when the structural response is very close to a sine wave. When it deviates significantly, impulse response functions need to be used. The figures below show the sway, heave, and roll steady state displacement for the standardised computation settings as shown in Appendix L, with a flow velocity of 2 m/s and a wave height / length / period of respectively 3 m / 80 m / 7 s. It shows that the movement can be very well approximated with a single sine wave.

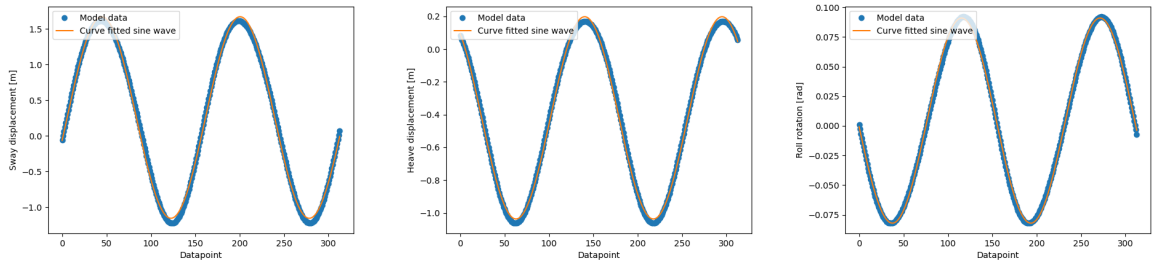

(a) Sway (b) Heave (c) Roll

Figure G.7: Curve fitting of steady state response for sway, heave, and roll using a single sine wave

H

Calculation of hydrodynamic coefficients using Ansys Aqwa

A relative simple Ansys Aqwa model has been created in order to evaluate the effect of addition of the turbines, and to use the obtained data to validate the correct magnitude of the hand-calculations. In addition to the work of Hoogsteder [5], this work also includes the pointed tips of the floaters. In the model, where only only one segment is implemented, two variants are evaluated: one without turbines and one with turbines. The size of the floaters has been based on the design proposal of the Palmerah Tidal Bridge. The size of the turbines has been estimated based on the Hammerfest HS1000 Tidal Turbines, as mentioned before [62]. The sizes are linearly scaled into a blade length of 8 meters and converted into a rhombus. The centre of the turbine is located 16.89 meter under the COG of the segment, as is the current design proposal. The connecting tubes are 1600 mm in diameter, The front tube being vertical and the back tube at an angle of 57.8. The centre of the front tube is placed 8 meters negative y direction. The model is defined as follows starting from the next page. It concluded that the radiation damping is hardly affected by the addition of the turbines. The added mass does slightly change, as more water needs to be displaced. However, this of negligible magnitude.

Project

Name	Project
Hydrodynamic Solver Unit System	Metric: kg, m [N]
Date of Creation	2019-10-21 09:10:06
Last Modified	2019-10-23 09:05:28
Data Folder Root	C:\Users\gerjan.dorgelo\Desktop\Thesis\Ansys\Ansys Less Simple_files\dp0\AQW\AQW
Product Version	19.2

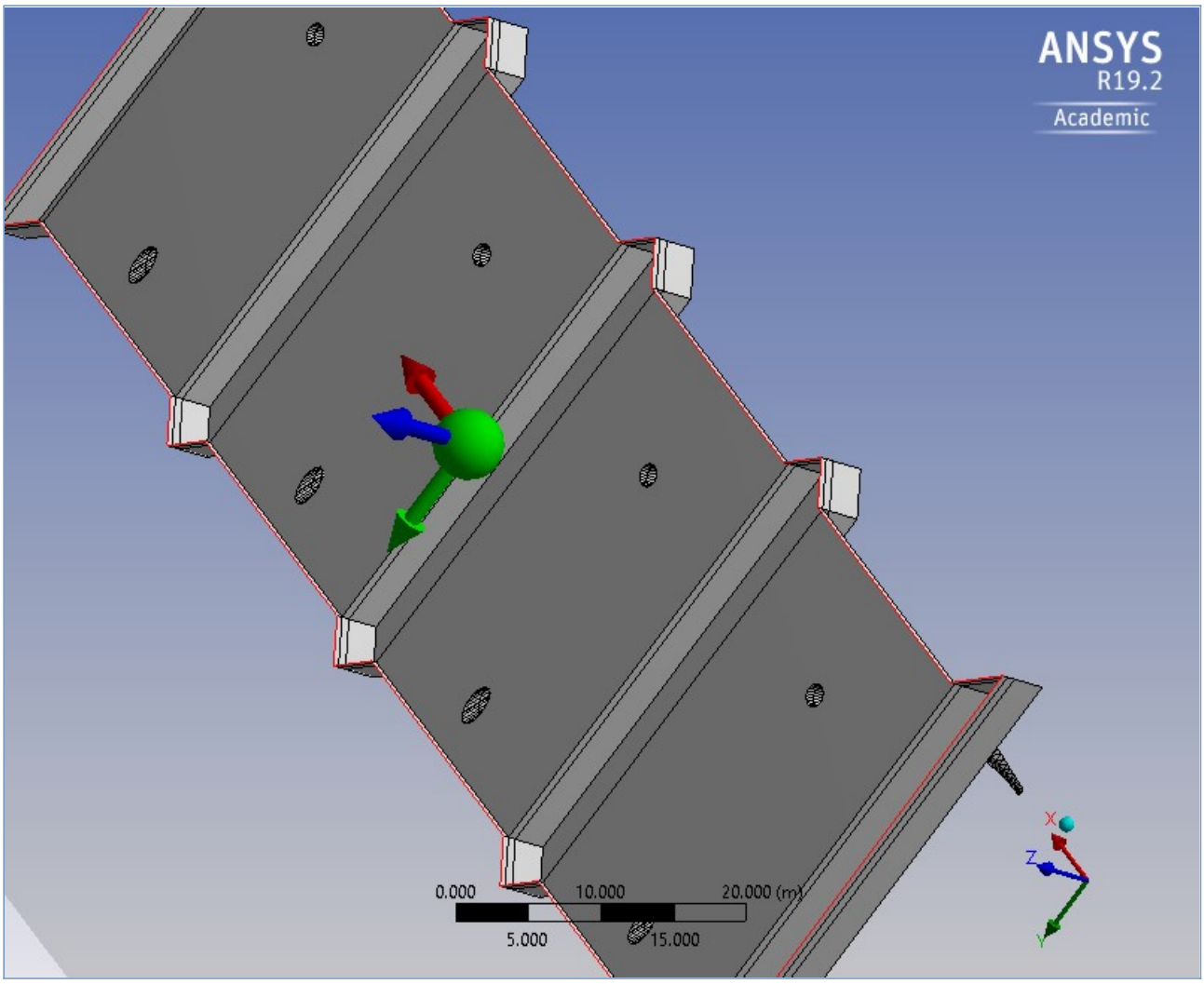

Contents

Units

TABLE 1

Length	Meter
Mass	Kilogram
Angle	Radian
Force	Newton
Frequency	Hertz
Time	Second

Model (A3)

Geometry

TABLE 2
Model (A3) > Geometry

Name	*Geometry*
State	Fully Defined
Details of Geometry	
Attached Assembly Path	C:\Users\gerjan.dorgelo\Desktop\Thesis\Ansys\Ansys Less Simple_files\dp0\AQW\DM\AQW.agdb
Environment Constants	
Water Depth	25 m
Water Density	1025 kg/m³
Gravity	9.8 m/s²
Water Size X	198 m
Water Size Y	124 m
Stability/Time Response-Specific Options	
Tube Drag Coefficients	Defined in Line Body Details
Seabed Inline Friction Coefficient	0.0
Seabed Lateral Friction Coefficient	0.0
Composite Cable Seabed Definition	
Seabed Type	No Composite Cable Seabed
Import Preferences	
Import Solid Bodies	No
Import Surface Bodies	Yes
Import Line Bodies	Yes

Fixed Points

TABLE 3
Model (A3) > Geometry > Fixed Points

Name	*Fixed Points*
State	Fully Defined
Details of Fixed Points	
Visibility	Visible

Part

TABLE 4
Model (A3) > Geometry > Part

Name	*Part*
State	Fully Defined
Details of Part	
Part Visibility	Visible
Activity	Not Suppressed
Part Color	14606046
Mass Properties from Solver	
Total Structural Mass	Solve Hydrostatics to Update
Advanced Options	
Generate Internal Lid	Yes
Lid Element Size Definition	Program Controlled
Current Calculation Position	At Fixed Depth
Current Calculation Depth	0.0 m
Submerged Structure Detection	Program Controlled
Override Calculated GMX	No
Override Calculated GMY	No
Fixity Options	
Structure Fixity	Structure is Free to Move
Force Multiplying Factors	
Drag Multiplying Factor	1
Mass Multiplying Factor	1
Slam Multiplying Factor	0.0
Shear Force/Bending Moment Options	
Calculate Shear Force/Bending Moment	Yes
Neutral Axis	Global X
Neutral Axis Position Definition	Through COG

TABLE 5
Model (A3) > Geometry > Part > Body

Name	*Sketchup 2 Geometry*
State	Fully Defined
Details of Sketchup 2 Geometry	
Body Visibility	Visible
Activity	Not Suppressed
Body Color Definition	Inherited from Part
Structure Type	Physical Geometry
Surface Type	Program Controlled

TABLE 6
Model (A3) > Geometry > Part > Body

Name	*Sketchup 2 Geometry*
State	Fully Defined
Details of Sketchup 2 Geometry	
Body Visibility	Visible
Activity	Not Suppressed
Body Color Definition	Inherited from Part
Structure Type	Physical Geometry
Surface Type	Program Controlled

TABLE 7
Model (A3) > Geometry > Part > Body

Name	*Sketchup 2 Geometry*
State	Fully Defined
Details of Sketchup 2 Geometry	
Body Visibility	Visible
Activity	Not Suppressed
Body Color Definition	Inherited from Part
Structure Type	Physical Geometry

Surface Type	Program Controlled

TABLE 8
Model (A3) > Geometry > Part > Body

Name	*Sketchup 2 Geometry*
State	Fully Defined
Details of Sketchup 2 Geometry	
Body Visibility	Visible
Activity	Not Suppressed
Body Color Definition	Inherited from Part
Structure Type	Physical Geometry
Surface Type	Program Controlled

TABLE 9
Model (A3) > Geometry > Part > Body

Name	*Sketchup 2 Geometry*
State	Fully Defined
Details of Sketchup 2 Geometry	
Body Visibility	Visible
Activity	Not Suppressed
Body Color Definition	Inherited from Part
Structure Type	Physical Geometry
Surface Type	Program Controlled

TABLE 10
Model (A3) > Geometry > Part > Body

Name	*Sketchup 2 Geometry*
State	Fully Defined
Details of Sketchup 2 Geometry	
Body Visibility	Visible
Activity	Not Suppressed
Body Color Definition	Inherited from Part
Structure Type	Physical Geometry
Surface Type	Program Controlled

TABLE 11
Model (A3) > Geometry > Part > Body

Name	*Sketchup 2 Geometry*
State	Fully Defined
Details of Sketchup 2 Geometry	
Body Visibility	Visible
Activity	Not Suppressed
Body Color Definition	Inherited from Part
Structure Type	Physical Geometry
Surface Type	Program Controlled

TABLE 12
Model (A3) > Geometry > Part > Body

Name	*Sketchup 2 Geometry*
State	Fully Defined
Details of Sketchup 2 Geometry	
Body Visibility	Visible
Activity	Not Suppressed
Body Color Definition	Inherited from Part
Structure Type	Physical Geometry
Surface Type	Program Controlled

TABLE 13
Model (A3) > Geometry > Part > Body

Name	*Sketchup 2 Geometry*
State	Fully Defined
Details of Sketchup 2 Geometry	
Body Visibility	Visible
Activity	Not Suppressed
Body Color Definition	Inherited from Part
Structure Type	Physical Geometry
Surface Type	Program Controlled

TABLE 14
Model (A3) > Geometry > Part > Body

Name	*Sketchup 2 Geometry*

State	Fully Defined
Details of Sketchup 2 Geometry	
Body Visibility	Visible
Activity	Not Suppressed
Body Color Definition	Inherited from Part
Structure Type	Physical Geometry
Surface Type	Program Controlled

TABLE 15
Model (A3) > Geometry > Part > Axes

Name	*Part Axes*
State	Fully Defined
Details of Part Axes	
Visibility	Visible
Axes Alignment	
Alignment Method	Global Axes
Rotation About Global Z	0.0 rad
Rotation About Local Y	0.0 rad
Rotation About Local X	0.0 rad
Unit Vector X	[1, 0.0, 0.0]
Unit Vector Y	[0.0, 1, 0.0]
Unit Vector Z	[0.0, 0.0, 1]

TABLE 16
Model (A3) > Geometry > Part > Structural Mass

Name	*Point Mass*
State	Fully Defined
Details of Point Mass	
Visibility	Visible
Activity	Not Suppressed
Point Mass Properties	
Mass Definition	Manual Definition
X	0.0 m
Y	0.0 m
Z	3.84 m
Mass	2320000 kg
Inertia Properties	
Define Inertia Values By	Direct Input of Inertia
Kxx	7.8317435412909 m
Kyy	28.7752887279921 m
Kzz	28.7655505170981 m
Ixx	142300000 kg.m²
Ixy	0.0 kg.m²
Ixz	0.0 kg.m²
Iyy	1921000000 kg.m²
Iyz	0.0 kg.m²
Izz	1919700000 kg.m²

Connections

TABLE 17
Model (A3) > Connections

Name	*Connections*
State	Fully Defined
Details of Connections	

TABLE 18
Model (A3) > Connections > Connection Data

Name	*Connection Data*
State	Fully Defined
Details of Connection Data	

Mesh

TABLE 19
Model (A3) > Mesh

Name	*Mesh*
State	Meshed
Details of Mesh	
Defaults	
Control Type	Basic Controls

Mesh Parameters	
Defeaturing Tolerance	0.4 m
Maximum Element Size	0.8 m
Maximum Allowed Frequency	0.651 Hz
Meshing Type	Program Controlled
Generated Mesh Information	
Total Nodes	32122
Total Elements	31965
Diffracting Nodes	16694
Diffracting Elements	16270
Line Body Nodes	0
Line Body Elements	0
Field Points	0

Hydrodynamic Diffraction (A4)

TABLE 20
Model (A3) > Analysis

Name	*Hydrodynamic Diffraction (A4)*
State	Solved
Details of Hydrodynamic Diffraction	
Analysis Type	Hydrodynamic Diffraction/Radiation

TABLE 21
Model (A3) > Hydrodynamic Diffraction (A4) > Analysis Settings

Name	*Analysis Settings*
State	Fully Defined
Details of Analysis Settings	
Parallel Processing	Program Controlled
Generate Wave Grid Pressures	Yes
Wave Grid Size Factor	2
Common Analysis Options	
Ignore Modelling Rule Violations	Yes
Calculate Extreme Low/High Frequencies	Yes
Include Multi-Directional Wave Interaction	Yes
Near Field Solution	Program Controlled
Linearized Morison Drag	No
QTF Options	
Calculate Full QTF Matrix	No
Output File Options	
Source Strengths	No
Potentials	No
Centroid Pressures	No
Element Properties	No
ASCII Hydrodynamic Database	No
Example of Hydrodynamic Database	No

TABLE 22
Model (A3) > Hydrodynamic Diffraction (A4) > Structure Selection

Name	*Structure Selection*
State	Fully Defined
Details of Structure Selection	
Structures to Exclude	None
Group of Structures	
Interacting Structure Groups	None
Structure Ordering	
Structure 1	Part

TABLE 23
Model (A3) > Hydrodynamic Diffraction (A4) > Wave Direction

Name	*Wave Directions*
State	Fully Defined
Details of Wave Directions	
Visibility	Visible
Type	Range of Directions, No Forward Speed
Required Wave Input	
Wave Range	-π rad to π rad
Interval	0.785398163397448 rad
Number of Intermediate Directions	7
Optional Wave Directions A	

Additional Range	None
Optional Wave Directions B	
Additional Range	None
Optional Wave Directions C	
Additional Range	None
Optional Wave Directions D	
Additional Range	None

TABLE 24
Model (A3) > Hydrodynamic Diffraction (A4) > Wave Directions

Direction Number	Wave Direction (rad)
1	-3.14159
2	-2.35619
3	-1.5708
4	-0.7854
5	0.0
6	0.7854
7	1.5708
8	2.35619
9	3.14159

TABLE 25
Model (A3) > Hydrodynamic Diffraction (A4) > Wave Frequency

Name	*Wave Frequencies*
State	Fully Defined
Details of Wave Frequencies	
Intervals Based Upon	Frequency
Incident Wave Frequency/Period Definition	
Range	Manual Definition
Definition Type	Range
Lowest Frequency Definition	Manual Definition
Lowest Frequency	0.04 Hz
Longest Period	25 s
Highest Frequency Definition	Manual Definition
Highest Frequency	0.5 Hz
Shortest Period	2 s
Number of Intermediate Values	98
Interval Frequency	4.64646e-3 Hz
Additional Frequencies A	
Additional Range	None
Additional Frequencies B	
Additional Range	None
Additional Frequencies C	
Additional Range	None
Additional Frequencies D	
Additional Range	None

Solution (A5)

Ansys Aqwa; a description

Ansys Aqwa is a software program part of the complete Ansys tool set. Aqwa can be used to model the hydrostatic and hydrodynamic behaviour of elements. As Ansys Aqwa had a significant involvement in the work of Hoogsteder [5], this study being an implementation of her acquired results, and this study also using the software package, deep understanding of the capabilities and limitations of Ansys Aqwa is needed.

Aqwa is a software program modelling waves around structures using numerical methods. The hydrostatic analysis, which will be used in the assessment of this study, is based on many assumptions. These include incompressibility of water, and its inviscid and irrotational fluid properties. The software, which can do this analysis for both linear Airy waves and for second order Stokes waves in all angles of incidence, uses the potential theory to simulate the behaviour of the waves. [63]

Greene's function is used to estimate the interaction with the structural elements. As water cannot enter the structure, a fictive source term needs to be added to satisfy the condition. Wave radiation and the diffraction terms can be modelled by calculating these fictive source terms. Drag forces can also be simulated using Ansys Aqwa, where Reynolds numbers are considered to be sufficiently large to allow for constant drag coefficients. However, the drag forces which Ansys Aqwa can compute are solely for circular shapes, meaning that the floaters cannot be simulated. [63]

If Ansys Aqwa is used to estimate the dynamic behaviour of a structure, a crude assumption is made that the structure is static. For the Tidal Bridge, this is far from truth. As drag is a function of relative velocity squared, variations in drag force in the directions of the oscillation can be considerably large. Also the Morison equation, which is used to model the wave forces on a structure, is a function of relative acceleration. Again, significant mistakes can develop if not evaluated properly. [63]

J

Mesh study on numerically found inertia force on floaters

To optimise calculation time, a mesh study is performed on the calculation of the inertia force term on the floaters. In this appendix, various grid sizes will be tested on various configurations of waves, meaning different wave lengths and different wave heights. Change of wave length, with wave celerity being approximately a constant function, results in the fact that wave period will scale about linearly. This has been assumed to be correct to determine an appropriate gridsize more efficiently.

J.1. Mesh structure

The wave subtool is invoked partially by defining the gridsize. In this mesh study, the length and height of a single mesh element on the side of a floater is defined as a ratio between the wave height and wave length. The width of two floaters is divided into N gridcells, being about the width that was defined. It may happen that the subtool decides that the gridcells are taken slightly longer, as the length of a floater may not be an exact multiple of the defined grid width. The same approach has been taken for the definition of the location of the gridcells vertically. A row of gridcells is defined starting from the bottom of the floater and increases making rows until no single grid is submerged anymore. The number of gridcells modelled vertically will vary over time, as function of the time dependent water elevation due to waves and the varying draught due to oscillations. Vertical pressures on the bottom side of a floater has been modelled with grids using the same length as was done for the sides of the floaters, the width of these cells are taken equal to the local width of the floater. This assumes that the water pressure under the floaters does not change when looking in the direction longitudinal to the wave crest.

These words describing the structure of the mesh, can also be presented in a drawing. See Figure J.1 for this visual guidance. The grid in this figure is partially filled with values, representing the width of the floater at that specific coordinate, whether water is present at that specific coordinate and the local water particle velocity/acceleration, both in y and z direction. In all these computations, it assumed that the value found exactly in the centre of the grid represents the average of the entire grid. For larger grids, this assumption will be less valid, especially as gridcells may be partially submerged, but are taken into account as 'fully submerged' or 'not submerged', creating larger errors. As example, the gridsize has been taken as an eighth of the length of the small floater, and a sixteenth of the height of the small floater. Making the grid smaller, approximates an integration over the submerged area.

J.2. Mesh tests

The mesh study will be performed for three wave heights (1, 2, and 3 meter) and three different wave lengths (30, 60, and 90 meter). The wave period will be scaled linearly to the wave length. In the computation, all other forces are neglected. For the nine wave scenarios, a set of 16 grid options will be tested. The size of this grid (in length and height) is taken as fraction of the wave length and wave height respectively. The ratios studied are: 1/5, 1/10, 1/20, and 1/40. All grid options considered are shown in Table J.1. The remaining settings used in the computations, except for the marine growth added mass coefficient being equal to 1.0, are the basic 2D-Palmerah version 1 settings, as presented in Appendix L.
When forces as a function of time are evaluated, mistakes up to 80 percent have been found. This is due to the nature of the subtool, which represents the wave with a grid of ones and zeros. It may happen that a significant amount of gridcells get attributed with a '0', meaning 'no water present', while still being partly

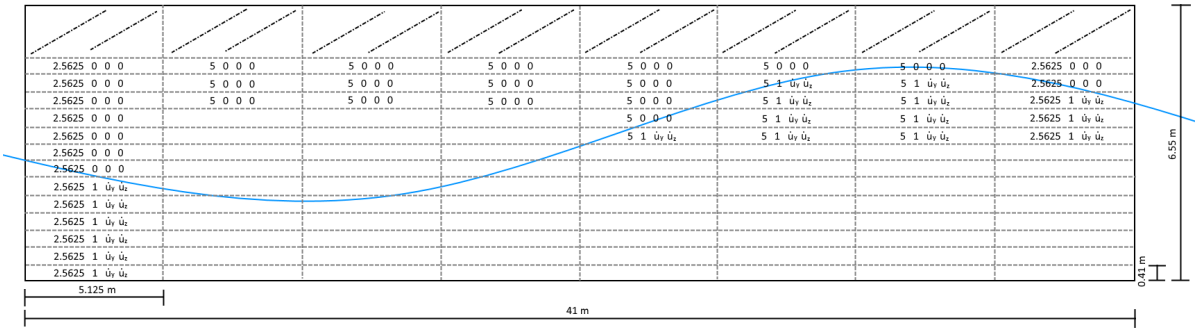

Figure J.1: Mesh configuration for small floater, grids partially filled with values representing local data

Configuration	**Gridsize [y,z]**	**Configuration**	**Gridsize [y,z]**
Option 1	$[L/5, H/5]$ m	Option 9	$[L/20, H/5]$ m
Option 2	$[L/5, H/10]$ m	Option 10	$[L/20, H/10]$ m
Option 3	$[L/5, H/20]$ m	Option 11	$[L/20, H/20]$ m
Option 4	$[L/5, H/40]$ m	Option 12	$[L/20, H/40]$ m
Option 5	$[L/10, H/5]$ m	Option 13	$[L/40, H/5]$ m
Option 6	$[L/10, H/10]$ m	Option 14	$[L/40, H/10]$ m
Option 7	$[L/10, H/20]$ m	Option 15	$[L/40, H/20]$ m
Option 8	$[L/10, H/40]$ m	Option 16	$[L/40, H/40]$ m

Table J.1: Gridsize options tested

submerged. This may result in vast under-representation or over-representation of the force. Large relative mistakes are also found when the force approaches zero in magnitude. Small differences in absolute value will form large relative errors. As timesteps in the iteration process are taken very small, small spikes in forcing do not contribute significant in the calculation of the dynamic behaviour. Therefore, the maximum displacement and acceleration will be compared for the different grids for the nine different configuration of waves. It can be assumed that configuration 16, being the configuration with the smallest gridsize, is most accurate. The results for maximum displacement and acceleration for a wave length of 30 meters, with wave heights of 1, 2, and 3 meters, for various grids are presented below for the inertia calculation. The drag contribution was solved without the need of a complex numerical method.

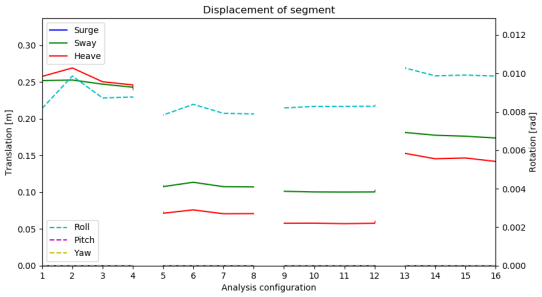

(a) Maximum displacement for wave height of 1 meters

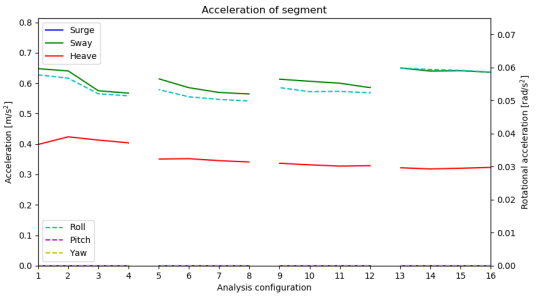

(b) Maximum acceleration for wave height of 1 meters

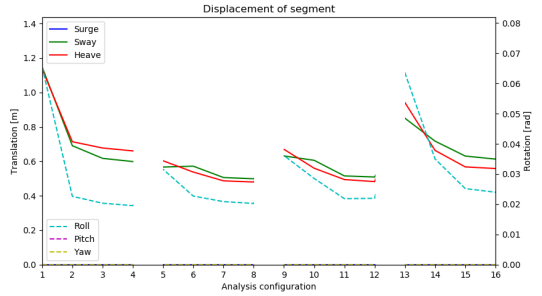

(c) Maximum displacement for wave height of 2 meters

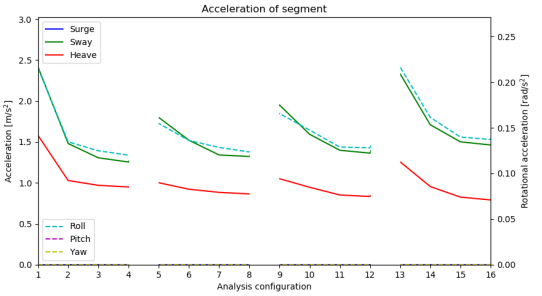

(d) Maximum acceleration for wave height of 2 meters

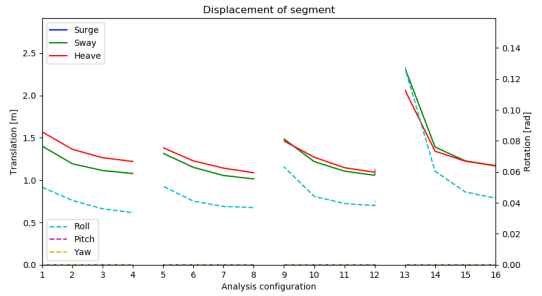

(e) Maximum displacement for wave height of 3 meters

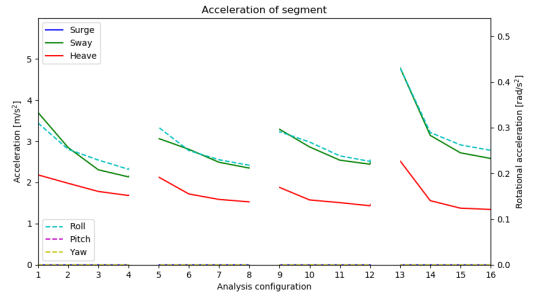

(f) Maximum acceleration for wave height of 3 meters

Figure J.2: Maximum displacement and acceleration for wave length of 30 meters, various wave heights and gridsizes

The same analysis for waves with a length of 60 meters are presented below:

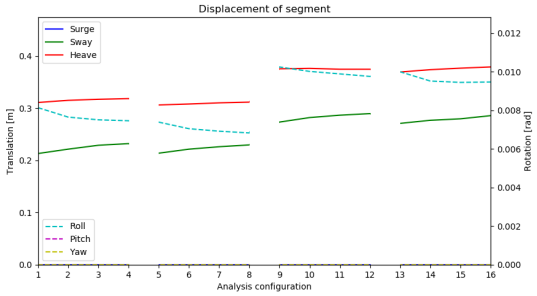

(a) Maximum displacement for wave height of 1 meters

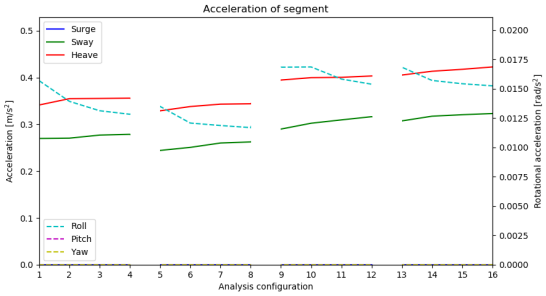

(b) Maximum acceleration for wave height of 1 meters

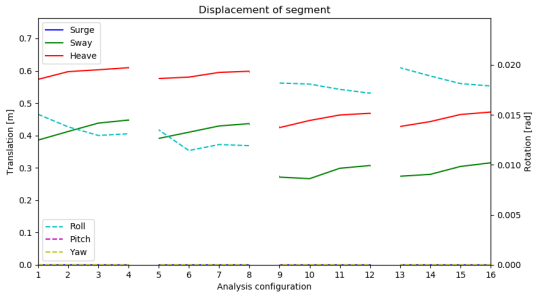

(c) Maximum displacement for wave height of 2 meters

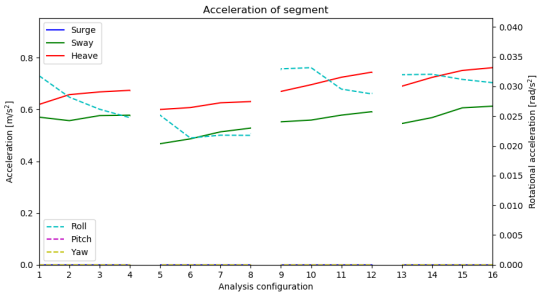

(d) Maximum acceleration for wave height of 2 meters

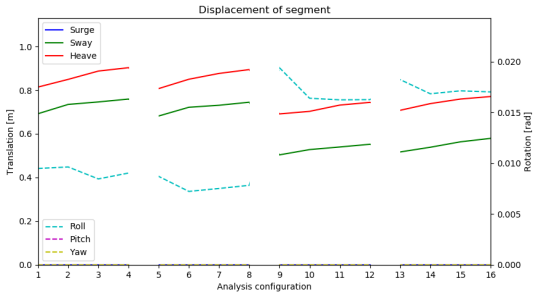

(e) Maximum displacement for wave height of 3 meters

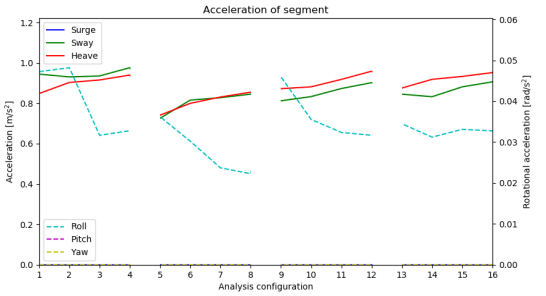

(f) Maximum acceleration for wave height of 3 meters

Figure J.3: Maximum displacement and acceleration for wave length of 60 meters, various wave heights and gridsizes

And the same analysis for waves with a length of 90 meters are presented now:

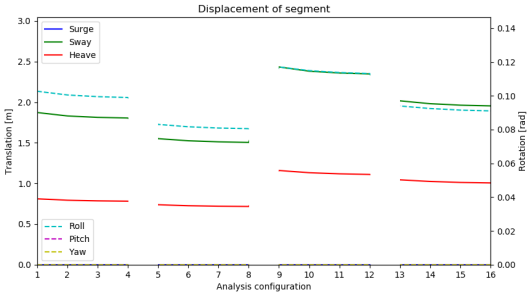

(a) Maximum displacement for wave height of 1 meters

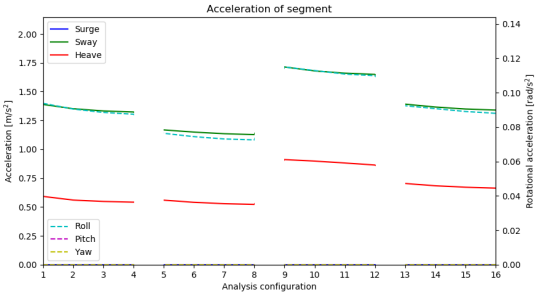

(b) Maximum acceleration for wave height of 1 meters

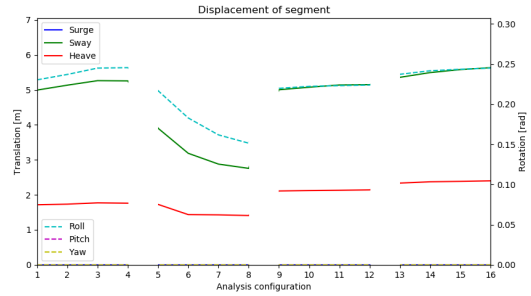

(c) Maximum displacement for wave height of 2 meters

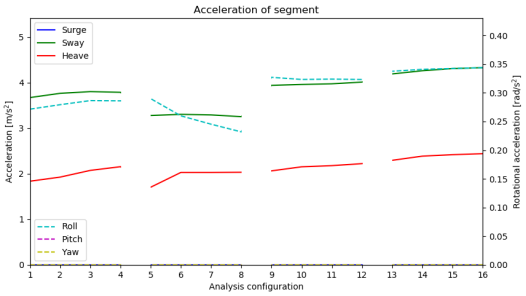

(d) Maximum acceleration for wave height of 2 meters

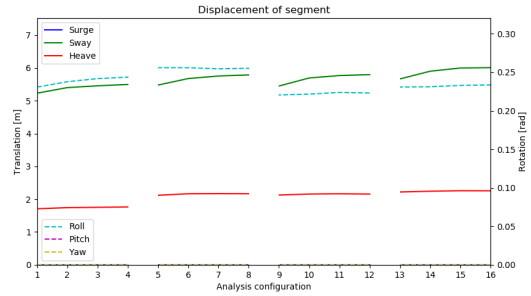

(e) Maximum displacement for wave height of 3 meters

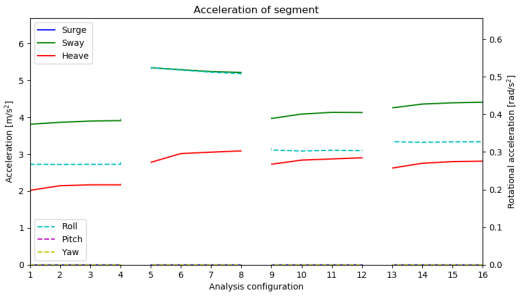

(f) Maximum acceleration for wave height of 3 meters

Figure J.4: Maximum displacement and acceleration for wave length of 90 meters, various wave heights and gridsizes

It can be noted that variation of the length of a gridsize does have a significant effect on most of the tests. Gridsizes wave length of a fifth or a tenth of the wavelength result in notable errors. A lower number of gridcells in this direction does result in an over-estimation of the results for small waves, but an under-estimation for longer waves. To reduce computation time, but to increase accuracy, it is recommended to use the following length for the gridcells:

$$\frac{L}{L_{grid}} = 25 \tag{J.1}$$

The same statements holds for making the vertical size of the gridcells smaller: it results in smaller displacements and accelerations. It can be observed that the number of vertical cells has little effect for smaller waves. For higher waves, this effect is notable. This phenomenon can be explained as the computation integrates over the total height of the floaters. If the wave height is small, and a constant ratio between wave height and grid height is chosen, the submerged part of the floater is represented by a lot of gridcells. Visa versa, a high wave results in less gridcells on the floater. Because of this, it is advised to use a gridratio as function of the wave height. The following equation is proposed:

$$\frac{H}{H_{grid}} = 15 + 10 \cdot H \tag{J.2}$$

Both the ratios are used in the computations in this report. A finer gridsize may also be used. However, this will result in extra computation time. The computation time of the model is a function of the area of a gridcell squared. A coarser grid does improve calculation time, but results in a larger error. Looking at the presented data, it can be stated that generally speaking, the error will be conservative. It is recommended to think about using a coarser grid for initial use of the model. This coarser grid can be used to find first estimations. A finer grid is recommended for more precise use, especially if forces are to be obtained. The proposed ratios do result in fast fluctuating acceleration and forces. However, these spikes disappear when looking at the second integral, being the displacement. If more precise forces are desired, smaller grids are recommended.

K

Additional information regarding experiment setups

K.1. Complete overview of the different experiment setups

This appendix elaborates on the different setups used during the performed experiments, as elaborated in Chapter 4. The following page lists all the setups and describes the state of the small floater, the large floater, and the draught[1] of the segment. The codes representing the states are described in the mentioned chapter.

Label	Small floater	Large floater	Draught
Setup 01	$S1$	$L1$	$D1$
Setup 02	$S1$	$L1$	$D2$
Setup 03	$S1$	$L1$	$D3$
Setup 04	$S2$	$L2$	$D1$
Setup 05	$S2$	$L2$	$D2$
Setup 06	$S2$	$L2$	$D3$
Setup 07	$S3$	$L3$	$D1$
Setup 08	$S3$	$L3$	$D2$
Setup 09	$S3$	$L3$	$D3$
Setup 10	$S4$	$L4$	$D1$
Setup 11	$S4$	$L4$	$D2$
Setup 12	$S4$	$L4$	$D3$
Setup 13	$S5$	$L5$	$D1$
Setup 14	$S5$	$L5$	$D2$
Setup 15	$S5$	$L5$	$D3$
Setup 16	$S6$	$L5$	$D1$
Setup 17	$S6$	$L6$	$D2$
Setup 18	$S6$	$L6$	$D3$
Setup 19	$S7$	$L7$	$D1$
Setup 20	$S7$	$L7$	$D2$
Setup 21	$S7$	$L7$	$D3$
Setup 22	$S8$	$L8$	$D1$
Setup 23	$S8$	$L8$	$D2$
Setup 24	$S8$	$L8$	$D3$
Setup 25	$S9$	$L9$	$D1$
Setup 26	$S9$	$L9$	$D2$
Setup 27	$S9$	$L9$	$D3$

Table K.1: Experiment setup variations and combinations

[1] Draught for Setup 01 could not be obtained as the own mass of the structure without lead creates a larger draught. Draught for this experiment is set to 25.7 mm.

K.2. Materials and measurement equipment

Materials:

- Pool: Intex opblaaszwembad Easy Pool Set 244 x 76 cm blauw (Blokker)
- Deck: Vuren Geschaard 18x143mm 210cm (Gamma)
- Floaters: Polystyreen EPS 60 6 cm 100x50cm 4 stuks (Gamma)
- Screws: Unischroef Rotadrillpk 6.0x60 50st (Gamma)
- PVC Tube: Buis Elektra 3/4" 2 meter (Gamma)
- Cardboard: Kalender (CIGO)
- Red paint: Spectrum spuitverf acryl 400ml rood (Action)
- Lead: Aqua-lood 15cm Lengte 1.5m (Gamma)
- Tape: AH plakband (AH)
- Glue: Verona secondenlijm 3st (Action)
- Background: (2x) Splittopper hoeslaken jersey 180x220cm (Action)

Measurement equipment:

- GoPro Hero5

K.3. Verification of model plate stiffness

The stiffness of the plate in the scale model needs to be verified for the two motions considered. The plate will be subjected to a horizontal force, creating a bending moment. Torsional forces may also be found by the eccentricity of the measuring stick. However, as rotations are small, and the measuring stick is light (about 100 grams), it is assumed that torsion will not form a significant roll.

The structure can be modelled using a continuous beam resting on 5 springs, the hydrostatic spring effect of the water. It is assumed that the mass of the bridge can be seen as a distributed load between two outer floater and that the bottom side of all floaters are of same height. The following properties have been used for the calculation, as this is the scenario with the most intense loads:

Properties	**Value**
H_{plate}	0.018 m
W_{plate}	0.143 m
L_{plate}	1.000 m
$W_{fl,s}$	0.042 m
$L_{fl,s}$	0.400 m
$W_{fl,l}$	0.060 m
$L_{fl,l}$	0.400 m
M_{total}	3.779 kg
E_{spruce}	8000 MPa

Table K.2: Scale model bending calculation properties [1, 64]

The continuous beam can now be modelled using four fields, the fields being in between the floaters. Each field rests on two springs, where the spring stiffness are defined as follows:

$$\begin{aligned} k_{hydro,s} &= \rho \cdot g \cdot \left(L_{fl,s} \cdot W_{fl,s} + W_{fl,s} \cdot W_{fl,s}\right) \\ k_{hydro,l} &= \rho \cdot g \cdot \left(L_{fl,l} \cdot W_{fl,l} + W_{fl,l} \cdot W_{fl,l}/2\right) \end{aligned} \tag{K.1}$$

The equations for displacement, rotation, bending moment and shear force as functions of the parameter x, are defined using the Bernoulli's beam principle, which results in the formulas below. In here, positive displacement has been assumed downwards.

$$
\begin{aligned}
w &= \frac{q \cdot x^4}{24 \cdot EI} + \frac{C_1 \cdot x^3}{6} + \frac{C_2 \cdot x^2}{2} + C_3 \cdot x + C_4 \\
\phi &= -\frac{q \cdot x^3}{6 \cdot EI} - \frac{C_1 \cdot x^2}{2} - C_2 \cdot x - C_3 \\
M &= -EI \cdot \left(\frac{q \cdot x^2}{2 \cdot EI} + C_1 \cdot x + C_2 \right) \\
V &= -EI \cdot \left(\frac{q \cdot x}{EI} + C_1 \right)
\end{aligned}
\tag{K.2}
$$

Two sets of boundary conditions apply. For the outer edges, shear force is equal to displacement multiplied with the hydrostatic spring stiffness of the small floaters. The connection between the fields is characterised by an equal displacement, rotation and bending moment on both sides of the connection. Shear force will deviate, by the exact amount of forces generated by the large floaters; being the displacement multiplied with the hydrostatic spring stiffness of the large floaters. During stationary placement in the water, the following results are found for the displacement and bending moment in the spruce plate:

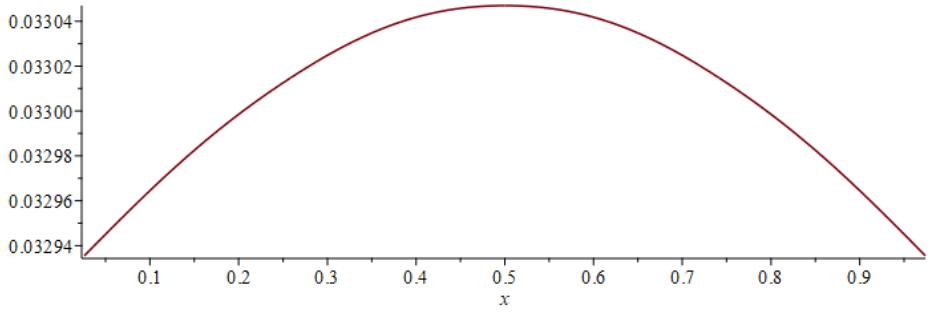

Figure K.1: Displacement of model structure

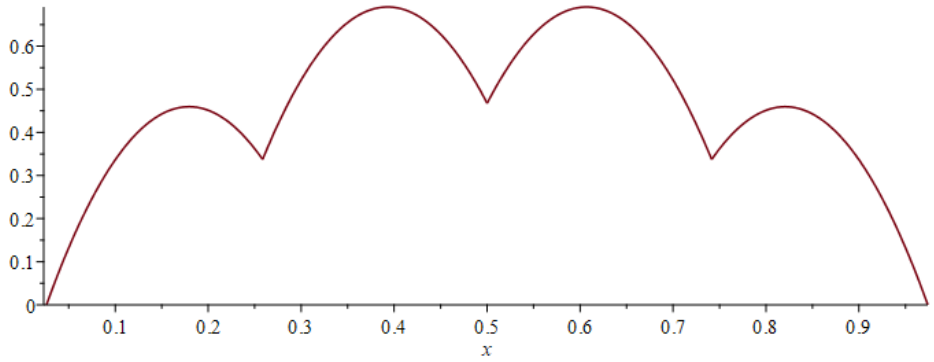

Figure K.2: Bending moment of model structure

It can be noted that the displacement averages on 33 mm, which was the design for the structure configuration. Maximum displacement relative to this value, are found at the edges, being about 0.06 mm. This value will be slightly lower, as slightly more weight is found in the middle of the bridge, reducing the magnitude of the curve. Dynamic will amplify the curve. However, even if a factor of 3 is assumed, little effect displacement will be present.

The maximum bending moment is equal to 0.691 Nm. This value will be doubly amplified, by the turbine weight in between the floaters and the dynamic effects. If these are neglected for a moment, the maximum stress in the timber plate can be calculated. This stress of 0.09 MPa is very low compared to the bending capacity of spruce, being 18 MPa [64]. Even when the amplification discussed above is taken into account, bending limits will definitely not be exceeded.

L

Standardised computation settings

The dimensions and settings below are the standardised settings for various computations. To avoid needing to present the different settings multiple times, this appendix serves as an overall guide for the computations.

Parameter	**Value**
rho	1025 [kg/m^3]
g	9.8 [m/s^3]
depth	18 [m]
Tidal_level	0 [m]
flow_velocity	4.5 [m/s]
Wave_height	3.54 [m]
Wave_period	7.5 [s]
Wave_length	90 [m]
Wind_Distributed_Load_Deck	2120 [N/m]
Wind_Distributed_Load_Super_Structure	3000 [N/m]
Traffic_load	128000 [kg]
Show_plot	*True*
Show_Tidal_Displacement_In_Plot	*False*
Three_Dimensional_Calculation	*False*
Smooth_Start	*True*
Total_time	100 [s]
Smallest_Period_Devider	10 [−]
gridsize	[Wave_length/25, Wave_height/ $(15+10\cdot$Wave_height$)$] [m]
smooth_time	0.3 · Total_time [*s*]
Add_Wind	*True*
Add_Flow	*True*
Add_Current	*True*
Traffic_Force	*True*
Constant_force	*False*
Integration_Of_Ansys_Aqwa_mass	*True*
Integration_Of_Ansys_Aqwa_damp	*True*
segments	3 [−]
Length_segment	100 [m]
free_space_between_segments	1 [m]
M_segment	2320000 [kg]
Jx_segment	142300000 [kgm^2]
Jy_segment	1921000000 [kgm^2]
Jz_segment	1919700000 [kgm^2]

Parameter	**Value**
z_location_bottom_floater	-6.635 [m]
z_location_deck	7.165 [m]
z_location_Super_Structure	3 [m]
z_location_turbines	-16.89 [m]
Angle_Pendulum_Mid_Tide	$40/180 \cdot \pi$ [rad]
Length_Pendulum	[31, 31, 31, 31] [m]
Pendulum_hinge_top_y_loc	6.5 [m]
Pendulum_hinge_top_z_loc	-7.2 [m]
Diameter_pendulum	[1.320, 1.320, 1.320, 1.320] [m]
Number_of_small_floaters	2 [$-$]
Width_small_floater	3.5 [m]
Length_small_floater	34 [m]
Number_of_large_floaters	3 [$-$]
Width_large_floater	5 [m]
Length_large_floater	34 [m]
Force_max_flow	2080000 [N]
Velocity_max_flow	4.5 [m/s]
Volume_turbine	7.0 [m^3]
Damping_Pendulum	[0, 0, 0, 0] [Ns/m]
Damping_Spudpole	[0, 0] [Ns/m]
Damping_connection_segments_y	0 [Ns/m]
Damping_connection_segments_z	0 [Ns/m]
Stiffness_Pendulum	[10^8, 10^8, 10^8, 10^8] [N/m]
Stiffness_Spudpole	[0, 0] [N/m]
Stiffness_connection_segments_y	0 [N/m]
Stiffness_connection_segments_z	0 [N/m]
C_drag_pointed_rectangle	1.15 [$-$]
C_drag_bottom_floater	0.75 [$-$]
C_Added_Mass_Pointed_Tip_Reduction	0.55 [$-$]
C_Added_Mass_Not_Infinite_Factor	1 [$-$]
C_Marine_Growth_Extra	1.1 [$-$]
C_Damping_Pointed_Tip_Reduction	0.8 [$-$]
Ansys_Aqwa_file_name	"ANALYSIS_HOOGSTEDER.LIS"
Ansys_small_floater	[2, 3.5, 34]
Ansys_large_floater	[3, 5, 34]
Ansys_Mass	$1.8 \cdot 10^6$ [kg]

Table L.1: 2D-Palmerah standardised settings

M

Dimensionless characteristics of the Tidal Bridge

This appendix shows the computed dimensionless heatmaps that were produced in Section 6.1. Each section in this appendix displays eight graphs: the maximum displacement and accelerating for the 3DOF system, and the minimum and maximum pendulum forces.

M.1. Wave height versus wave length: positive propagating waves

This section accompanies Subsection 6.1.1.

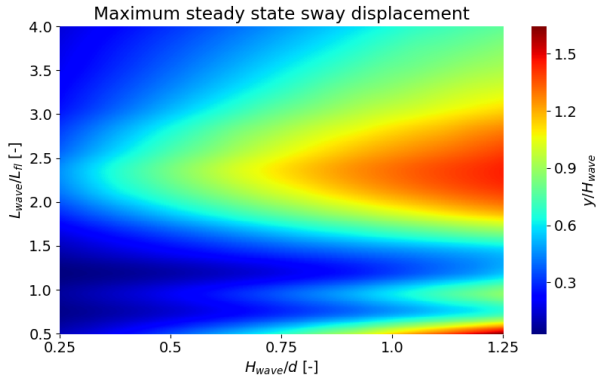

(a) Sway displacement

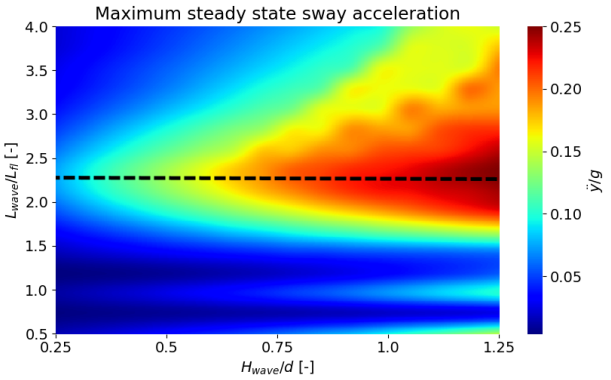

(b) Sway acceleration

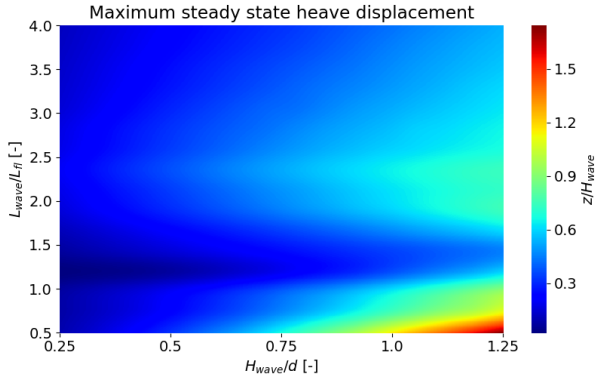

(c) Heave displacement

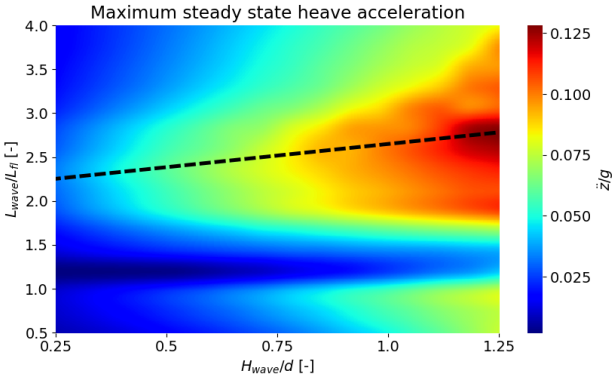

(d) Heave acceleration

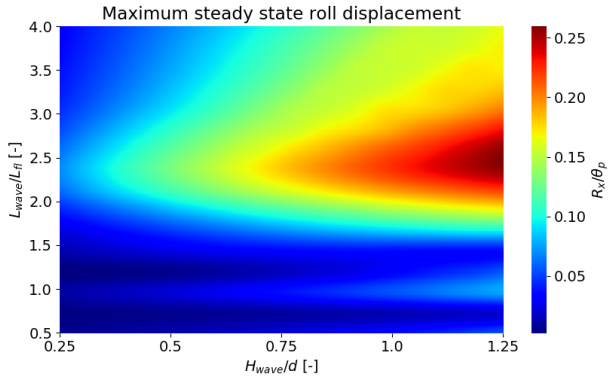

(e) Roll rotation

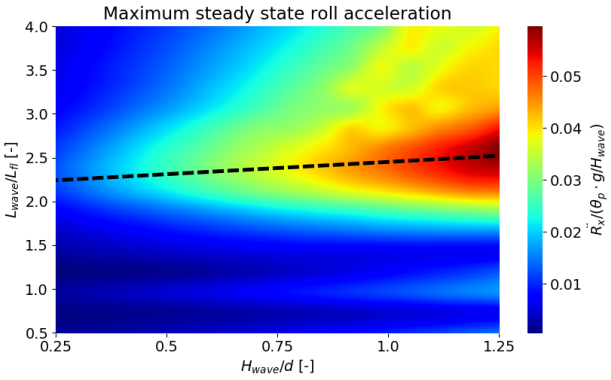

(f) Roll acceleration

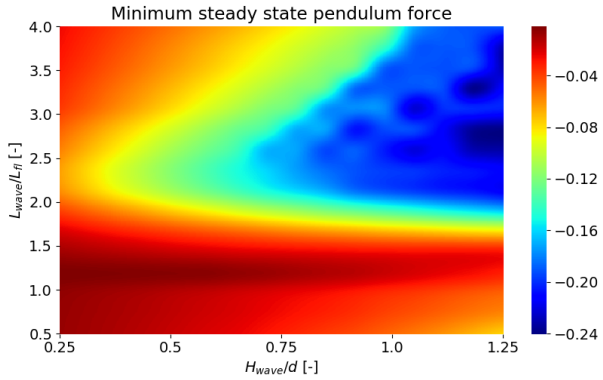

(g) Lowest (most negative) pendulum force

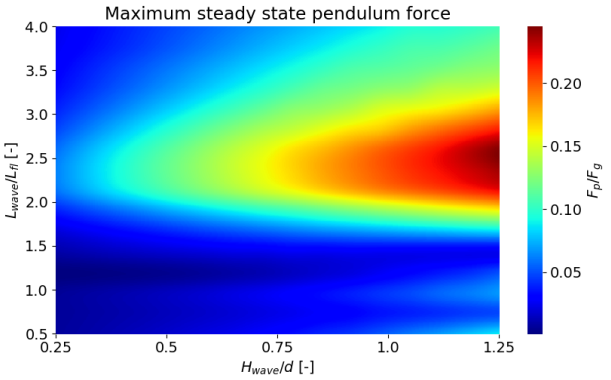

(h) Highest (most positive) pendulum force

Figure M.1: Steady state motion characteristics for positive directed waves as function of wave height and wave length

M.2. Wave height versus wave length: negative propagating waves

This section accompanies Subsection 6.1.1.

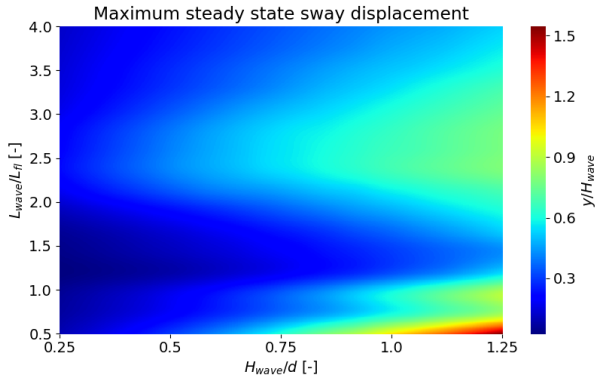

(a) Sway displacement

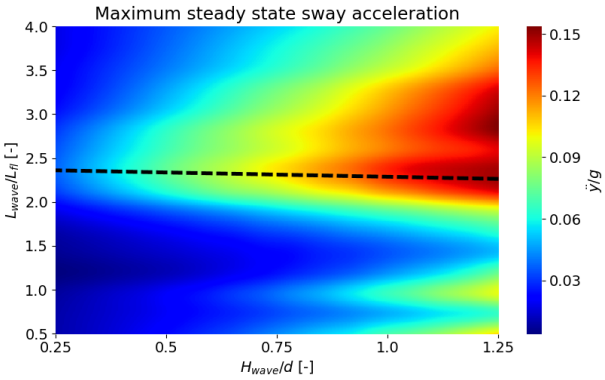

(b) Sway acceleration

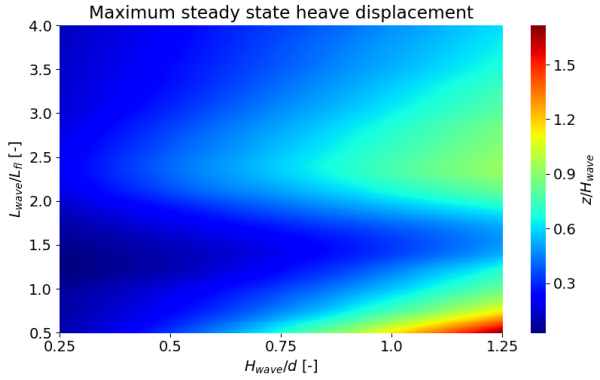

(c) Heave displacement

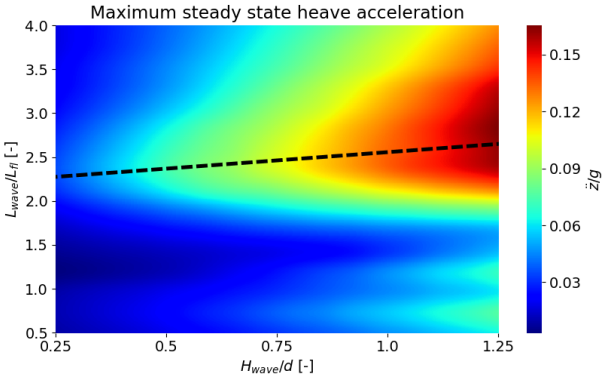

(d) Heave acceleration

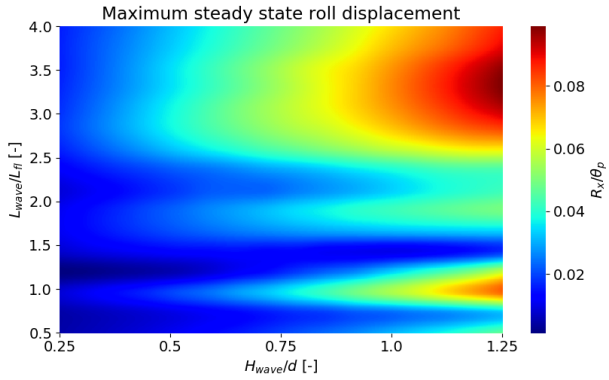

(e) Roll rotation

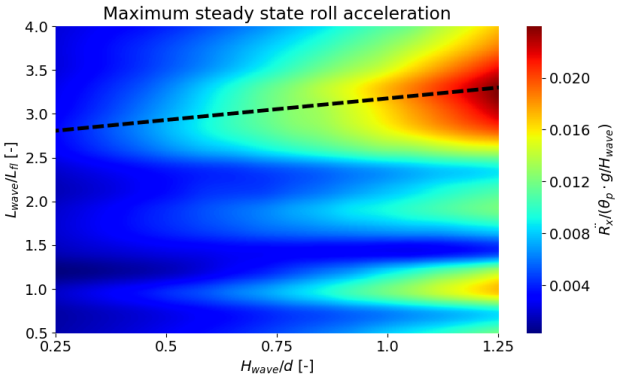

(f) Roll acceleration

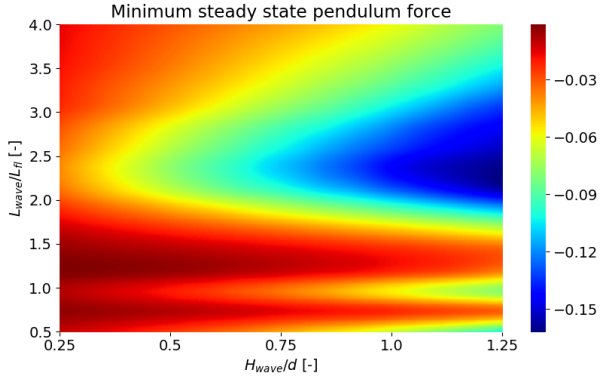

(g) Lowest (most negative) pendulum force

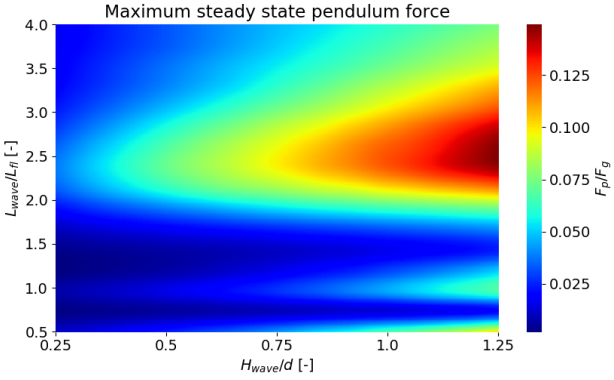

(h) Highest (most positive) pendulum force

Figure M.2: Steady state motion characteristics for negative directed waves as function of wave height and wave length

M.3. Flow velocity versus wave length (+ wave height)

This section accompanies Subsection 6.1.2.

Case A1

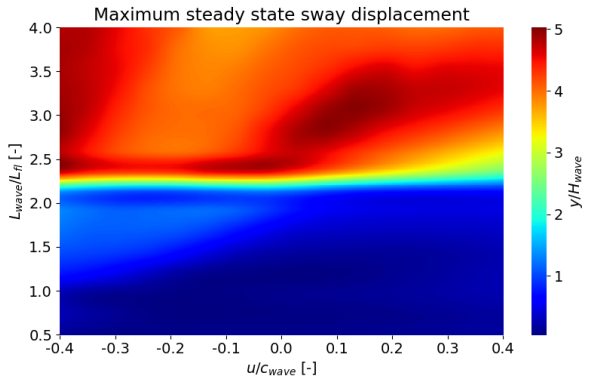

(a) Sway displacement

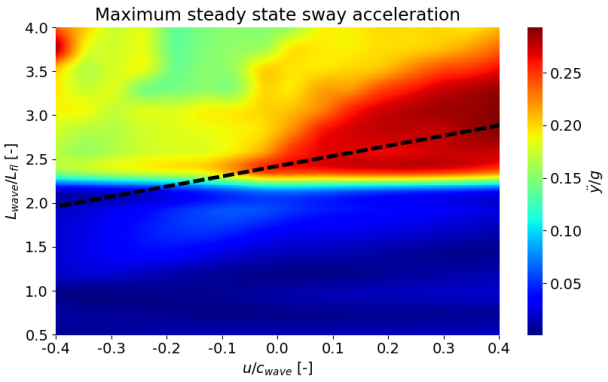

(b) Sway acceleration

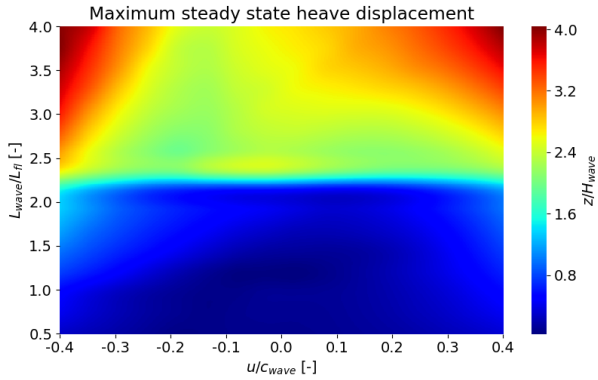

(c) Heave displacement

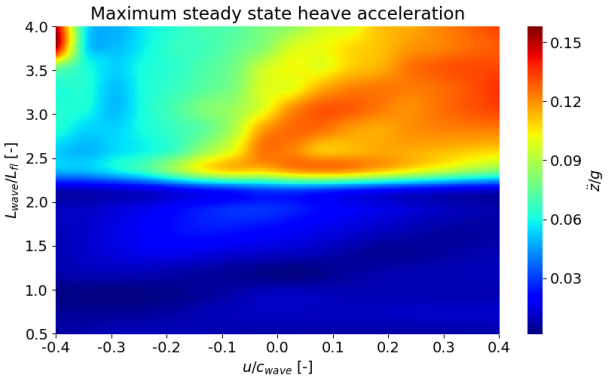

(d) Heave acceleration

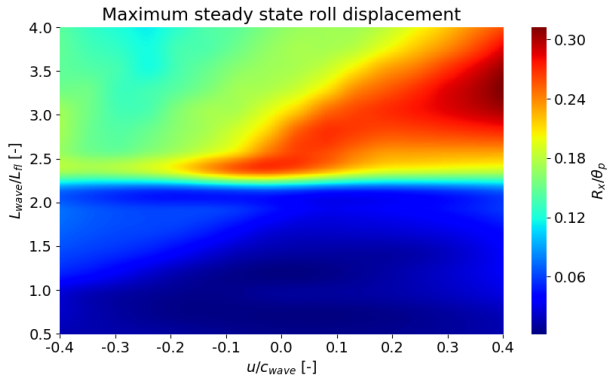

(e) Roll rotation

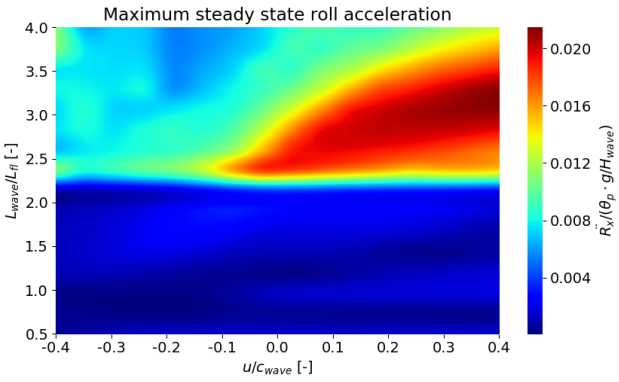

(f) Roll acceleration

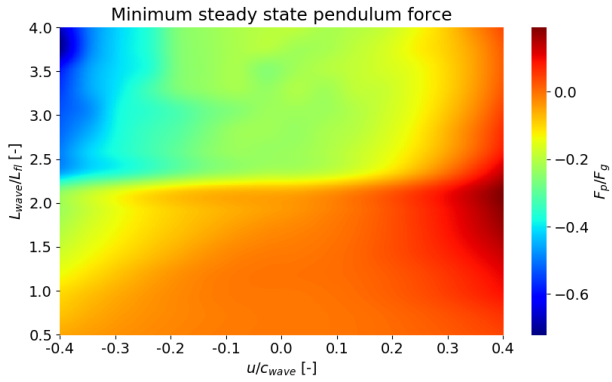

(g) Lowest (most negative) pendulum force

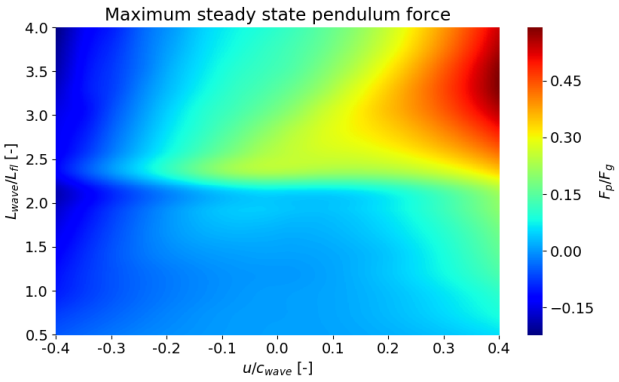

(h) Highest (most positive) pendulum force

Figure M.3: Steady state motion characteristics for Case A1 as function of flow velocity and wave length

Case A2

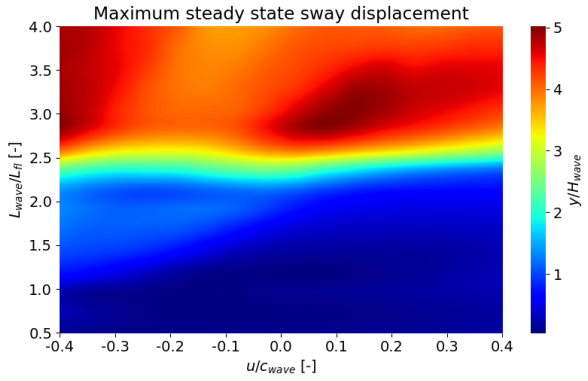

(a) Sway displacement

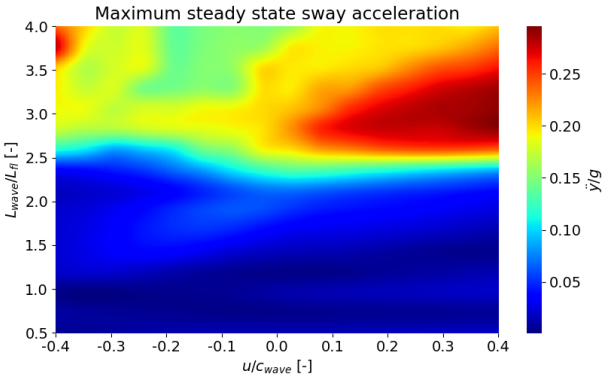

(b) Sway acceleration

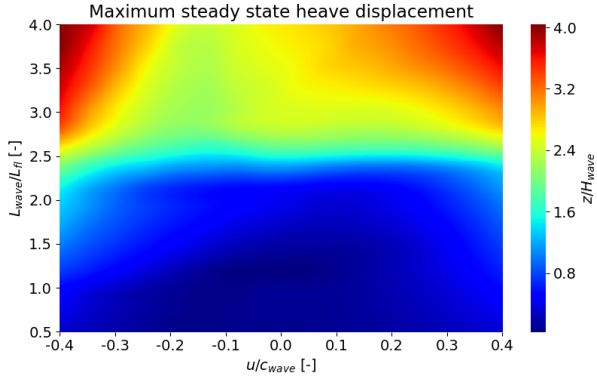

(c) Heave displacement

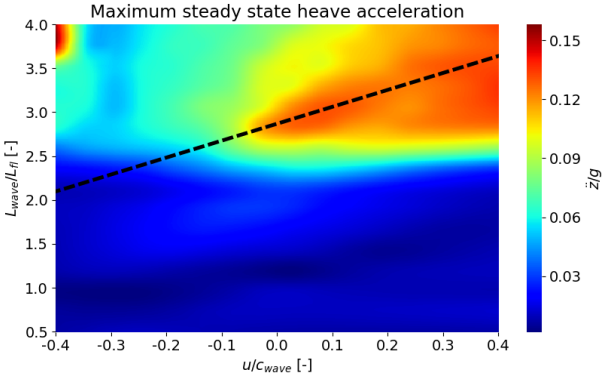

(d) Heave acceleration

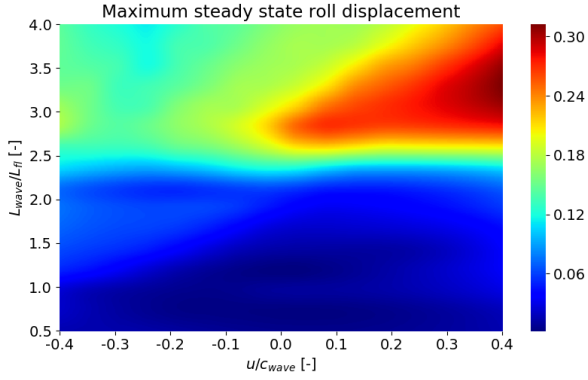

(e) Roll rotation

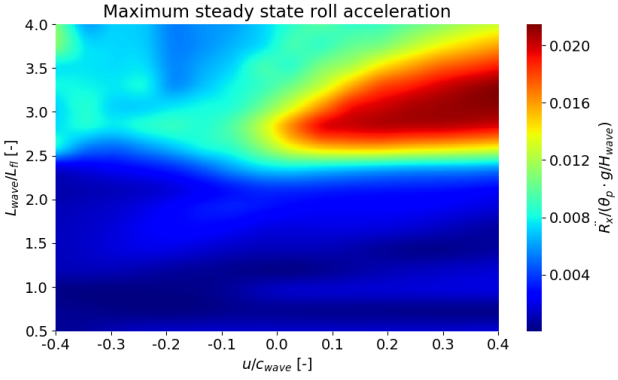

(f) Roll acceleration

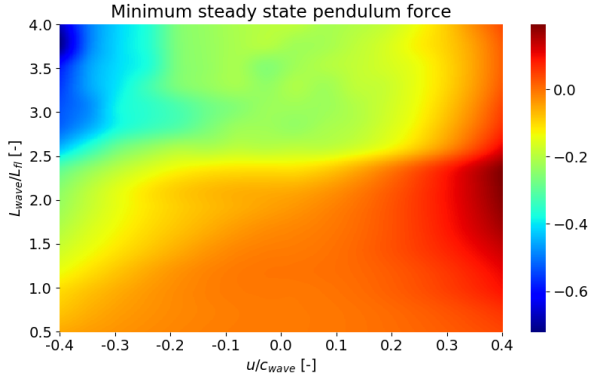

(g) Lowest (most negative) pendulum force

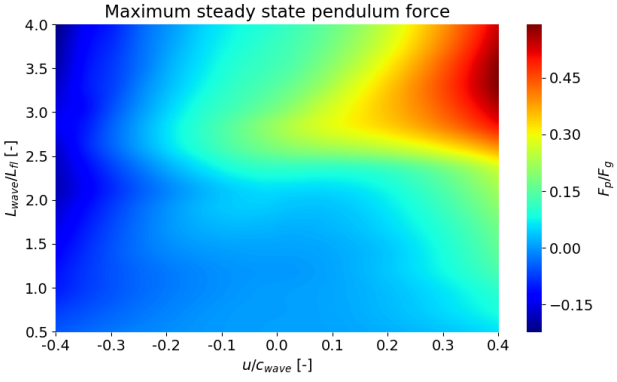

(h) Highest (most positive) pendulum force

Figure M.4: Steady state motion characteristics for Case A2 as function of flow velocity and wave length

Case A3

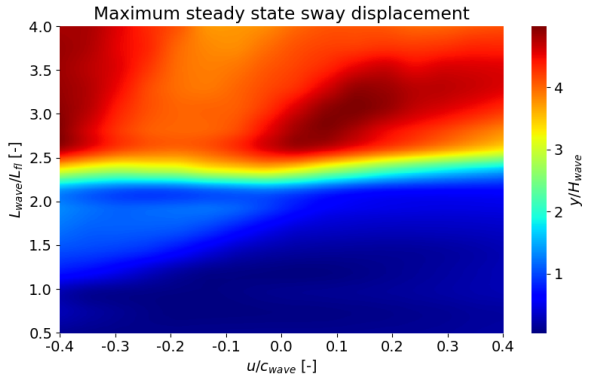

(a) Sway displacement

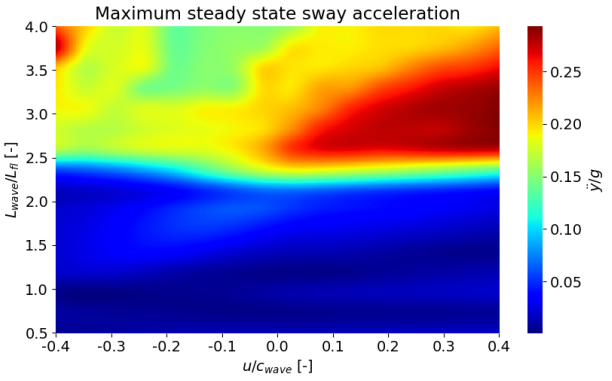

(b) Sway acceleration

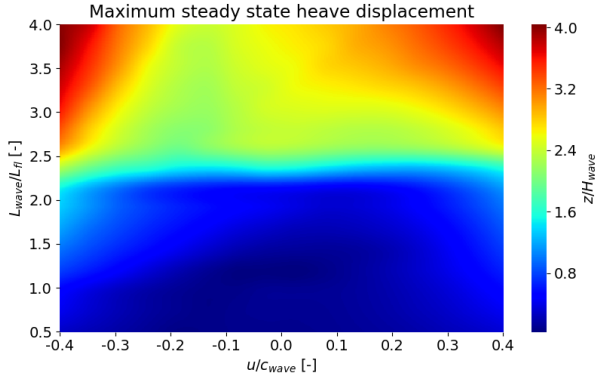

(c) Heave displacement

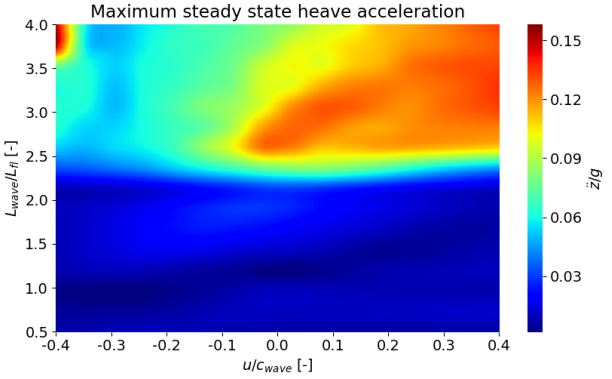

(d) Heave acceleration

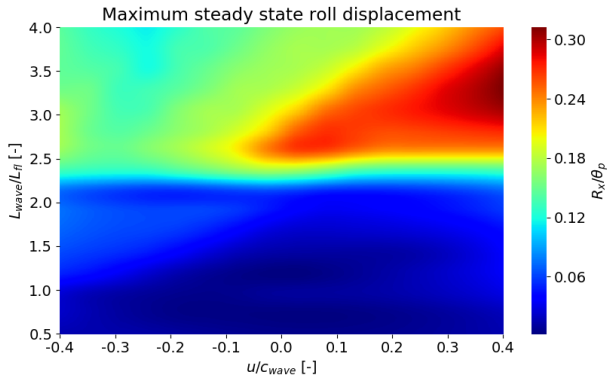

(e) Roll rotation

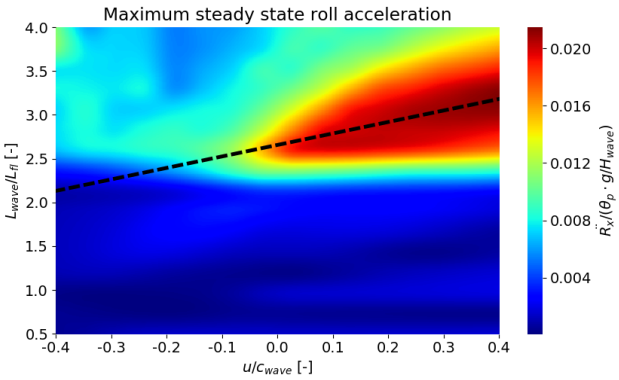

(f) Roll acceleration

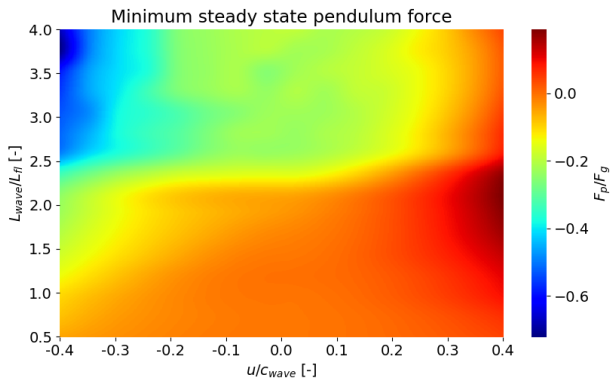

(g) Lowest (most negative) pendulum force

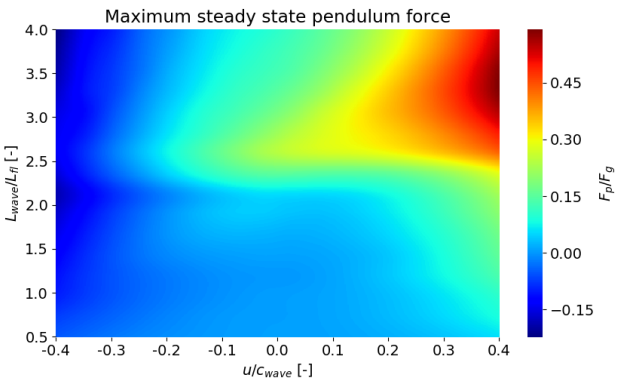

(h) Highest (most positive) pendulum force

Figure M.5: Steady state motion characteristics for Case A3 as function of flow velocity and wave length

Case A4

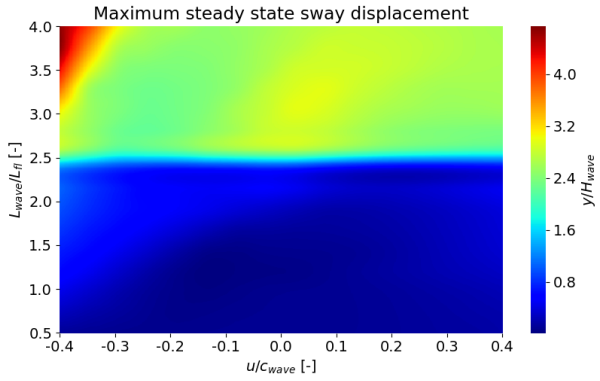

(a) Sway displacement

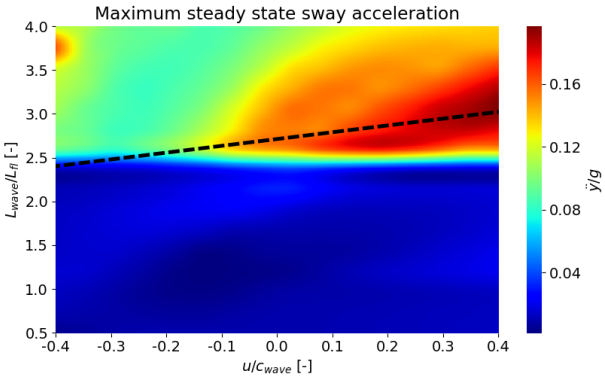

(b) Sway acceleration

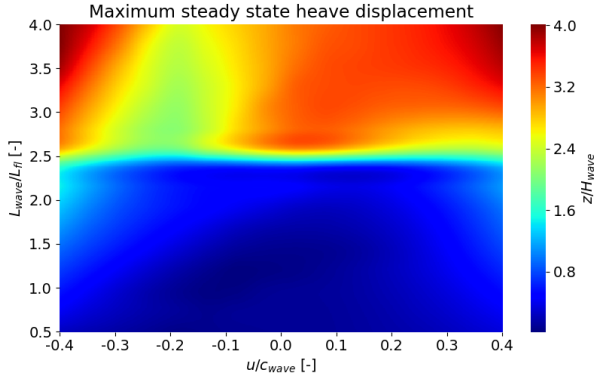

(c) Heave displacement

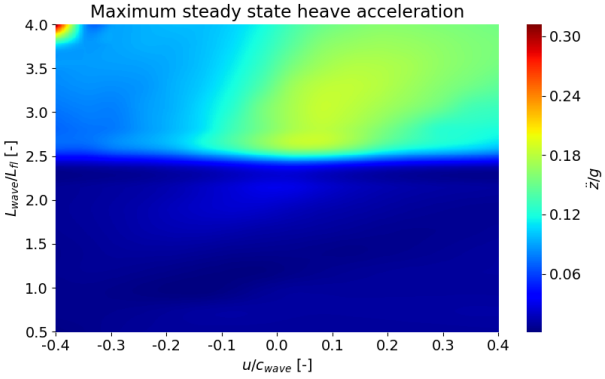

(d) Heave acceleration

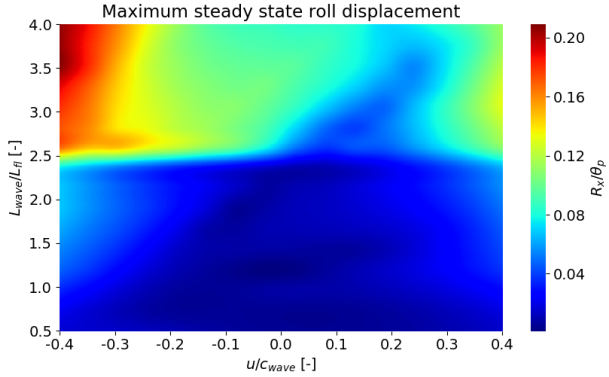

(e) Roll rotation

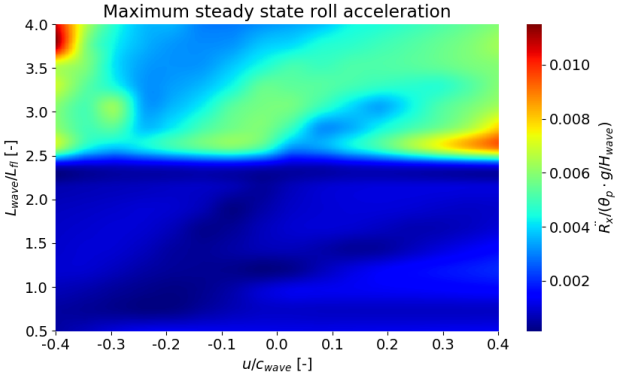

(f) Roll acceleration

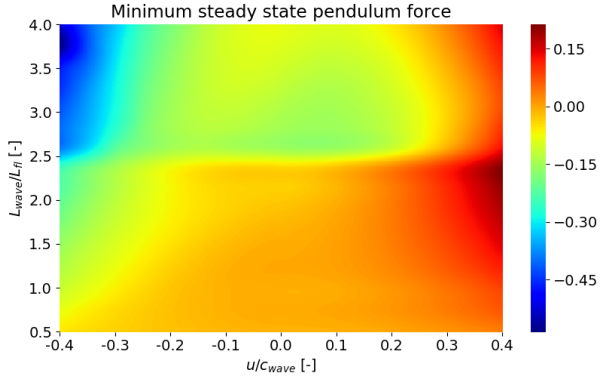

(g) Lowest (most negative) pendulum force

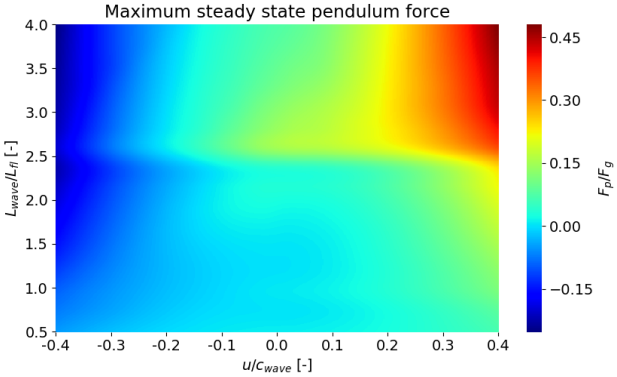

(h) Highest (most positive) pendulum force

Figure M.6: Steady state motion characteristics for Case A4 as function of flow velocity and wave length

Case A5

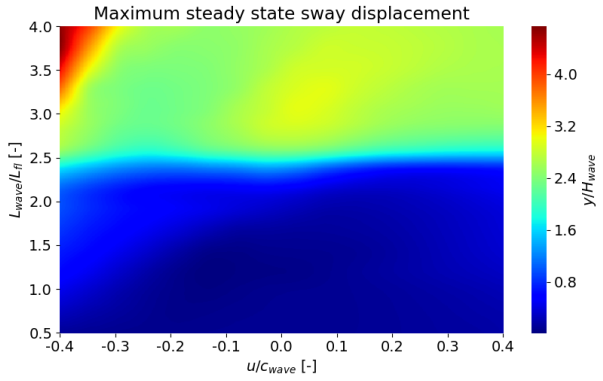

(a) Sway displacement

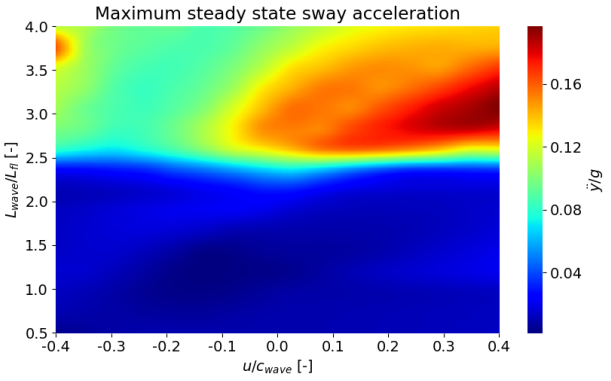

(b) Sway acceleration

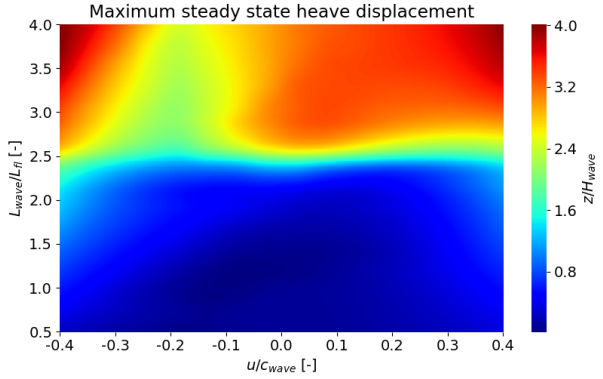

(c) Heave displacement

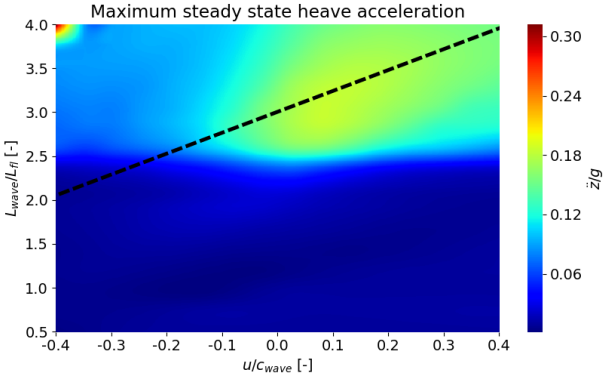

(d) Heave acceleration

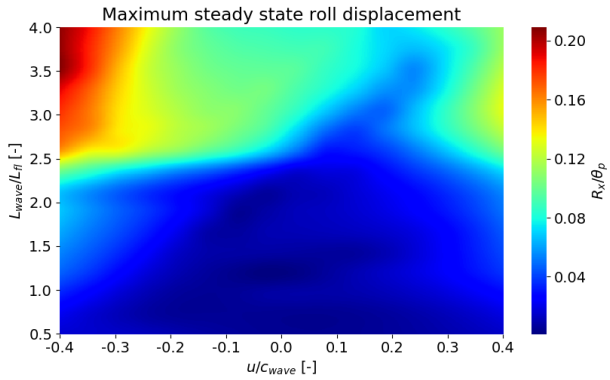

(e) Roll rotation

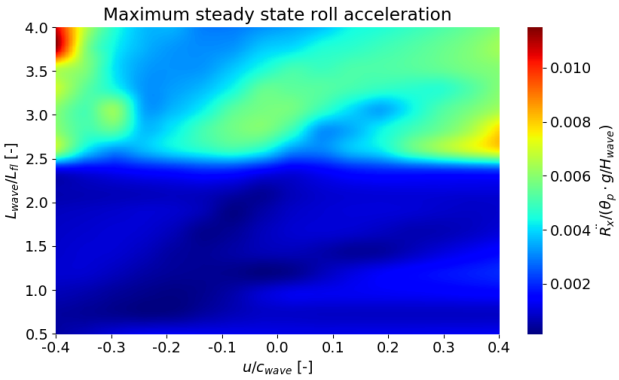

(f) Roll acceleration

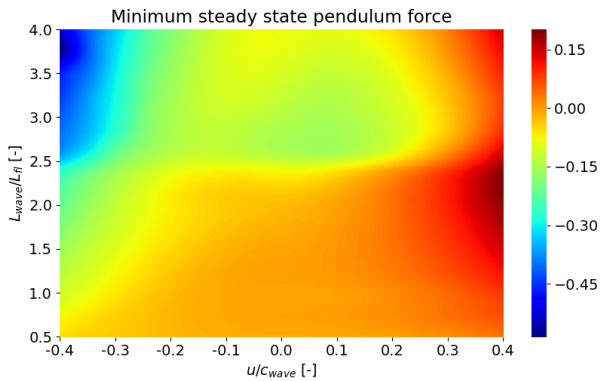

(g) Lowest (most negative) pendulum force

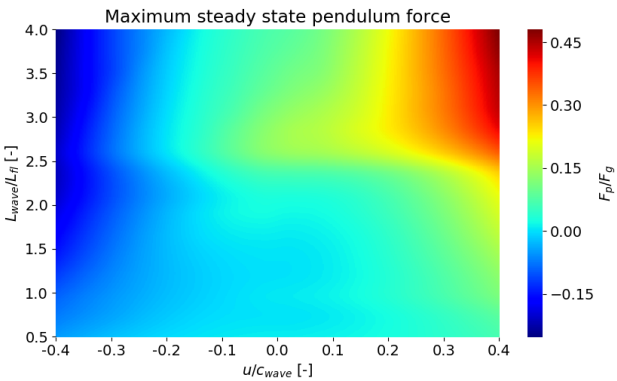

(h) Highest (most positive) pendulum force

Figure M.7: Steady state motion characteristics for Case A5 as function of flow velocity and wave length

Case A6

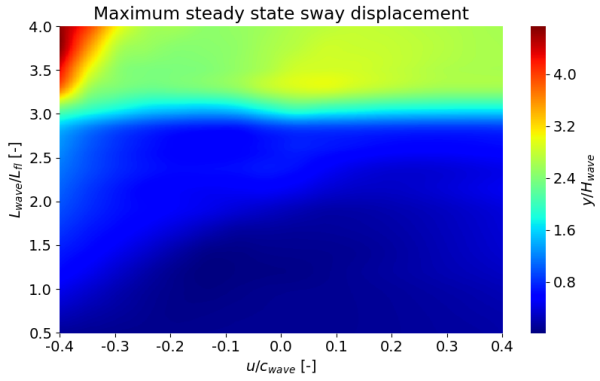

(a) Sway displacement

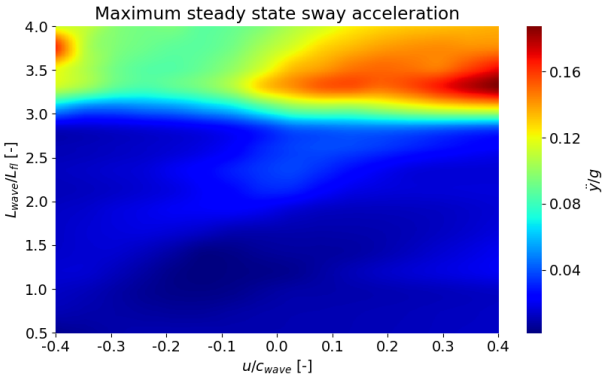

(b) Sway acceleration

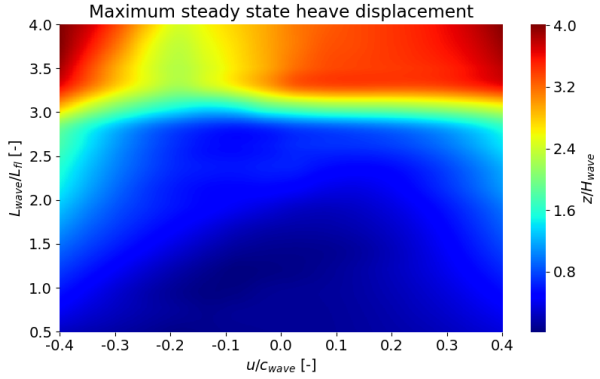

(c) Heave displacement

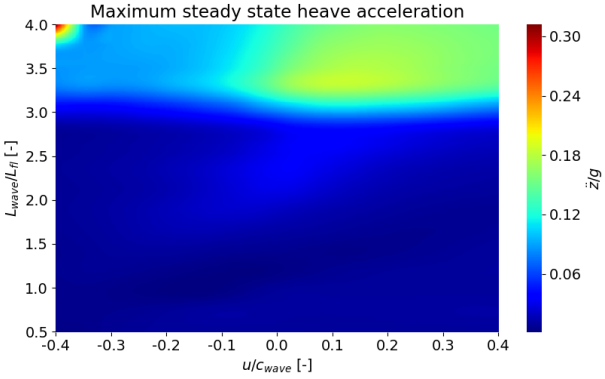

(d) Heave acceleration

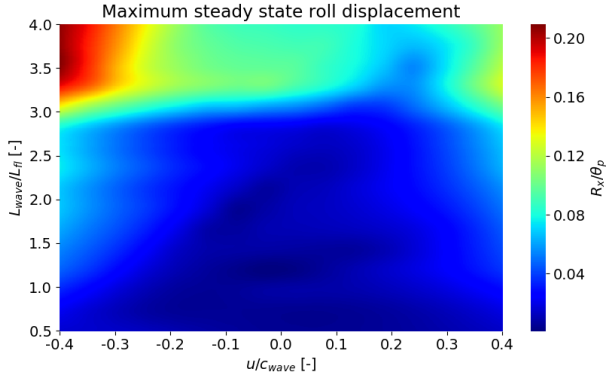

(e) Roll rotation

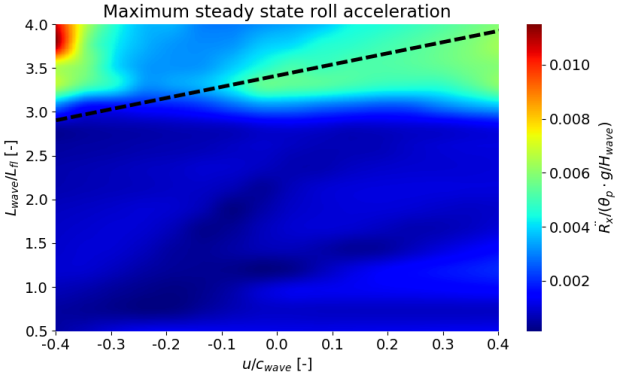

(f) Roll acceleration

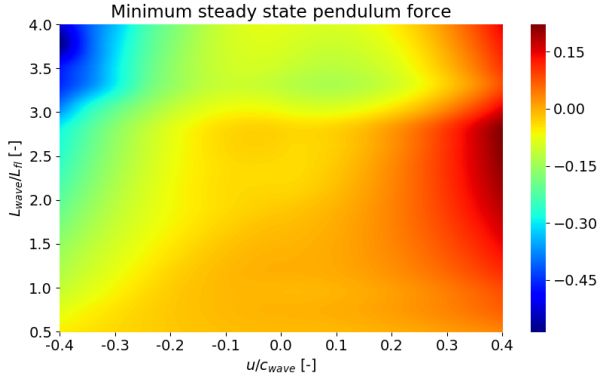

(g) Lowest (most negative) pendulum force

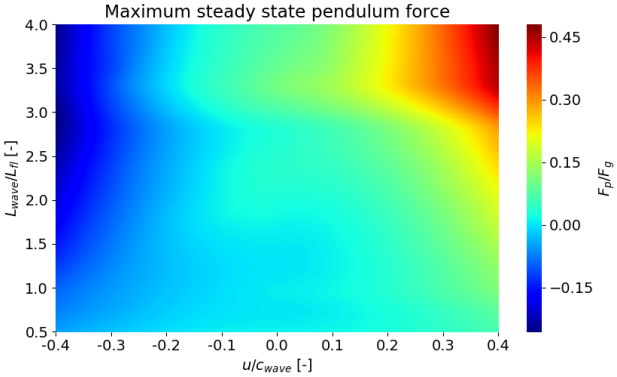

(h) Highest (most positive) pendulum force

Figure M.8: Steady state motion characteristics for Case A6 as function of flow velocity and wave length

M.4. Wind force versus wave length (+ wave height + flow velocity)

This section accompanies Subsection 6.1.3.

Case B1

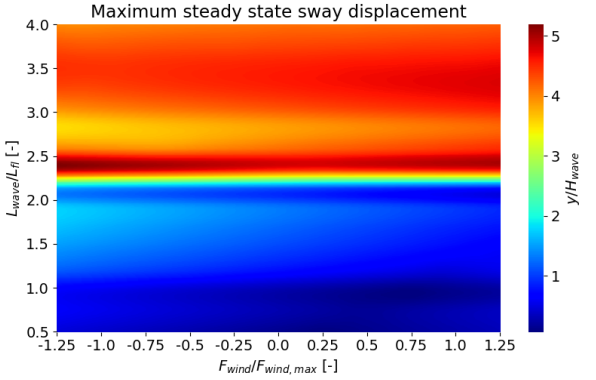

(a) Sway displacement

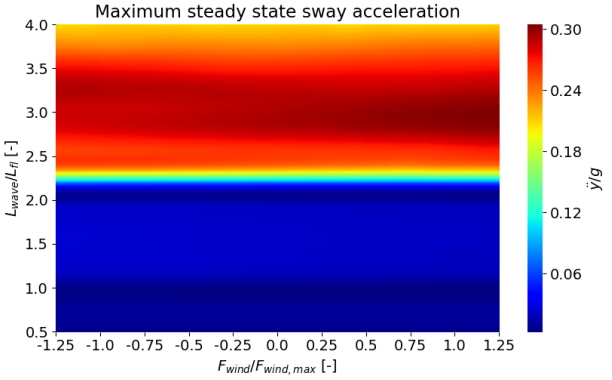

(b) Sway acceleration

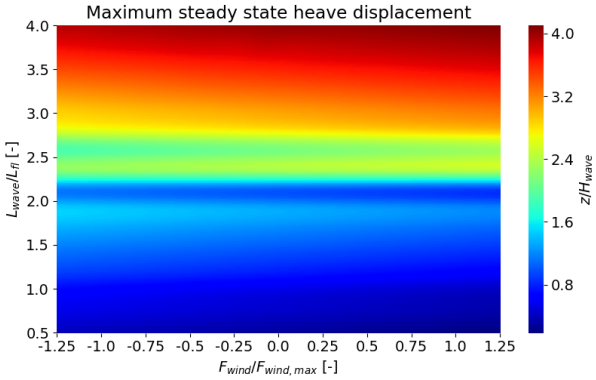

(c) Heave displacement

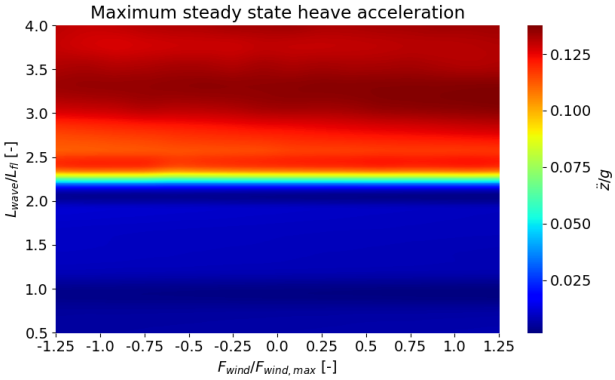

(d) Heave acceleration

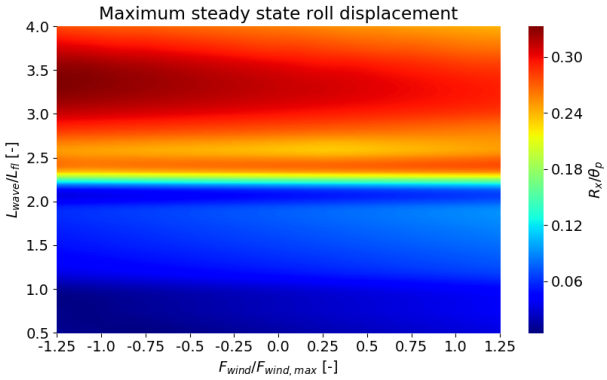

(e) Roll rotation

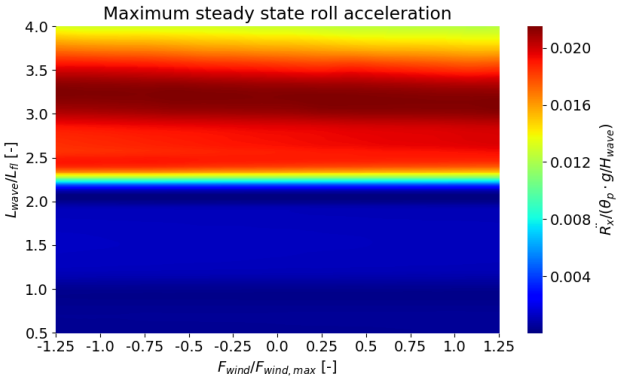

(f) Roll acceleration

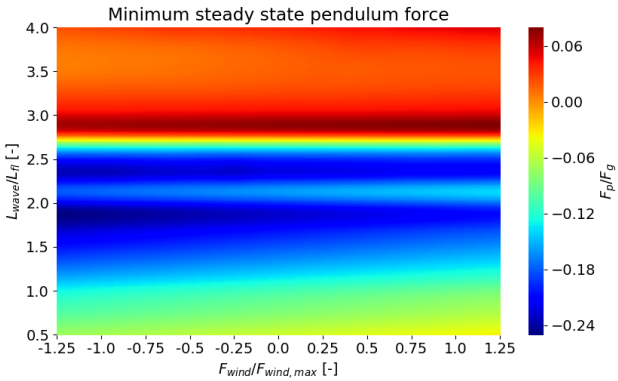

(g) Lowest (most negative) pendulum force

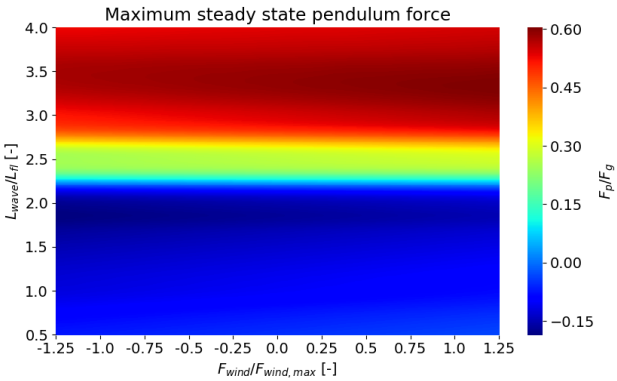

(h) Highest (most positive) pendulum force

Figure M.9: Steady state motion characteristics for Case B1 as function of wind pressure and wave length

Case B2

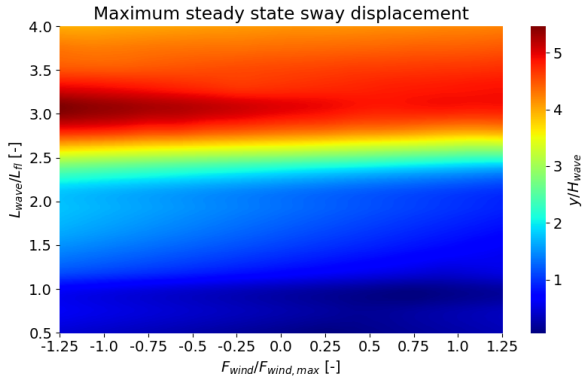

(a) Sway displacement

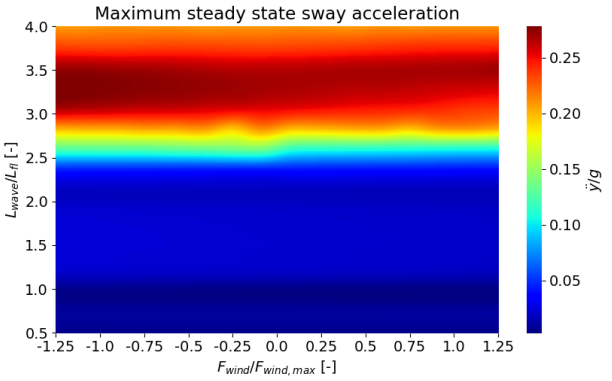

(b) Sway acceleration

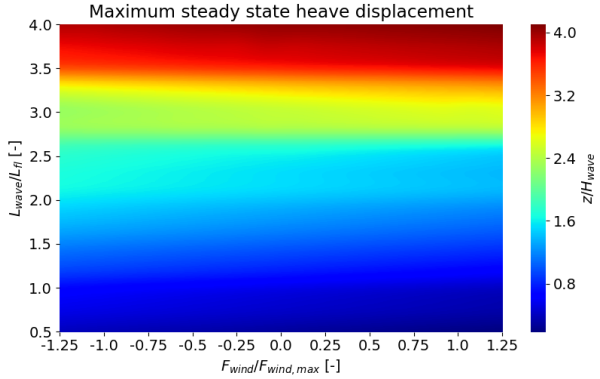

(c) Heave displacement

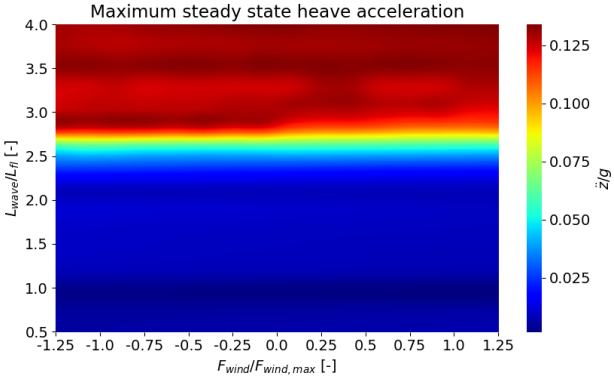

(d) Heave acceleration

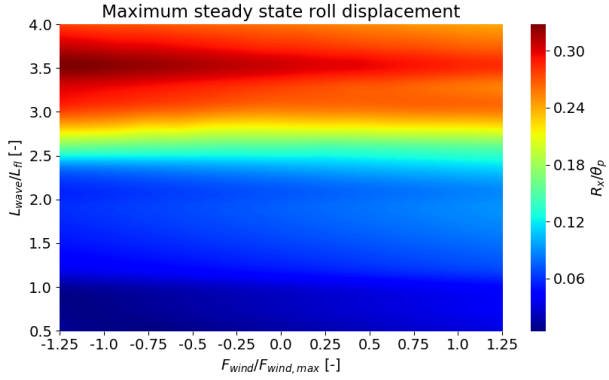

(e) Roll rotation

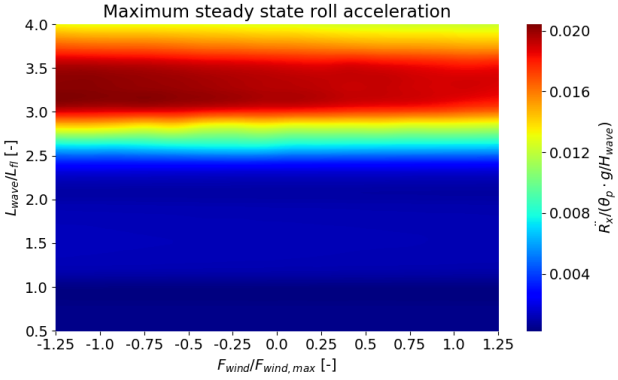

(f) Roll acceleration

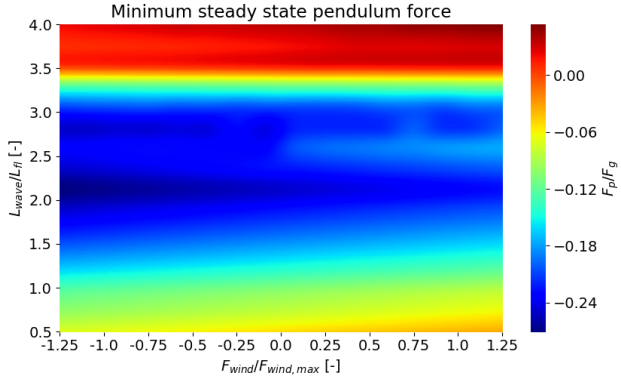

(g) Lowest (most negative) pendulum force

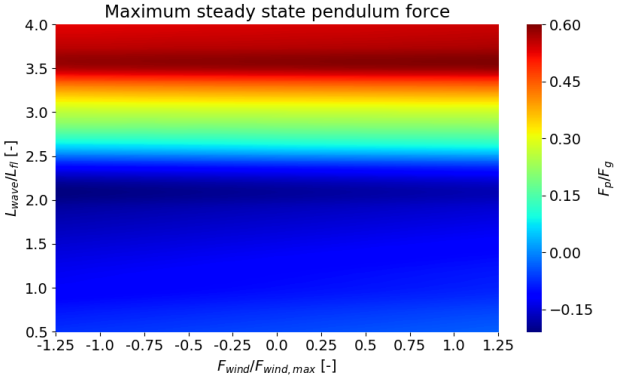

(h) Highest (most positive) pendulum force

Figure M.10: Steady state motion characteristics for Case B2 as function of wind pressure and wave length

Case B3

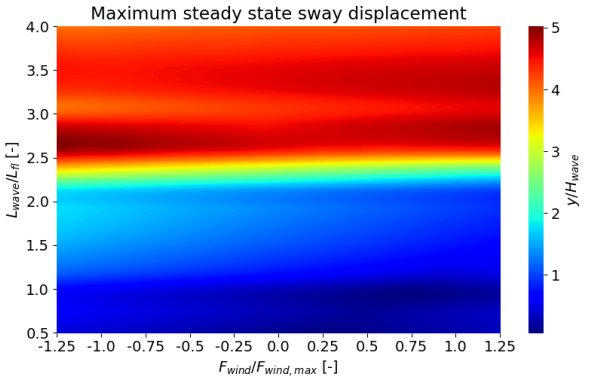

(a) Sway displacement

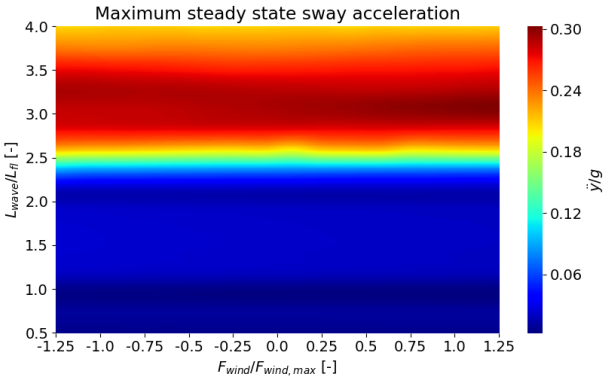

(b) Sway acceleration

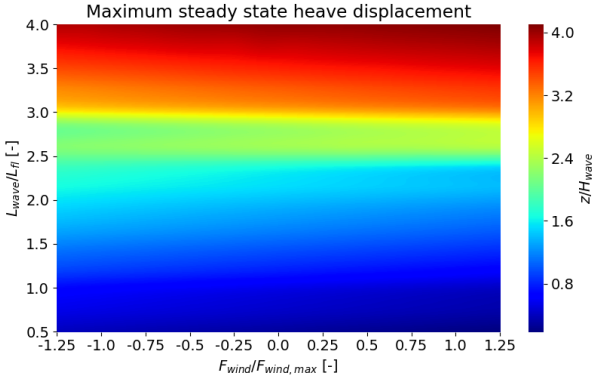

(c) Heave displacement

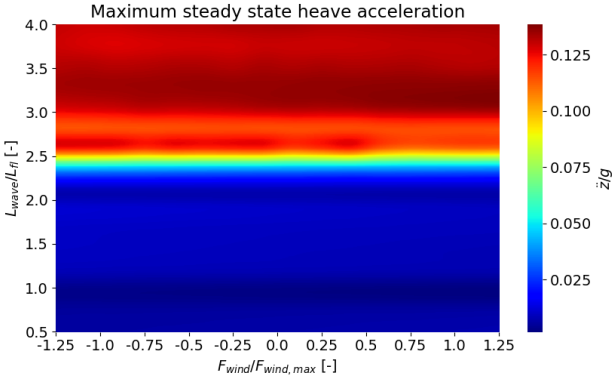

(d) Heave acceleration

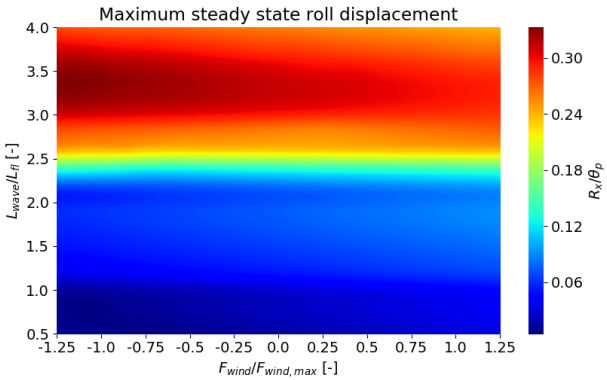

(e) Roll rotation

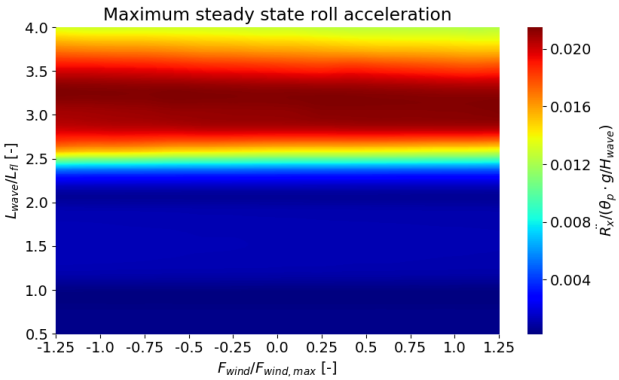

(f) Roll acceleration

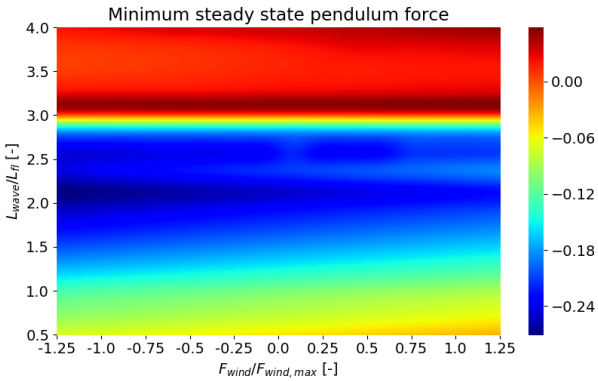

(g) Lowest (most negative) pendulum force

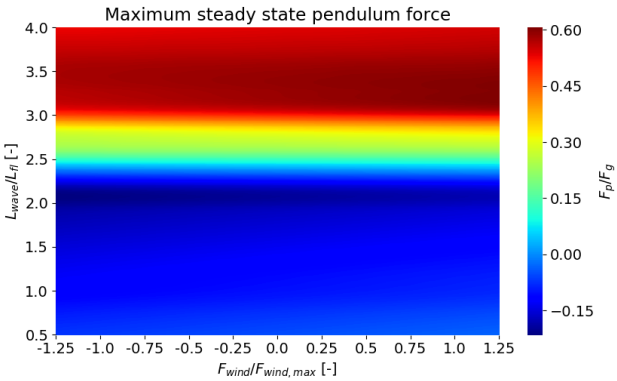

(h) Highest (most positive) pendulum force

Figure M.11: Steady state motion characteristics for Case B3 as function of wind pressure and wave length

Case B4

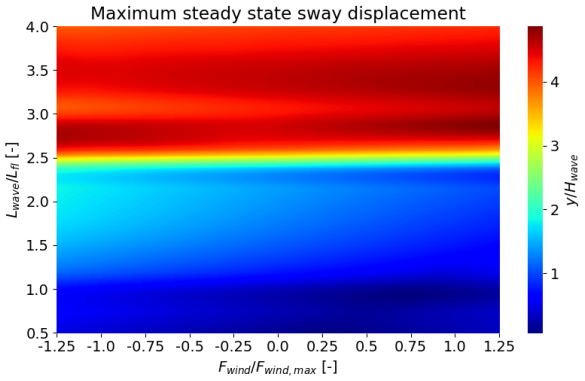

(a) Sway displacement

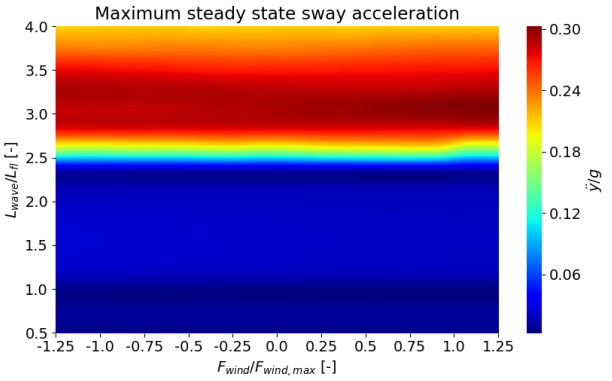

(b) Sway acceleration

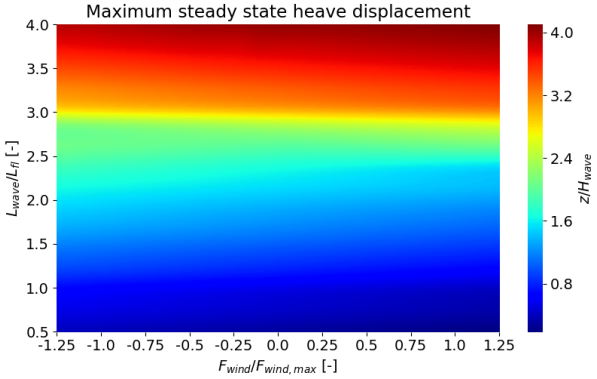

(c) Heave displacement

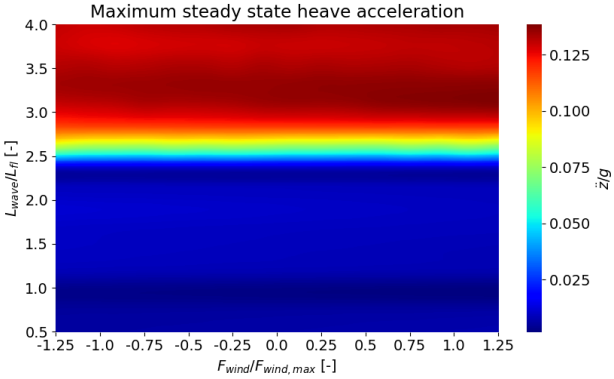

(d) Heave acceleration

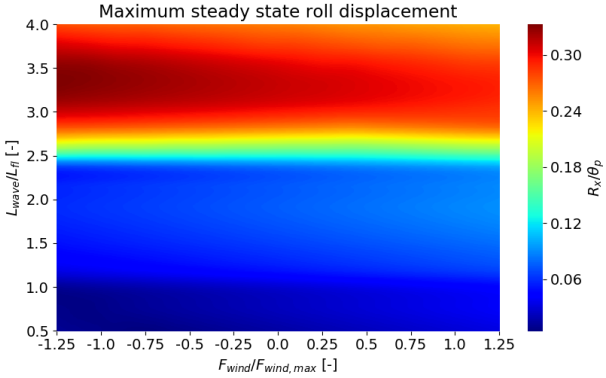

(e) Roll rotation

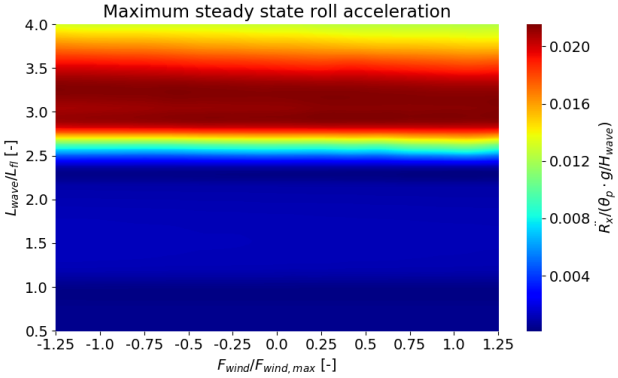

(f) Roll acceleration

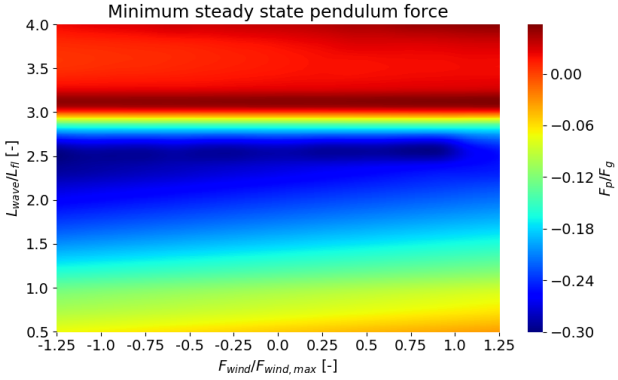

(g) Lowest (most negative) pendulum force

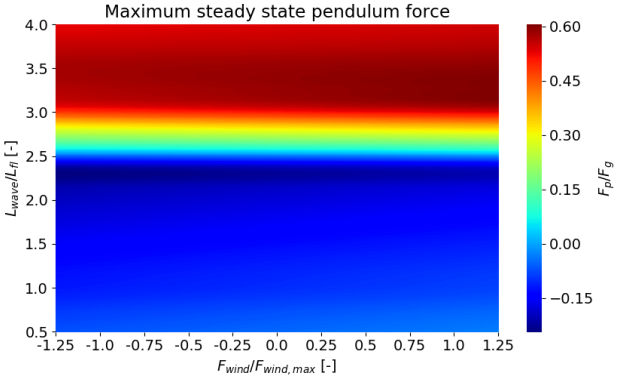

(h) Highest (most positive) pendulum force

Figure M.12: Steady state motion characteristics for Case B4 as function of wind pressure and wave length

Case B5

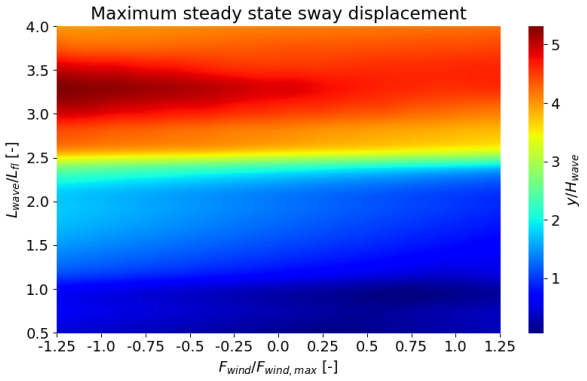

(a) Sway displacement

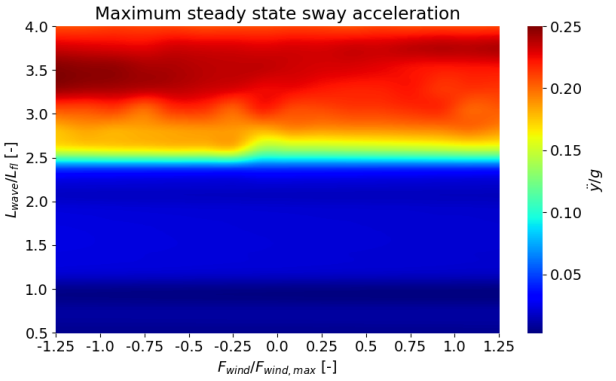

(b) Sway acceleration

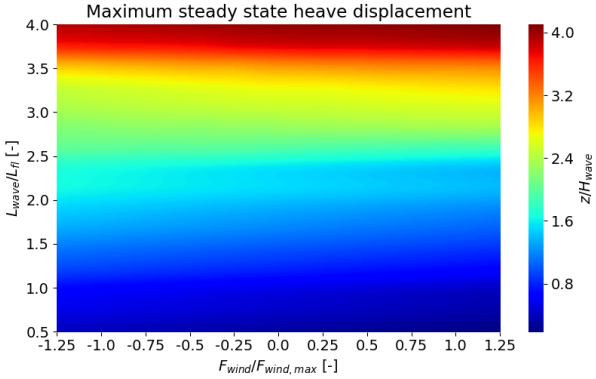

(c) Heave displacement

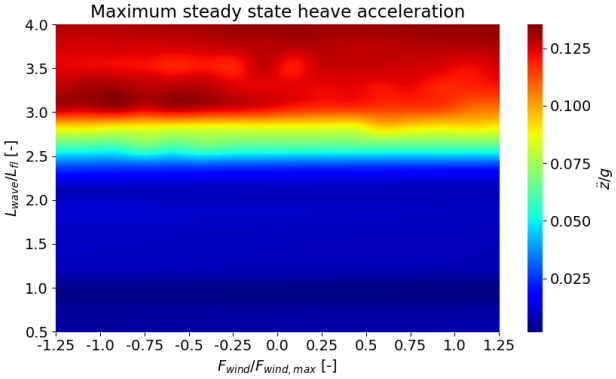

(d) Heave acceleration

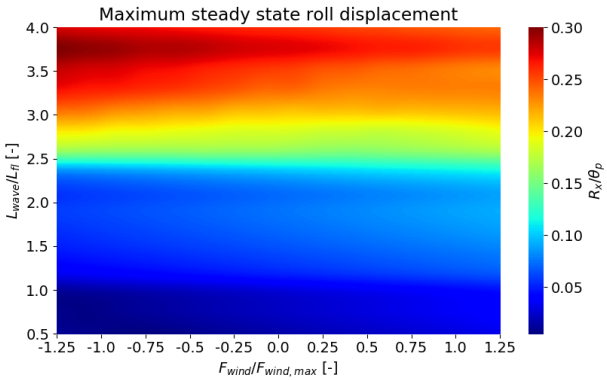

(e) Roll rotation

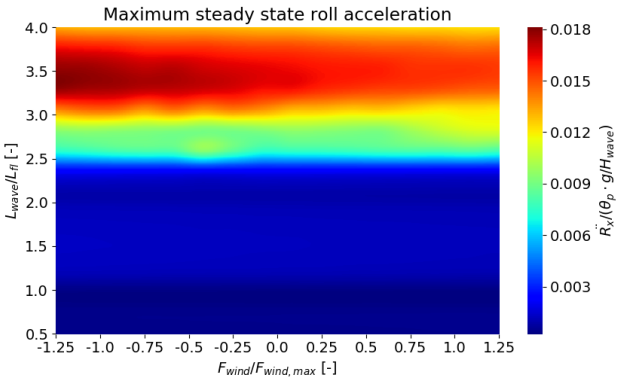

(f) Roll acceleration

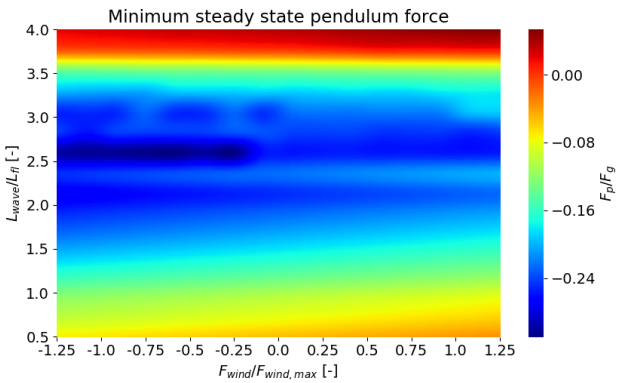

(g) Lowest (most negative) pendulum force

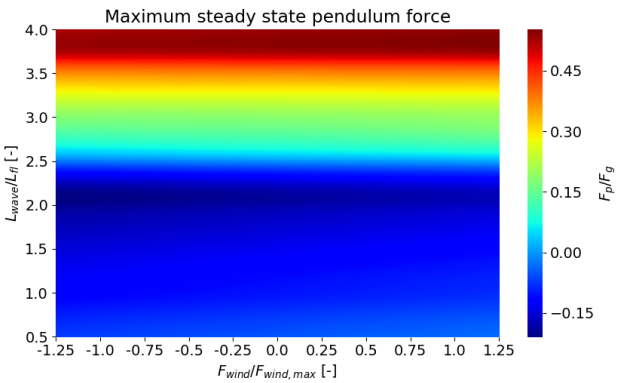

(h) Highest (most positive) pendulum force

Figure M.13: Steady state motion characteristics for Case B5 as function of wind pressure and wave length

Case B6

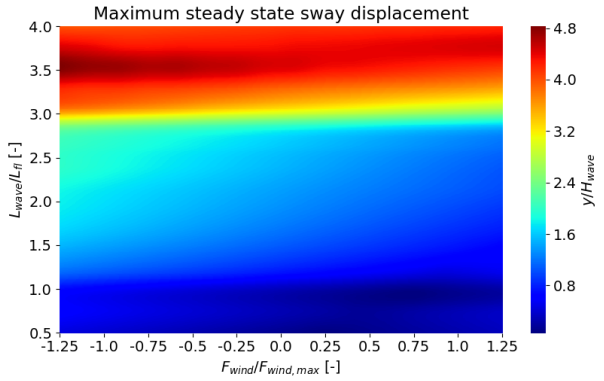

(a) Sway displacement

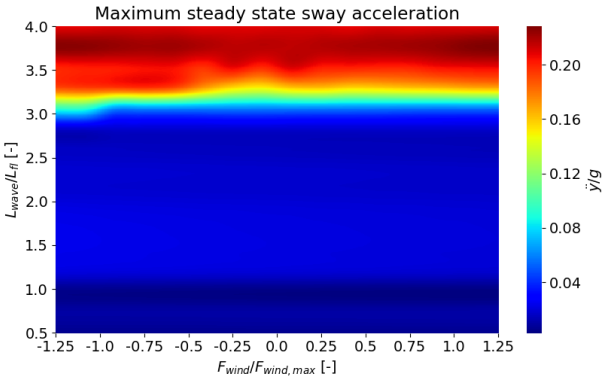

(b) Sway acceleration

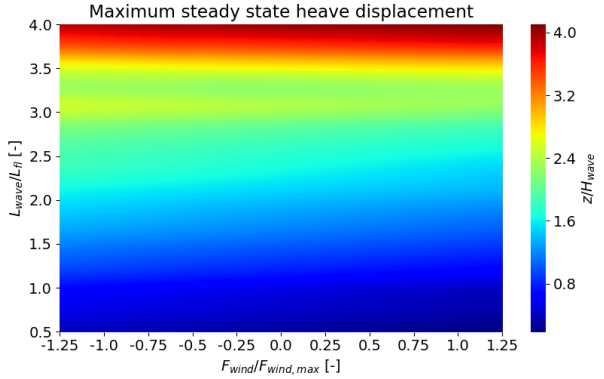

(c) Heave displacement

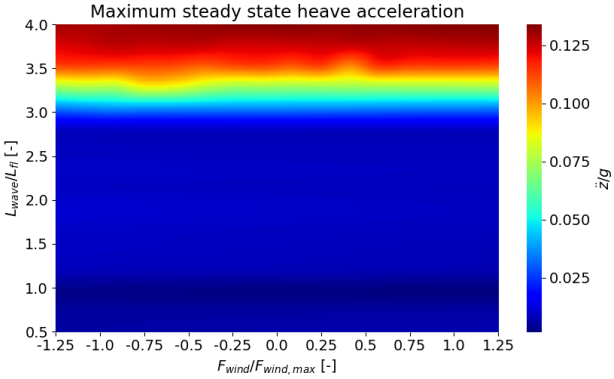

(d) Heave acceleration

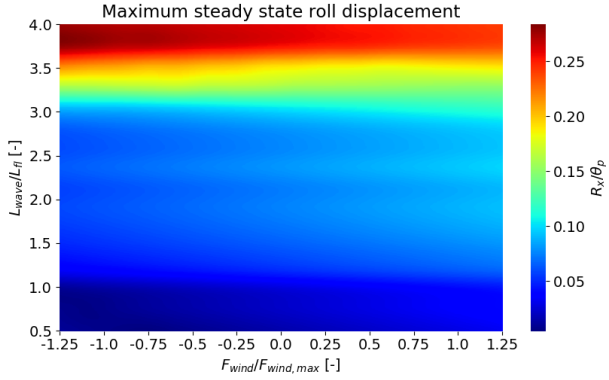

(e) Roll rotation

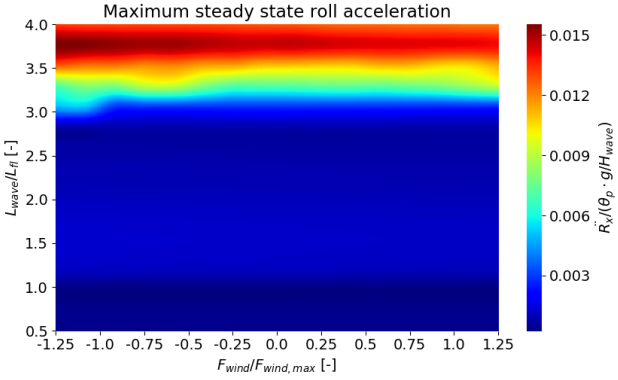

(f) Roll acceleration

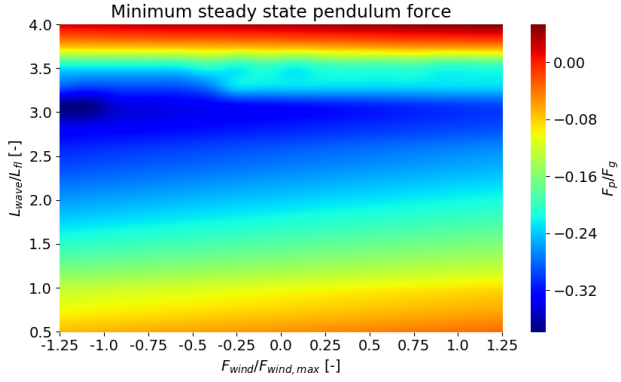

(g) Lowest (most negative) pendulum force

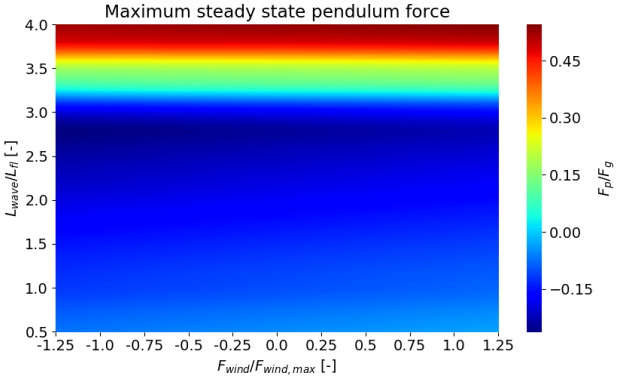

(h) Highest (most positive) pendulum force

Figure M.14: Steady state motion characteristics for Case B6 as function of wind pressure and wave length

M.5. Pendulum angle versus wave length (+ wave height + flow velocity + wind force)

This section accompanies Subsection 6.1.4.

Case C1

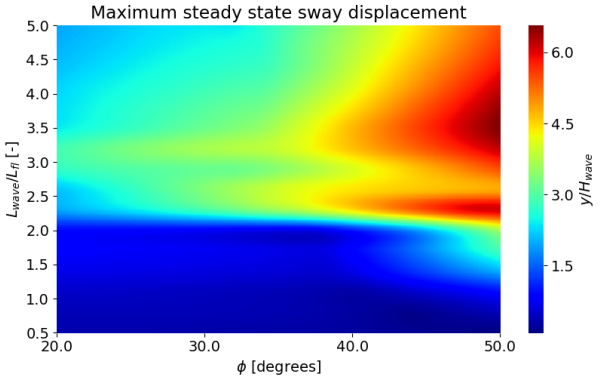

(a) Sway displacement

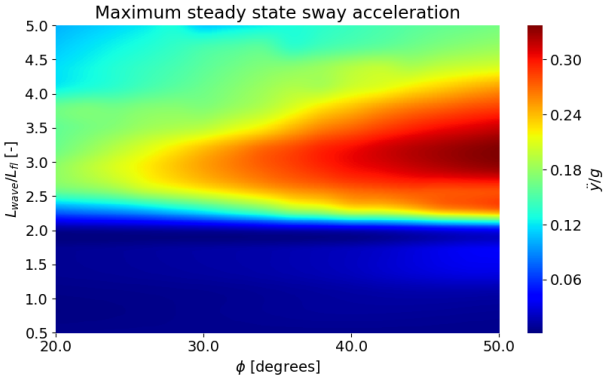

(b) Sway acceleration

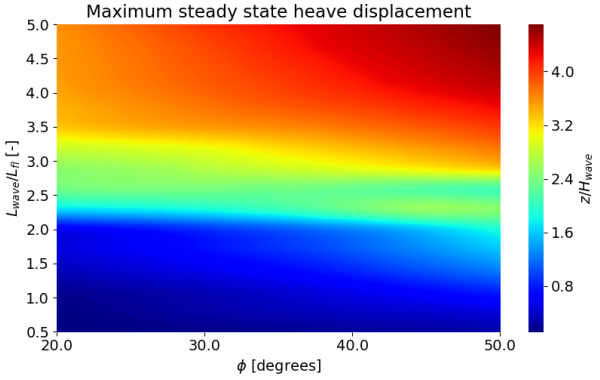

(c) Heave displacement

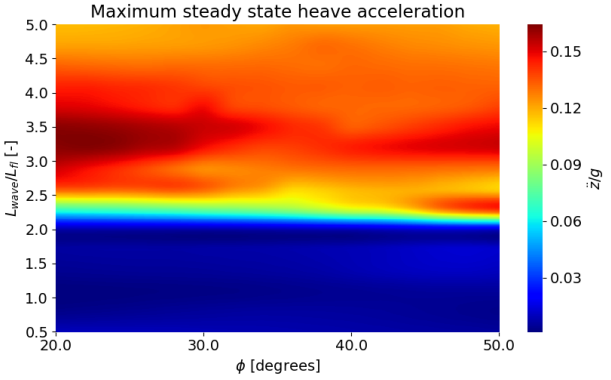

(d) Heave acceleration

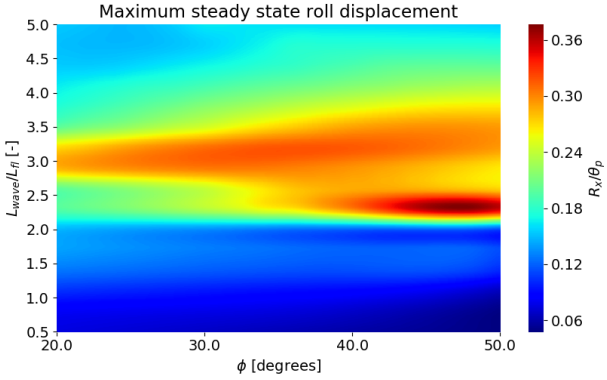

(e) Roll rotation

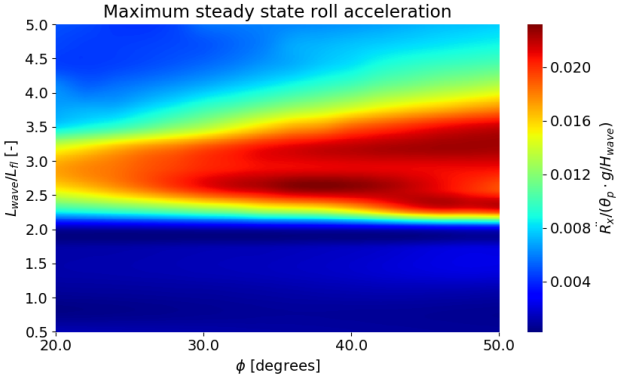

(f) Roll acceleration

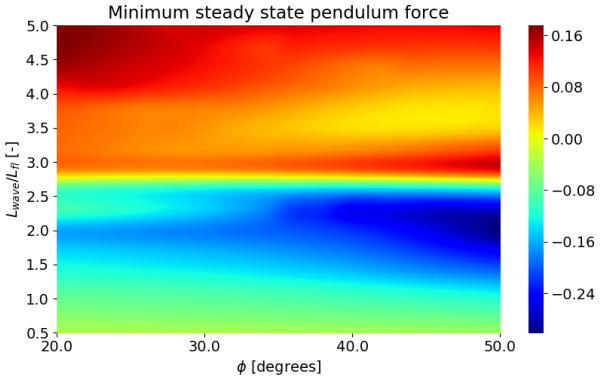

(g) Lowest (most negative) pendulum force

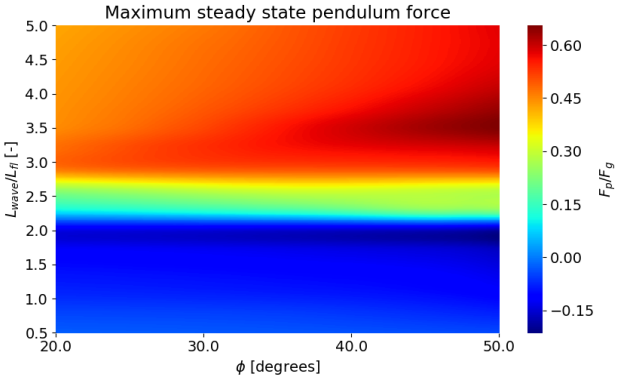

(h) Highest (most positive) pendulum force

Figure M.15: Steady state motion characteristics for Case C1 as function of pendulum angle and wave length

Case C2

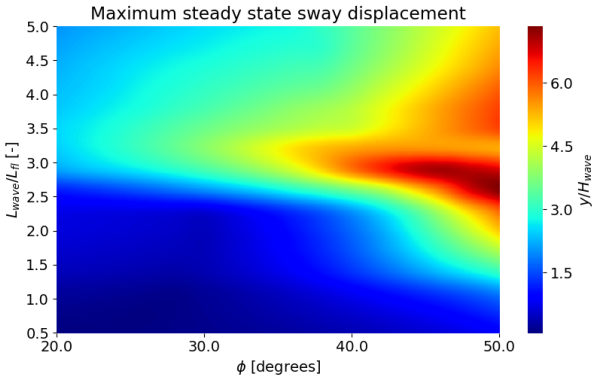

(a) Sway displacement

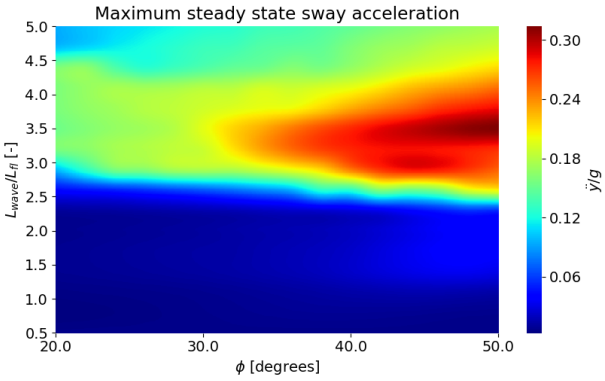

(b) Sway acceleration

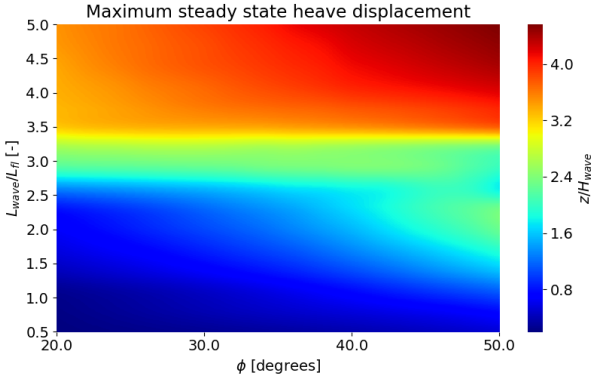

(c) Heave displacement

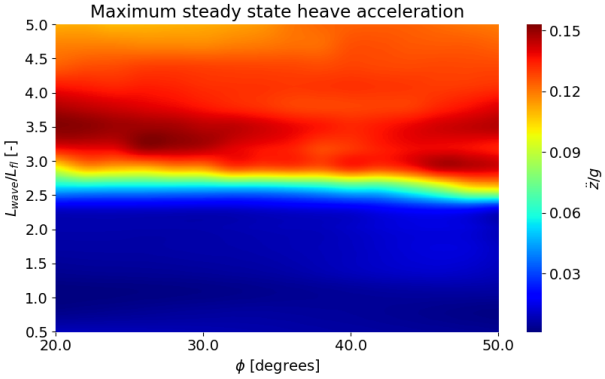

(d) Heave acceleration

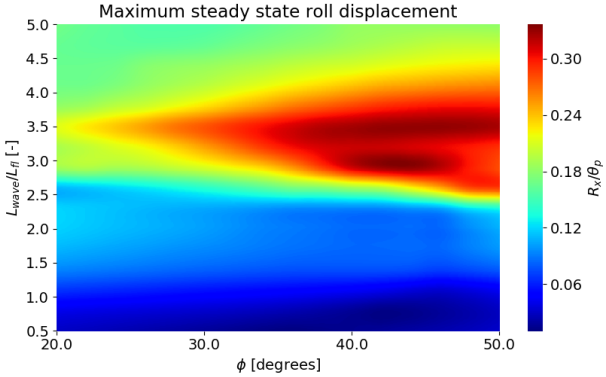

(e) Roll rotation

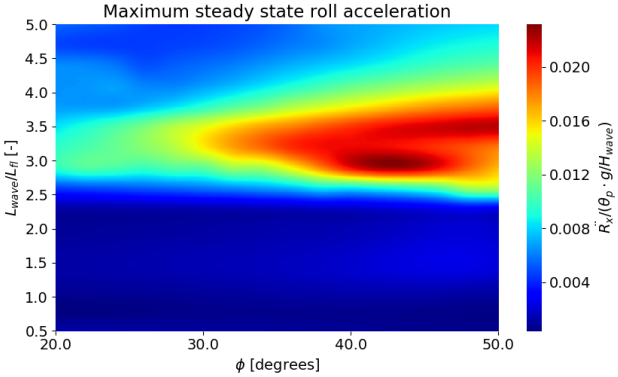

(f) Roll acceleration

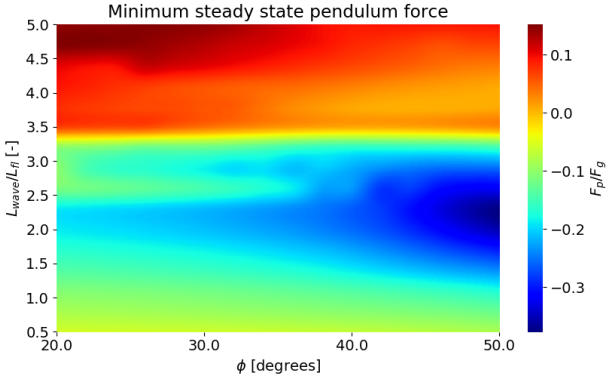

(g) Lowest (most negative) pendulum force

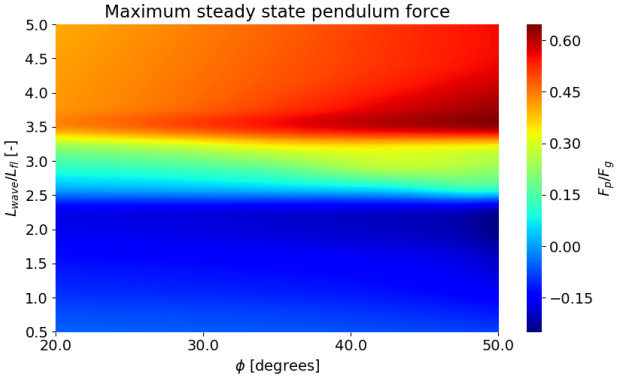

(h) Highest (most positive) pendulum force

Figure M.16: Steady state motion characteristics for Case C2 as function of pendulum angle and wave length

Case C3

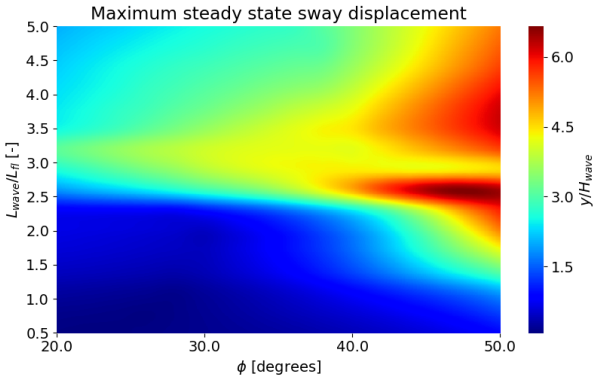

(a) Sway displacement

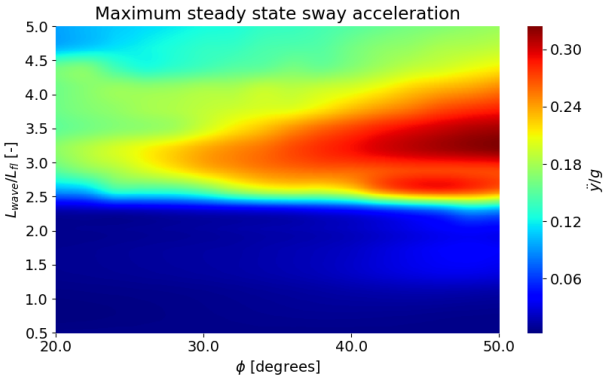

(b) Sway acceleration

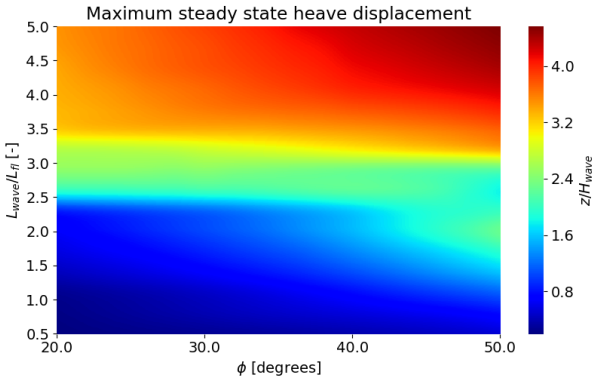

(c) Heave displacement

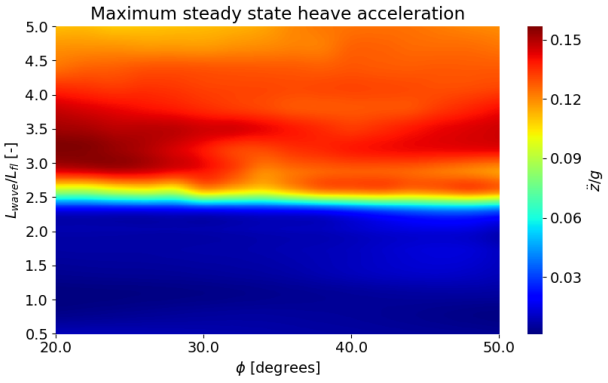

(d) Heave acceleration

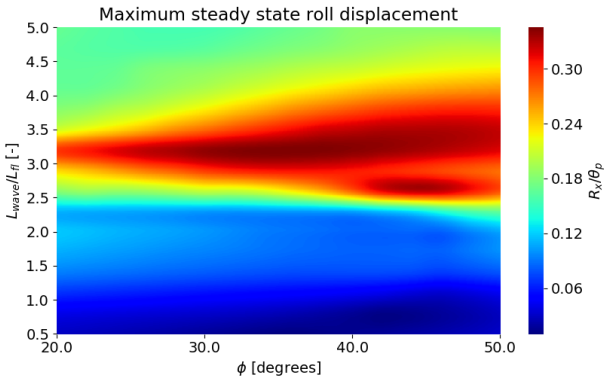

(e) Roll rotation

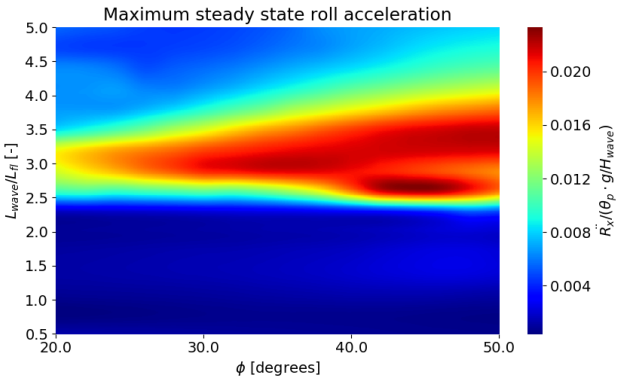

(f) Roll acceleration

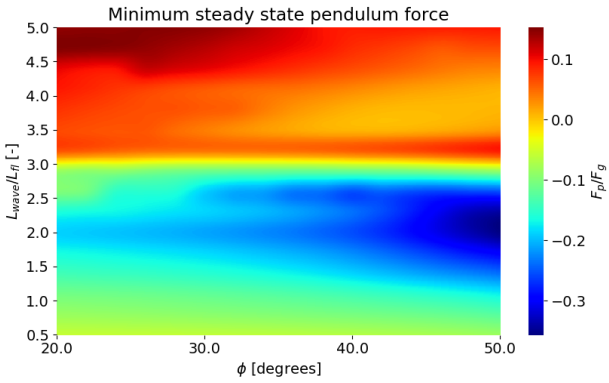

(g) Lowest (most negative) pendulum force

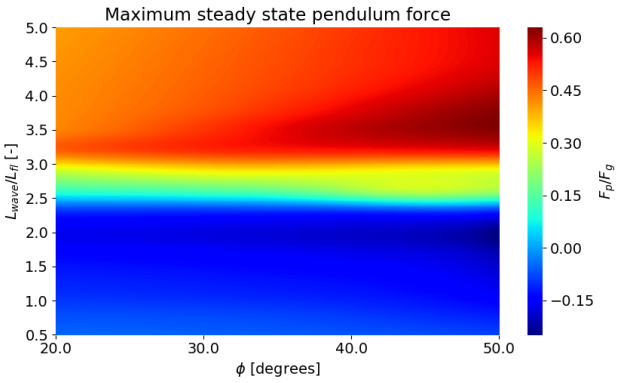

(h) Highest (most positive) pendulum force

Figure M.17: Steady state motion characteristics for Case C3 as function of pendulum angle and wave length

Case C4

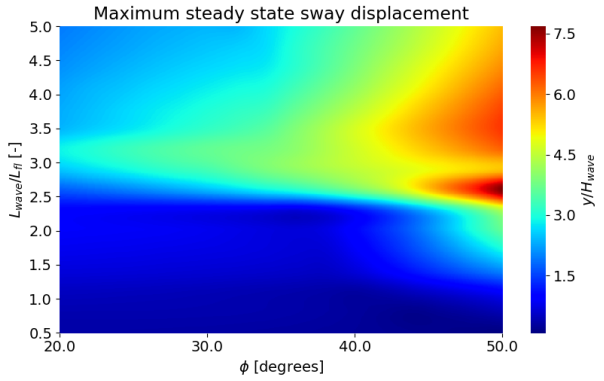

(a) Sway displacement

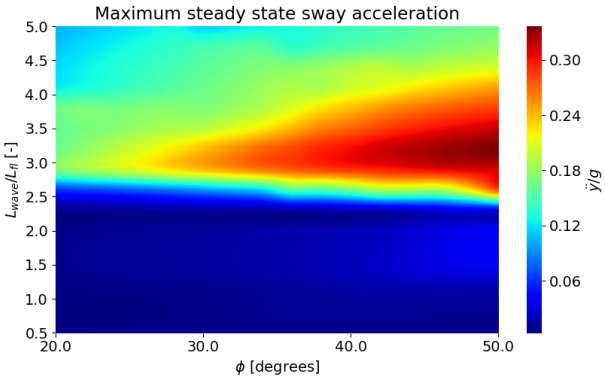

(b) Sway acceleration

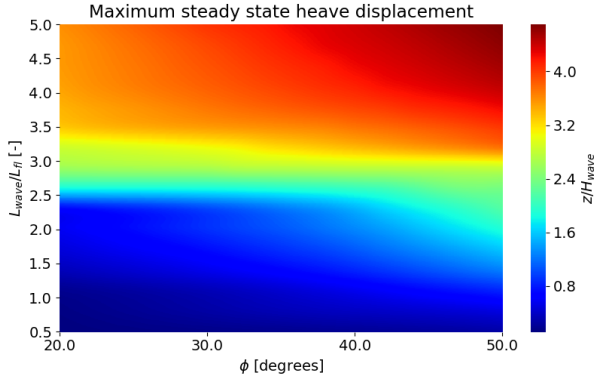

(c) Heave displacement

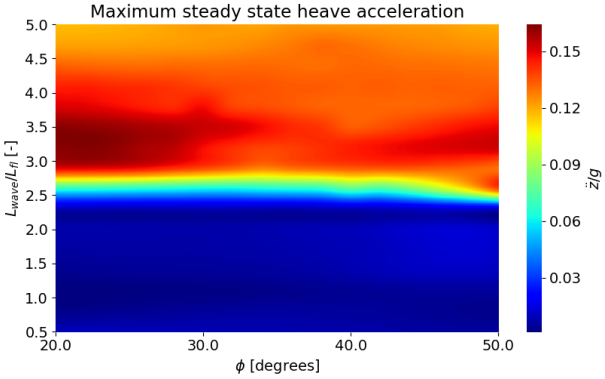

(d) Heave acceleration

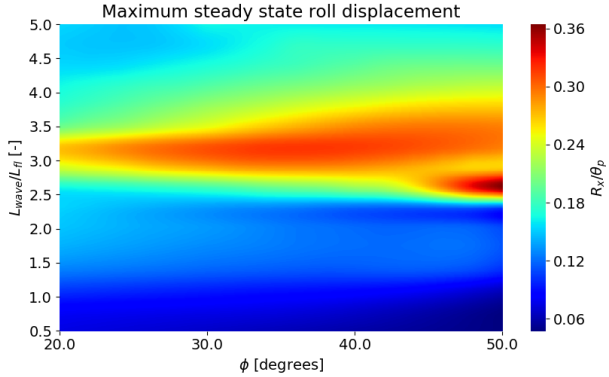

(e) Roll rotation

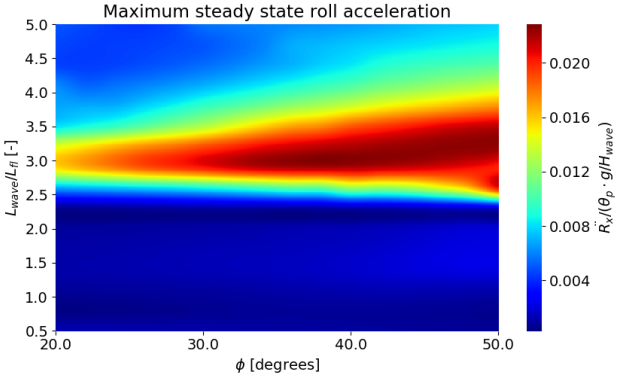

(f) Roll acceleration

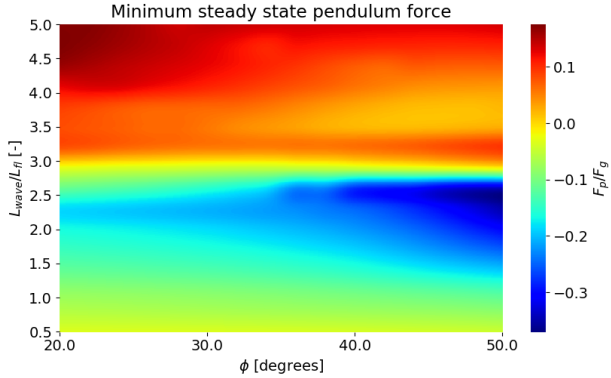

(g) Lowest (most negative) pendulum force

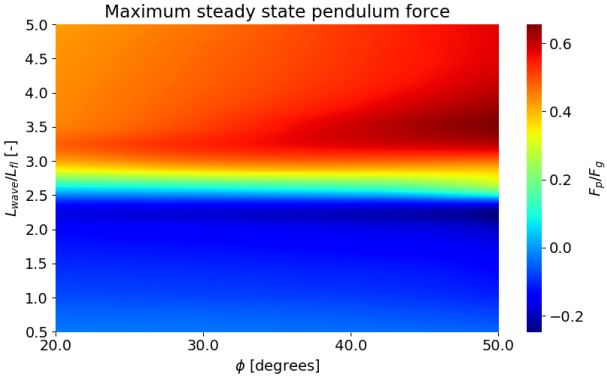

(h) Highest (most positive) pendulum force

Figure M.18: Steady state motion characteristics for Case C4 as function of pendulum angle and wave length

Case C5

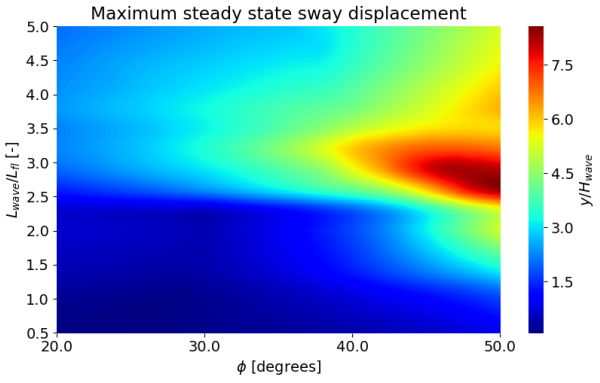

(a) Sway displacement

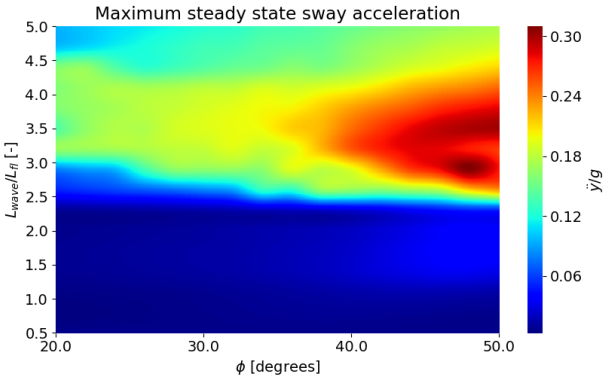

(b) Sway acceleration

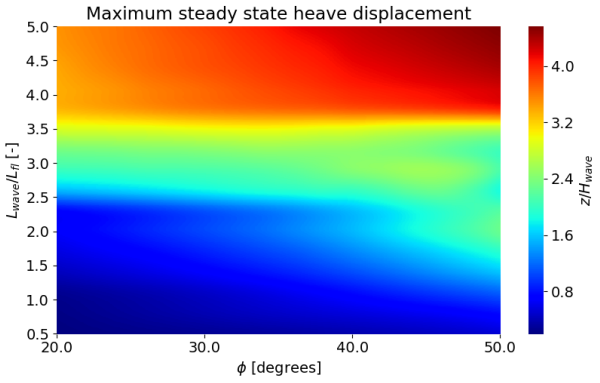

(c) Heave displacement

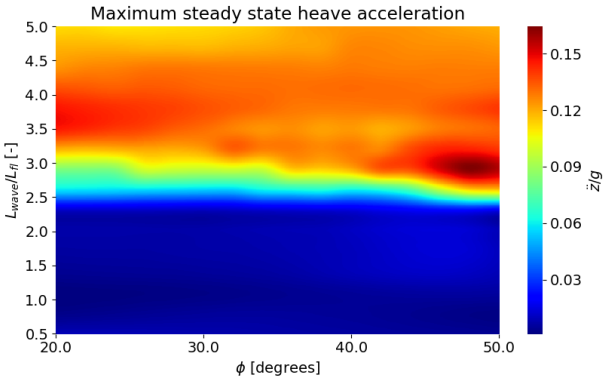

(d) Heave acceleration

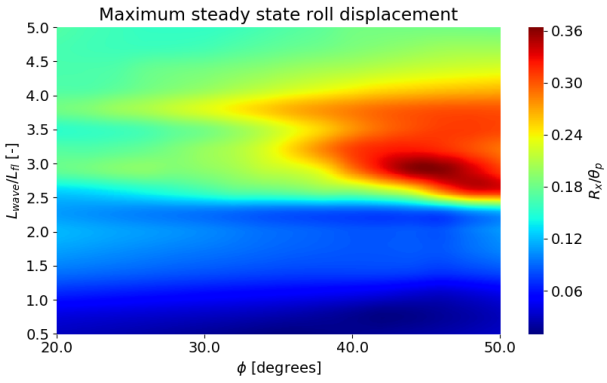

(e) Roll rotation

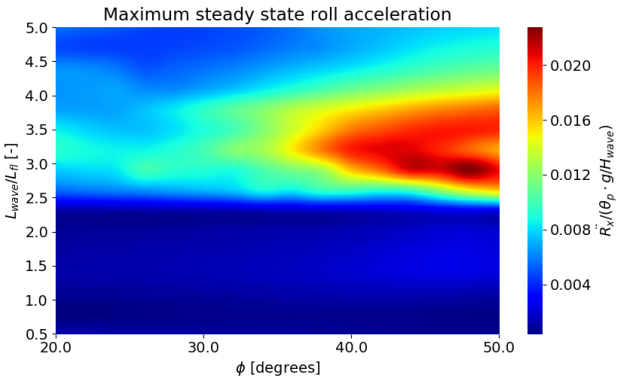

(f) Roll acceleration

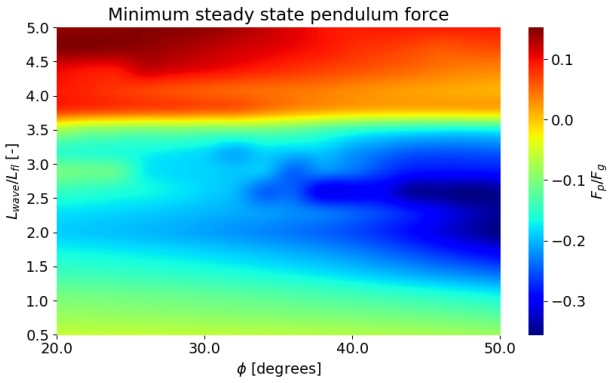

(g) Lowest (most negative) pendulum force

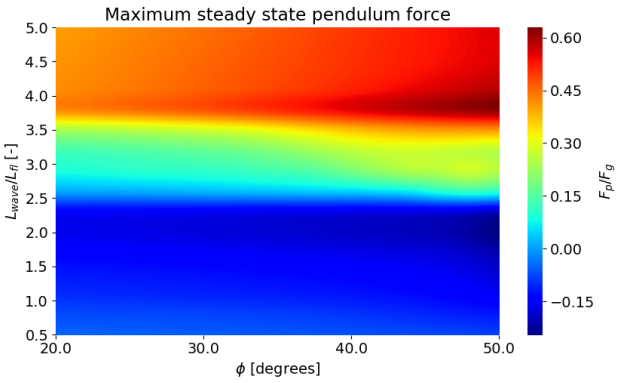

(h) Highest (most positive) pendulum force

Figure M.19: Steady state motion characteristics for Case C5 as function of pendulum angle and wave length

Case C6

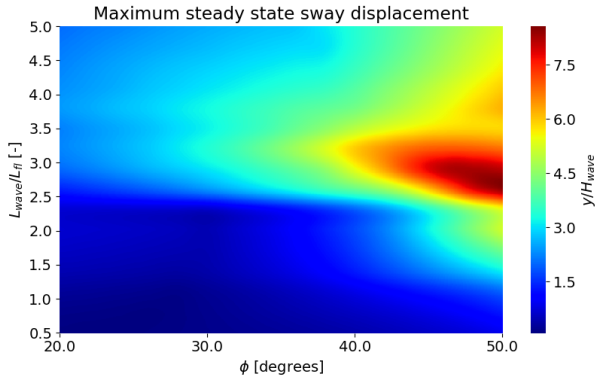

(a) Sway displacement

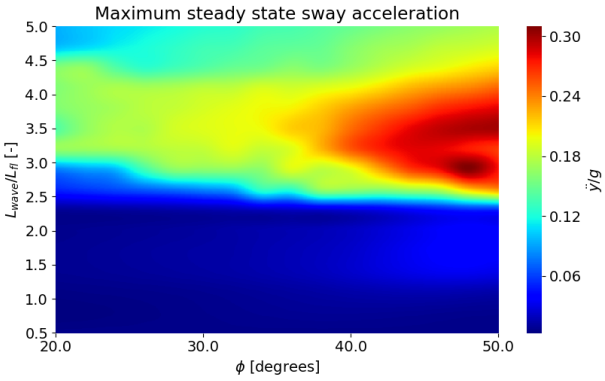

(b) Sway acceleration

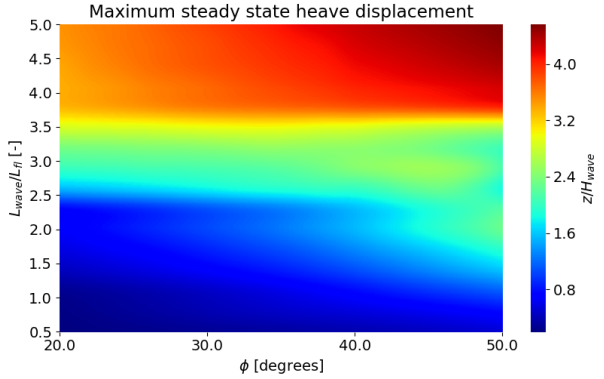

(c) Heave displacement

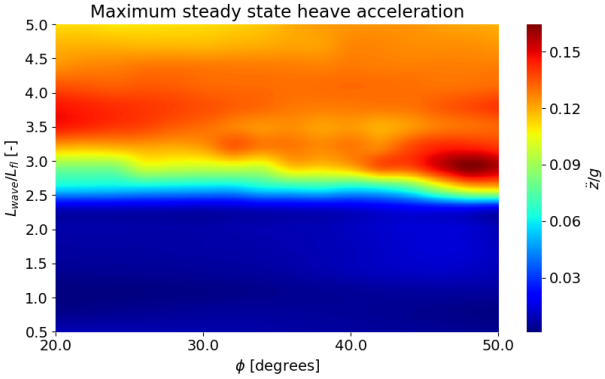

(d) Heave acceleration

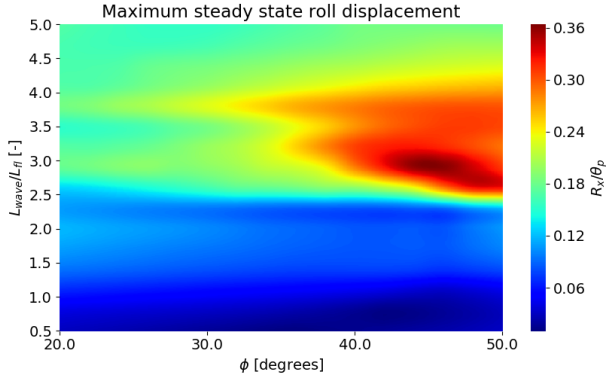

(e) Roll rotation

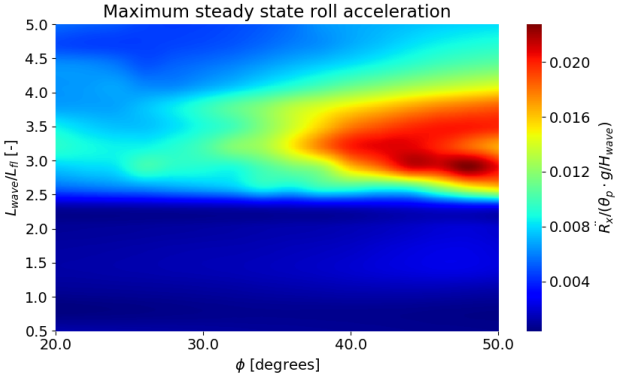

(f) Roll acceleration

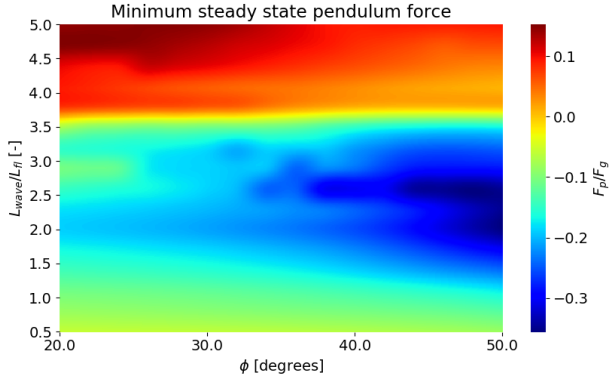

(g) Lowest (most negative) pendulum force

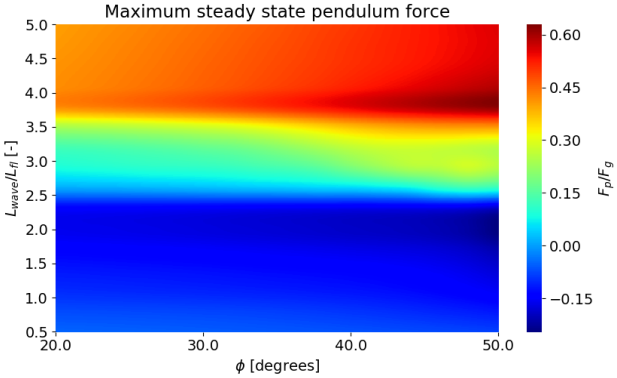

(h) Highest (most positive) pendulum force

Figure M.20: Steady state motion characteristics for Case C6 as function of pendulum angle and wave length

M.6. Pendulum hinge location versus wave length (+ wave height + flow velocity + wind force)

This section accompanies Subsection 6.1.5.

Case C1

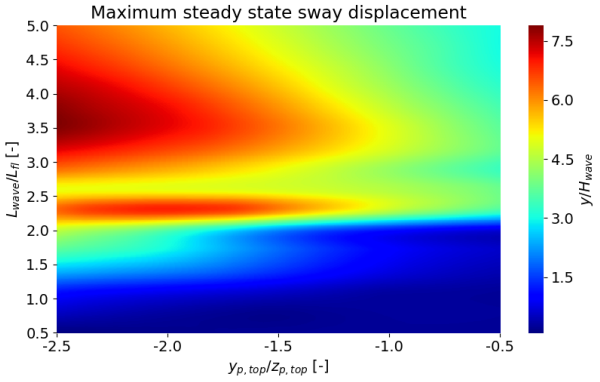

(a) Sway displacement

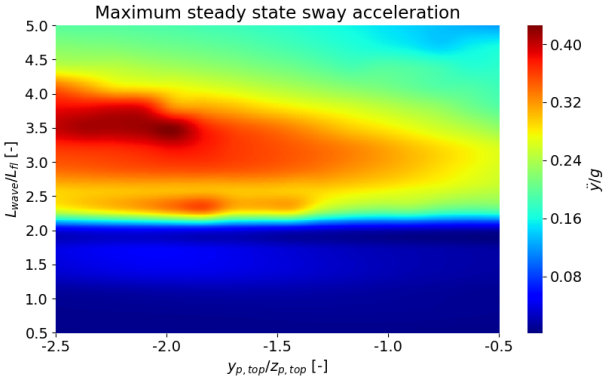

(b) Sway acceleration

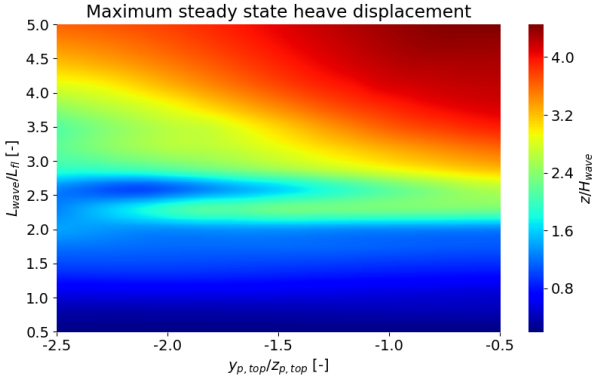

(c) Heave displacement

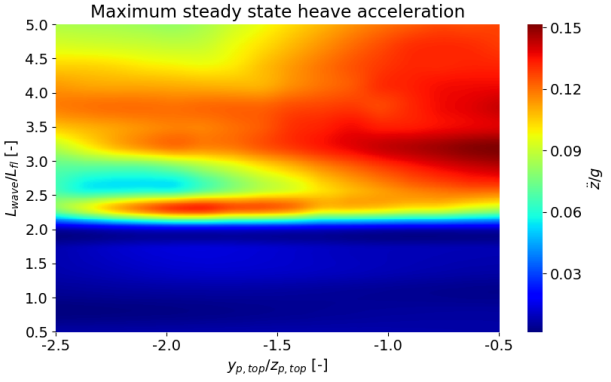

(d) Heave acceleration

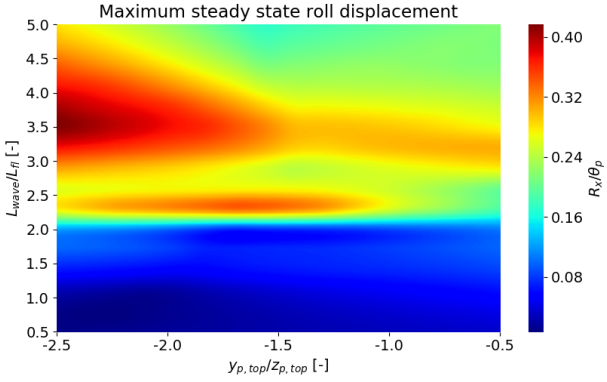

(e) Roll rotation

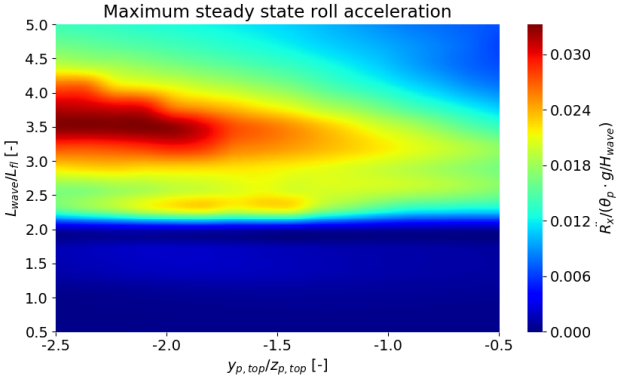

(f) Roll acceleration

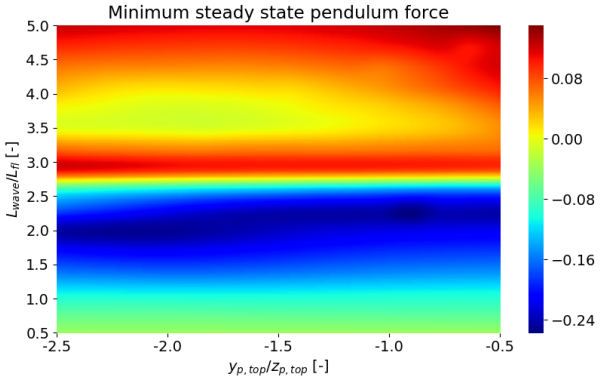

(g) Lowest (most negative) pendulum force

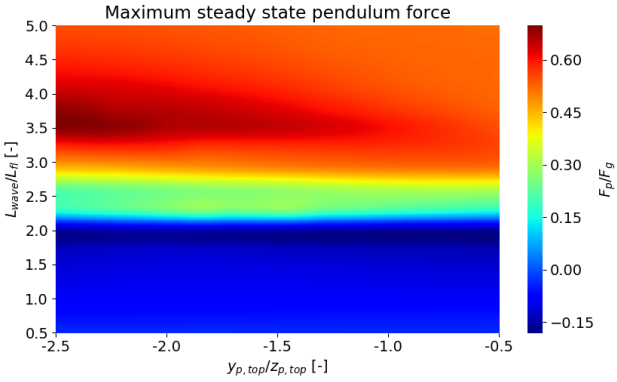

(h) Highest (most positive) pendulum force

Figure M.21: Steady state motion characteristics for Case C1 as function of hinge location and wave length

Case C2

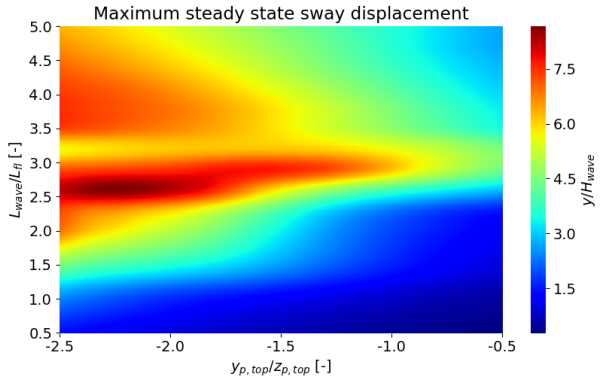

(a) Sway displacement

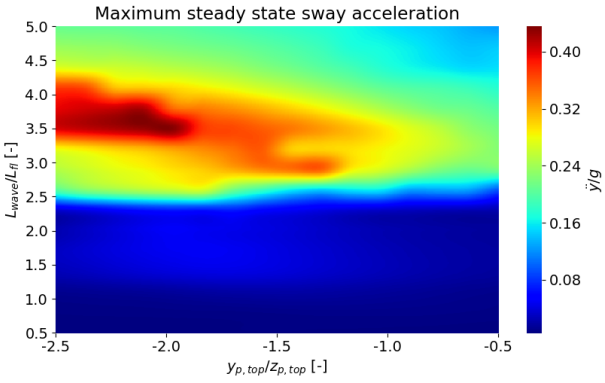

(b) Sway acceleration

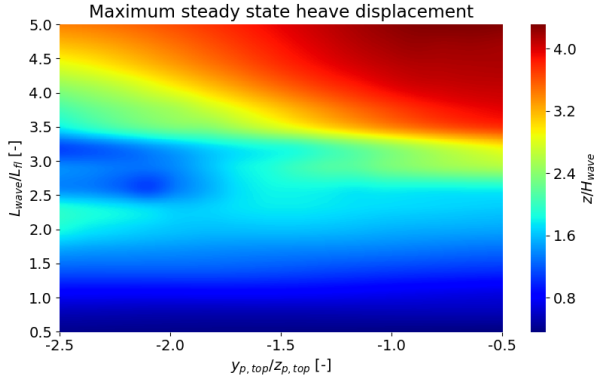

(c) Heave displacement

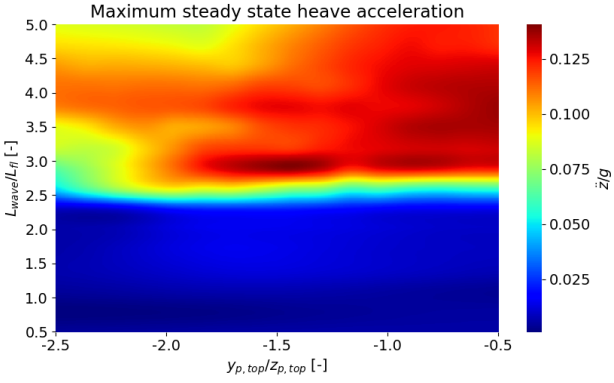

(d) Heave acceleration

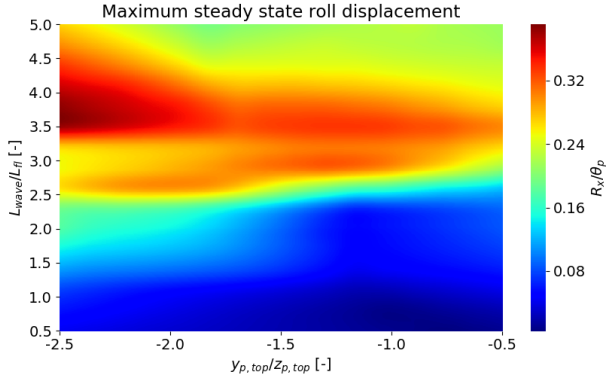

(e) Roll rotation

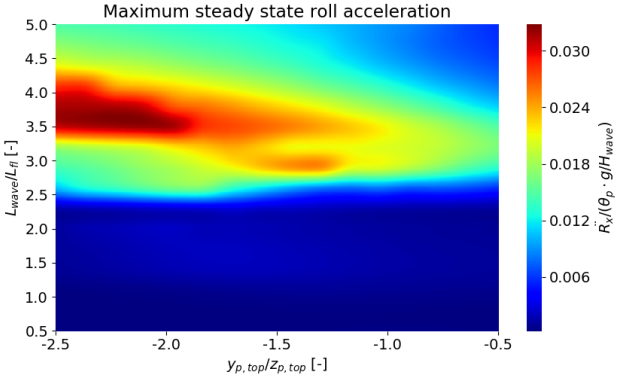

(f) Roll acceleration

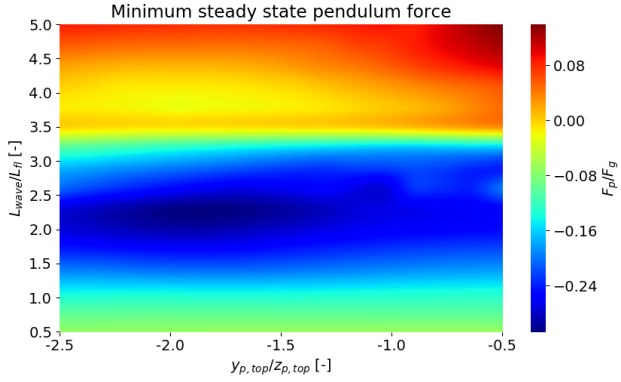

(g) Lowest (most negative) pendulum force

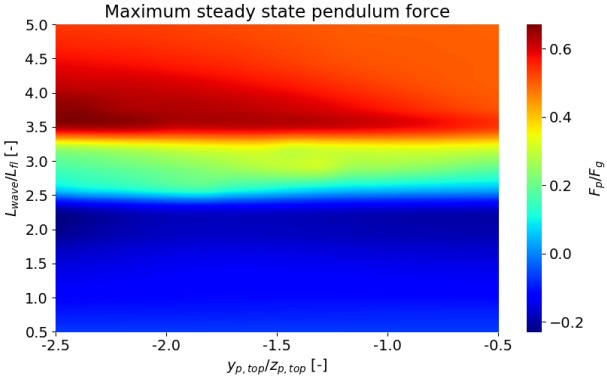

(h) Highest (most positive) pendulum force

Figure M.22: Steady state motion characteristics for Case C2 as function of hinge location and wave length

Case C3

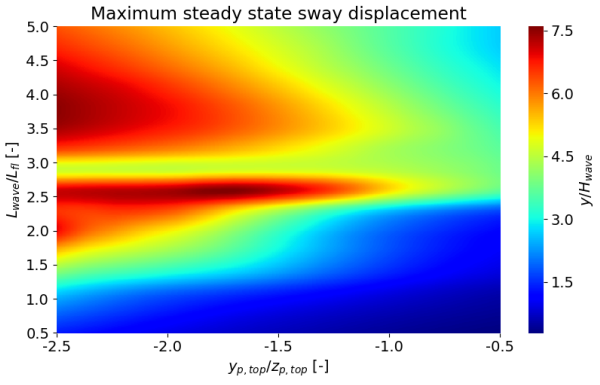

(a) Sway displacement

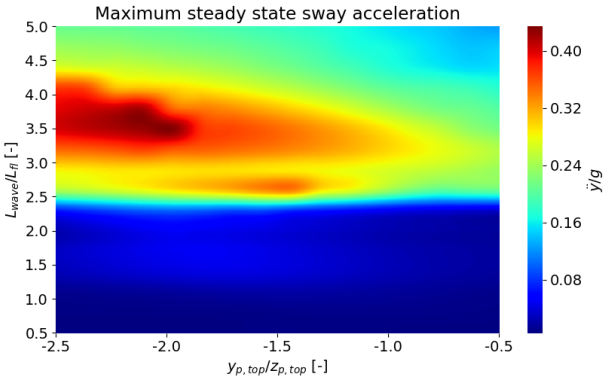

(b) Sway acceleration

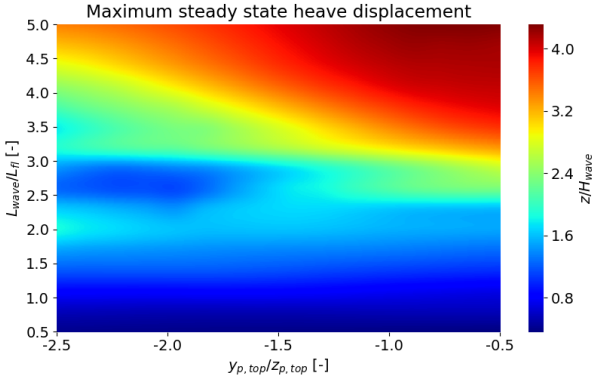

(c) Heave displacement

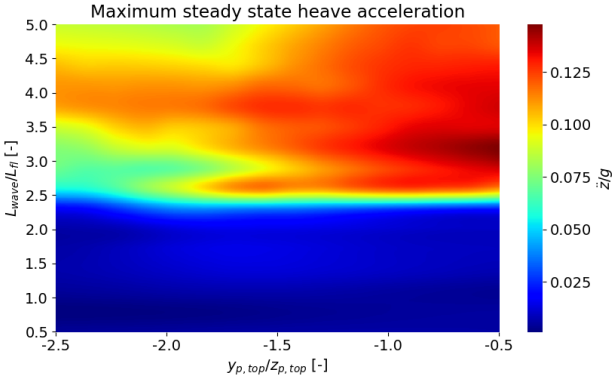

(d) Heave acceleration

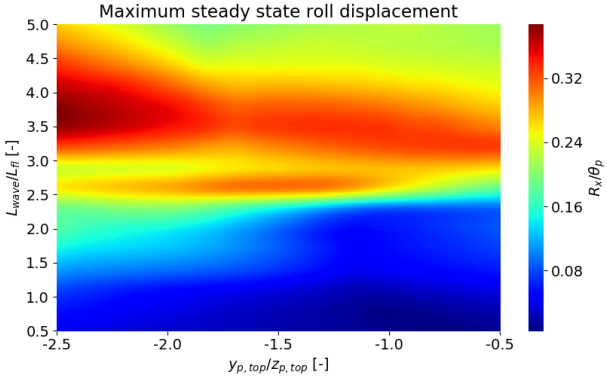

(e) Roll rotation

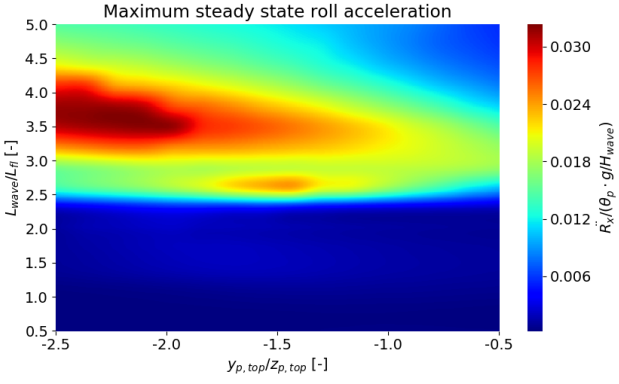

(f) Roll acceleration

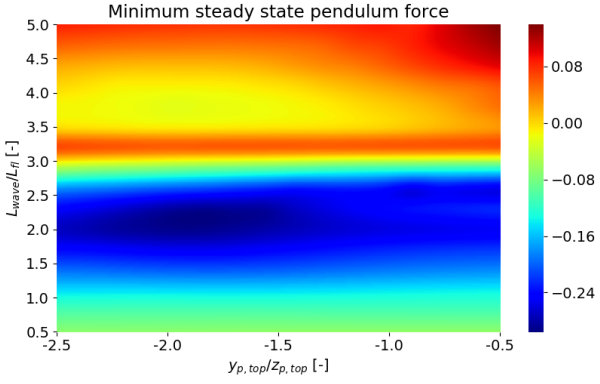

(g) Lowest (most negative) pendulum force

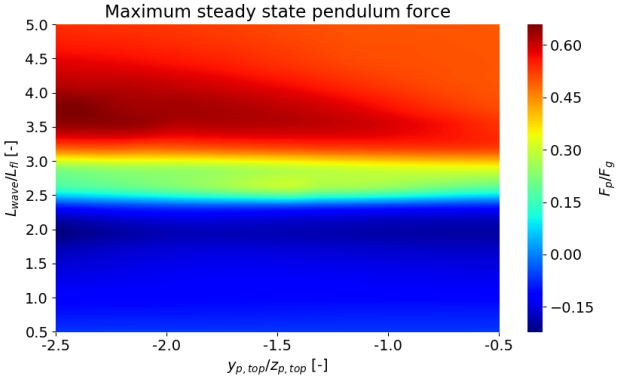

(h) Highest (most positive) pendulum force

Figure M.23: Steady state motion characteristics for Case C3 as function of hinge location and wave length

Case C4

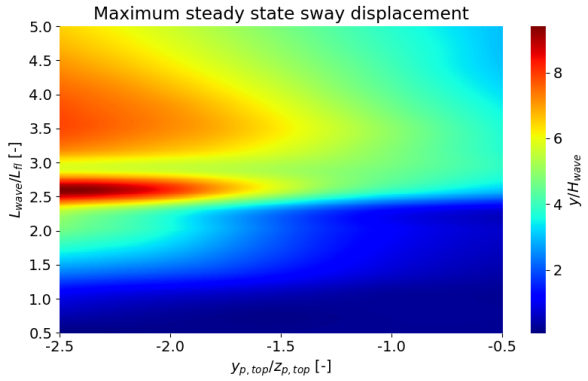

(a) Sway displacement

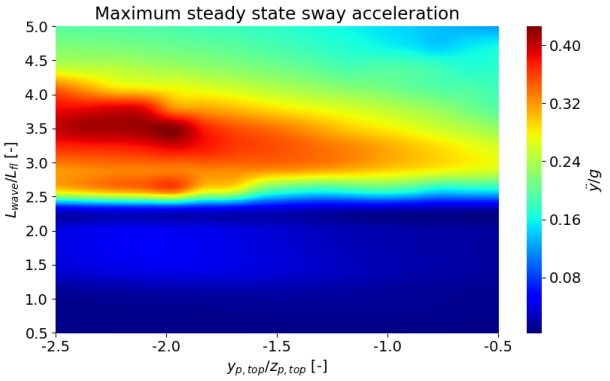

(b) Sway acceleration

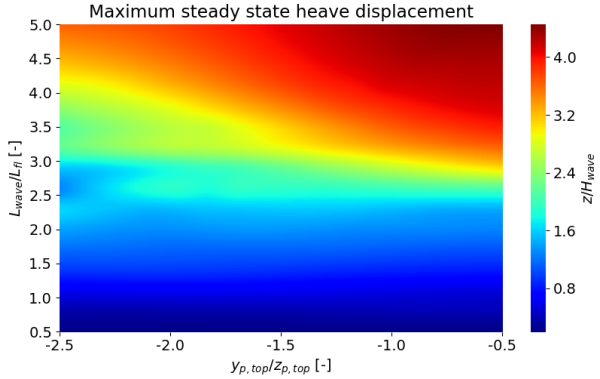

(c) Heave displacement

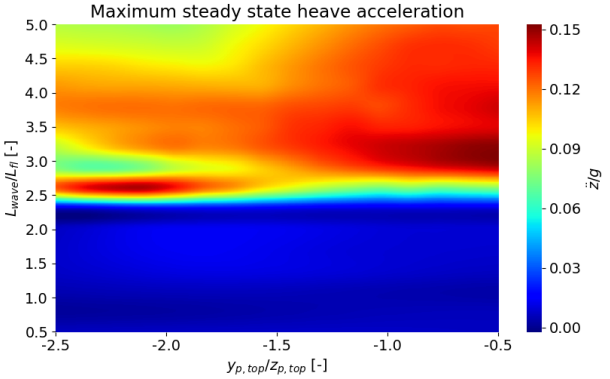

(d) Heave acceleration

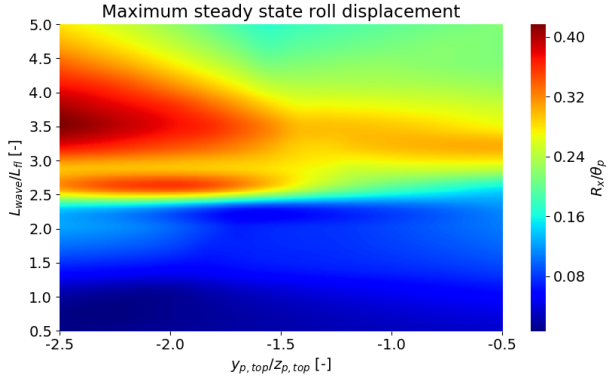

(e) Roll rotation

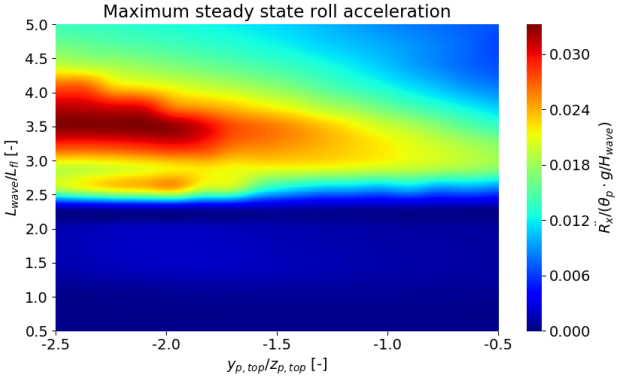

(f) Roll acceleration

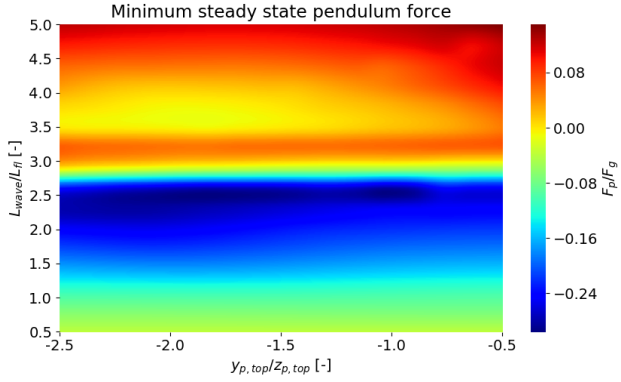

(g) Lowest (most negative) pendulum force

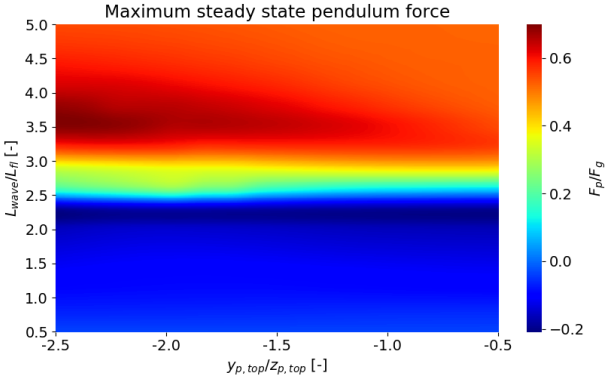

(h) Highest (most positive) pendulum force

Figure M.24: Steady state motion characteristics for Case C4 as function of hinge location and wave length

Case C5

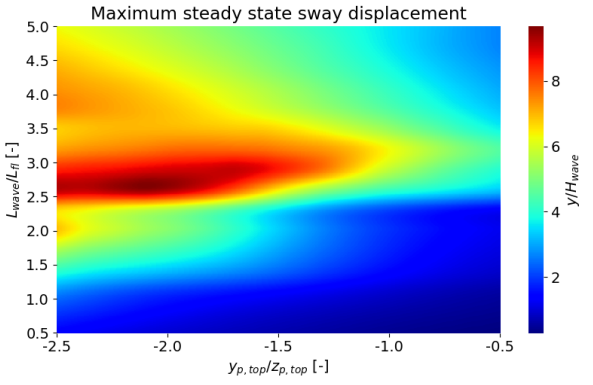

(a) Sway displacement

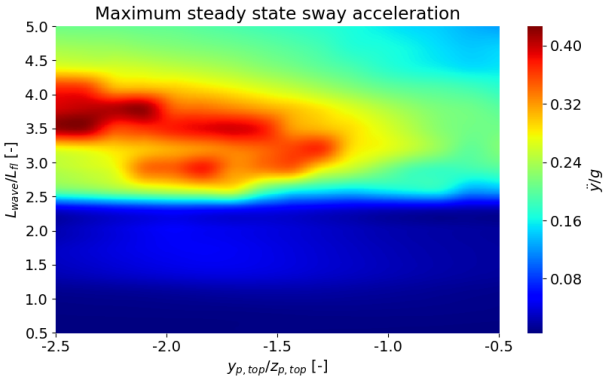

(b) Sway acceleration

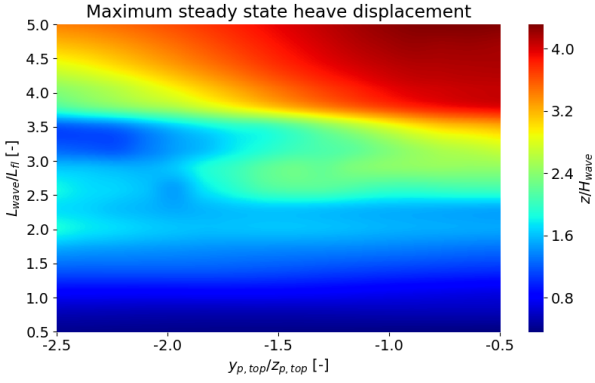

(c) Heave displacement

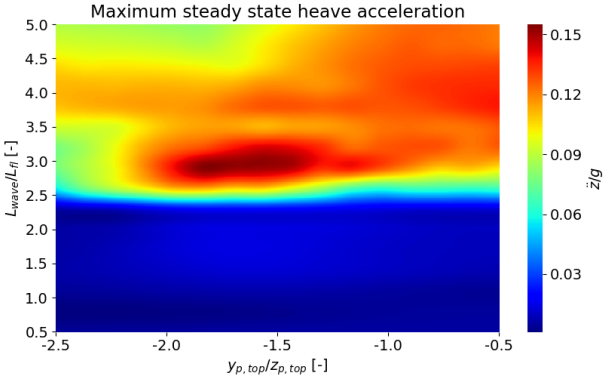

(d) Heave acceleration

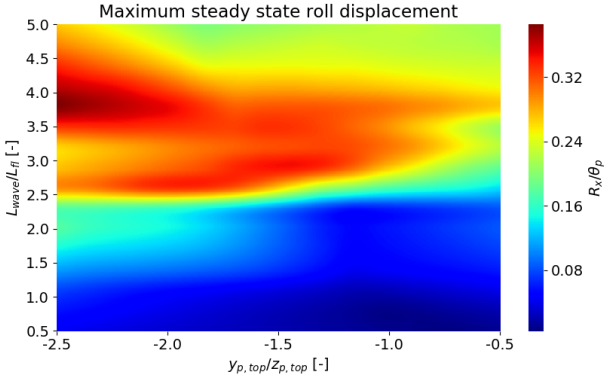

(e) Roll rotation

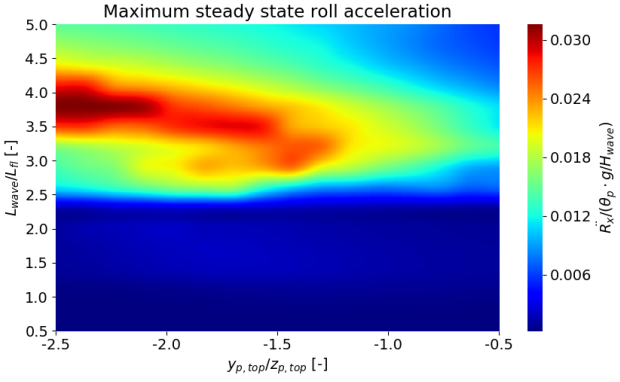

(f) Roll acceleration

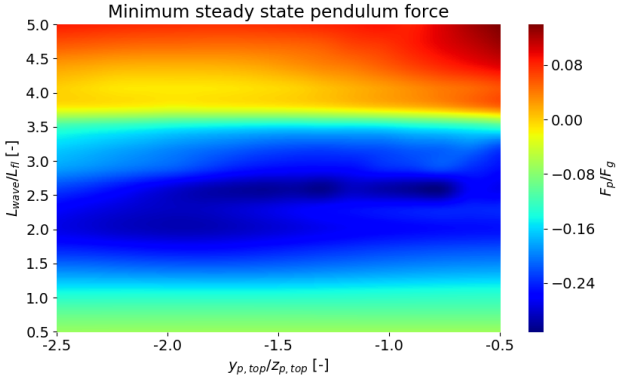

(g) Lowest (most negative) pendulum force

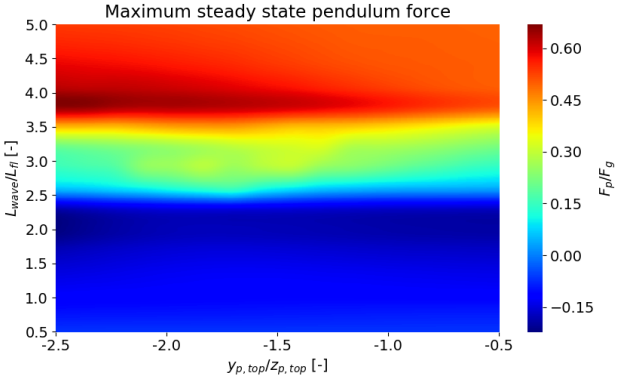

(h) Highest (most positive) pendulum force

Figure M.25: Steady state motion characteristics for Case C5 as function of hinge location and wave length

Case C6

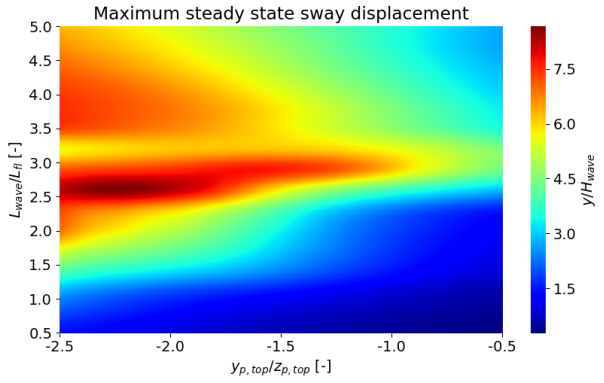

(a) Sway displacement

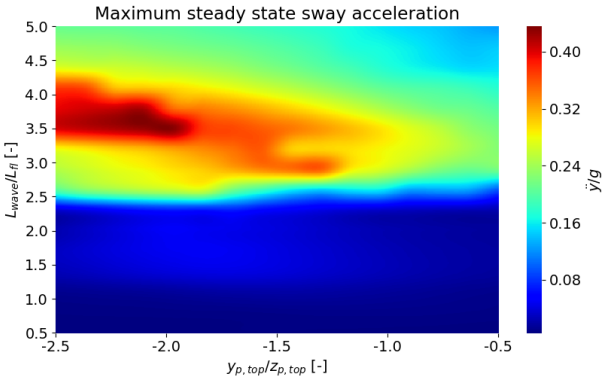

(b) Sway acceleration

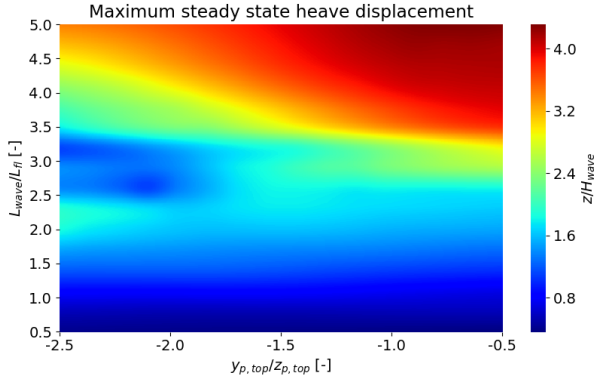

(c) Heave displacement

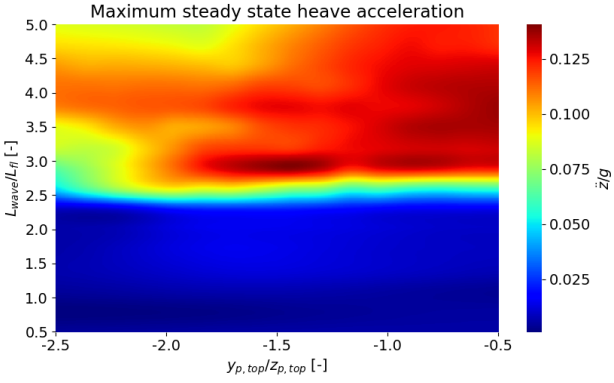

(d) Heave acceleration

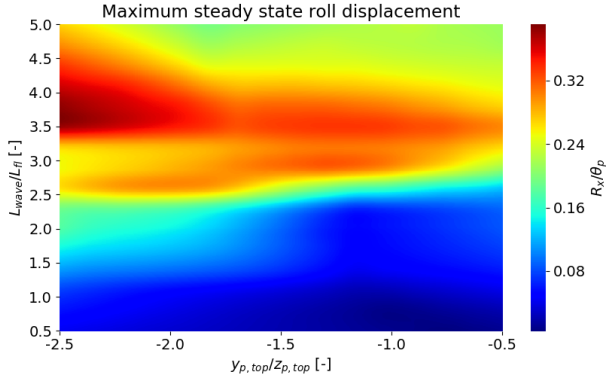

(e) Roll rotation

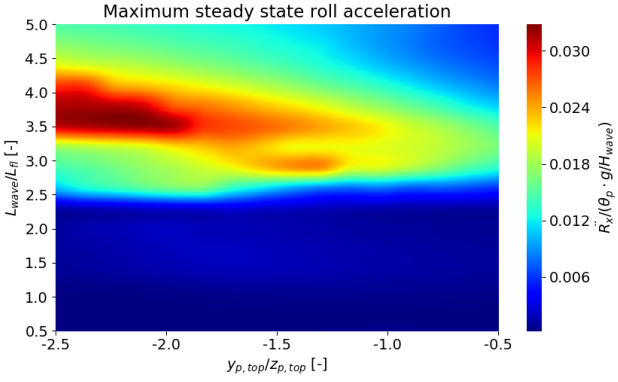

(f) Roll acceleration

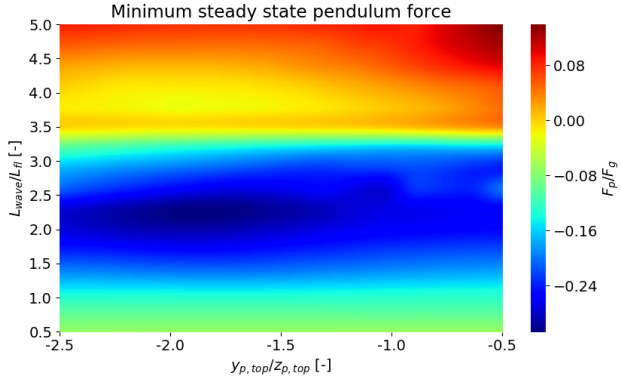

(g) Lowest (most negative) pendulum force

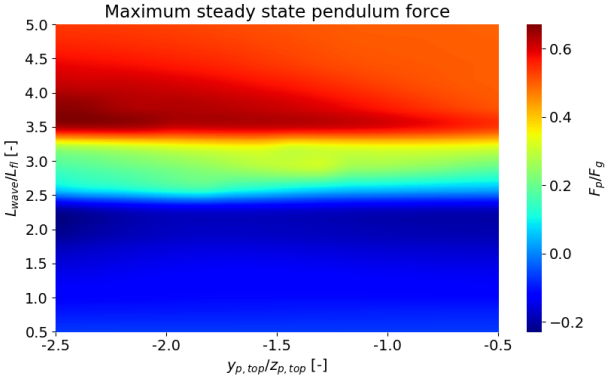

(h) Highest (most positive) pendulum force

Figure M.26: Steady state motion characteristics for Case C6 as function of hinge location and wave length

M.7. Water depth versus wave length (+ wave height + flow velocity + wind force)

This section accompanies Subsection 6.1.6.

Case C1

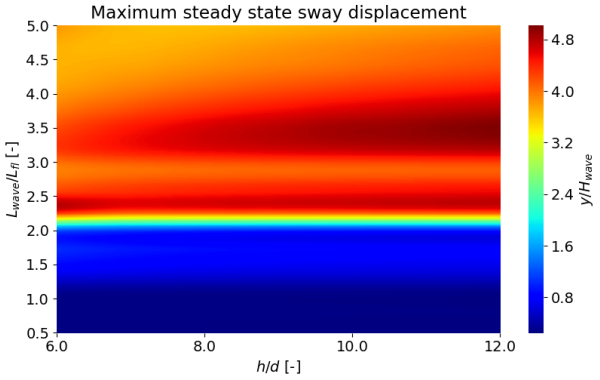

(a) Sway displacement

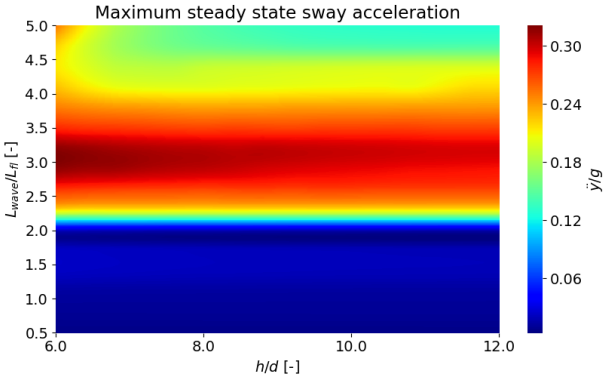

(b) Sway acceleration

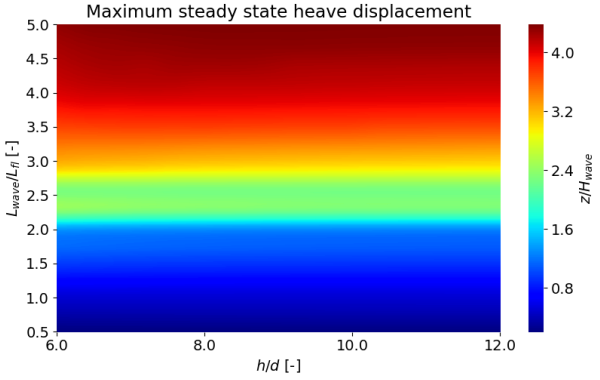

(c) Heave displacement

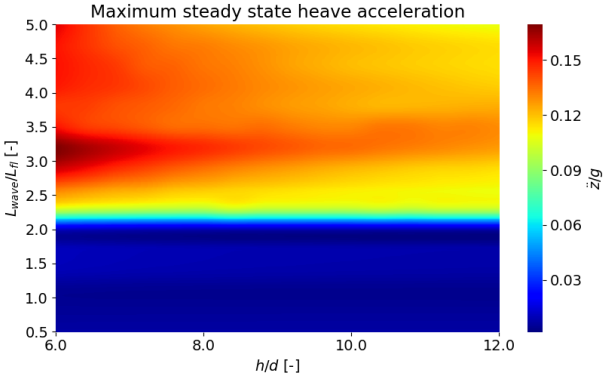

(d) Heave acceleration

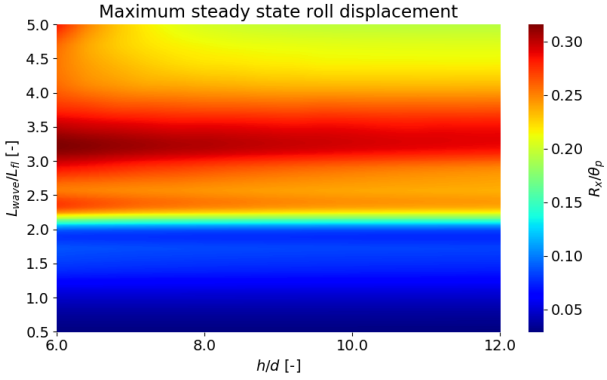

(e) Roll rotation

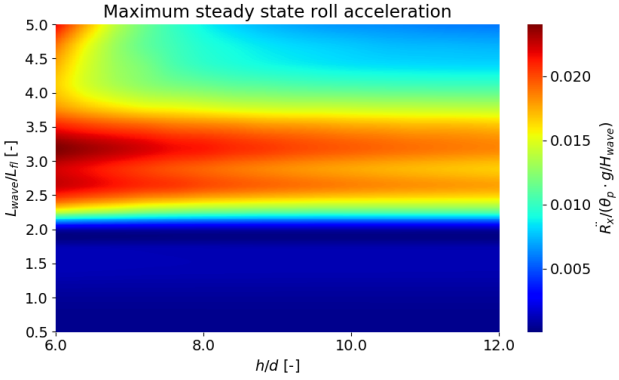

(f) Roll acceleration

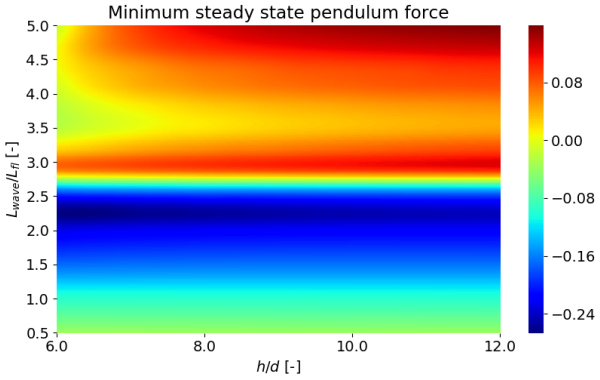

(g) Lowest (most negative) pendulum force

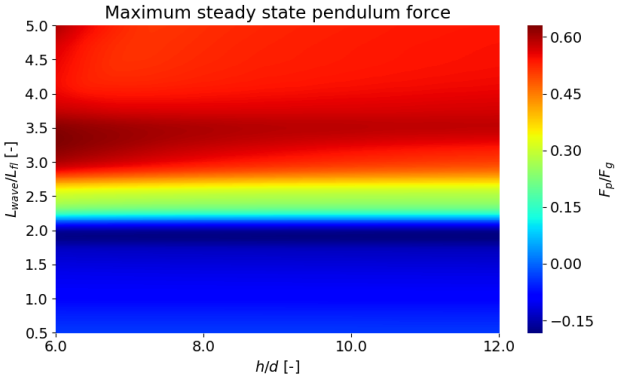

(h) Highest (most positive) pendulum force

Figure M.27: Steady state motion characteristics for Case C1 as function of water depth and wave length

Case C2

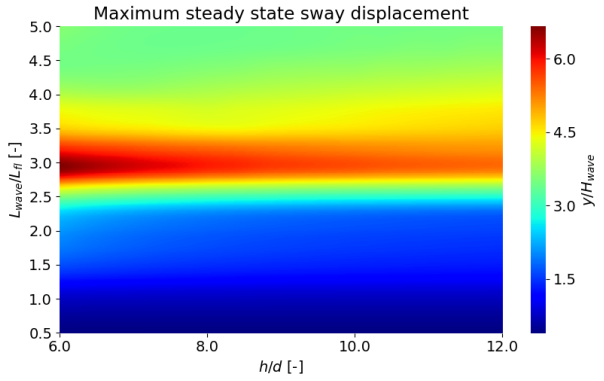

(a) Sway displacement

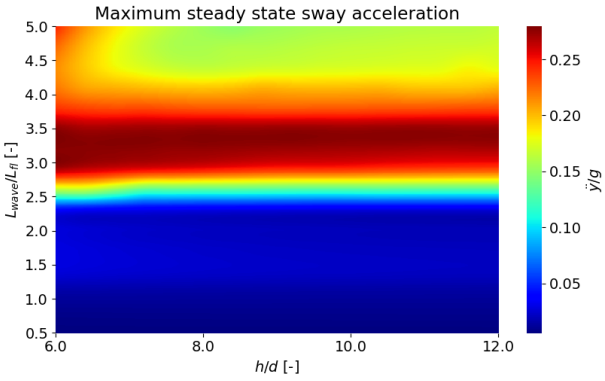

(b) Sway acceleration

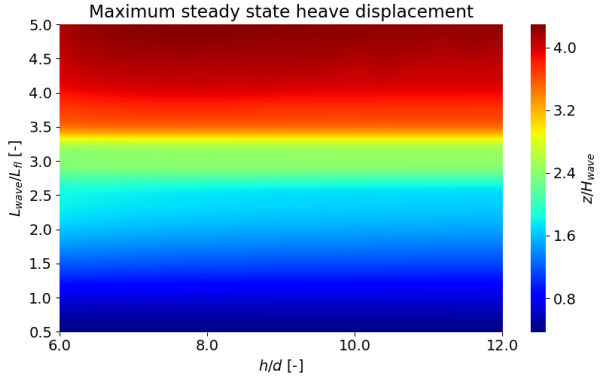

(c) Heave displacement

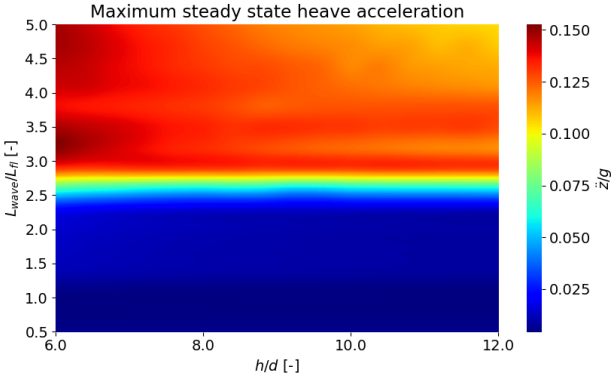

(d) Heave acceleration

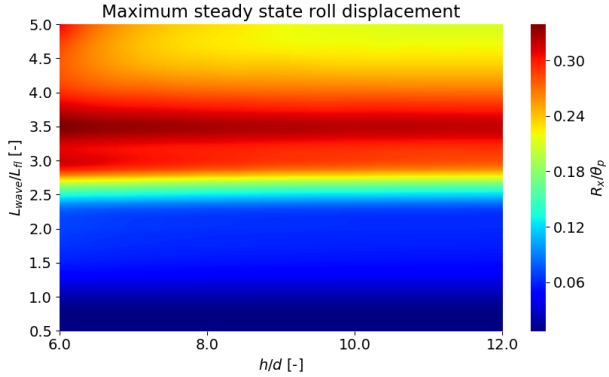

(e) Roll rotation

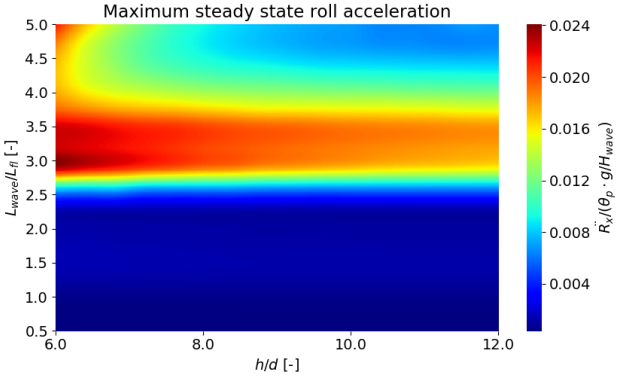

(f) Roll acceleration

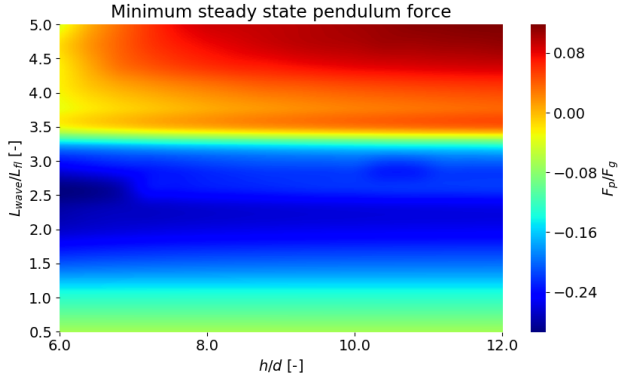

(g) Lowest (most negative) pendulum force

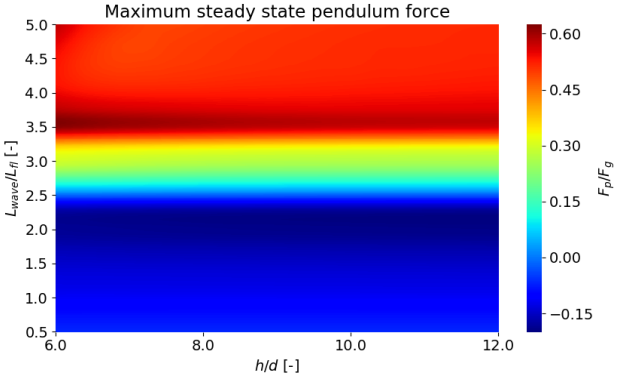

(h) Highest (most positive) pendulum force

Figure M.28: Steady state motion characteristics for Case C2 as function of water depth and wave length

Case C3

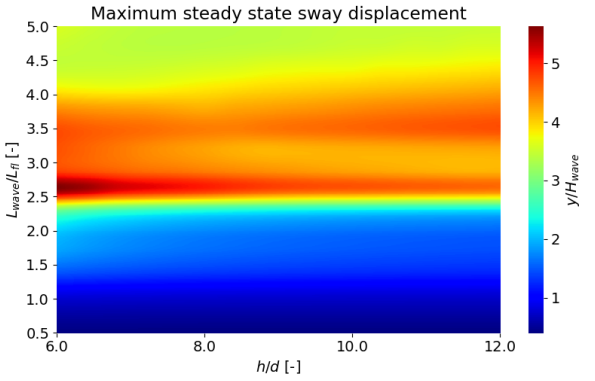

(a) Sway displacement

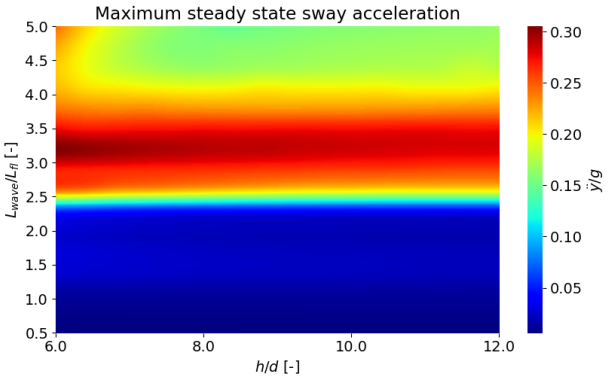

(b) Sway acceleration

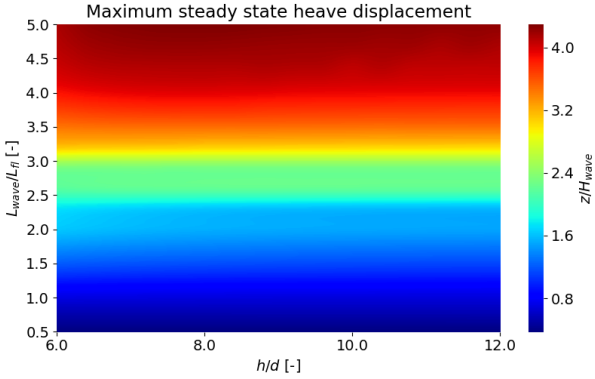

(c) Heave displacement

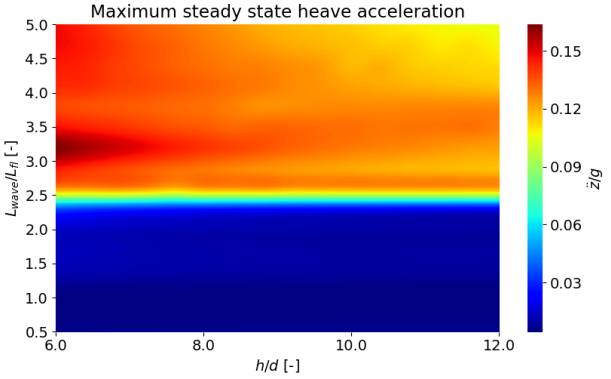

(d) Heave acceleration

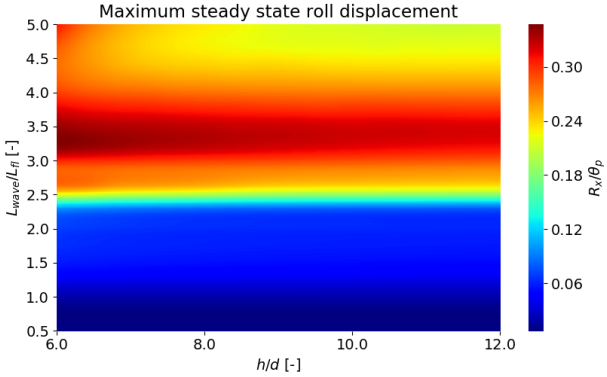

(e) Roll rotation

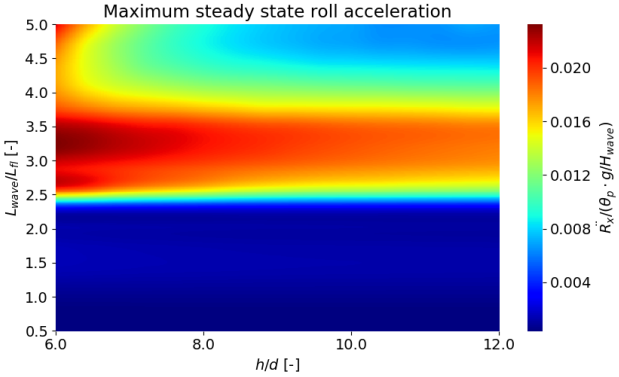

(f) Roll acceleration

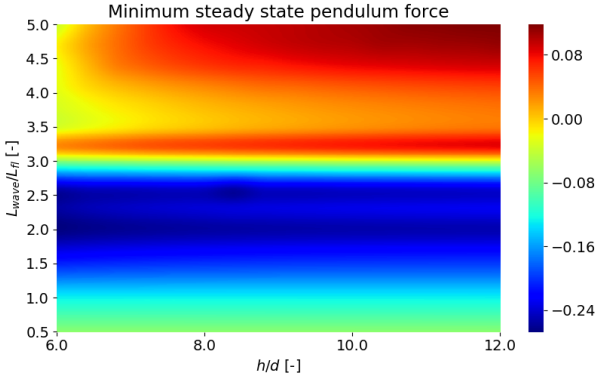

(g) Lowest (most negative) pendulum force

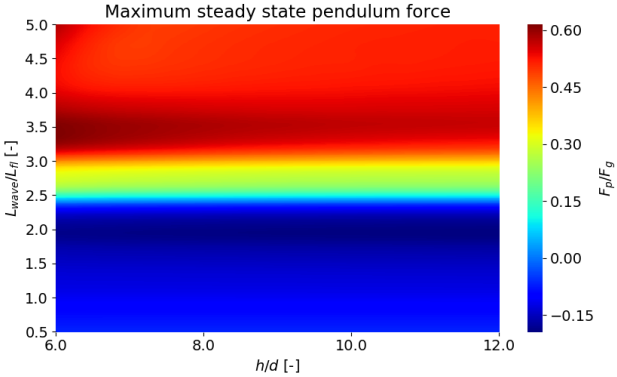

(h) Highest (most positive) pendulum force

Figure M.29: Steady state motion characteristics for Case C3 as function of water depth and wave length

Case C4

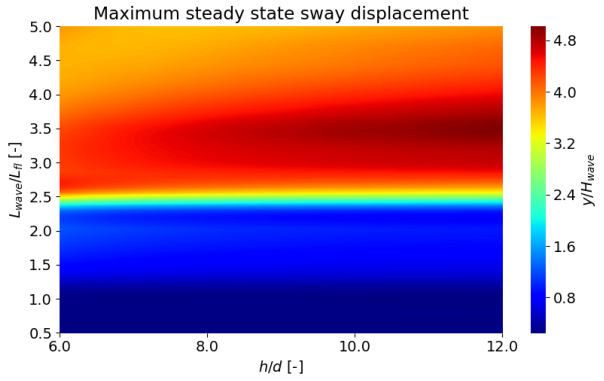

(a) Sway displacement

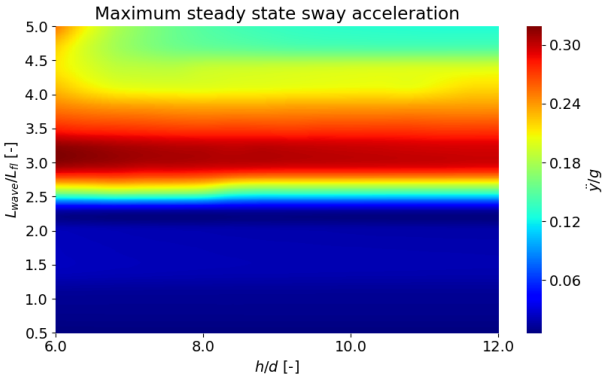

(b) Sway acceleration

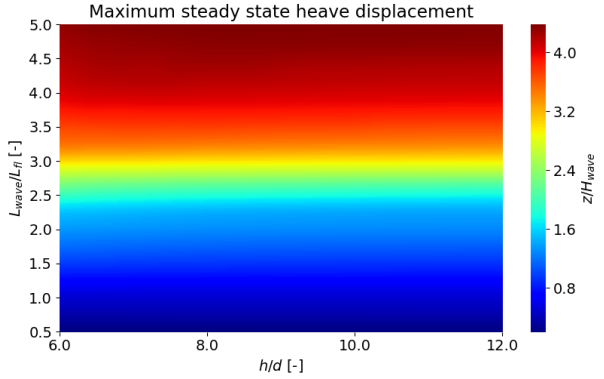

(c) Heave displacement

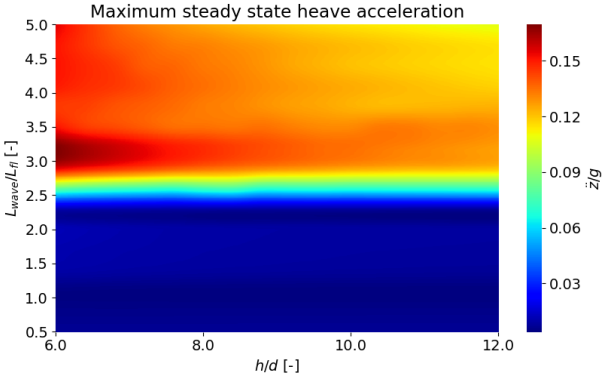

(d) Heave acceleration

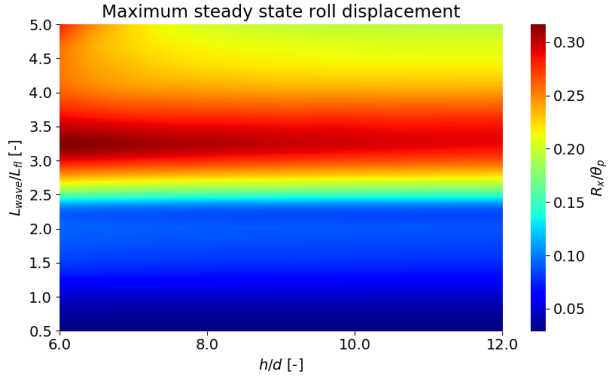

(e) Roll rotation

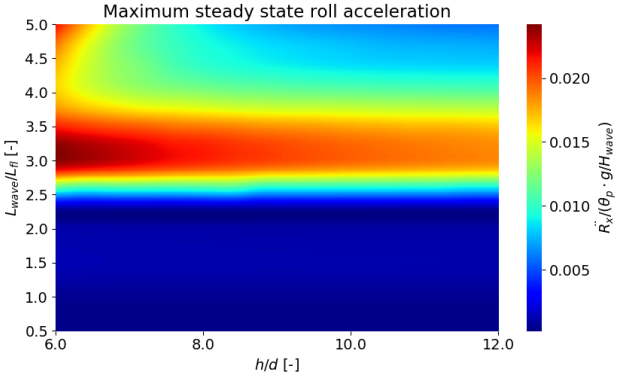

(f) Roll acceleration

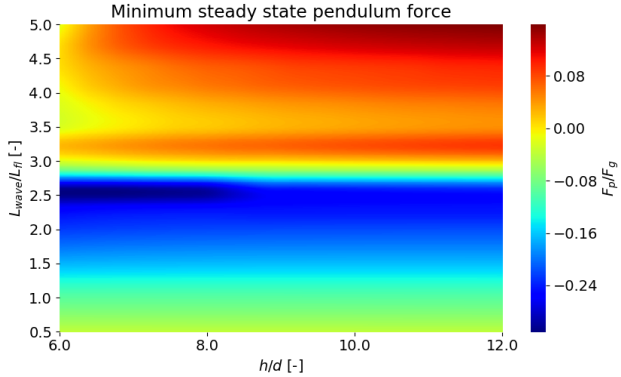

(g) Lowest (most negative) pendulum force

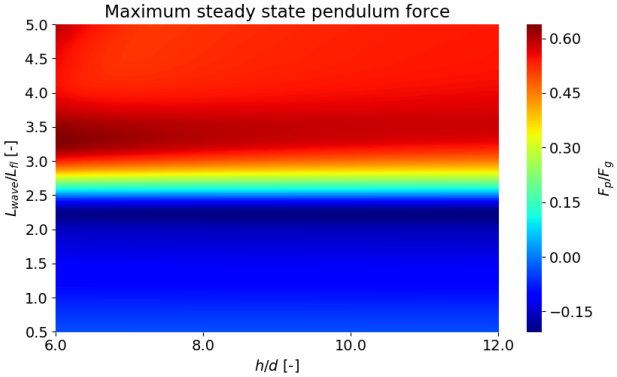

(h) Highest (most positive) pendulum force

Figure M.30: Steady state motion characteristics for Case C4 as function of water depth and wave length

Case C5

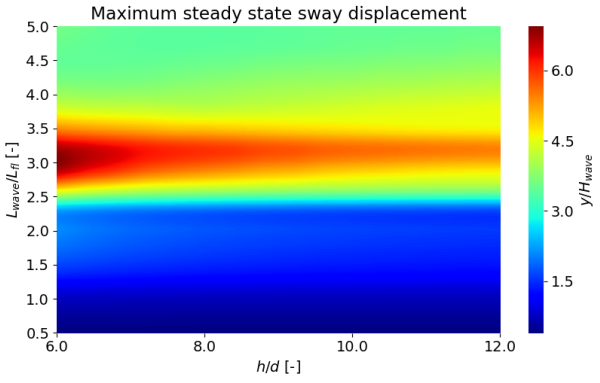

(a) Sway displacement

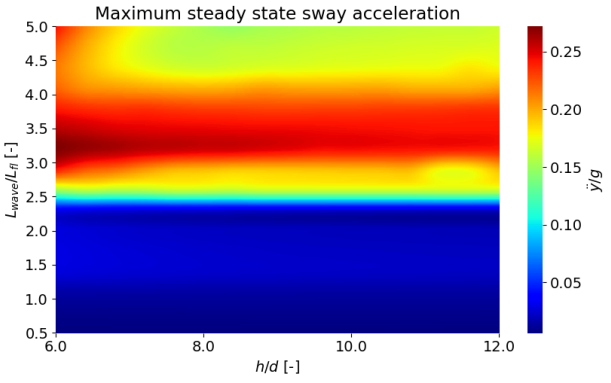

(b) Sway acceleration

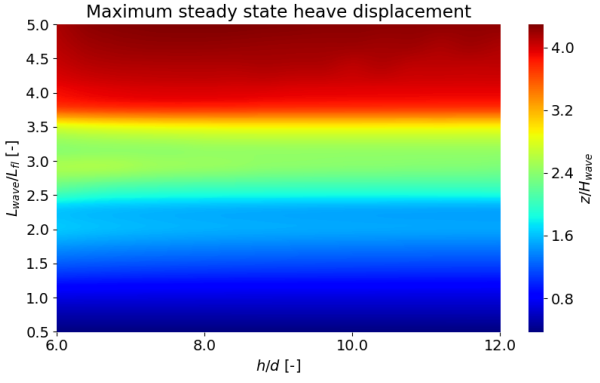

(c) Heave displacement

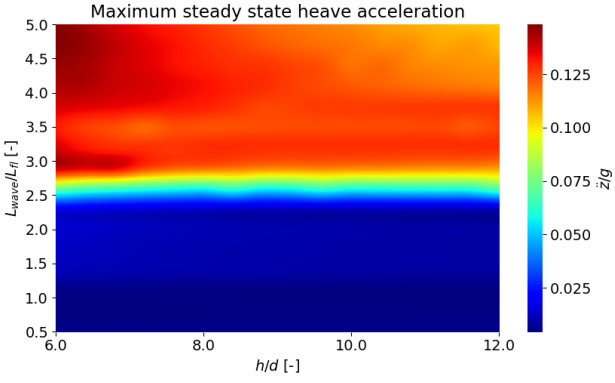

(d) Heave acceleration

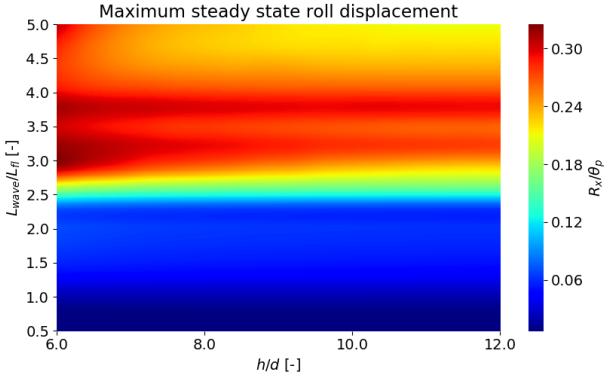

(e) Roll rotation

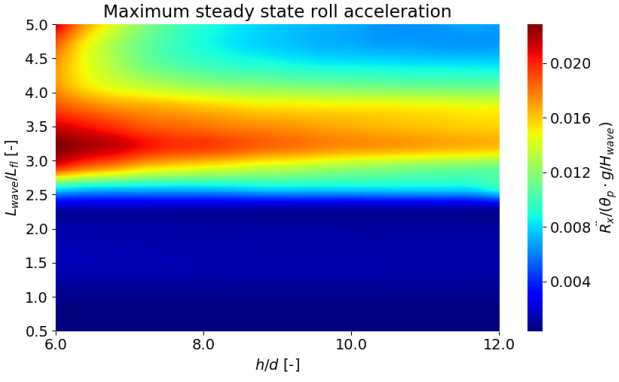

(f) Roll acceleration

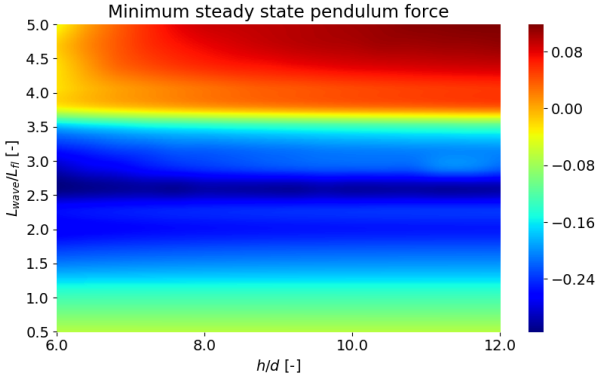

(g) Lowest (most negative) pendulum force

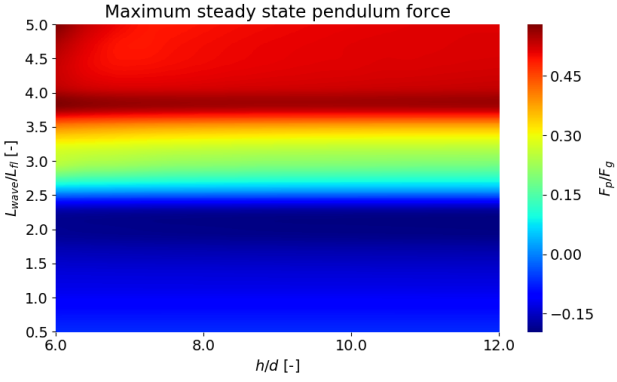

(h) Highest (most positive) pendulum force

Figure M.31: Steady state motion characteristics for Case C5 as function of water depth and wave length

Case C6

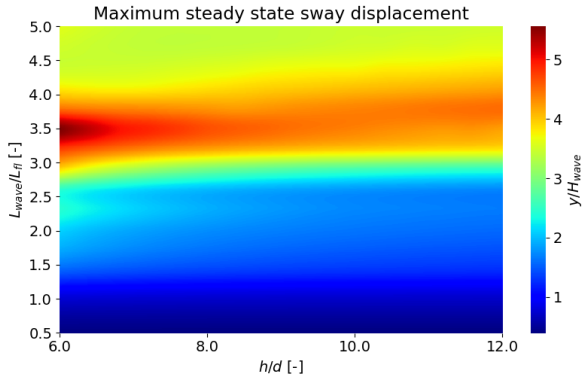

(a) Sway displacement

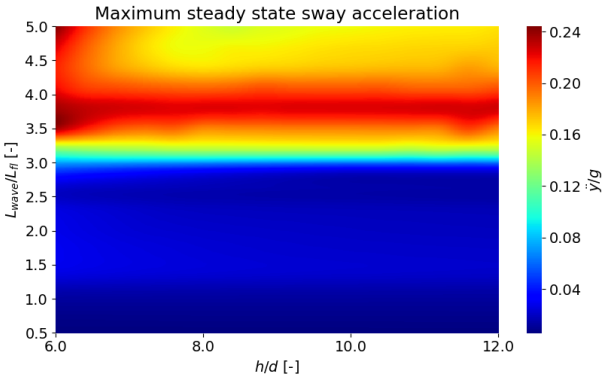

(b) Sway acceleration

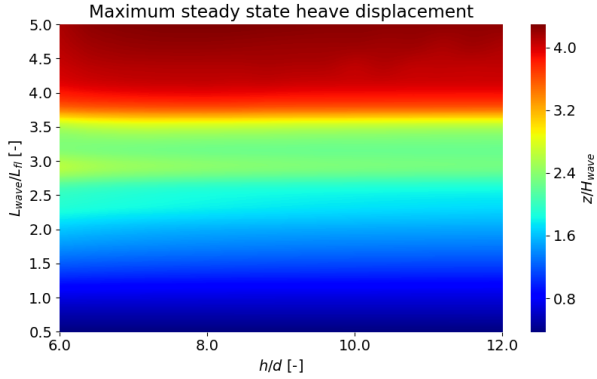

(c) Heave displacement

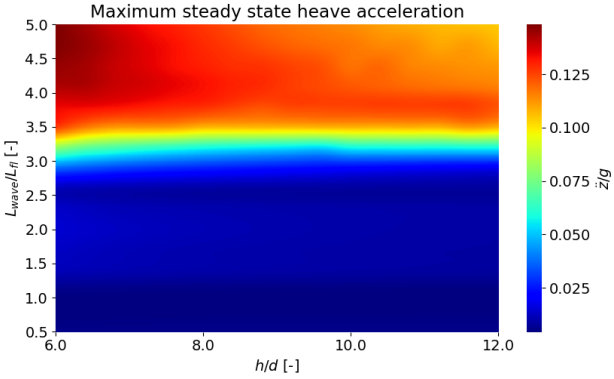

(d) Heave acceleration

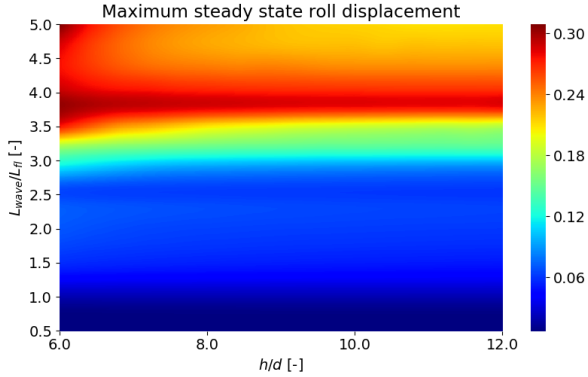

(e) Roll rotation

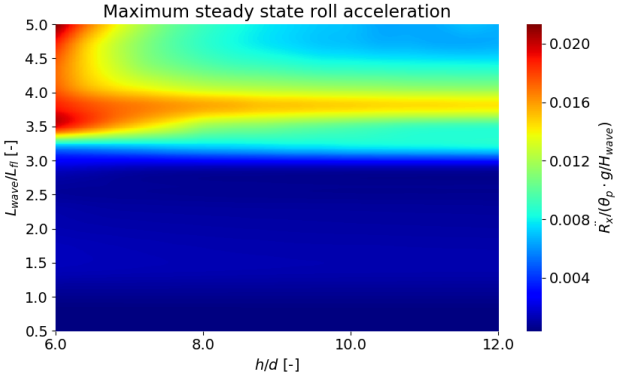

(f) Roll acceleration

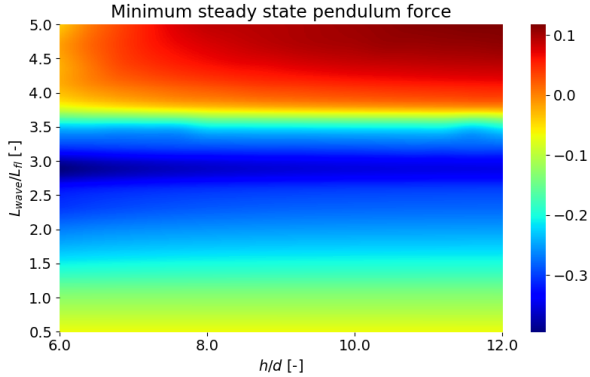

(g) Lowest (most negative) pendulum force

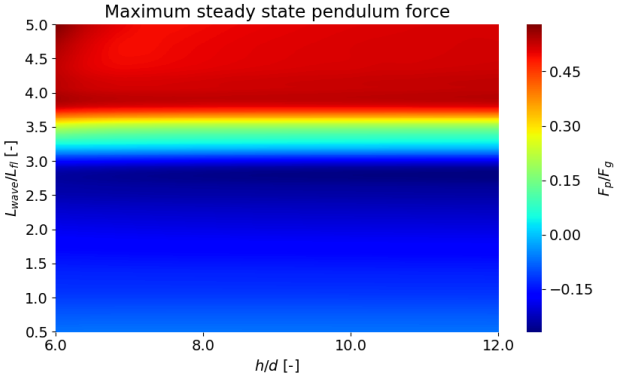

(h) Highest (most positive) pendulum force

Figure M.32: Steady state motion characteristics for Case C6 as function of water depth and wave length